Interaction Notes

Note 410

February 1981

Surface Field Measurements On Scale Models In The Time Domain

H. S. Cabayan, J. Zicker, S. J. Deadirck,
J. Candy, D. Gavel and E. J. Bogdan
Lawrence Livermore National Laboratory
Livermore, California 94550

ABSTRACT

Time-domain measurements have been performed of the surface densities of current and charge induced on scale models when illuminated by a transient electromagnetic pulse in order to provide test points to validate numerical models. Three bodies--a cylinder, a crossed-cylinder, and a 1:100 scale-model 747 aircraft--were used in the experiments. Responses were measured for objects in a simulated free-space environment and in the proximity of a perfectly conducting plane. The measured time-domain data are Fourier transformed to the frequency domain, and analyzed via parameter estimation algorithms to extract the complex natural frequencies of the structures.

Preface

The work presented was originally performed during the 1977 fiscal year and a first draft was sent to the Air Force Weapons Laboratory (AFWL) in April of 1979. Upon review by AFWL, it became apparent that the data did not exhibit the expected behavior. The discrepancy was subsequently attributed to inaccurate data processing by Lawrence Livermore National Laboratory (LLNL). The present report incorporates improved data processing techniques.

The authors would like to acknowledge the interest and support of Capt. H. G. Hudson and Mr. W. D. Prather of the AFWL. Many thanks also to Gail Simpson, Vicky Martinez, Lisa Lopez, Jody Reyes-Harris and Raylene Cooper of LLNL for typing of the manuscript.

Table of Contents

Table of Contents
(continued)

1.0 Introduction

1.1 Purpose and Scope

The objective of this effort is to experimentally measure the current and charge distributions of various analytical models, such as cylinders, crossed cylinders and a scale model 747 aircraft, in free space and in proximity to a perfectly conducting ground plane. Such experimental data will aid in better understanding the mutual interaction of the Horizontally Polarized Dipole and Vertically Polarized Dipole (HPD/VPD) simulators and test objects as well as providing a data base for comparison with calculations.

The report describes results obtained from a series of time-domain scale model electromagnetic measurements. The tests were conducted at the Lawrence Livermore National Laboratory (LLNL) Transient Electromagnetic Range and involve the use of subnanosecond electromagnetic pulses to illuminate the bodies under test. Small $\dot{B}$ and $\dot{D}$ sensors were used to measure the local fields on the bodies to determine the induced currents and charges.

1.2 Background

Major concerns in the evaluation of a full-scale simulator such as the Air Force Weapons Laboratory (AFWL) VPD and HPD include more accurate knowledge of simulator-test object interaction and the relationship between the response of the object in the simulator and its response in free space. The full-scale simulator data are extrapolated to object response in the actual operational environment by use of extrapolation functions. These functions are often generated by means of numerical models which predict response of objects in free space (if such is the operational environment) and the response when the object is in close proximity to a ground screen (which is now the ground of the VPD constructed). An ongoing need therefore exists for experimental data to confirm the validity of numerical models.

One method for generating such data is with transient scale-model measurements. It is only within the past few years that subnanosecond pulse generation and sampling technology has advanced to the point where useful scale model time-domain electromagnetic pulse (EMP) measurements may be performed in the laboratory. The Lawrence Livermore National Laboratory has such a facility which was used to obtain the data presented in this report.

1.3 Organization of Report

In Section 2, data collection techniques are described. Included is a description of the operation of the transient range, description of sensors and data collection procedures. In Section 3, the test objects in question are described. These include a cylinder, crossed cylinder and the 747 aircraft model. In Section 4, critical issues in the collection of the raw data and the encountered difficulties are described. Data processing techniques follow in Section 5. The data for the three test objects (both raw and processed) are summarized in tabular form in Section 6. The bulk of the data is relegated to appendices. Comparisons with test data from the University of Michigan and with numerical prediction follow in Section 7. Results for pole extraction are summarized in Section 8.

2.0 Data Collection Techniques

2.1 LLL Transient Range

The LLNL transient range facility [Ref. 1] consists of a monocone antenna that radiates electromagnetic pulses over a horizontal aluminum ground plane. A photograph of the range is shown in Figure 1.

---

1. Deadrick, F. J., Miller, E. K., and Hudson, H. G., The LLL Transient-Electromagnetics-Measurement Facility, Lawrence Livermore National Laboratory, Livermore, CA, Rept. UCRL-51933 (1975).

The ground plane is 8.5 m x 8.5 m large. Radiated electric and magnetic field measured on the ground at 2.43 m from the base of the monocone antenna are shown in Figures 2 and 3 (this corresponds to the location of test objects where the experimental data are obtained). The rise time of the pulse is typically less than 100 ps and the pulse width is about 300 ps. Reflections from the edges have been found to be small and the range has been used with data records up to 200 ns.

Additional information pertinent to the data reported here is given in Appendix A, which also includes a description of range improvements that were undertaken in conjunction with this effort. Validation and calibration issues concerning the range have been dealt with elsewhere [Ref. 2].

2.2 Field Sensors: Both tangential magnetic fields and normal electric fields on the test objects were measured. These were performed with the ACD-1 $\dot{D}$ sensor (Ref. 3) and the MGL-8 $\dot{B}$ sensors (Ref. 4). Both of these precision sensors have been precalibrated; the calibration factor is $A_{eq} = 10^{-4}$ m^2 for the $\dot{D}$ sensor and $A_{eq} = 10^{-5}$ m^2 for the $\dot{B}$ sensor.

Figures 2 and 3, which show the incident E and H fields at the test location on the ground plane, were determined from measurements with

---

2. Bevensee, R. M., Deadrick, F. J., Miller, E. K., and Okada, J. T., Validation and Calibration of the LLL Transient Electromagnetic Measurement Facility, Lawrence Livermore National Laboratory, Livermore, CA, Rept. UCRL-52225 (1977).

3. Baum, C. E., Breen, E. L., Giles, J. C., O'Neill, J., and Sower, G. D., "Sensors for Electromagnetic Pulse Measurements Both Inside and Away from Nuclear Source Regions," IEEE Trans. Antennas Propag. AP-26, No. 1, January, 1978, also Sensor and Simulation Notes, Note 239, 1 Jan 78.

4. Olsen, S. L., "Sensor MGL-8B sensor DW," AL-1186, September 1975, Albuquerque Division, EG&G Inc., 9733 Coors, R., N. W., Albuquerque, NM.

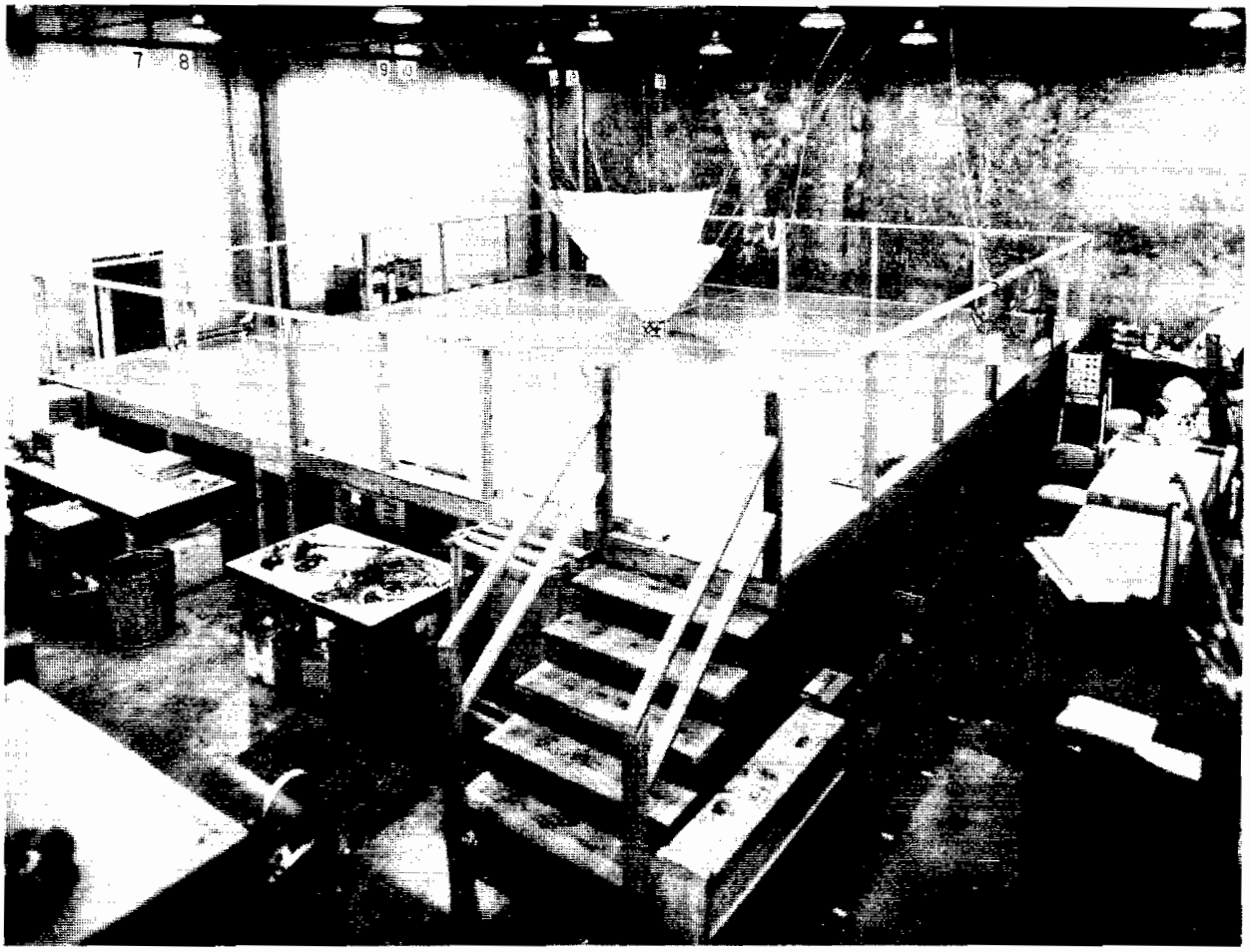

Figure 1. LLNL Transient Antenna Range showing the Ground Plane and the Monocone Source Antenna.

these sensors. The absolute electric field is found by numerically integrating the voltage output of the $\dot{D}$ sensor:

$$E(t) = \frac{1}{\epsilon_o A_{eq} z_L} \int_o^t V_{out_{\dot{D}}}(t)\, dt \,, \qquad (1)$$

where E(t) is the electric field in V/m as a function of time, $_o$ is the permittivity of free space, z_L is the impedance of the load connected to the sensor output, (nominally 50 here), and A_{eq} is the equivalent area of the $\dot{D}$ sensor. Similarly, the magnetic field can be found from the output of the $\dot{B}$ sensor by the expression

$$H(t) = \frac{1}{\mu_o A_{eq}} \int_o^t V_{out_{\dot{B}}}(t)\, dt \,, \qquad (2)$$

where H(t) is the magnetic field in amperes/meter, μ_o is the permeability of free space, A_{eq} is the equivalent area of the $\dot{B}$ sensor and $V_{out_{\dot{B}}}(t)$ is the output of the $\dot{B}$ sensor as a function of time.

Particularly good agreement in both magnitude and temporal shape is obtained when we integrate and calibrate the sensor outputs. (Note that in free space $E = \eta_o H$, where η_o is the impedance of free space). Typically, the peak electric field at the test point is on the order of 480 V/m and the peak magnetic field $\simeq$ 1.3 A/m, when the conical antenna is driven with an impulse generator with a peak voltage of 1.5 kV.

A photograph of the $\dot{D}$ and $\dot{B}$ sensors used is shown in Figure 4.

3.0 Description of Test Objects and Experimental Setup

In these experiments, two types of measured electromagnetic quantities were obtained: the normal electric field and the surface magnetic fields at specific points on the scale models. These measurements were obtained

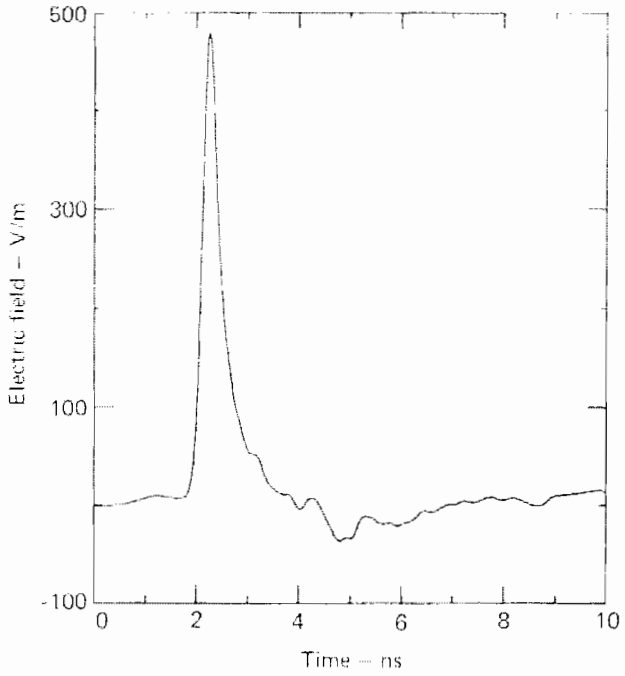

Figure 2. Measured Electric Field at Test Point 2.43 m from Conical Antenna on the Image Plane.

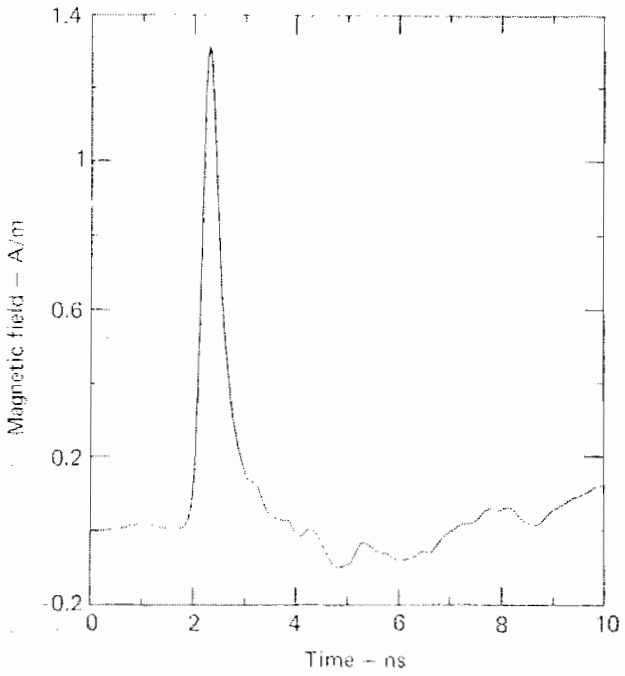

Figure 3. Measured Magnetic Field at a Test Point 2.43 m from the Conical Antenna on the Image Plane.

for objects in both a "free-space" configuration and in the presence of a perfectly conducting ground.

The free-space measurements are actually a simulated free space where a plane of symmetry is used as shown in Figure 5(a). This configuration allows only antisymmetric excitation on the model, and thus is a special case of free-space operation.

For the measurements of models near a perfectly conducting ground plane, a second vertically oriented plane was used as shown in Figure 5(b). The vertical ground plane was constructed so that it could easily be moved in and out. For these experiments the model remained fixed relative to the source monocone antenna; the ground plane was moved as required. A sketch of the experimental layout with dimensions is shown in Figure 6. The vertical ground plane was made of a thick aluminum plate with dimensions of 1.2 X 4. m.

3.1 Cylinder

Figure 7 is a photograph of the cylinder model used in all these tests. The length-to-radius ratio for the cylinder model is $L/a = 20$, where L is the total length of the cylinder, and a is the radius. While L is defined as the total length of the cylinder being simulated, only one half appears above the symmetry plane used in these experiments. The cylinder model was constructed of a section of brass pipe with a wall thickness of 0.635 cm.

A flat end cap was machined to fit the end of the cylinder, and the metal to metal joint was sealed with a conductive silver compound to insure a good electrical junction. Two small flat surfaces were milled on the surface of the cylinder to accommodate the $\dot{B}$ and $\dot{D}$ sensors.

To obtain a good electrical contact between the cylinder and the conductive symmetry plane, a silver-loaded conductive paste was also applied to the bottom of the cylinder over the area that comes in

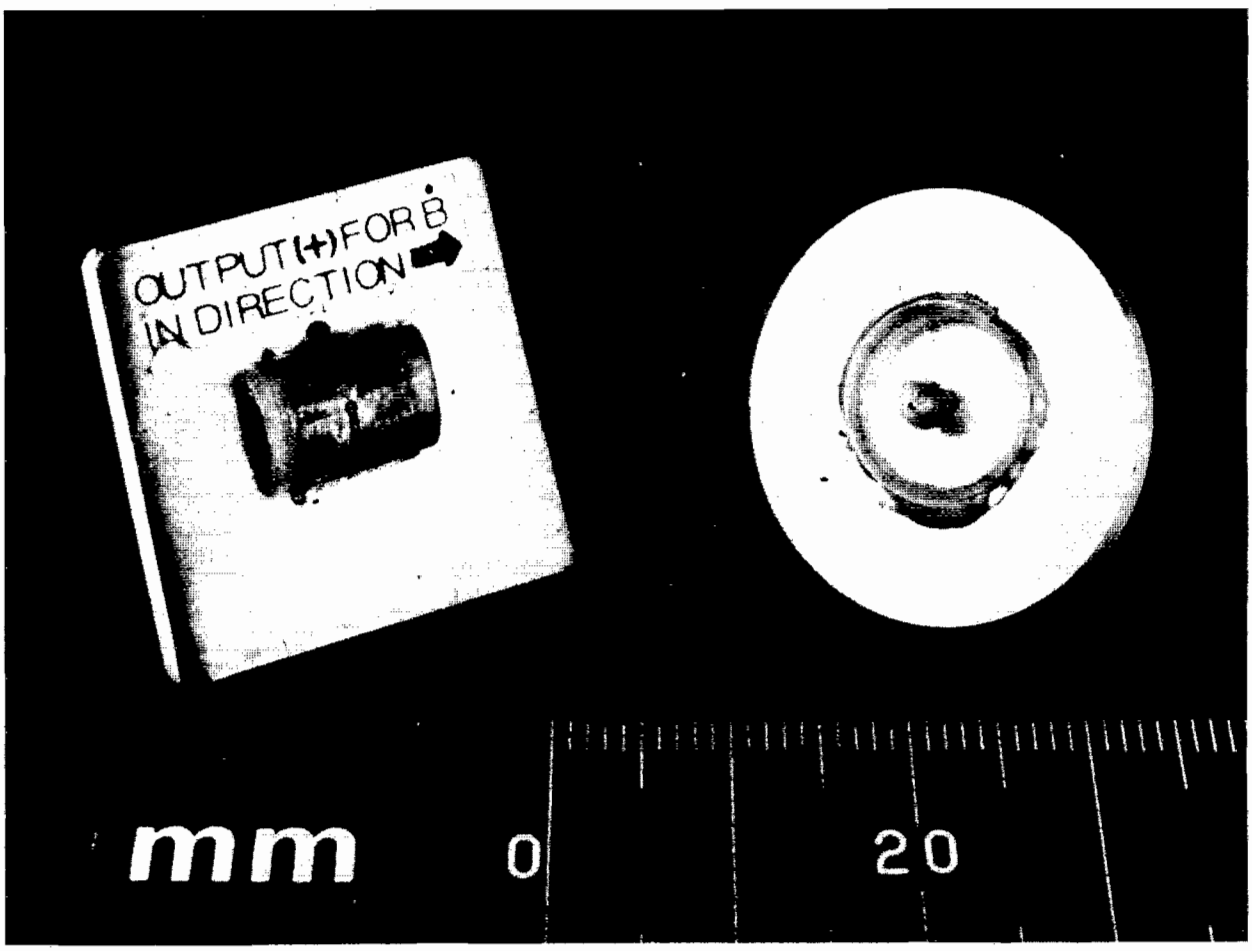

Figure 4. AFWL MGL-8 $\dot{B}$ and ACD-ϕ $\dot{D}$ sensors used in the time-domain measurements.

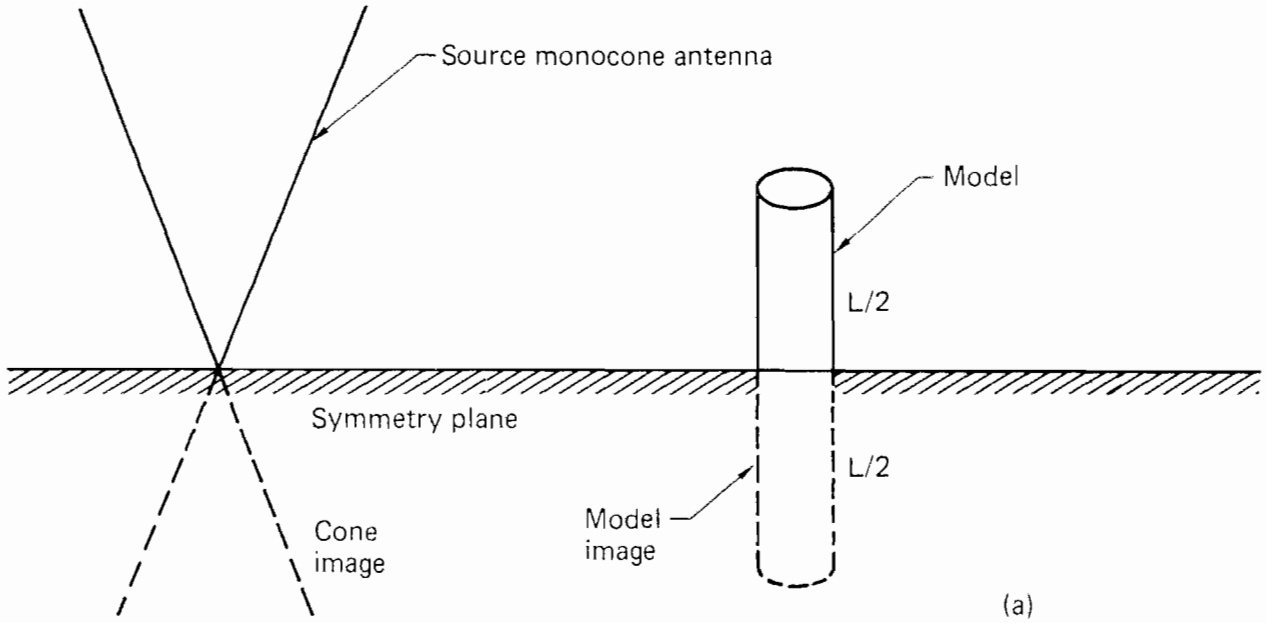

Figure 5(a). "Free-space" experimental configuration.

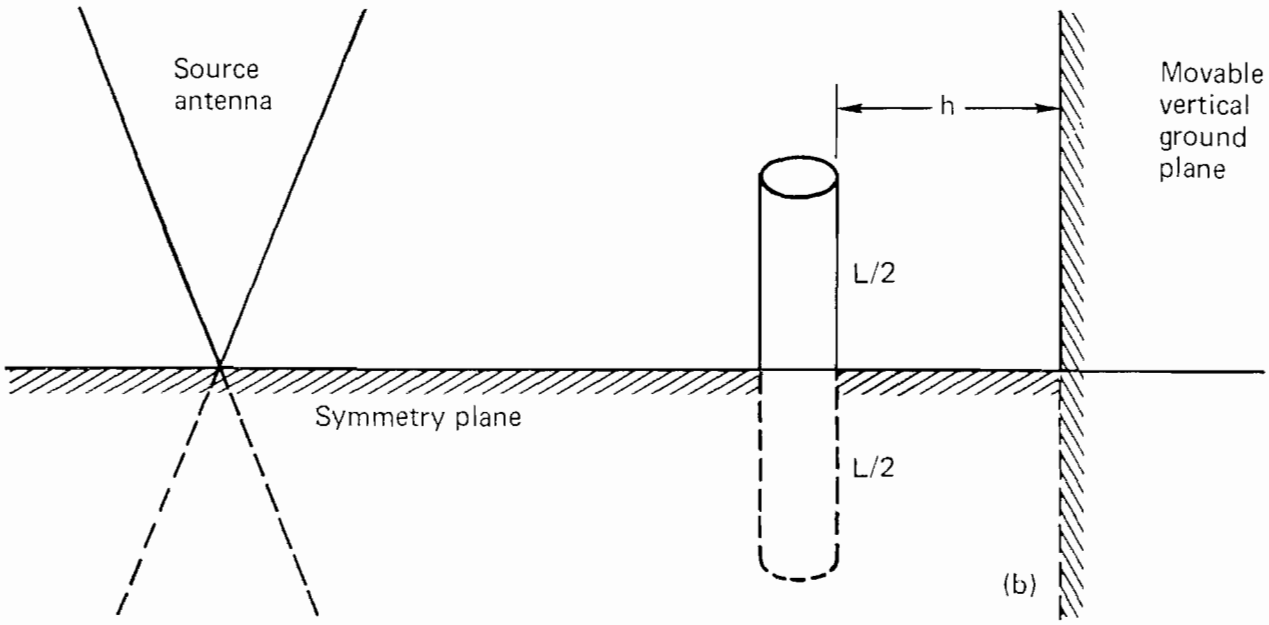

Figure 5(b). Experimental configuration for a cylinder over a ground plane.

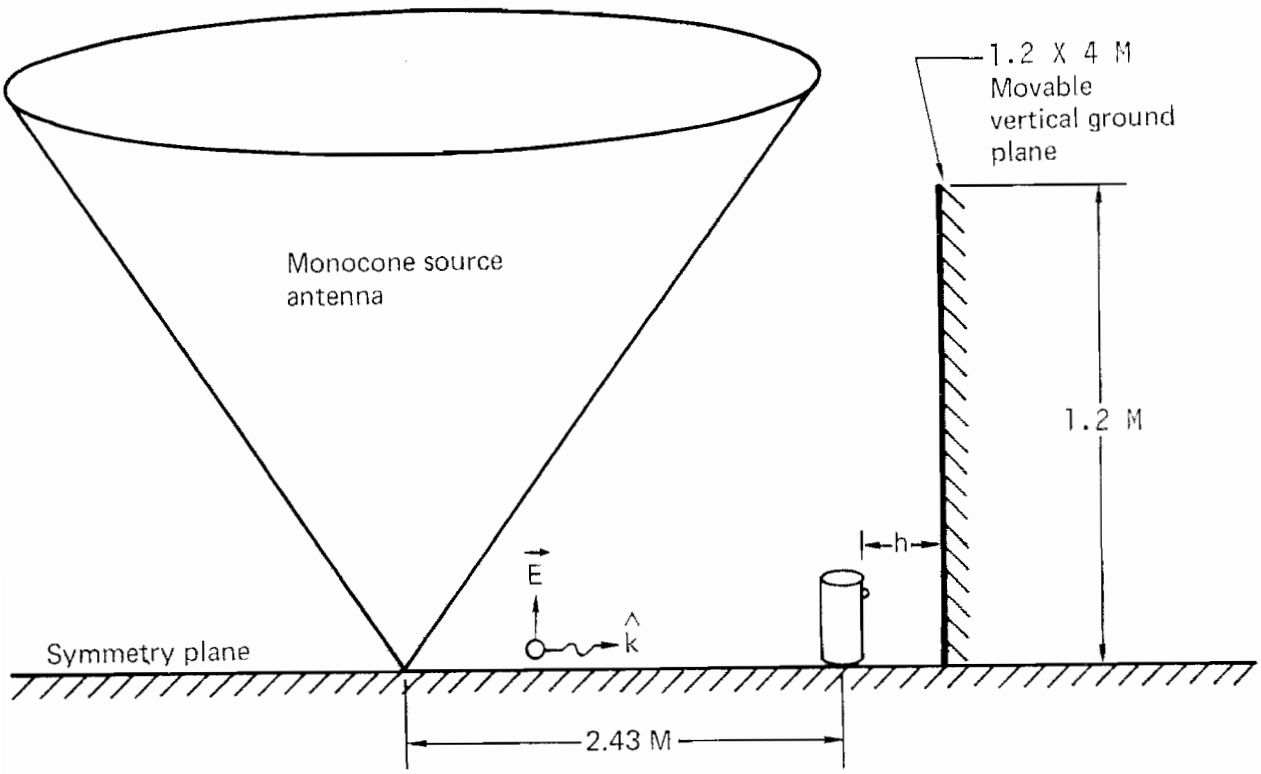

Figure 6. Experimental configuration for measurements of bodies near a perfectly conducting ground plane. (The distance h was set at a, 5a, 10a, and 20a [10 cm, 50 cm, 1 m, and 2 m].)

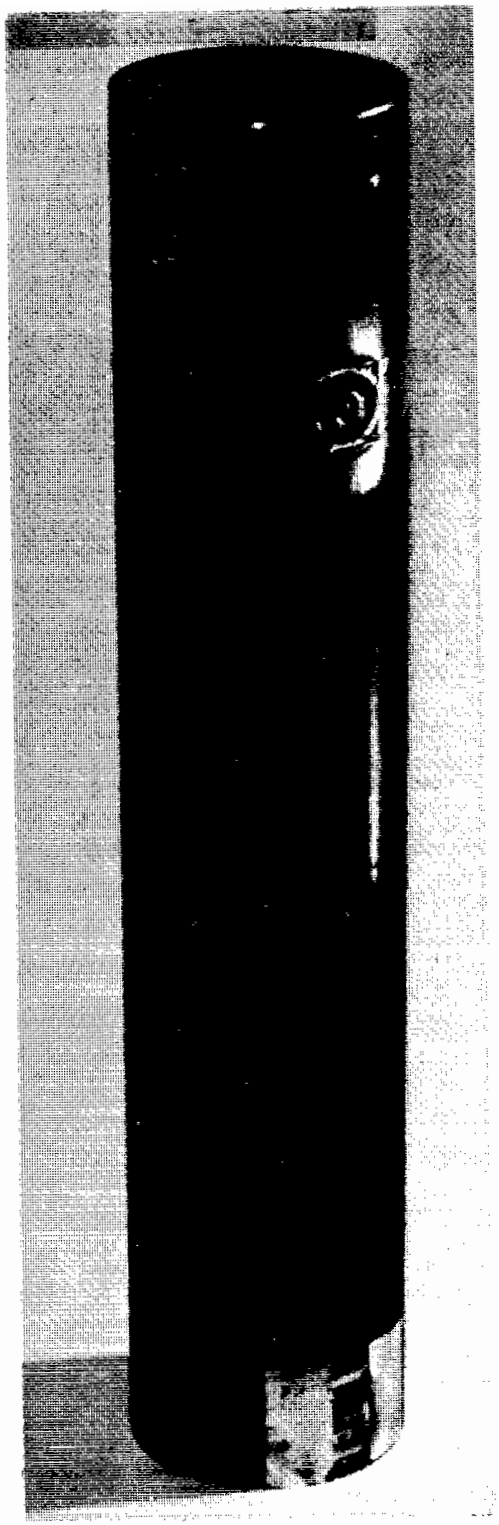

Figure 7. Cylinder Model Showing the Locations of the $\dot{B}$ and $\dot{D}$ sensors.

contact with the aluminum plane. The miniature field sensors were held in position with a copper foil tape with a conductive adhesive. The dimensions of the cylinder and sensor locations are shown in a sketch in Figure 8. A top view of the cylinder in the range with dimensions is shown in a sketch in Figure 9.

The rationale for using the half-length shown in Figure 8, which has to do with several considerations including phase angle errors, is given in Appendix B.

3.2 Crossed Cylinder

The second model to be tested is the crossed cylinder shown in the photograph of Figure 10. The dimensions of the model are shown on the sketch in Figure 11. These dimensions correspond to those of the cylinder model used in the previous section. Semicircular end caps were brazed to the ends of the bottom section of the cross, and a flat, removable end cap was used at the top of the cross so as to allow connections to be made to the $\dot{D}$ sensor located at the top of the cross. The $\dot{B}$ sensor was oriented so as to measure the surface current flowing down the vertical section of the cross; it was mounted near the junction of the cross members. To ensure a good contact between the cross and symmetry plane, a thin sheet of brass plate was epoxied to the base of the cross with conductive epoxy (the joint was also painted over with silver paint), and the brass plate was then taped to the symmetry plane with conductive tape.

3.3 747 Scale-Model Aircraft

A third series of measurements was performed on a 1:100 scale model of a Boeing 747 aircraft. The model used is a commercially available plastic kit that is conveniently sectioned into right and left halves, 69-cm long, as shown in the photograph of Figure 12. One-half of the plane was assembled in a wheels-up configuration and epoxied to a thin sheet of brass plate as shown in the photograph. Four sensor mounting holes, three on the wing top and a fourth on

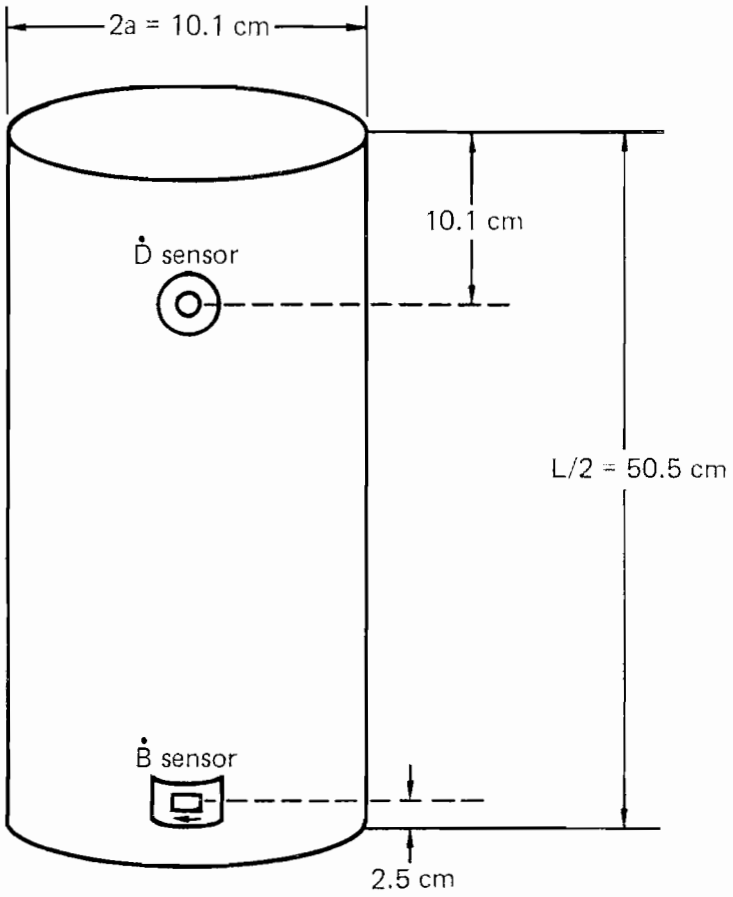

Figure 8. Dimensions of cylinder used in scale-model tests.

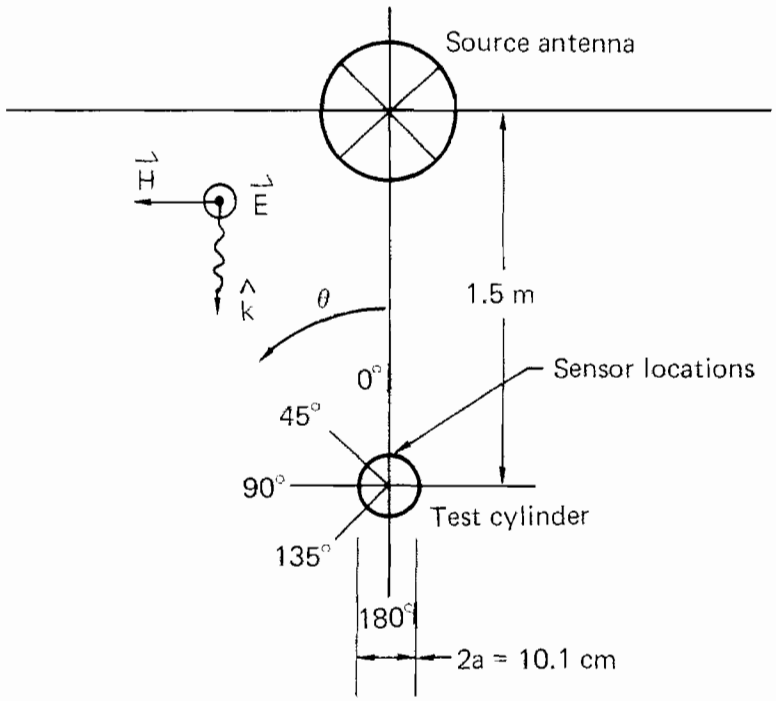

Figure 9. Top view of configuration used for cylinder free-space measurements.

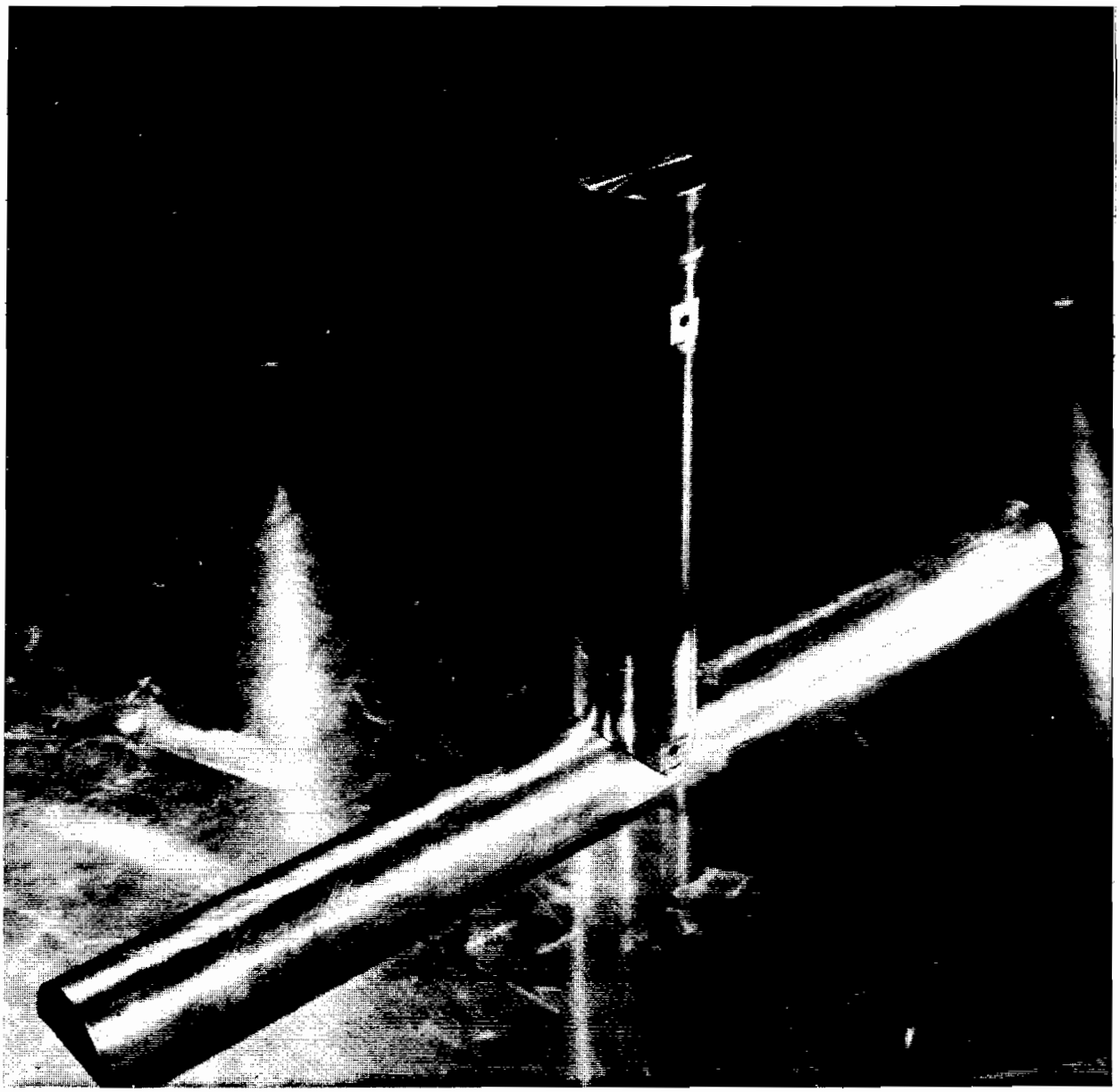

Figure 10. Crossed cylinder model.

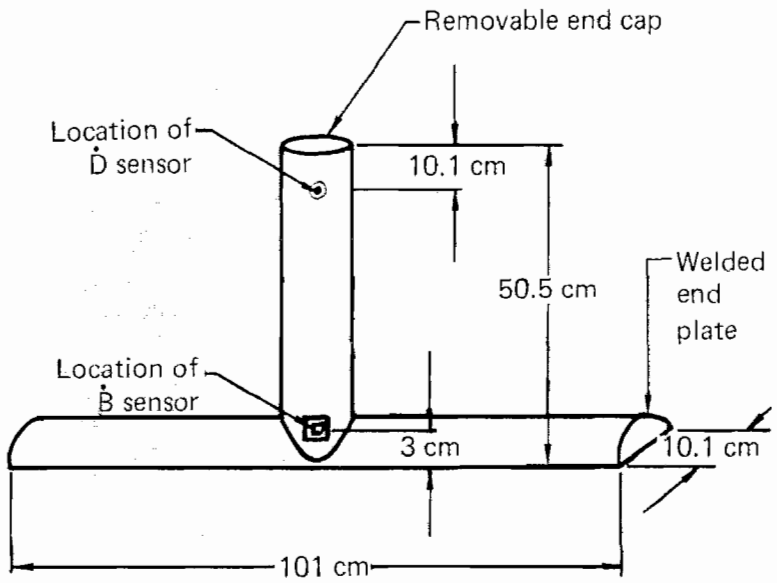

Figure 11(a). Dimensions of crossed cylinder model used in transient measurement tests.

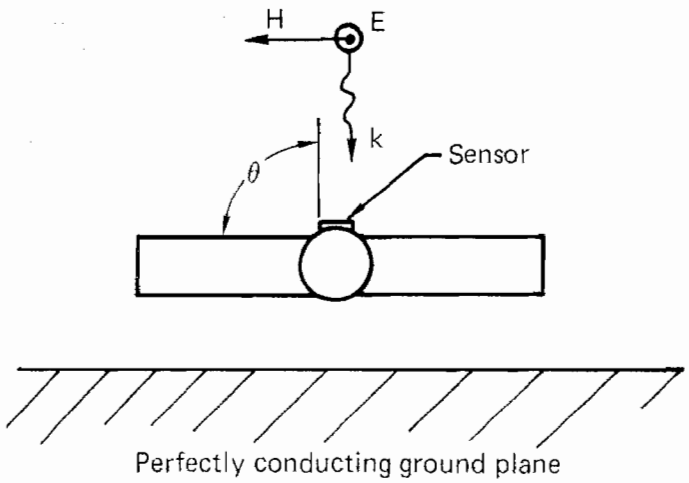

Figure 11 (b). Top view of crossed cylinder showing direction of incident electric field.

the fuselage between the front and rear wings, were formed with expoxy and milled to form a flat surface to accommodate the $\dot{D}$ and $\dot{B}$ sensors. The entire model was then given several coats of a conductive silver paint to form a thin metallic surface. The pertinent dimensions of the model are shown in Figure 13.

4.0 Critical Issues in Raw Data Collection

Much of the data collected and processed as part of this effort is characterized by a rather high Q. For data processing purposes, this has necessitated the taking of data records over time durations far in excess of those previously used. For example, prior to this effort, the range had been used for taking data records of up to typically 20 ns. Some of the data collected and processed here was recorded over a 200 ns duration. This gave rise to some problems that had to be resolved.

The first area of concern was edge reflections from the extremities of the range. From purely dimensional considerations, the clear time was established to be 20 ns. However, data for the simulator free-field taken over longer records indicated reflections far lower than 10% of the simulator output signal. The uncertainty this introduced to the data was not considered to be deleterious.

The other problem encountered had to do with drift in the signal baseline. The data taken with the combination of the sampling oscilloscope as shown in Figure A1 exhibited excessive low frequency drift for time durations exceeding 50 ns. The drift can introduce complications when processing the data. The use of a Tektronix 7912 transient digitizer in combination with an LSI-11 microcomputer helped eliminate the problem. In this report, data for the objects in free-space (where 20 ns records are sufficient) were taken with the older system as shown in Figure A1. Longer data records have all been taken with the Tektronix 7912 digitizer.

Both the older and the new data acquisition system have the potential of sampling the data at 512 points. Depending on the highest frequency

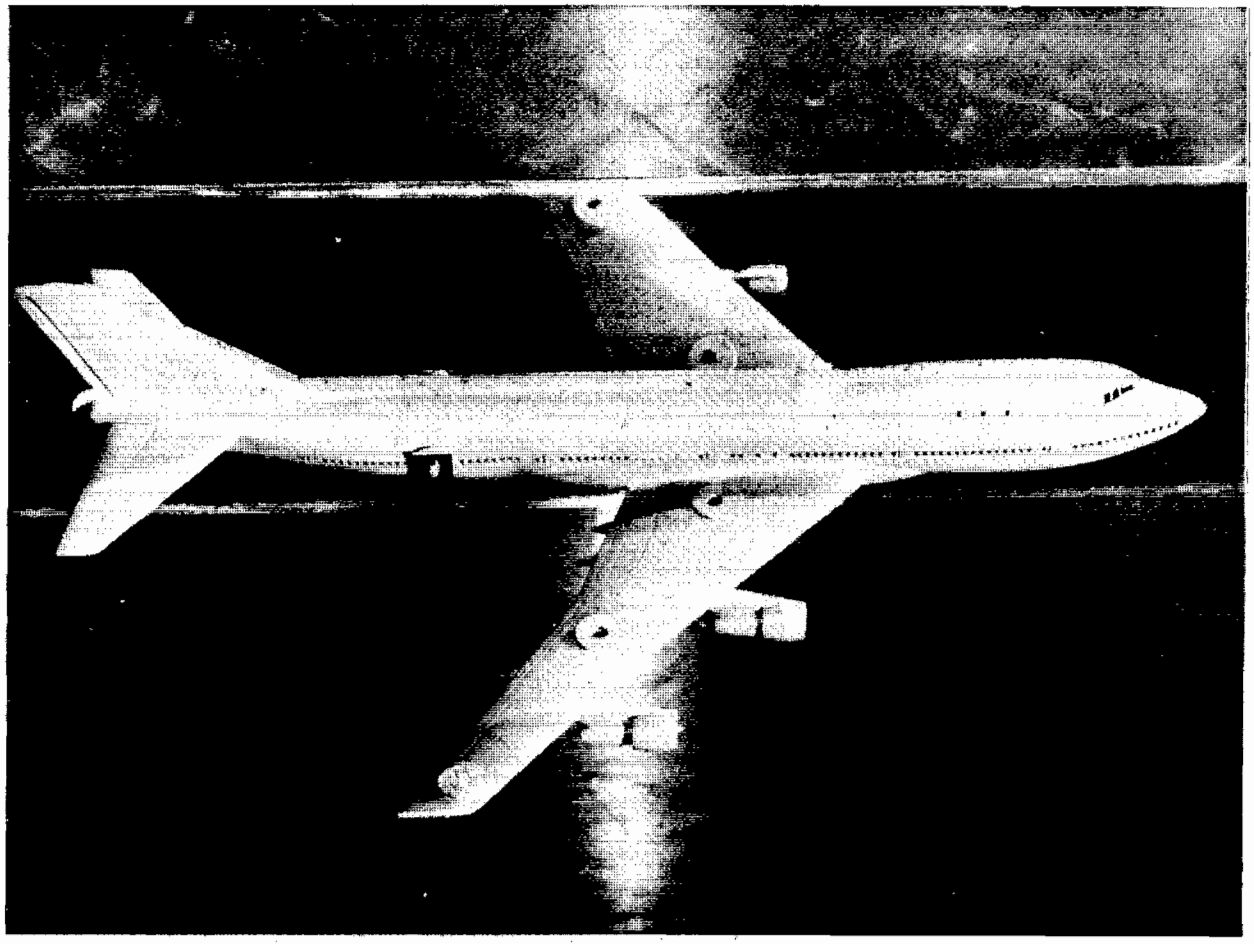

Figure 12. One-to-one-hundred scale model of Boeing 747 aircraft showing location of sensors.

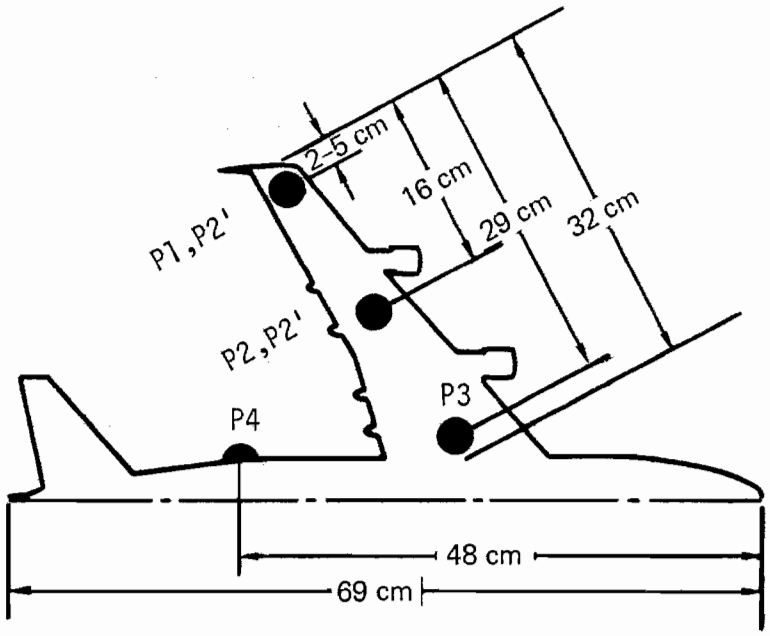

Figure 13. Dimensions of 1:100 scale model 747 aircraft used in tests.

content of the signal, this can limit the total time duration over which the data are sampled. For example, the output free-field of the simulator could only be sampled adequately up to a total time duration of 50 ns.

Above this a noticeable drop in peak amplitudes results due to insufficient time resolution. The object responses on the other hand were not characterized by rise times as fast as those of the incident field and no sampling problems were encountered even for 200 ns time durations.

The time durations used for collecting the data varied depending on configuration. These are listed in Table 1. These time durations were found to be adequate to perform the required signal processing.

5.0 Data Processing Techniques

Two sorts of signal processing techniques were used. In the first place, the Fourier transforms were computed for all responses, and from this information the transfer function of the objects (i.e., ratio of object response to incident field) was evaluated. The time records used to obtain the frequency spectra are listed in Table 1. For the objects in free space, the data were collected with the older system shown in Figure A1 processed on a CDC-7600 using Filon's Method (the Fourier integral is performed using straight line interpolation to the sampled time amplitudes). The data with longer time records were recorded with the Tektronix 7912 transient digitizer in combination with an LSI-11 microcomputer. In processing the data, a fast Fourier transform algorithm in the LSI-11 system was used.

Besides the frequency spectra, the poles were extracted for some of the responses. The techniques used to extract the poles are described in Appendix C. Three techniques were used; namely, Prony's technique, the extended Kalman filter and the maximum likelihood identifier. The trade-offs between these various techniques are discussed in great detail in the Appendix.

TABLE 1. OBJECT CONFIGURATION AND CORRESPONDING DATA RECORD TIME DURATION

Configurations	Time Duration (ns)
Simulator free-field	20
Object in free-space	20
Object 2 m from ground plane	50
Object 1 m from ground plane	50
Object 50 cm from ground plane	100
Object 10 cm from ground plane	200

In the cases where time domain record lengths are less than or equal to 50 ns, the processing is relatively simple. The time domain responses are multiplied by a Hamming window function to reduce spectral leakage. Spectral leakage is caused by the calculation of the Fourier transform for a finite data sequence. The Hamming window equation is:

$$W(t) = .54 + .46 \cos(2\pi t/\tau)$$

where τ is the length of the signal to be windowed. These then are transformed into the frequency domain and divided by the incident pulse frequency response. The 100 ns records were processed in the same way except the 50 ns incident pulse was used for the division. The proper frequency response for the 50 ns record can be obtained by either of two methods. One method is to straight line interpolate new frequency points between the calculated points. The other method is to append zeroes to the 50 ns record until it is the desired length and then transform into the frequency domain. Either method can be used to obtain the proper frequency spaced points.

The incident pulse record could be obtained only for a 50 ns duration. Since the transient digitizer collects a fixed number of points, as the record length increases the time resolution between points decreases. This is a problem for the incident pulse because it has very high

frequency components and a low signal amplitude. The model responses, however, are higher in signal amplitude and do not contain the high frequency components so a large time resolution is acceptable.

6.0 Results

For each of the test objects, the data at appropriate positions were collected with the $\dot{B}$ and $\dot{D}$ sensors. The ambient E- and H-fields at the location of the test objects were also obtained. The transfer functions in the frequency domain were obtained by dividing the test objects' responses by the incident field in the frequency domain.

The results of these tests are tabulated in this section and the bulk of the data is shown in appropriate appendices. In all the tables, the entries denote the following:

- Separation distance h: Distance from cylinder and cross-cylinder to ground plane. See Figures 5, 6 and 11.
- Angle θ : Incidence Angle in Degrees. See Figure 9.
- Peak : Peak amplitude of the transfer function at the first harmonic.
- Fig. # : Indicates figure number for case under consideration in the appropriate appendix.

6.1 Cylinder:

The experimental predictions for the cylinder are tabulated in Table 2.

6.2 Cross Cylinder:

The experimental predictions for the cross-cylinder are tabulated in Table 3.

TABLE 2. SUMMARY OF RESULTS FOR CYLINDER

Separation Distance h.	Angle θ Degrees	$\dot{D}$-Sensor Fig. #	$\dot{B}$-Sensor Fig. #	Transfer Function E/E^{inc} Fig. #	Peak	Transfer Function H/H^{inc} Fig. #	Peak
FAR SPACE	0	D1	D1	D6	9	D11	22
	45	D2	D2	D7	9	D12	22
	90	D3	D3	D8	10	D13	20
	135	D4	D4	D9	9	D14	20
	180	D5	D5	D10	9	D15	20
10 • cm	0	D16	D24	D32	36	D40	43
	180	D20	D28	D36	23	D44	190
50 • cm	0	D17	D25	D33	50	D41	56
	180	D21	D29	D37	43	D45	50
1 • m	0	D18	D26	D34	25	D42	33
	180	D22	D30	D38	24	D46	27
2 • m	0	D19	D27	D35	38	D43	43
	180	D23	D31	D39	37	D47	45

TABLE 3. SUMMARY OF TIME DOMAIN RESULTS FOR CROSS-CYLINDER

Separation Distance h.	Angle θ Degrees	$\dot{D}$-Sensor Fig. #	$\dot{B}$-Sensor Fig. #	Transfer Function E/E^{inc} Fig. #	Peak	Transfer Function H/H^{inc} Fig. #	Peak
Free Space	0	E1	E3	E5	23	E7	35
	180	E2	E4	E6	24	E8	28
17*• cm	0	E9	E17	E25	70	E33	98
	180	E13	E21	E29	58	E37	180
50 • cm	0	E10	E18	E26	46	E34	40
	180	E14	E22	E30	45	E38	36
1 • m	0	E11	E19	E27	25	E35	24
	180	E15	E23	E31	22	E39	16
2 • m	0	E12	E20	E28	37	E36	32
	180	E16	E24	E32	37	E40	29

*The cross-cylinder could be brought only as close as 17 cm to the ground due to physical obstructions.

6.3 747 Scale-Model Aircraft

The experimental predictions for the 747 scale-model aircraft are tabulated in Table 4. The positions on the model are identified in Figure 13. The entries in the Table refer to the following positions:

P1 : Wing Tip; Top
P1': Wing Tip; Bottom
P2 : Wing Center; Top
P2': Wing Center; Bottom
P3 : Wing Root; Top
P4 : Fuselage

For simulating the aircraft over ground plane configuration, the model was placed an equivalent distance from the ground plane as if it were sitting on its wheels. This placed the bottom of the fuselage at the wings 2 cm from the ground plane.

7.0 Comparison with University of Michigan CW Data and with Analytical Predictions

The University of Michigan conducted CW tests of three test objects [Ref. 5]. Two of these tests (i.e., cylinders and a scale model of a 747 aircraft) correspond to tests described in this report. In this section, the two sets of data will be compared. Enough detail of the Michigan set-up and data will be given here to make the comparisons meaningful. Interested readers should consult the original Michigan report for additional information.

The Michigan measurements include induced current and charge results for plane electromagnetic wave incidence. These were performed in the model frequency range of 45 MHz to 4.25 GHz using the image plane techniques.

---

5. Liepa, V. V., et al., "Surface Field Measurements with Image and Ground Planes", AFWL Sensor and Simulation Note 244, Albuquerque, NM, November, 1977.

TABLE 4. SUMMARY OF TIME DOMAIN RESULTS FOR 747 SCALE-MODEL AIRCRAFT

Aircraft Location	Free Space (FS) or Ground Plane (GP)	$\dot{D}$-Sensor Fig.#	E/E^{inc} Fig.#	E/E^{inc} Peak	$\dot{B}$-Sensor Fig.#	H/H^{inc} Fig.#	H/H^{inc} Peak
P1	FS	F1	F6	13	N/A	N/A	N/A
P1'	FS	F13	F17	12	N/A	N/A	N/A
	GP	F11	F15	90	N/A	N/A	N/A
P2	FS	F2	F7	7	F3	F8	8
P2'	FS	N/A	N/A	N/A	F14	F18	6
	GP	N/A	N/A	N/A	F12	F16	25
P3	FS	N/A	N/A	N/A	F4	F9	6
P4	FS	N/A	N/A	N/A	F5	F10	4

N/A - Data not taken.

Data were obtained for free space and in the presence of perfectly conducting ground planes. The only Michigan data quoted here correspond to cases where a one-to-one comparison could be made with LLNL data.

Comparisons between the cylinder data will be taken up first and the results summarized in tabular form. The Michigan and LLNL cylinder radii and length are very close (radii: 5.08 cm vs. 5.05 cm lengths: 50.83 cm vs. 50.5 cm). The positioning of the sensors is not quite close ($\dot{D}$ sensor: 4.83 cm vs. 10.1 cm from top plate; $\dot{B}$ sensor: 4.83 cm vs. 2.5 cm from bottom plate; refer to Figure 6). It is not obvious how much uncertainty this introduces into the comparisons. Most probably the effect on surface current measurements near the bottom of the cylinder may be small; the uncertainty may be larger for the D measurement close to the top of the cylinder. For the cylinder over ground plane measurements, the height h in all cases are almost identical (10 • cm vs. 10.16 cm; 50 • cm vs. 50.8 cm; 100 cm vs. 101.6 cm; and 200 cm vs. 203.2 cm). The results of these comparisons are shown in Table 5 where the peak value of the transfer function at the fundamental resonance is tabulated.

For the 747 scale-model aircraft, the comparisons are summarized in Table 6. For details on location notation, please refer to Section 6.3.

In addition to Michigan's CW data for the cylinder, analytical predictions were made for the same configuration by Sancer, et al.[6] The predictions are entered in Table 5 in the third column. Ref. 6 also included predictions for h = 7.5 cm and 25 cm where transfer function peaks at the fundamental frequency of 404 and 67, respectively, are predicted. In order to facilitate the comparisons, the LLNL, U. of M. and the Ref. 6 predictions for the peak transfer function at the fundamental frequency are shown in Figure 14 for the cylinder above ground.

In Figures 15, 16, and 17, actual frequency domain spectral content are shown for various cylinder configurations. These include LLNL and University of Michigan measurement predictions and analytical predictions in Ref. 6. The top curve in each figure includes the smoothed out

Table 5. Summary of the Comparisons for the Cylinder
(Transfer function peak value)

Transfer Function	Height h	Angle θ	U. of M.	LLNL	Analytical Prediction (Ref. 6)
	F	0	13.5	22	14.7
	R	45	13.0	22	----
	E				
	S	90	12.0	20	12.7
	P	135	10.5	20	----
H/H^{inc}	A	180	10.5	20	----
	C				
	E				
	10 • cm	180	57.0	190	----
	50 • cm	180	56.0	50	----
	1 • m	180	16.0	27	----
	2 • m	180	35.0	45	----
E/E^{inc}	Free Space	0	15.0	9	----

TABLE 6. SUMMARY OF COMPARISONS FOR THE 747 SCALE-MODEL AIRCRAFT (TRANSFER FUNCTION PEAK VALUE)

Location	Free Space (FS) or Ground Plane (GP)	Transfer Function Type	U. of M.	LLNL
P1	FS	E/E^{inc}	15.0	13
P2	FS	H/H^{inc}	9.6	8
	GP	H/H^{inc}	16.7	25
P3	FS	H/H^{inc}	7.0	5
P4	FS	H/H^{inc}	8.0	4

P1 - Wing Tip, Top
P2 - Wing Center, Top
P3 - Wing Root, Top
P4 - Fuselage

version of the Michigan data as reported in Ref. 6, and the analytical predictions. The bottom portion is the corresponding LLNL data. The free space case is shown in Figure 15. The case for a cylinder 25.4 cm over a perfectly conducting ground plane is shown in Figure 16. The results for a cylinder very close to ground are shown in Figure 17. The Michigan data and the predictions are for h = 7.6 cm. The corresponding LLNL data is for h = 8.2 cm since the cylinder could not be brought any closer to the ground plane because of physical obstructions at the base.

In Figure 14, note that for separations larger than h = 50 cm, both the LLNL and University of Michigan data are close and exhibit similar trends. For separations closer than h = 50 cm, the LLNL data exhibits larger transfer function peaks than the corresponding University of

6. Sancer, M. I. et al., "Formulation of Electromagnetic Pulse External Interaction Above a Lossy Earth/Comparison of Numerical Results with Experimental Data for Limiting Cases," AFWL Interaction Notes, Note 354, Albuquerque, NM, October 1978.

Michigan data. In this, the LLNL data exhibit the trend suggested by the analytical predictions for h < 10 cm. There is a wide discrepancy.

however, at h = 25 cm. Considering the difficulties in taking such highly resonant data, this may not be too surprising. The agreement between the LLNL and the University of Michigan data for the 747 scale-model aircraft is also quite encouraging as shown in Table 6.

The spurious peeks observed at the higher frequencies in the LLNL data in Figures 16 and 17, which do not appear in the University of Michigan data are produced by the division of one transform by another. The small baseline numbers generated by the FFT routine are very noisy. When these small baseline numbers approach zero the division process will cause a numerical noise peak to appear since 1/X goes to a large value as X approaches zero.

8.0 Pole Extraction Results

Three parameter estimation algorithms were applied to the data to extract the poles. These are the Prony techniques,* extended Kalman filter, EKF and the maximum likelihood estimator. All three are discussed and compared in terms of their respective theories in Appendix C. The application of the EKF and the maximum likelihood estimator to the data are discussed in Appendix C and the results tabulated in this section. These two parameter estimators were only applied to the cylinder data. The application of the Prony technique is covered in Appendix G. This algorithm was applied to all three objects and all the results are tabulated in that appendix. For purposes of comparison with available theoretical predictions and the results from the two other estimators, Prony results for the cylinder are extracted from the appendix and shown in tabulated fashion in this section.

---

* The Prony technique could really be termed "interactive" Prony, since many runs through the data were accomplished, all used to filter out the noise and increase signal levels.

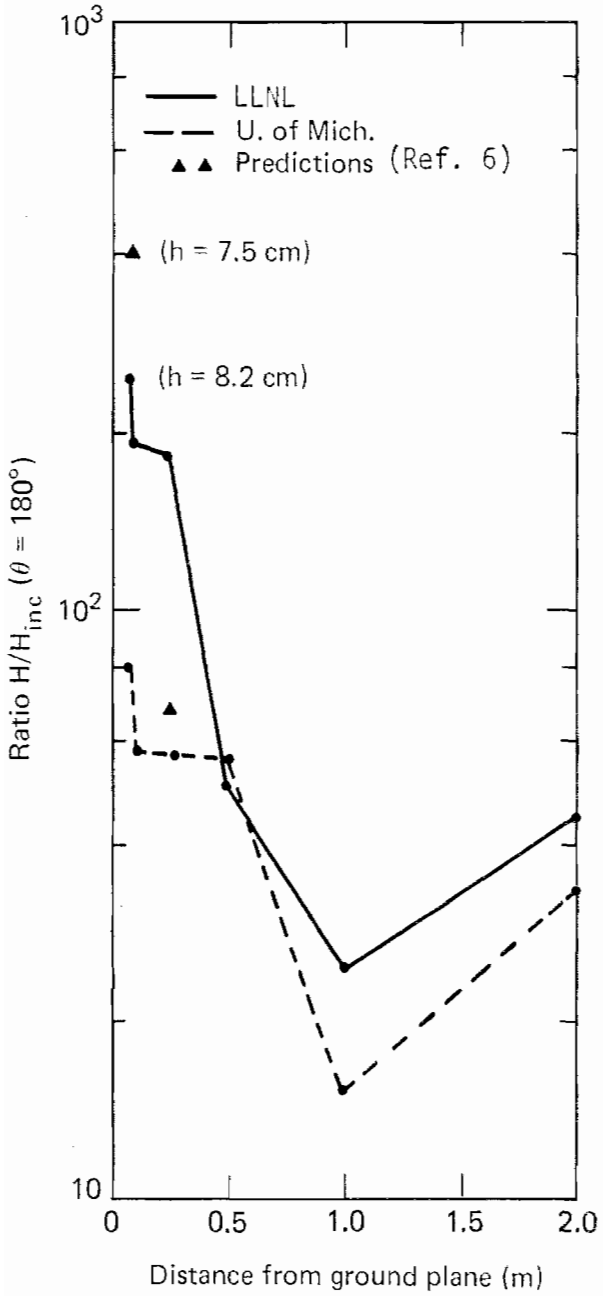

Figure 14. Predictions for the cylinder.

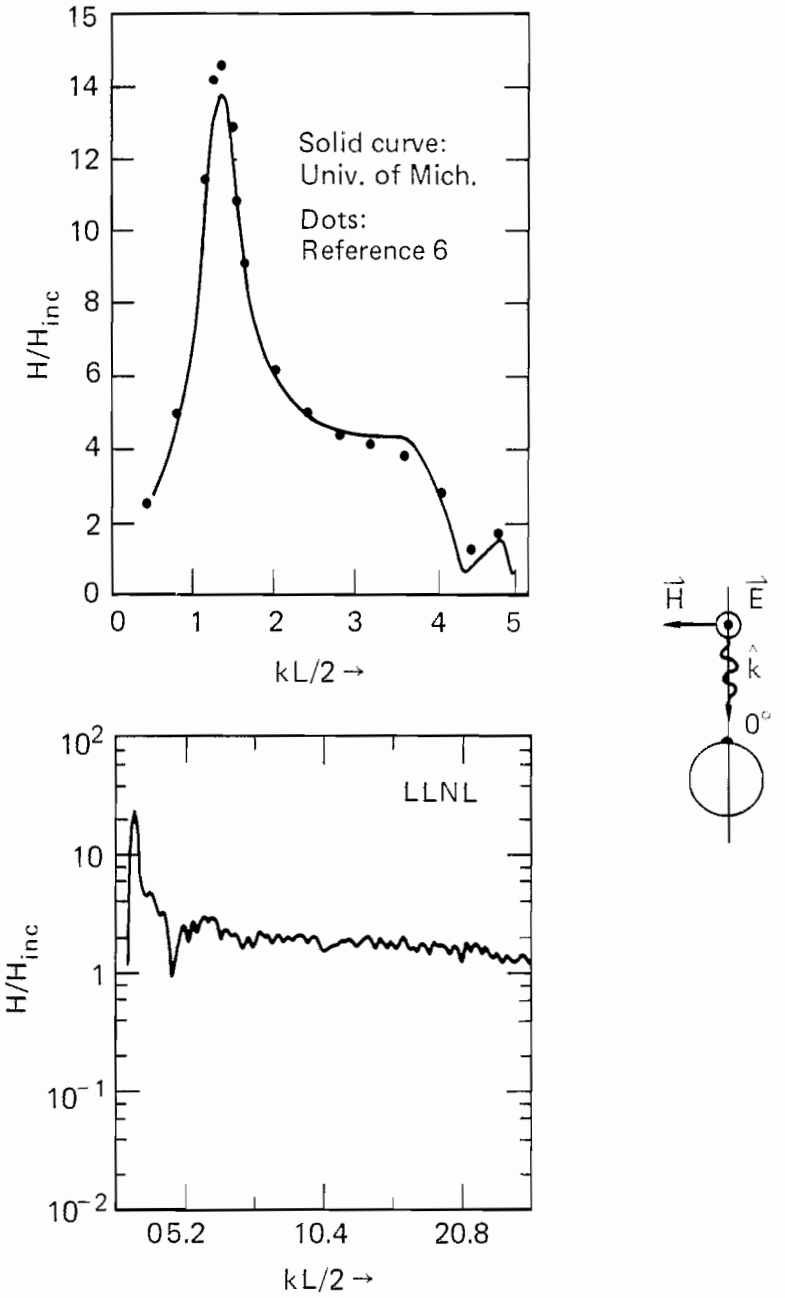

Figure 15. Comparison between LLNL, Univ. of Mich., and Sancer's predictions (H/H_{inc}; cylinder model; $\theta = 0^{o}$; free space)

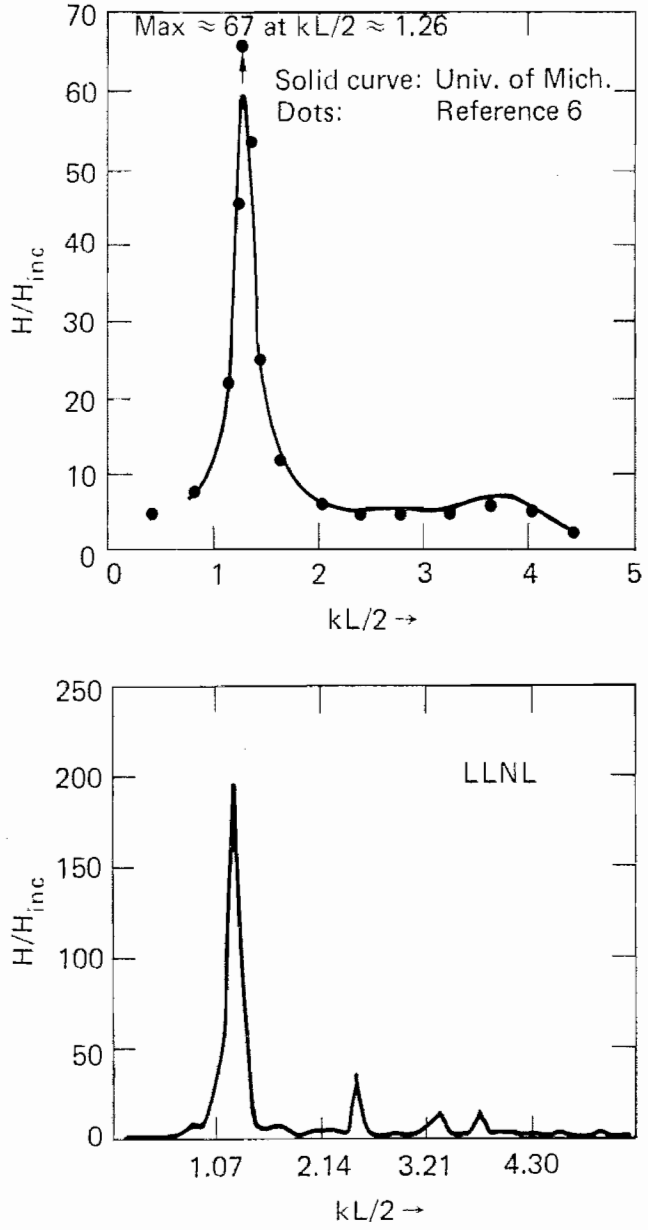

Figure 16. Comparison between LLNL, Univ. of Mich., and Sancer's predictions (H/H_{inc}; cylinder over ground; h = 25 A cm; $\theta = 180^{\circ}$)

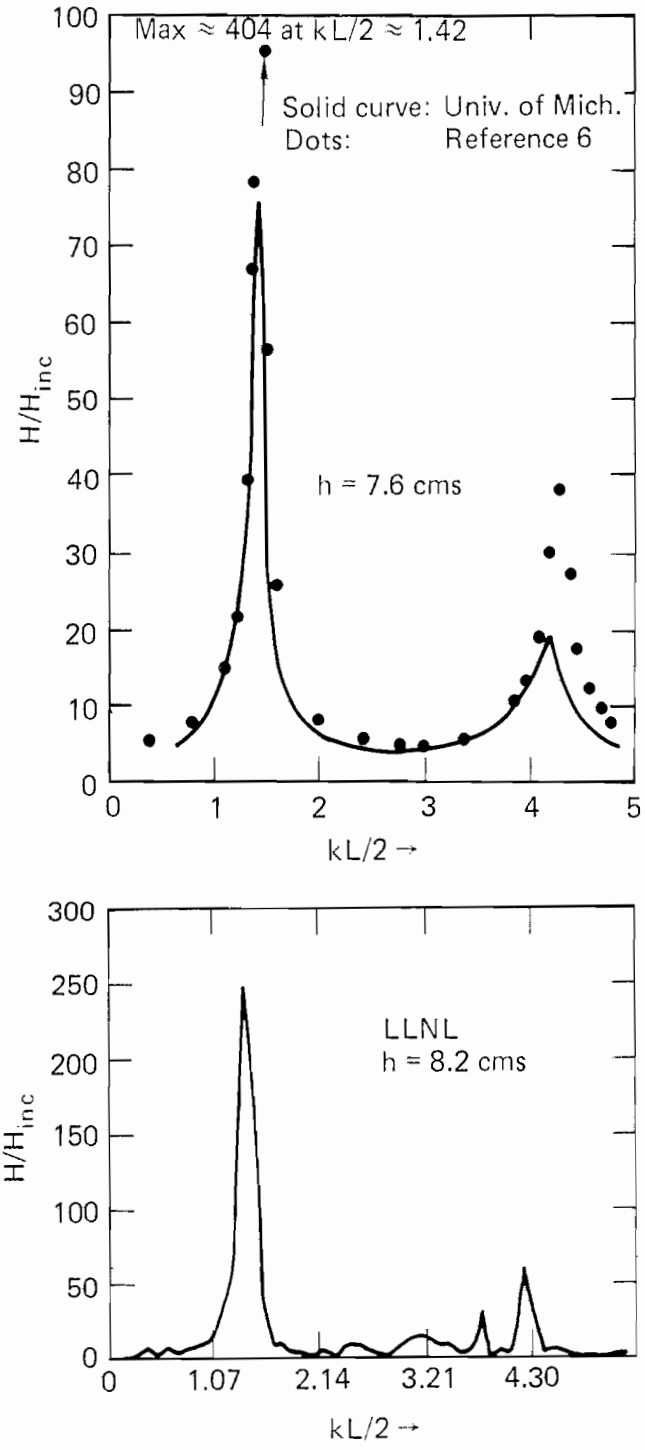

Figure 17. Comparison between LLNL, Univ. of Mich., and Sancer's predictions (H/H_{inc}; cylinder over ground; $\theta = 180°$)

The result of the pole extraction exercise is shown in Table 7. Here, the Prony, Extended Kalman Filter, and Maximum Likelihood Estimator predictions are listed as well as analytical predictions by Shumpert and Galloway [Ref. 7]. Only the cylinder case is considered for three configurations: free space, h = 50 cm and h = 10 cm. Only the first three poles are shown. The table shows estimates for the poles (real part, σ, and imaginary part, ω). The maximum likelihood identifier was run using two different underlying signal model assumptions types A and B. These two model types are decribed briefly in the text below.

We make the following comments concerning the tabulated results. The second harmonic (pole #2) parameters are generally hard to identify since the second harmonic does not ideally exist for image plane data. The current probe on the cylinder happened to be near a node for the even harmonics. Therefore, the Prony technique did not even assign a pole at the second harmonic. The maximum likelihood method forces identification of second harmonic parameters because the system model internal to this algorithm requires that the second pole be present. The high estimated damping terms (σ) can be explained when we consider that second harmonic exists in the initial transient (the electromagnetic impulse) but is not above the noise level in the remainder of the data record. Analytical predictions for the third harmonic, 50 cm and 10 cm data, are not available.

Because second harmonic information is virtually unobservable in the data, we restrict our comparisons to the fundamental and third harmonic only. Fundamental frequency parameter estimates using analytical, Prony, and maximum likelihood (model types A and B) methods are plotted in the s-plane in Figure 18. The graph shows the migration of the pole (the fundamental) as the distance between the cylinder and the wall becomes smaller according to the results of each analysis method. Figure 19 shows a similar graph for the third harmonic pole.

---

7. Shumpert, T. H., and Galloway, D. J., "Transient Analysis of a Finite Length Cylindrical Scatterer Very Near a Perfectly Conducting Ground" AFWL Sensor and Simulation Notes, Note 226, Albuquerque, New Mexico, August 1976.

TABLE 7. SUMMARY OF POLE LOCATIONS FOR CYLINDER ($s = \sigma + j\omega$)

Pole #		Analytical Prediction	Prony	Extended Kalman Filter	Max. Likelihood A*	Max. Likelihood B**
	Free Space	-131.4 ------ 775.4	-99.6 ------ 720.7	-190 ------ 750	-215 ------ 526	-137 ------ 829
1	h = 50 cm	-66.3 ------ 736.2	-74 ------ 541.0	-65 ------ 736	-102 ------ 770	-70 ------ 722
	h = 10 cm	-16.9 ------ 824.0	-22.9 ------ 661.0	-25 ------ 758	-28.9 ------ 767	-25 ------ 775
	Free Space	-206.4 ------ 1665.3	-N/A-	-N/A- ------ -N/A-	-654 ------ 1052	-N/A-
2	h = 50 cm	-301.5 ------ 1589.0	-N/A-	-N/A- ------ -N/A-	-1536 ------ 1540	-N/A-
	h = 10 cm	-55.3 ------ 1658.0	-N/A-	-N/A- ------ -N/A-	-723 ------ 1534	-N/A-
	Free Space	-236 ------ 2523.6	-297.3 ------ 2433.5	-710 ------ 2250	-721 ------ 1578	-654 ------ 2480
3	h = 50 cm	-N/A- ------ -N/A-	-258.9 ------ 2383.2	-460 ------ 2208	-440 ------ 2310	-206 ------ 2166
	h = 10 cm	-N/A-	-63.7 ------ 2311.6	-160 ------ 2274	-50.5 ------ 2301	-200 ------ 2379

Note: For each entry, the top number is σ and the bottom ω.

* A: With measurement noise model only.

** B: With both measurement and random excitation noise models included.

N/A: data not available.

The EKF and maximum likelihood B results appear to best agree with the analytically predicted values.

A significant difference between two types of internal signal models (A & B) used should be pointed out at this time. As applied to the pole extraction problem, the maximum likelihood A internal system model assumes that the cylinder has been illuminated by an ideal impulse, and the resulting response is thereby a sum of damped exponetials. The EKF and the maximum likelihood B models have the more general assumption that the cylinder is, over the period of the experiment, randomly excited. The maximum likelihood A identifier therefore attempts to fit the data to a sum of exponentials, whereas the EKF and maximum likelihood B essentially fits the autocorrelation function (ACF) of the data to the ACF of a sum of expontials.

It is not yet clear which technique is best for use on the EMP problem, since EMP data is usually a combination of responses to an ideal impulse and to random excitations. A future task would be to include both the ideal impulse and random excitation models into EKF and maximum likelihood identifiers. This would fold in to the proposed statistical characterization of the EMP range as described in Appendix C.

9.0 Conclusions and Recommendations

In this work, we have demonstrated the utility of the Transient Range Simulator to record and process transient data. Three objects were tested, namely a cylinder, crossed cylinders, and a scale-model 747 aircraft. The data were processed to find the frequency spectral content and the poles. In each case, comparisons were made with other available test data or analytical predictions. The following paragraphs contain pertinent comments concerning several aspects of this work.

A recurring problem in time-domain measurements is the lack of stable, high-amplitude pulse generators. This series of experiments used the IKOR IMP impulse generator, which produces an impulse of voltage, 300 ps

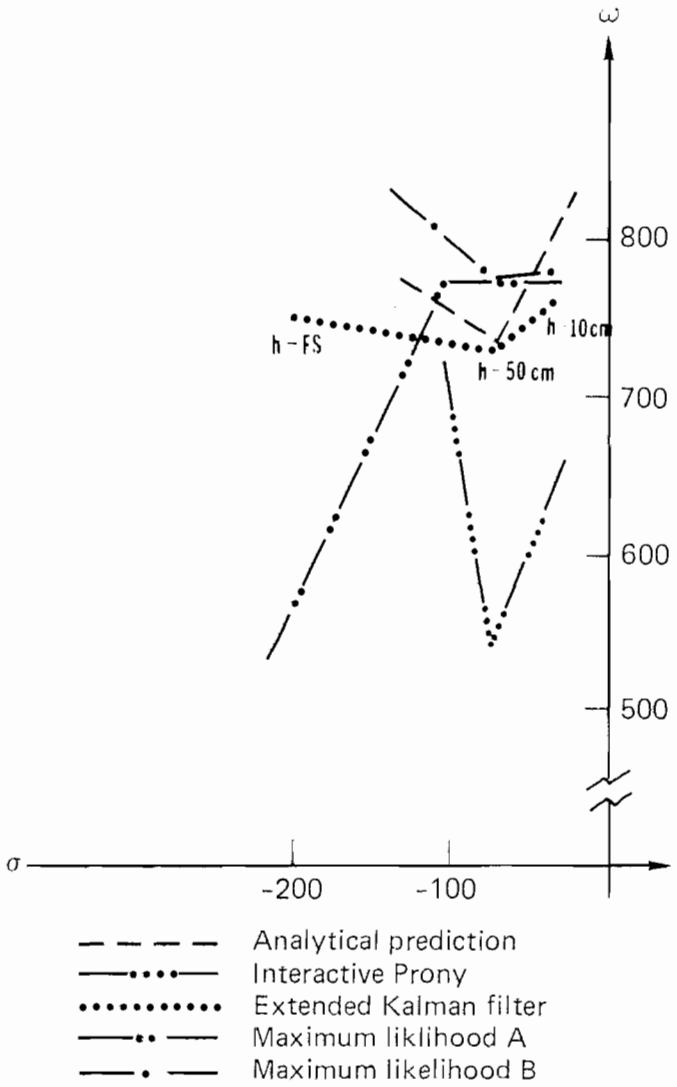

Figure 18. Migration of the Fundamental Pole.

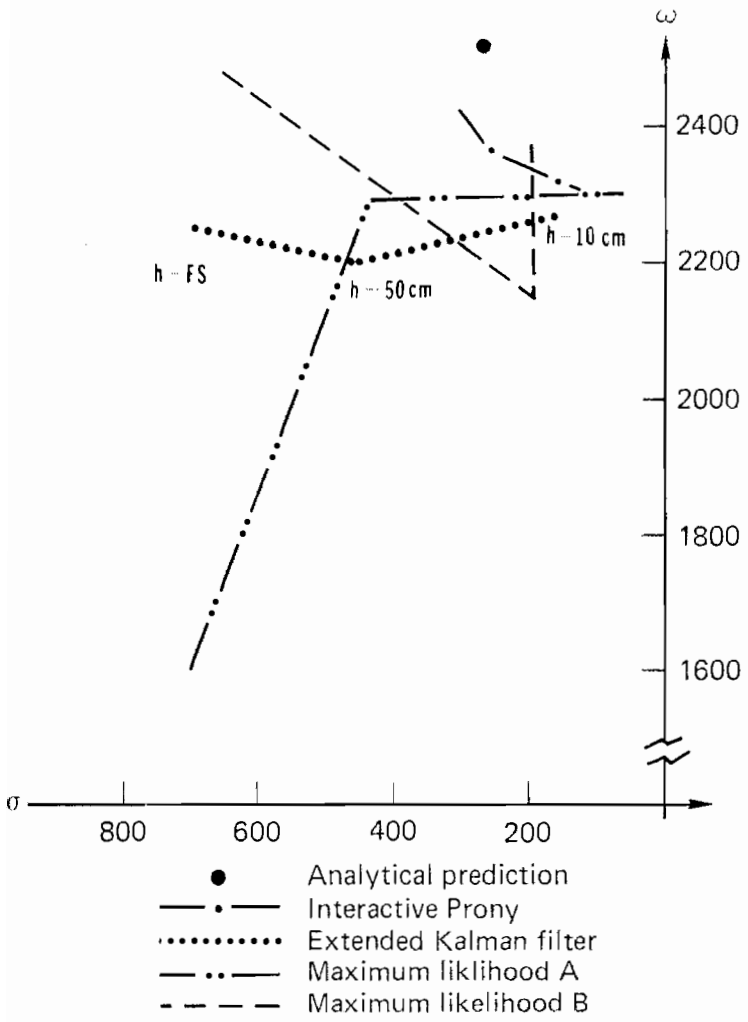

Figure 19. Migration of the third Harmonic.

wide at 50% amplitude point into a 50-Ω load (Ref. 2). Other commercially available pulsers do not have the amplitude or spectral content required to make wide-band measurements. Coupled to this problem are the sensors used to make the measurements. Ideal sensors have high sensitivity and are sufficiently small in size to minimize the perturbation of the fields they are designed to measure. For these measurements we used the AFWL ACD-1 $\dot{D}$ and the MGL-8 $\dot{B}$ sensors - two well-designed devices. But, even with the highest amplitude pulser available, we found ourselves close to the noise level on several measurements. Advances will probably have to come in the design of pulsers if measurements like those employed here are to be extended to more stringent conditions.

The possible use of a higher amplitude pulse generator to improve the signal to noise ratio is linked to the question of signal processing methods. If higher amplitude signal generators with the proper frequency spectrum cannot be located, then improved signal processing methods need to be used to compensate for the poor signal to noise ratio.

The greatest difficulty encountered in this project was the recording and processing of the highly resonant responses of the objects as they were brought closer to the ground plane. This necessitated taking longer time records which accentuated problems of sampling, drift and reflections. These in turn cause problems in the determination of the spectral content by classical means such as the Fast Fourier Transform or the Filon Method. Most of these problems were solved by recording the data with a Tektronix 7912 in conjunction with an LSI-11.

One of the recurring problems during the course of this project was the lack of adequate characterization of the range. A successful application of signal processing/identification methods to the range will require one to thoroughly characterize the nature of the measurement system and background noise. Current improvements on the range instrumentation should improve the attainable signal-to-noise ratios significantly; however, specific tailoring of the measurement techniques to signal processing needs will need to be implemented to assure: 1) enough data

are taken to assure observability of the parameters of interest, and 2) data rates are sufficient to prevent aliasing. A further subject of interest is the characterization of an EMP response by a more complex dynamic model than the simple sum of damped sinusoids model which is now used. This model would include generally nonlinear coupled differential equations and correlated driving noise. The complex model would hopefully incorporate knowledge of the phenomenological aspects of the experiment such as elements of the EM field equations, pulse reflection off the ground plane, etc.

In analyzing the data and obtaining the transfer functions for the various objects, FFT techniques were used. In retrospect, this seems like a rather poor method to perform the signal processing. The process of dividing frequency transforms is prone to large errors. We recommend that in the future, time domain signal processing methods which do not require FFT's be used. Two such methods are becoming currently available and have been discussed in the main body of the report; namely the extended Kalman filter and the maximum likelihood estimator. These process the time domain data directly. Models of the incident pulse can be employed to "remove" its effect from the data. In this way, the numerical problems created by frequency domain (FFT) division are avoided.

References

1. Deadrick, F. J., Miller, E. K., and Hudson, H. G., The LLL Transient-Electromagnetics-Measurement Facility, Lawrence Livermore National Laboratory, Livermore, CA, Rept. UCRL-51933 (1975).

2. Bevensee, R. M., Deadrick, F. J., Miller, E. K., and Okada, J. T., Validation and Calibration of the LLL Transient Electromagnetic Measurement Facility, Lawrence Livermore National Laboratory, Livermore, CA, Rept. UCRL-52225 (1977).

3. Baum, C. E., Breen, E. L., Giles, J. C., O'Neil, J., and Sower, G. D., "Sensors for Electromagnetic Pulse Measurements Both Inside and Away from Nuclear Source Regions," IEEE Trans. Antennas Propag. AP-26, No. 1, January 1978, also Sensor and Simulation Notes, Note 239, 1 Jan 78.

4. Olsen, S. L., "Sensor MGL-8B sensor DW," AL-1186, September 1975, Albuquerque Division, EG&C Inc., 9733 Coors R., N. W., Albuquerque, NM 87114; ibid. "MGL-S8 B-dot sensor development," AL-1187, September 1975.

5. Liepa, V. V. et al., "Surface Field Measurements with Image and Ground Planes," AFWL Sensor and Simulation Notes, Note 244, Albuquerque, NM, November 1977.

6. Sancer, M. I., et al., "Formulation of Electromagnetic Pulse External Interaction Above a Lossy Earth/Comparison of Numerical Results with Experimental Data for Limiting Cases," AFWL Interaction Notes, Note 354, Albuquerque, NM, October 1978.

7. Shumpert T. H., and Galloway, D. J., "Transient Analysis of a Finite Length Cylindrical Scatterer Very Near a Perfectly Conducting Ground," AFWL Sensor and Simulation Notes, Note 226, Albuquerque, NM, August 1976.

Appendix A
LLNL Transient Range Facility

Measurements at the LLNL Transient Range Facility are made over a large 8.5 m x 8.5 m aluminum covered ground plane mounted 3 feet off the floor using a conical antenna which extends from the image plane to the room ceiling. All instrumentation is located beneath the image plane, and at this facility a sampling oscilloscope is utilized as the signal sampling device.

The operation of the transient range is conceptually very simple. A very narrow electrical pulse is used to drive a wide-bandwidth radiating antenna which illuminates the target under test. The surface densities of currents and charges induced on the target are measured by surface-mounted B and D sensors. The outputs from the sensors are fed to a sampling oscilloscope which records the response of the target as a function of time. The results may be displayed in the time domain or transformed to the frequency domain via the Fourier transform. Figure A1 shows a block diagram of the system; the diagram shows that a minicomputer controls the operation of the equipment and handles the data logging tasks. The nature of the sampling oscilloscope is such that not one, but many pulses must be radiated by the source antenna to provide a complete time-history waveform. The computer controls the oscilloscope and, in the process, obtains 512 equally spaced samples of the transient waveform. These transient data are then plotted on an on-line plotter and then written onto magnetic tape for later off-line data processing.

Two factors determine the working bandwidth of the transient measurement system. At the low frequency end, the range clear time, or time it takes unwanted reflections from discontinuities in the cone, and from the walls and surrounding environment to reach the target area, establishes a lower limit.

For the LLNL range, reflections from simulator edges (building ceiling and other objects in the room have been found to be nondetectable) and the range have been used to obtain data records in excess of 200 ns. For limited number of samples, this limits the time resolution and may introduce large sampling errors. A 200 ns time record corresponds to a minimum useful frequency of 5 MHz. At the high frequency end, the limits are a complex combination of

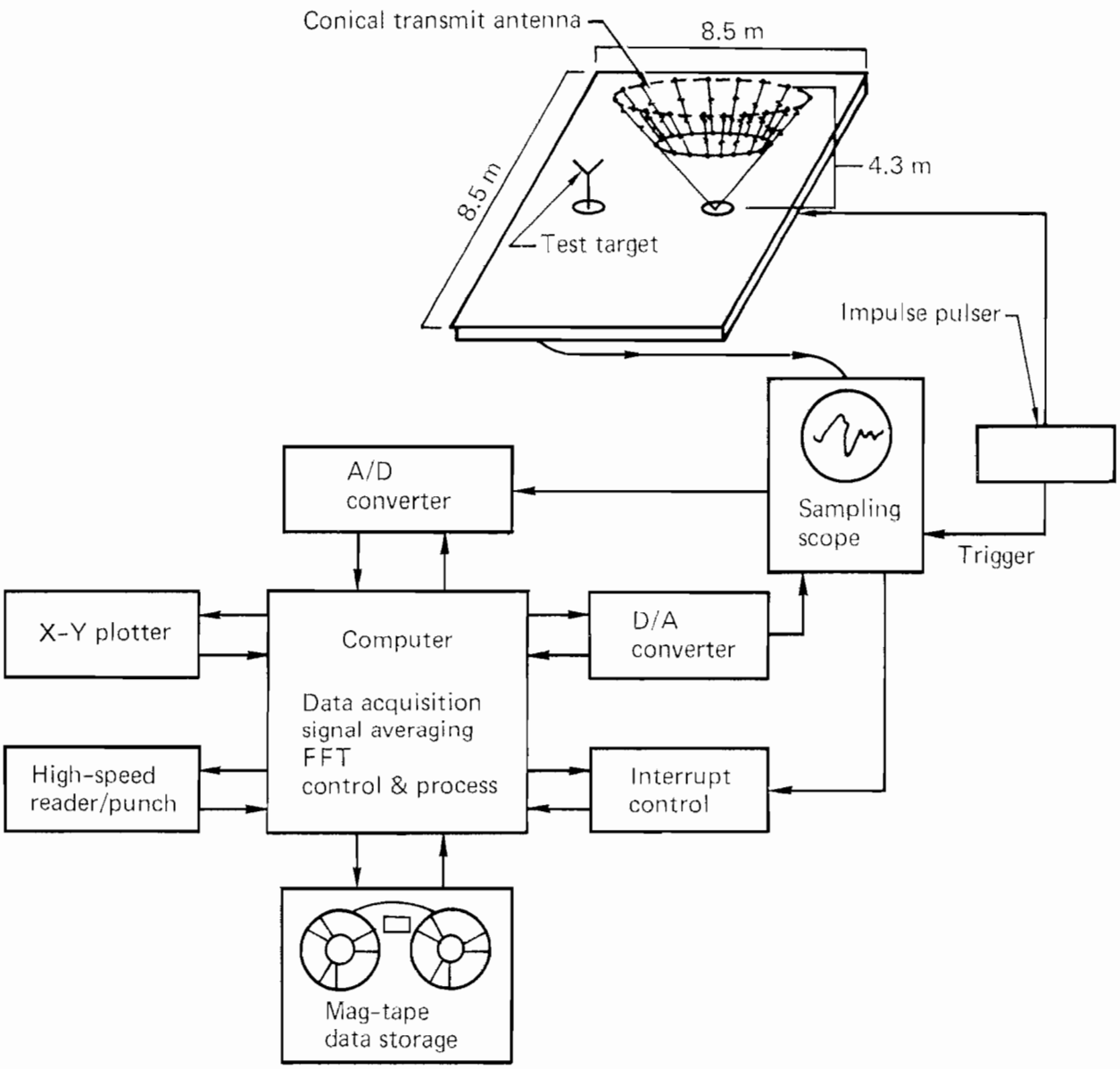

Figure A1. Schematic of LLNL Transient EM-Measurement Facility.

many factors including the rise-time of the exciting pulse, rise-time of the oscilloscope, and losses in the cables, delay lines, and connectors. Our measurements indicate that the maximum frequency is in excess of 3 GHz, depending on the pulse generator used to drive the antenna and the quality of the cables and delay lines used.

The associated electronics with the range are comprised of a pulser, sampling oscilloscope and a control computer, plus its various ancillary components. A measurement sequence involves a sequential sampling of 2^N discrete points of the transient waveform, typically 512, with each final data value being the average of several samples to reduce the effects of time-base and amplitude jitter. The IKOR IMP pulser has been used which has a rise time of less than 100 ps. The sampling oscilloscope consists of a Tektronix 7408 Mainframe together with a 7M11 input delay, a 7S11 sampling unit, a 7T11 sampling time base and an S4 sampling head. In addition, a CT-3 signal pickoff unit is used with the pulser output as a trigger source for the system. The upper frequency cutoff of the sampling system exceeds 10 GHz. A Digital Computer Controls, D112 minicomputer is used to control the experiment. Together with various peripheral units it performs the following:

1. Asks the experimenter for run descriptions and scope calibration factors.

2. Plots results (including scales and titles) on an on-line Calcomp plotter.

3. Records accumulated experimental data on magnetic tape for later off-line post processing.

4. Controls the sampling oscilloscope concerning the number, location and averaging of the sampled points.

The above data collection system was found to be adequate for time records not in excess of 20 ns. For longer records, the system was beset with problems. The use of a Tektronix 7912 transient digitizer and the LSI-11 microcomputer to control and process the data was found to be far superior.

The LSI-11 is used with dual density floppy disks, a Tektronix 4025 terminal and a hard copy unit. The greatest advantage of the LSI-11 system was the ability to use interactive on-line analysis techniques to quicky analyze the data at the experimental site. This procedure allowed us to quickly optimize our experimental technique.

Other advantages of using a 7912 transient digitizer instead of a sampling scope were elimination of time-base jitter, elimination of grounding problems and reduction of amplitude distortion.

Range Improvement

In preparing the LLNL transient range to make this series of measurements, three items which had the effect of reducing the available signal and bandwidth of the measurements were investigated and improved. These items include the monocone antenna, the delay line used with the sampling oscilloscope, and the connectors and cables used to instrument the models.

Cables--The last of these items, the cables and connectors, were upgraded by converting to the SMA (3-mm) series of 50-Ω cables, connectors, and attenuators. Short sections of commercially available (Tektronix) cable assemblies were used for the instrumentation; they introduced insignificant loss and distortion in the measured signals.

Delay Lines--High speed sampling devices, such as the sampling oscilloscope used on the transient range, must be pretriggered approximately 70 ns before the signal is input to the vertical deflection unit. For pulse generators which do not have this pretrigger feature (such as the 1.5 kV, 300 ps impulse IKOR used in these experiments), one must delay the signal by the required amount. Typically, this is achieved by introducing a 70-ns delay line in the signal path; it is this line which introduces a degradation in the signal.

Several candidate delay lines were evaluated to find the one with the widest bandwidth and the least amount of attenuation. The ideal line would be a cryogenically cooled super-conducting delay, but such a unit was not available. Instead, we selected the best available coaxial delay line of

several types evaluated. Figure A2 shows the transfer functions of the lines tested. Of these, the 7/8 in. Heliax Tektronix unit performed best and was therefore selected for these measurements.

Conical Antenna--The final item we improved was the conical antenna used to radiate the transient EM pulse. By increasing the cone angle, as shown in Figure A3 [Ref. A1], the conical antenna can be made to match the 50-Ω feed-line. This occurs at a cone half-angle of ≈ 45°.

To evaluate the design of the cone, we first utilized a Time-Domain Reflectometer (TDR) to match the cone impedance to the feedline. Figure A4 shows a cross section of the transition region and the way the feed is adjusted for an impedance match.

By adjusting the length of the feed screw, we can raise and lower the cone into the cylindrical coax section. If the cone tip is too long, the match to the cone is inductive; if it is too short, the capacitance of the cone to sides of the coaxial feed can be observed. Proper adjustment of the feed length can be attained for a perfect match. This is shown on the TDR plots of Figure A5.

Away from the feed region, the cone is composed of three regions, as shown in Figure A6. The bottom section is formed with a piece of sheet brass, while the upper sections are composed of 16 symmetrically located wires which extend from the brass cone to the room ceiling. Aluminum foil was also used to cover the lower part of the wire section. Above the foil, each of the 18 wires are loaded with eight discrete 100-Ω resistors. These loads help to attenuate the pulse propagating on the cone, thus minimizing the pulse reflected from the ceiling back into the experimental area. Figure A7 shows a TDR plot of the whole conical structure in which the various sections of the cone may be noted.

A1. Antenna Engineering Handbook, Jasik, H., Ed., McGraw-Hill Book Co., New York, 1961, pp. 3-11.

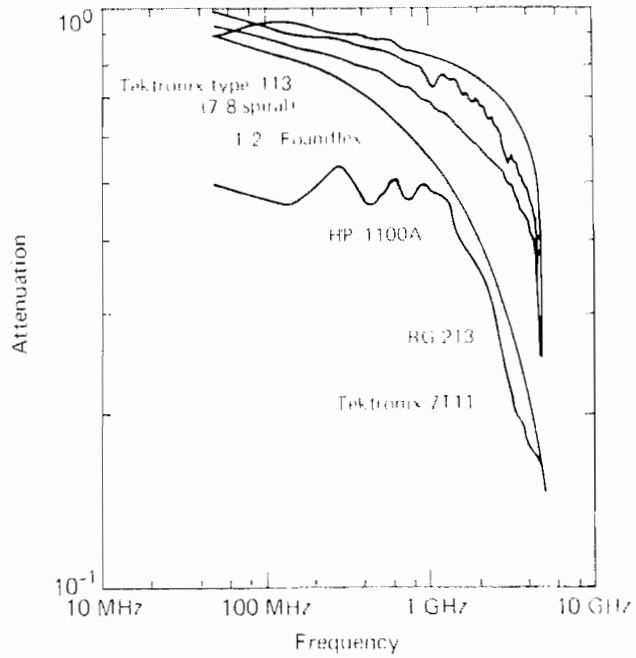

Figure A2. Voltage Transfer Functions of Several 70-ns Delay Lines Evaluated.

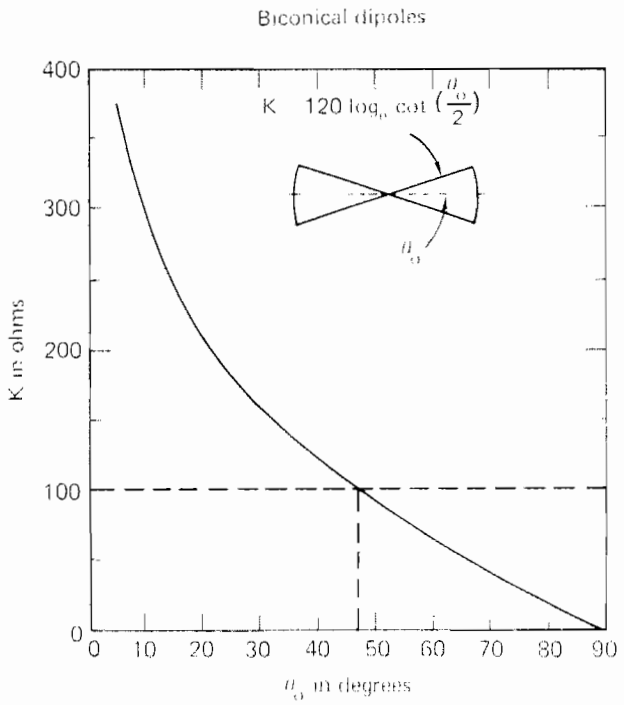

Figure A3. Characteristic impedance of a biconical dipole as a function of cone angle (Ref. 2).

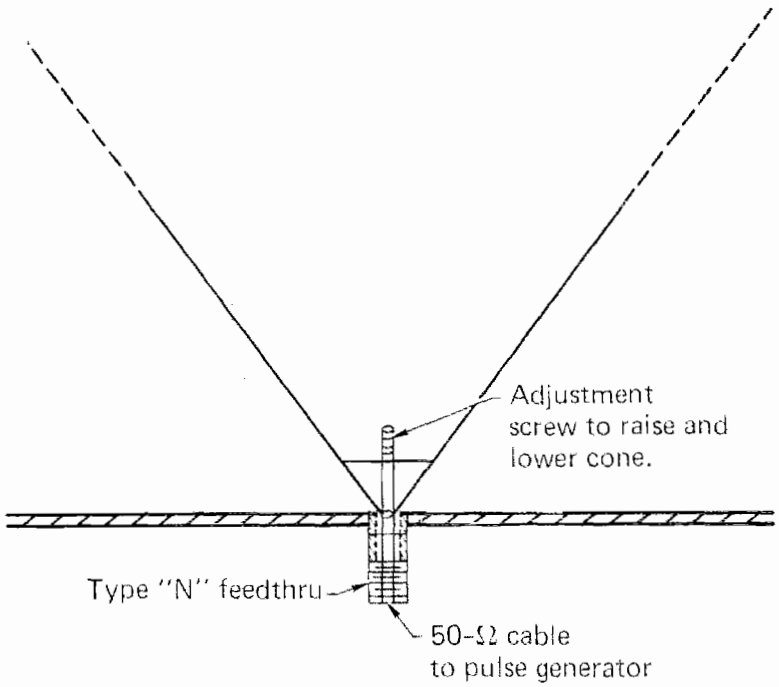

Figure A4. Cross section of Monocone feed region of the conical antenna showing the adjustment screw used to raise and lower cone in the coaxial fitting.

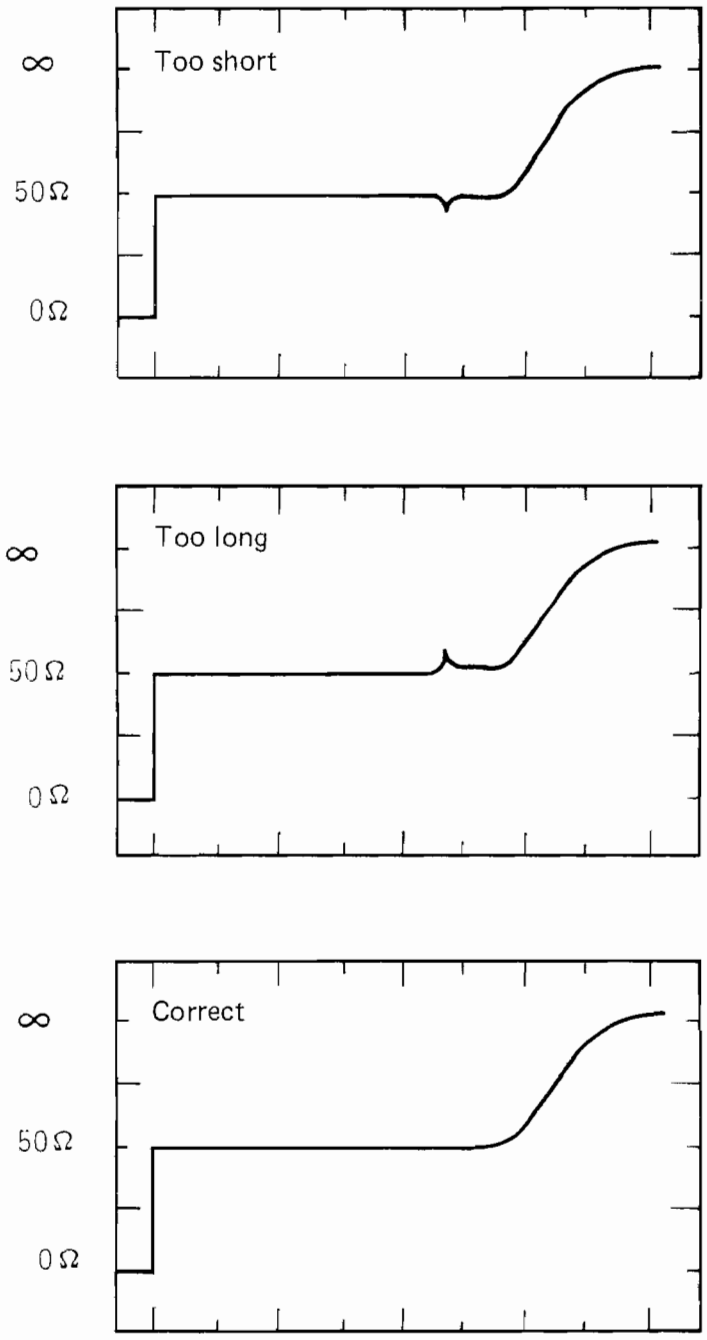

Figure A5. TDR of Cone Feed Region showing proper adjustment of Feed length.

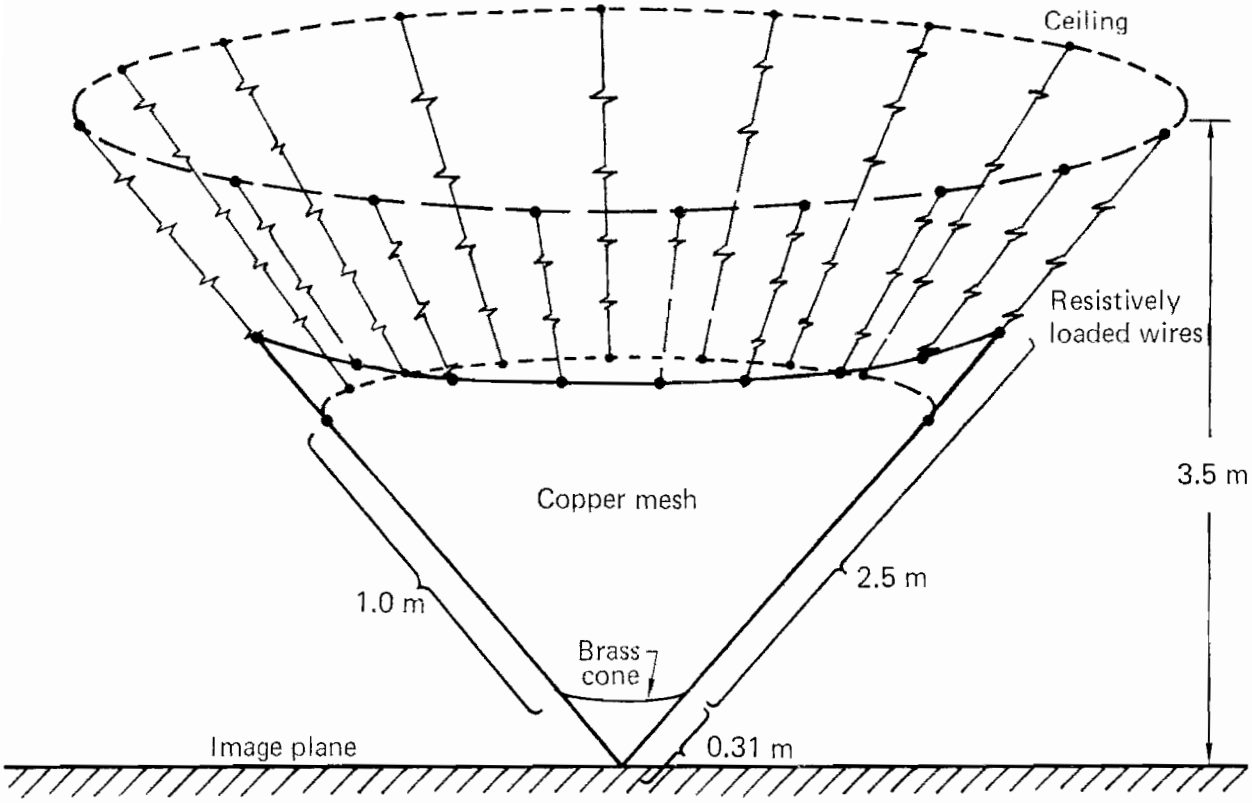

Figure A6. Construction details of monocone antenna.

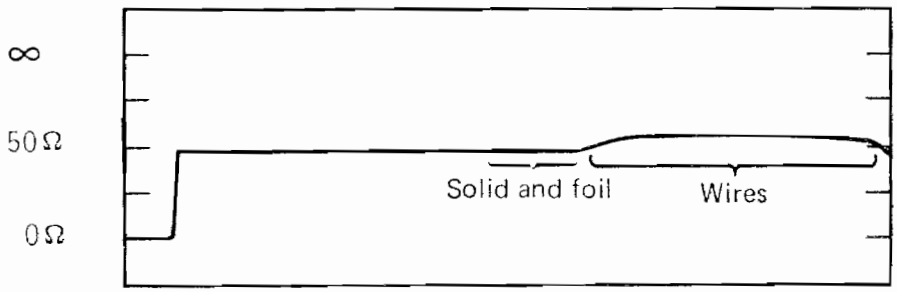

Figure A7. TDR Plot of monocone input impedance, showing the various regions of the cone.

Appendix B
Rationale for Cylinder Length Choice

Several factors influence the choice of a test object size for scale model measurement, and the selection is a trade-off between these various factors discussed in the following paragraphs.

Phase Error: The incident wave that illuminates the test object at the LLNL Transient Range facility is a spherical wave. Therefore, the whole object is not illuminated at the same time. This gives rise to phase errors that depend on the frequency components of interest.

For a test object that is a vertical cylinder of length L/2 (see Figure 5) located a distance R from the base of the monocone antenna, the maximum time difference over the object in the arrival time of the incident pulse is

$$\Delta t = \frac{1}{c} \left[\sqrt{R^2 + L^2/4} - R \right] \tag{B1}$$

which for $R >> L/2$ reduces to

$$\Delta t = L^2/8\,Rc \tag{B2}$$

where c is the speed of light. At the fundamental resonance of the test object ($\lambda = 2L$), this transforms into a phase error $\Delta\theta$, where

$$\Delta\theta = \frac{\pi}{L} \left[\sqrt{R^2 + L^2/4} - R \right] \tag{B3}$$

or $$\Delta\theta = \pi\, L/8\, R. \quad [R >> L/2] \,. \tag{B4}$$

For the cylinder used in the experiments reported here, L = 1.01 m and R = 2.43 m, which gives a $\Delta\theta \simeq 9°$. The statement of work called for a phase error not to exceed 45° at the fundamental resonance. Note that if L is made to increase, the phase error will similarly increase almost linearly with L. Therefore, it is preferable to keep the largest dimension of the test object as small as possible.

Amplitude Variation: Another reason for keeping L small is to avoid large incident field amplitude variations across the object. In ratio this is given by

$$\text{Amplitude Variation} = [\sqrt{R^2 + L^2/4} - R\ ]\ /R \qquad (B5)$$

which for $R >> L/2$ becomes

$$\text{Amplitude Variation} = L^2/8\ R^2 \qquad (B6)$$

For the cylinder in question, this is $\approx$ 2.%.

Signal-to-noise: This is a function of the pulser energy and bandwidth, target response and sensor sensitivity. If everything else is left unchanged, better signal-to-noise ratio is usually obtained by larger sized objects. A larger sized object is also easier to instrument. As we have seen however, this can only be pushed so far, since phase and amplitude errors will become unacceptable.

It was decided at the start of the effort that a good compromise for object size was a largest dimension equal to about .5 m.

Appendix C
Pole Estimation Techniques

1.0 Introduction

The study of EMP phenomena has promoted the development of techniques to investigate transient electromagnetic response data. The characterization of EMP transient response information is a matter of national concern. Since large amounts of data are necessary to pointwise define an arbitrary transient response, it is quite reasonable to "identify" a parameterization or model of the "response". The model developed is useful, not only to merely parameterize the response, but also to give more meaningful information about the physical process producing the response itself.

In this appendix we discuss the implementation of some signal processing algorithms which can be used to "estimate" the parameters of an electromagnetic response model from noisy transient measurements. The techniques employed range from simplified algorithms which perform well for high signal-to-noise ratios, to complex model-based estimators, which perform well for low signal-to-noise ratios. In Section 2 we present the necessary background information. The various algorithms are discussed (simply) in Section 3. In Section 4, the application to transient EM data is presented.

2.0 Background

In electromagnetic wave theory it is possible to represent the response of an object to various excitations by the singularity expansion method (SEM). The SEM represents an electromagnetic variable (field, current, etc.) as the impulse response of the object [Ref. C1], i.e.,

$$\underline{U}_p(\underline{r},t) = \sum_i \eta_i(\underline{e},s_i)\underline{v}_i(\underline{r})e^{s_i t} \qquad (C1)$$

where

$\underline{U}_p$ vector impulse response

η complex coupling coefficient

$\underline{v}$ complex natural mode describing the behavior of $\underline{U}p$ over the object

$\underline{e}$ exciting field characteristics (e.g., polarization, direction of evidence, etc.)

$\underline{r}$ spatial coordinates or position

s_i complex natural frequency (or pole, or natural resonance)

The sets of parameters $(\{s_i\}, \{\underline{v}_i(\underline{r})\})$ are dependent on the object parameters only and independent of the excitation. The effect of the exciting wave is contained entirely within the set of coupling coefficients $\{_i\underline{e}, s_i\}$ which are independent of the position on the body. Thus, the electromagnetic interaction is completely characterized by these sets. In fact, the response to an arbitrarily shaped waveform can be generated using concepts of linear system theory where the response y to an arbitrary impulse is given by the convolution(*)

$$y(\underline{r},t) = U_p(\underline{r},t) * u(\underline{r},t) \qquad (C2)$$

Implicit in (C2) is that $\underline{e}$ is the same for the new exciting waveform. However, $(\{s_i\}, \{\underline{v}_i(\underline{r})\})$ are invariant; therefore, these sets can be used to "parameterize" a given object for <u>any</u> excitation. We are not concerned at this point in the partitioning of the natural modes and coupling coefficients, so we define the set of complex residues at a point $\underline{r}_o$ as

$$\underline{C}_i(\underline{r}_o) := \eta_i\ (\underline{e},s_i)\underline{v}_i(\underline{r}_o) \qquad (C3)$$

and for this work concern ourselves only with scalar response functions.† Thus, the impulse response of the linear system of (C2) can be represented as

† It should be noted that the sophisticated model-based estimators discussed subsequently can be used to identify separately the $_i$ and $\underline{v}_i$ parameters, if desired, as well as vector response functions (multiple measurement instruments); however, this work was not feasible in the allotted time.

$$y(t) = H(t) * \delta(t) = \sum_{i=1}^{N} C_i e^{s_i t} \qquad (C4)$$

where

$s_i := \sigma_i + j\,\omega_i$, σ the damping ratio and ω the natural frequency

$H(t)$ is the object impulse response at position $\underline{r}_o$; i.e., $U_p(\underline{r}_o, t)$. Thus, the parameterization of the object can be stated simply by the electromagnetic parameter estimation problem.

"Given a set of noisy electromagnetic response† measurements $z(t)$, find the (best) (minimum variance) estimates $(\{\sigma_i, \omega_i\}, \{c_i\})$ characterizing an unknown object."

We will assume that the noise contaminates the response y as

$$z(t) = y(t) + v(t) \qquad (C5)$$

where v is zero mean, Gaussian with covariance R.

Before we begin discussing the various estimation algorithms applied to the problem, we must define an alternate way of representing a linear system which is equivalent to (C3) and (C4). Recall from ordinary differential equations [Ref. C2] that (C4) represents the solution of a N^{th} order differential equation. It is well known that this equation can be broken down to the solution of N first order differential equations of the general form:

$$\dot{\underline{x}}(t) = F\underline{x}(t) + \underline{g}\,u(t)$$

$$y(t) = \underline{h}^T\underline{x}(t) \qquad (C6)$$

† This representation is not limited only to scalar systems; e.g., u and y can be vectors and g, h^T become matrices.

where

x is the N-state vector, u, y are the respective input and output. F is a N x N matrix and q, h are N-vectors

This representation is called the "state space" form in linear system theory [Ref. C2] and forms the basis of various parameter estimation schemes [e.g., see Ref. C4]. It is easily shown that the impulse response of (C6) is

$$y(t) = \underline{h}^T e^{Ft} \underline{q} = \sum_{i=1}^{N} C_i e^{s_i t} \tag{C7}$$

or in transfer function form, we have

$$H(s) = \underline{h}^T (sI-F)^{-1} \underline{q} = \sum_{i=1}^{N} \frac{C_i}{(s+s_i)(s+s_i^*)} \tag{C8}$$

In the next section, we discuss three parameter estimation algorithms applied to this problem: (1) Prony's technique which utilizes the models of (C6), or (C8); (2) extended Kalman filter technique; and (3) the maximum likelihood identifier, both of which use the state space form of (C6).

3.0 Parameter Estimation Algorithms

In this section we discuss the three parameter estimation algorithms employed to extract the set of object parameters $(\{\hat{\sigma}_i\ \hat{\omega}_i\},\{\hat{C}_i\})$ from noisy measurement data. The algorithms employed were: (1) Interactive Prony's technique (IPT); (2) extended Kalman filter (EKF); and (3) maximum likelihood identifier (MXLKID). We will not discuss the mathematical details of these algorithms, but rather include the primary references for the interested reader. After presenting each algorithm, we will compare them and discuss the various tradeoffs.

Interative Prony's technique (IPT) is basically a linear least squares estimator for poles in the discrete (z transform) domain [Ref. C1]. The

algorithm is depicted (simply) in Figure C1. Depending on the signal-to-noise ratio (SNR) [Ref. C3] either the impulse response (high SNR) or the autocorrelation response (low SNR) is estimated using fast Fourier transforms or sample autocorrelation estimators, respectively. The filtered data is then "windowed", and poles estimated from each data window by solving a set of linear matrix equations to obtain linear least squares estimates of the coefficients of a polynomial, the roots of which are the discrete (z domain) poles. These poles are then transformed to the continuous domain and identified directly with the object response [Ref. C1]. This technique is repeated by the processor many times and "pole clusters" are obtained. It should be noted that the discrete or sampled data domain representation is necessary because of the use of "sampled" response data. Not accounting for the sampling phenomenon, will result in erroneous estimates for the continuous poles.

The extended Kalman filter (EKF) is basically a nonlinear state estimation algorithm which can be used to estimate unknown parameters by redefining them as states. Recall that a state estimator is a computer algorithm which may incorporate: (1) knowledge of the physical process phenomonology; (2) knowledge of the measurement system; (3) knowledge of process and measurement uncertainties in the form of mathematical models to produce an estimate of the state.

Most state estimators can be placed in a recursive form with the various subtleties emerging in the calculation of the current estimate ($\hat{x}_{old}$). The standard technique employed is based on updating the current estimate as new pieces of measurement data become available. The state estimates generally take the recurrence form

$$\hat{x}_{new} = \hat{x}_{old} + K_k \epsilon_{new} \tag{C9}$$

where

$$\epsilon_{new} = z_k - \hat{z}_{old} = z_k - h(\hat{x}_{old}) \tag{C10}$$

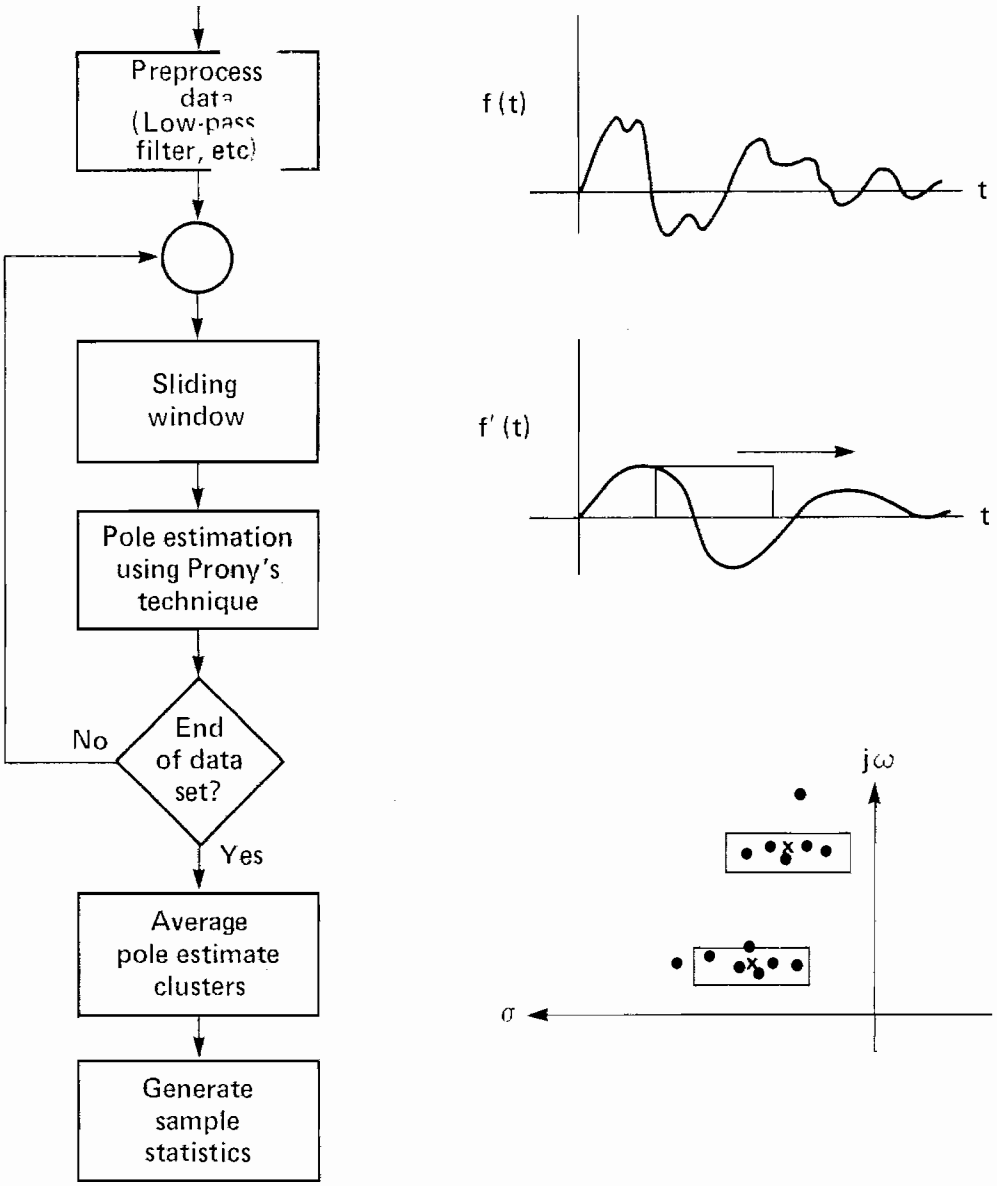

Figure C1. Interactive Prony Technique.

Here we see that the new state estimate is obtained by correcting the old estimate by a K-weighted amount. The term ϵ_{new} is the new information or innovations [Ref. C4]; i.e., it is the difference between the actual measurement and the predicted measurement ($\hat{z}_{old}$) based on our old state estimate. The computation of the weight K depends on the error criterion used (e.g., mean-squared, absolute, etc.) [Ref. C5].

Note that a physical process model (e.g., state equation in (C6) for linear case) is used to produce $\hat{x}_{old}$. The interested reader should see Gelb [Ref. C6] for details.

Thus, the EKF is a state estimator capable of producing estimates for nonlinear as well as linear processes and measurements. A simplified diagram of the algorithm is depicted in Figure C2. Here we see that the state estimate $\hat{x}_{old}$ is calculated (or predicted) based on the process model, after the estimator is initialized. The calculation of the gain, K, and innovations, ϵ, follows. Note that the measurement at a given time step is utilized in calculating the current ϵ. From these calculations the new or corrected state estimate is obtained. The algorithm continues in this loop, processing measurement data as it becomes available. This processing is considered on-line because it can be accomplished in conjunction with the response measurements, i.e., the state estimates are updated in real time, each time a new measurement becomes available.

The final algorithm is the maximum likelihood identifier (MXLKID). The MXLKID algorithm is a complex off-line technique which utilizes a parameter optimization algorithm looped around the EKF to obtain parameter estimates. The algorithm maximizes the likelihood function, or equivalently minimizes the negative log-likelihood function $J(\theta)$; i.e.,

$$\min_{\theta} J(\theta) = -1/2\ell n(2\pi) - 1/2 \sum_{i=1}^{N} \epsilon_{new}^{T}(i,\underline{\theta}) \left(R(i,\underline{\theta})\right)^{-1} \epsilon_{new}(i,\theta) + \ell n|R_{\epsilon}(i,\underline{\theta})| \qquad (C11)$$

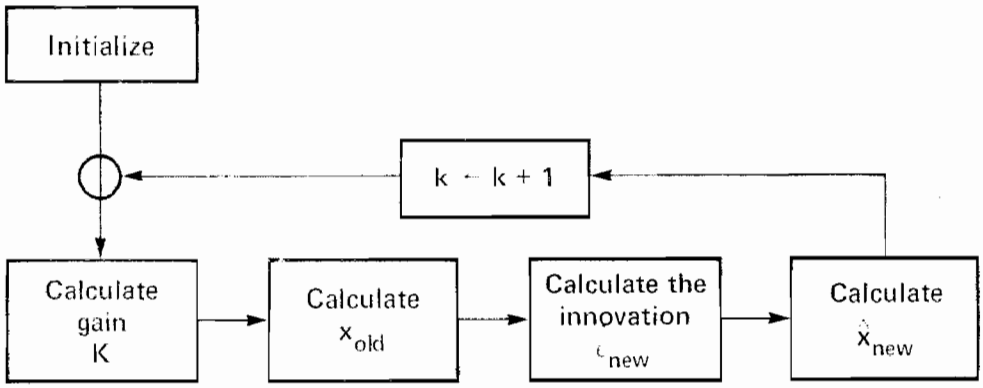

$$\hat{x}_{new} = x_{old} + K_k \epsilon_{new}$$

where

$$\hat{\epsilon}_{new} = z_k - H(x_{old})$$

Figure C2. Extended Kalman Filter Algorithm.

where

ϵ_{new} is the innovation of equation (C10)

R_{ϵ} is the corresponding innovation covariance matrix.

The parameter estimator (optimization algorithm) is usually a gradient-based technique [Refs. C7 and C8], i.e.,

$$\hat{\theta}_{new} = \hat{\theta}_{old} + \rho H \frac{\partial J}{\partial \theta} \qquad (C12)$$

where $\hat{\theta}$ are the parameter estimates

ρ is a step parameter

H is a weighting matrix dependent on the particular optimization technique used.

The simplified algorithm operation is depicted in Figure C3. The Kalman filter is used to produce uncorrelated innovations, ϵ, from the correlated measurements, z. The likelihood formation operation (C11) is calculated using results from the Kalman filter. In some optimization algorithms the filter is also used to calculate elements in the weighting matrix, H (e.g., see [C8]).

Before we discuss the performance of these three algorithms on the electromagnetic parameter estimation problem, we first compare their basic attributes. Referring to Table C1, we see that the interactive Prony algorithm is a simple technique valid for high SNR, and because of the lack of system modeling it is restricted in scope of application (linear, time invariant problems only). Of course, because of its simplicity, it is less complex and faster than the EKF and MXLKID algorithms. The IPT requires several runs to generate an ensemble of samples for statistical validation of the parameter estimates whereas the two other techniques have statistical validation built in.

The EKF and MXLKID algorithms appear similar in many categories, which is expected since the MXLKID technique actually uses an EKF as an integral part of its computation. The main differences between MXLKID and the EKF

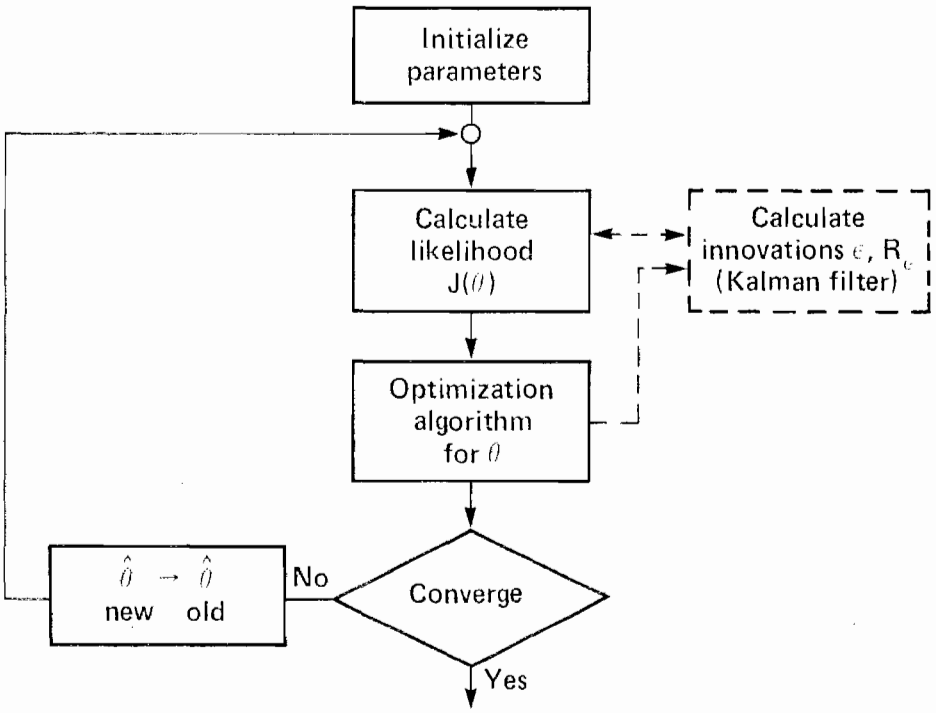

Figure C3. Maximum likelihood identification algorithm.

TABLE C1. IDENTIFICATION ALGORITHM COMPARISONS

	PT	EKF	MXLKID
Problem scope	Linear, time invariant	Linear, nonlinear, time varying	Linear, nonlinear
Signal models	Scalar	Vector	Vector
Noise models	None	Stationary, non-stationary	Stationary non-stationary
Complexity	Simple†	Complex	Very complex
Application	Off-line	On-line	Off-line
Limitations	High SNR	Medium SNR	Low SNR
Computer time	Small†	medium	large
Accuracy	Reasonable	Reasonable	Excellent
Statistical validation	Sample calculations†	Generated	Generated

†Neglecting FFT, Autocorrelation, and/or Ensemble Statistic Calculations

are application, complexity, and accuracy. The MXLKID algorithm is more accurate; however, the price paid is complexity, computer time and the necessity of running the algorithm off-line, i.e., with a complete set of measurements available beforehand.

This completes our discussion of the parameter estimation algorithms. In the next section we discuss the application of these techniques to the EM parameterization problem.

4.0 Application to EM Response Parameterization

The three analysis methods described in the previous sections have been applied to some of the transient data described in Appendices C, D, and E. The extended Kalman filter and the maximum likelihood estimator have been applied to the cylinder data only. These are described in this section. The Prony results which are described in Appendix G include pole predictions for all three objects tested as part of this effort.

Both the extended Kalman filter and maximum likelihood identifier require preprocessing of the data (described later in this section) to obtain initial estimates for noise statistics, etc. After completion of preprocessing, the following parameters from the signal model (Eq. C4) were estimated: $\{\sigma_i, \omega_i\}$, $i = 1,2,3$.

Three sets of cylinder data were used in this analysis: 1) cylinder in free space; 2) cylinder 50 cm from a ground plane; and 3) cylinder 10 cm from a ground plane. Figure C4 shows the data records used which consist of the first 20 ns of the response for each of the above three cases. All three correspond to the $\dot{B}$ probe response at $\theta = 180°$.

The parametric model for this experiment with measurement noise is the following:

$$z(t) = \sum_{i=1}^{N} \mathrm{Re}[C_i e^{s_i t}] + v(t) \qquad (C13)$$

where

$z(t)$ is the measured signal of interest

$v(t)$ is the measurement noise

$N = 6$*

C_i is the complex residue;

$C_i = Re[A_i] + j[m[A_i]$

s_i is the complex frequency;

$s_i = \sigma_i + j\omega_i$

The pole extraction problem then becomes:

Identify $(C_i, \omega_i, \sigma_i)$
for $i = 1,2,3$ given $\{z(t)\}$

An alternative and more complete noise model considers process as well as measurement noise. Process noise is correlated (as opposed to independent or "white" noise characteristic of a measurement probe) and typically has power spectral components within the signal bandwidth of interest. Process noise sources can include unmodeled EMP reflections, unknown environmental electromagnetics, and signal mismodeling. Process noises are modeled as driving noises, i.e., random excitations, and hence are convolved with the impulse response of the object.

The following parametric model includes both process and measurement noises:

$$z(t) = \sum_{i=1}^{N} C_i e^{s_i t} + \int_{\tau=0}^{t} w_i(\tau) e^{s_i(t-\tau)} d\tau + v(t) \qquad (C14)$$

---

* We chose the first three harmonics (N=6, ie., a complex conjugate pair of poles for each harmonic) to form our signal model; however, because of probe location, very little of the second harmonic was observable, therefore the forthcoming pole extraction results will apply to the fundamental and third harmonic only.

Where

$w_i(t)$ is process driving noise

The pole extraction problem is now:

$$\text{Identify } \{C_i, \omega_i, \sigma_i, \text{Cov}(w_i)\}$$
$$\text{for } i = 1,2,3 \text{ given } \{z(t)\}$$

We now have the additional task of identifying the covariance (noise power) of the driving noise. To extract poles from the three response data sets shown in Figure C4, the Prony technique, extended Kalman filter (EKF) and two versions of the maximum likelihood identifier were applied. The Prony technique accounts only for a measurement noise model, whereas the EKF uses both a process and a measurement noise model. The maximum likelihood identifier was designed for both cases. Version A accounted only for measurement noise whereas Version B included both process and measurement noise models.

The raw incident pulse response data was preprocessed in two steps: a) low pass filtering, to eliminate noise components in the high frequency bands and in which no signal of interest lies,* b) discard data which are obviously before and during the incident pulse transient ($\sim$ first 5 ns). The low pass filter cut-off was chosen to reflect the need for a sampling rate of at least twice the highest frequency component of interest (which is three times the fundamental frequency of $\sim$ 140 MHz, i.e., $\sim$ 420 MHz). The identification algorithms (EKF, MXLKID) were applied to the resultant preprocessed data.

The results from EKF and maximum likelihood techniques are shown in Table 7 in the main body of the report. For a discussion of these results, the reader is referred to Section 8 of this report.

---

* An 8-point window averaging filter was used (on the time domain data) to produce a low pass effect.

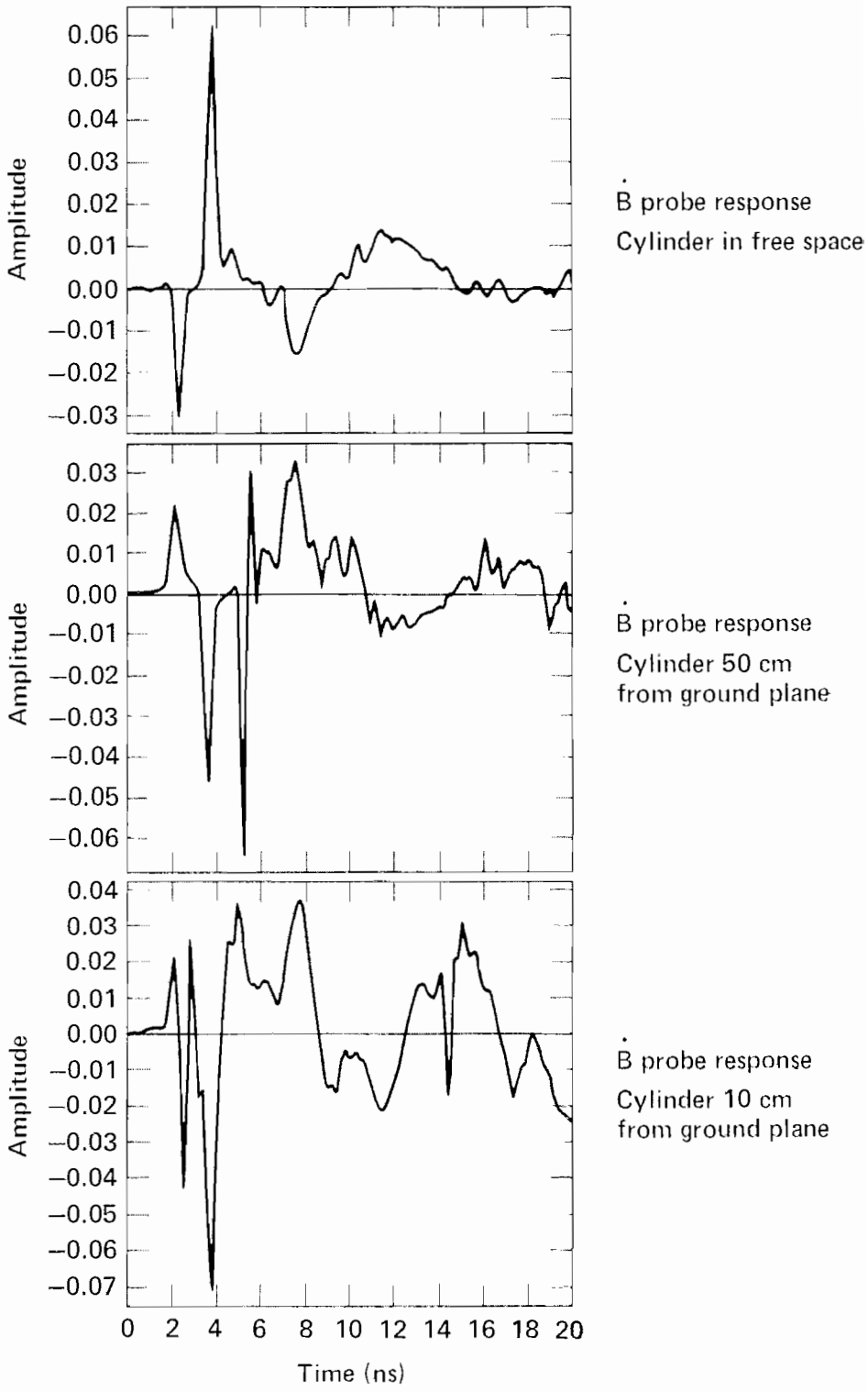

Figure C4. EMP response data.

References

C1. Poggio, A. J., Van Blaricum, M. L., Miller, E. K. and Mitra, R., "Evaluation of a Processing Technique for Transient Data," IEEE Trans. Antennas Propagat., AP-26, 1978.

C2. Padulo, P. and Arbib, M., System Theory. Philadelphia: Saunders, 1974.

C3. Smith, W. D. and Lager, D. L., "Parametric Characterization of Random Processes Using Prony's Method," Lawrence Livermore National Laboratory Report, UCRL-52673, 1979.

C4. Kailath, T., Lectures on Linear Least Squares Estimation, Berlin: Springer-Verlag, 1975.

C5. Goodwin, G. C. and Payne, R. L., Dynamic System Identification, New York: Academic Press, 1977.

C6. Gelb, A., Applied Optimal Estimation, Boston: MIT Press, 1974.

C7. Gupta, N. K. and Mehra, R. K., "Computational Aspects of Maximum Likelihood Estimation," IEEE Trans. Autom. Contr., AC-19, 1974.

C8. Gavel, D. T., "MXLKID - A Maximum Likelihood Parameter Identifier," UCID-18744, 1980.

Appendix D
Cylinder Data

Five initial measurements were made of the cylinder in free space. Figure 9 in the text shows the configuration used for these measurements, where the cylinder was rotated to obtain illumination at angles of $\theta = 0^\circ$, 45°, 90°, 135°, and 180°. The transient response waveforms obtained by the $\dot{B}$ and $\dot{D}$ sensors for an incident impulse field like that shown in Figures 2 and 3 are shown in Figures D1 through D5.

To obtain the desired transfer functions of $E/E_{inc}(f)$ and $H/H_{inc}(f)$ in the frequency domain from the time-domain transient measurements, the Fourier transforms for the $\dot{B}$ and $\dot{D}$ sensor outputs at the test points on the model are obtained. These transforms are then divided by the Fourier transforms of the integrated $\dot{D}_{inc}$ and $\dot{B}_{inc}$ signals measured at the reference point with the model absent, i.e., the incident field. Figures D6 through D10 present the magnitude of the transfer functions $\left|E/E_{inc}\right|$ as a function of frequency. The various figures correspond to the angles of incidence of $\theta = 0^\circ$, 45°, 90°, 135°, and 180°. Analogously, Figures D11 through D15 show the magnitude of the magnetic field transfer function $\left|H/H_{inc}\right|$. For the cylinder near a perfectly conducting ground plane, measurements of $\dot{B}$ and $\dot{D}$ on the cylinder were again obtained for $\theta = 0^\circ$ and 180° incident field, for the cases of $h = a$, $5a$, $10a$ and $20a$ (10 cm, 50 cm, 1 m and 2 m), where h is the distance between the cylinder and the ground plane, and a is the radius of the cylinder. In all cases, the model position remained fixed, and the ground screen was moved in and out.

Figures D16 through D23 show the transient response of the cylinder with the ground plane in place for the $\dot{D}$ sensor located at $\theta = 0^\circ$ and 180° incidence. Only the first 20 ns of the response is shown.

Similar results are obtained for the currents on the cylinder, as shown in the integrated $\dot{B}$ measurements in the time domain for the Figures D24 through D31. Again, only the first 20 ns of the response are shown.

In the frequency domain, the transfer functions for E/E_{inc} for the cases of $\theta = 0^{\circ}$ and 180° incident field, and the four cases of the ground-plane position are shown in Figures D32 through D39. Note that the incident field used in these expressions is the free space field, i.e., the field measured with the ground plane removed. Figures D40 through D47 show the results obtained for the surface currents, as expressed by the transfer function H/H_{inc}.

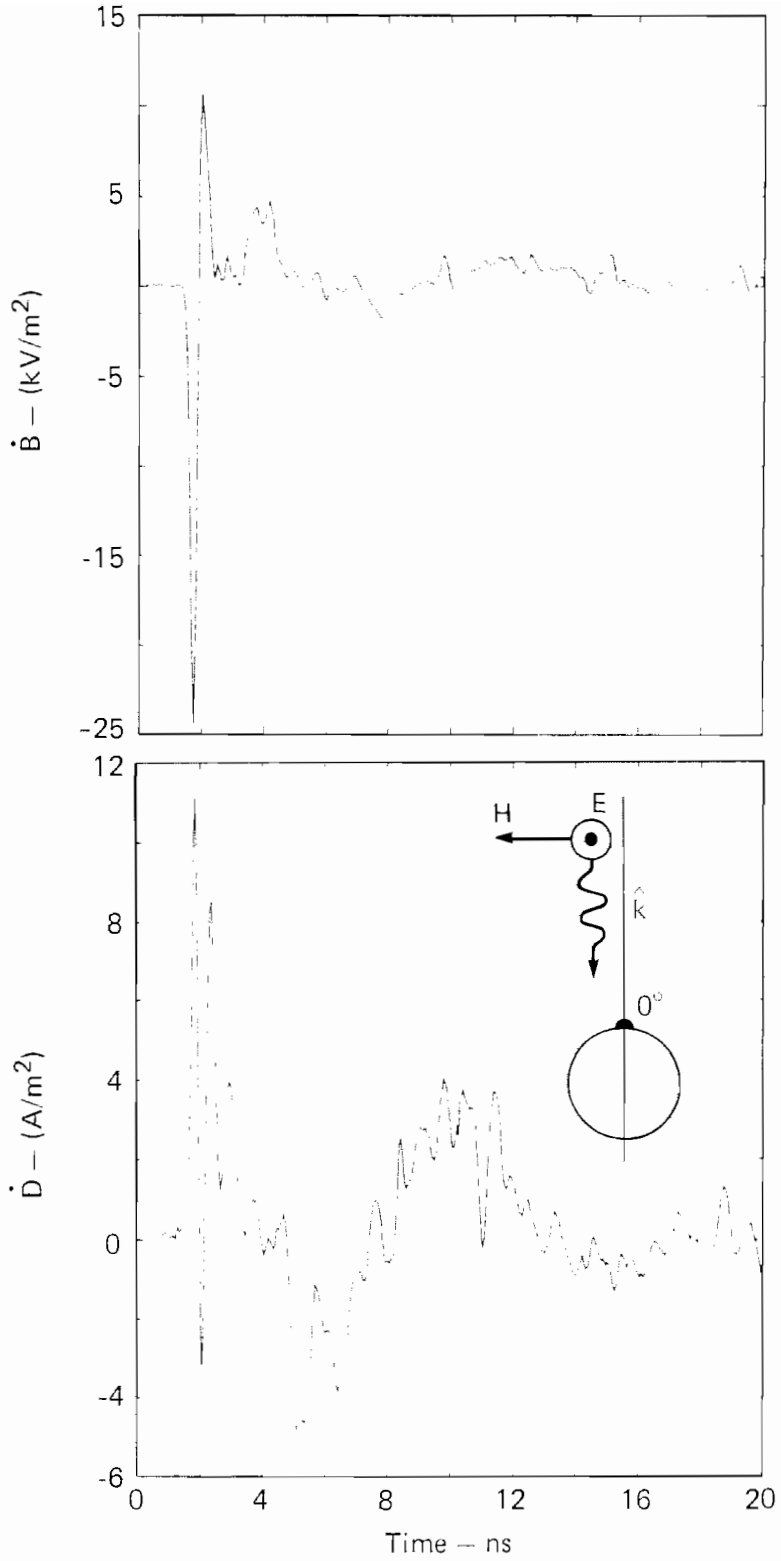

Figure D1. Time domain $\dot{B}$ and $\dot{D}$ sensor outputs for cylinder in free space ($\theta = 0^\circ$).

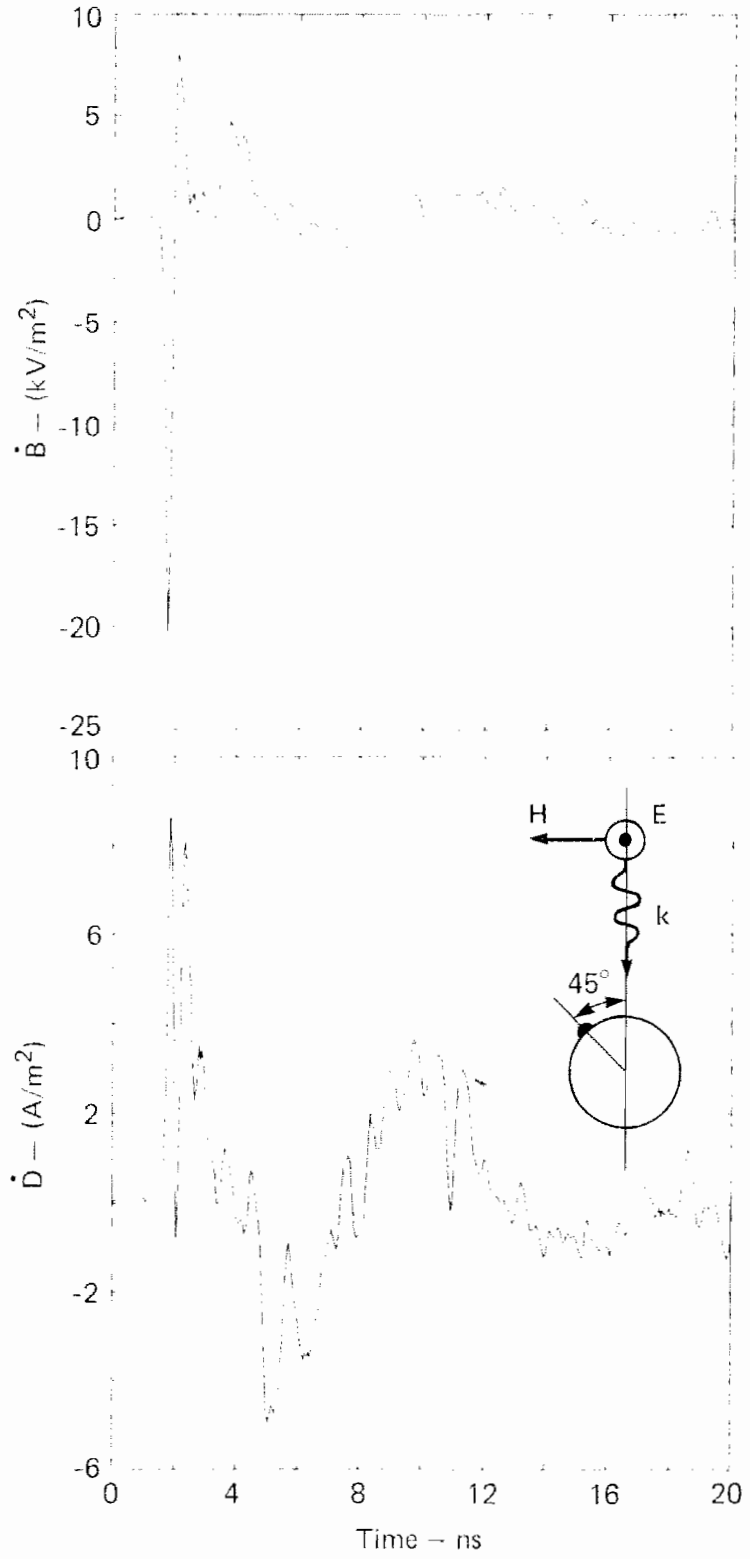

Figure D2. Time domain $\dot{B}$ and $\dot{D}$ sensor outputs for cylinder in free space ($\theta = 45^{\circ}$).

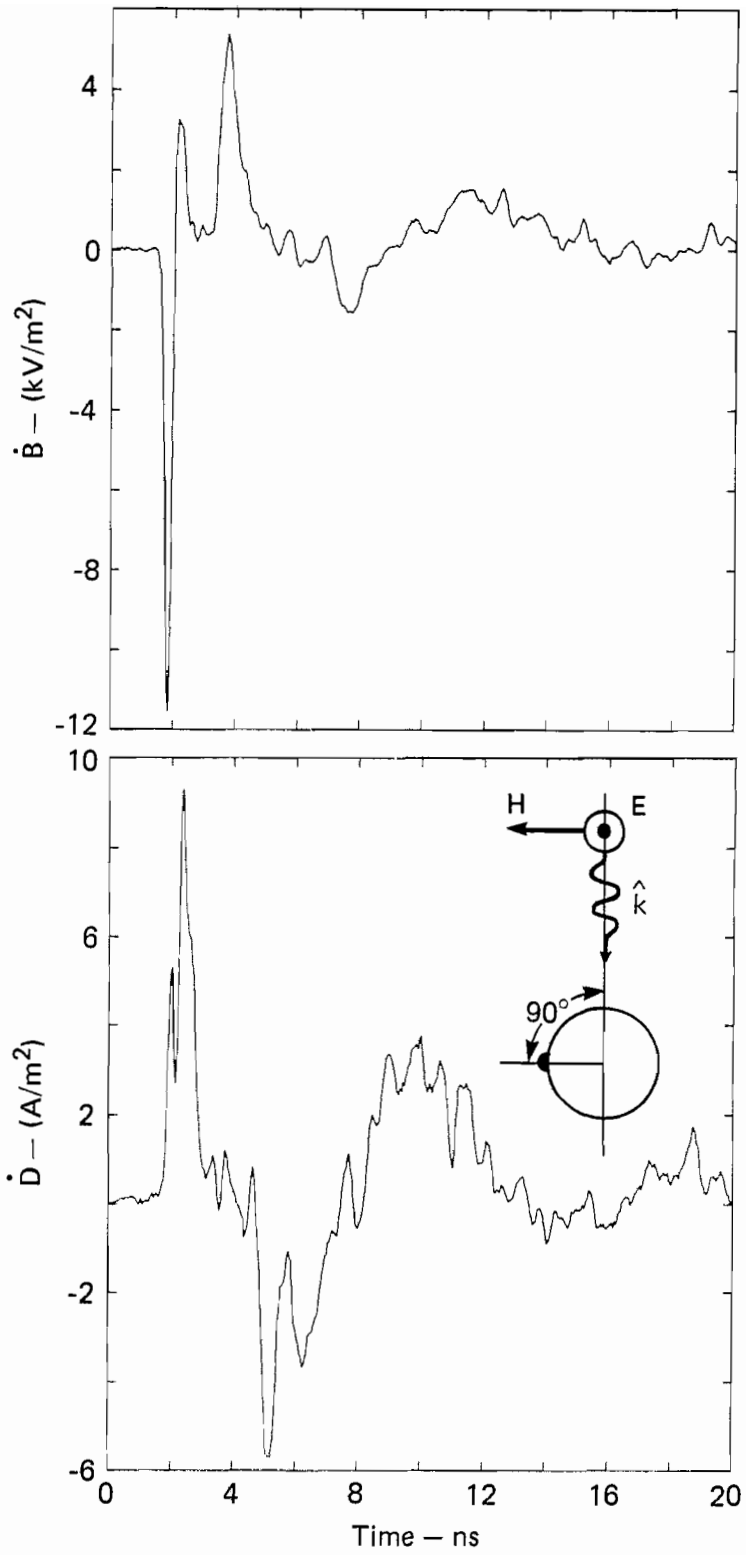

Figure D3. Time domain $\dot{B}$ and $\dot{D}$ sensor outputs for cylinder in free space ($\Theta = 90^{\circ}$).

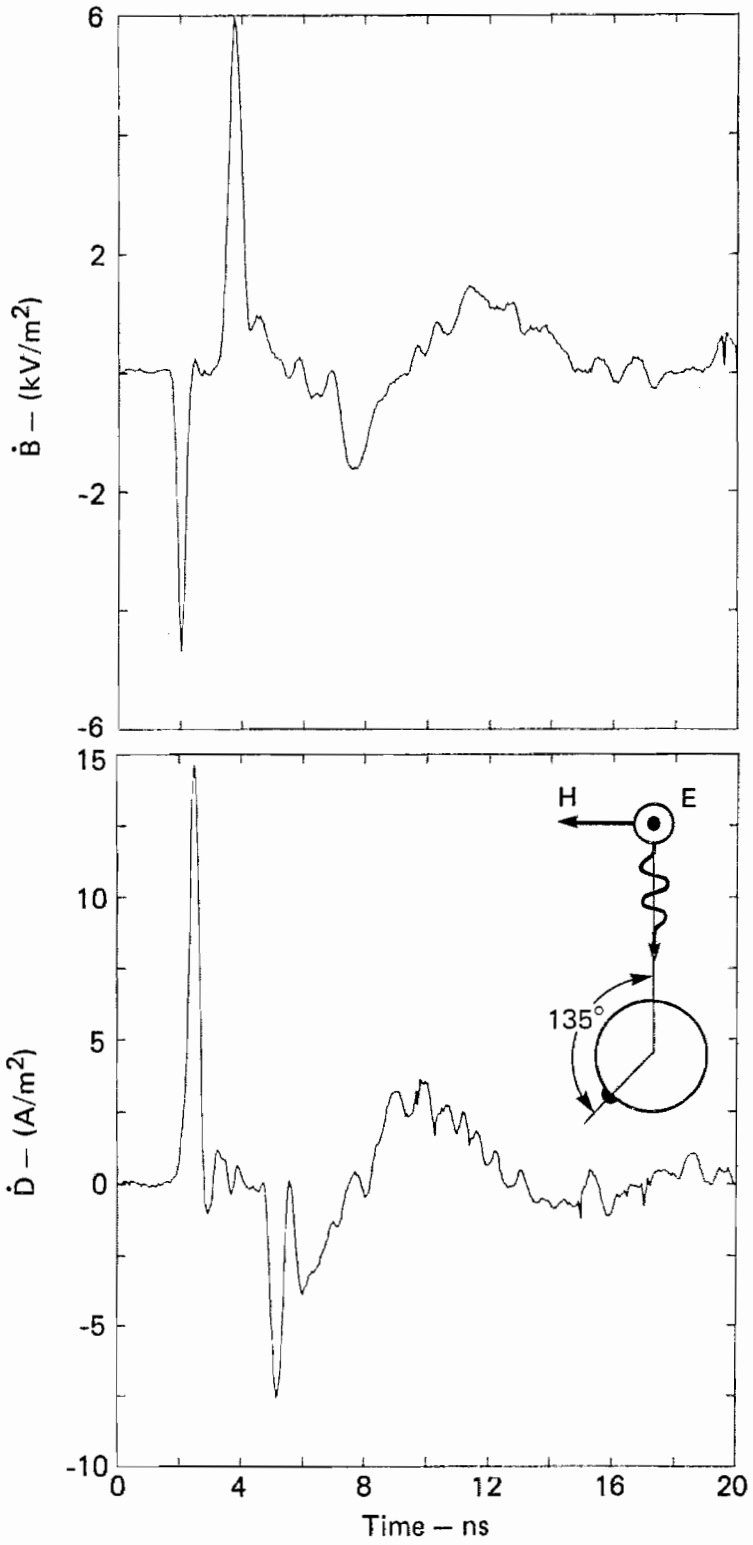

Figure D4. Time domain $\dot{B}$ and $\dot{D}$ sensor outputs for cylinder in free space ($\theta = 135^{o}$).

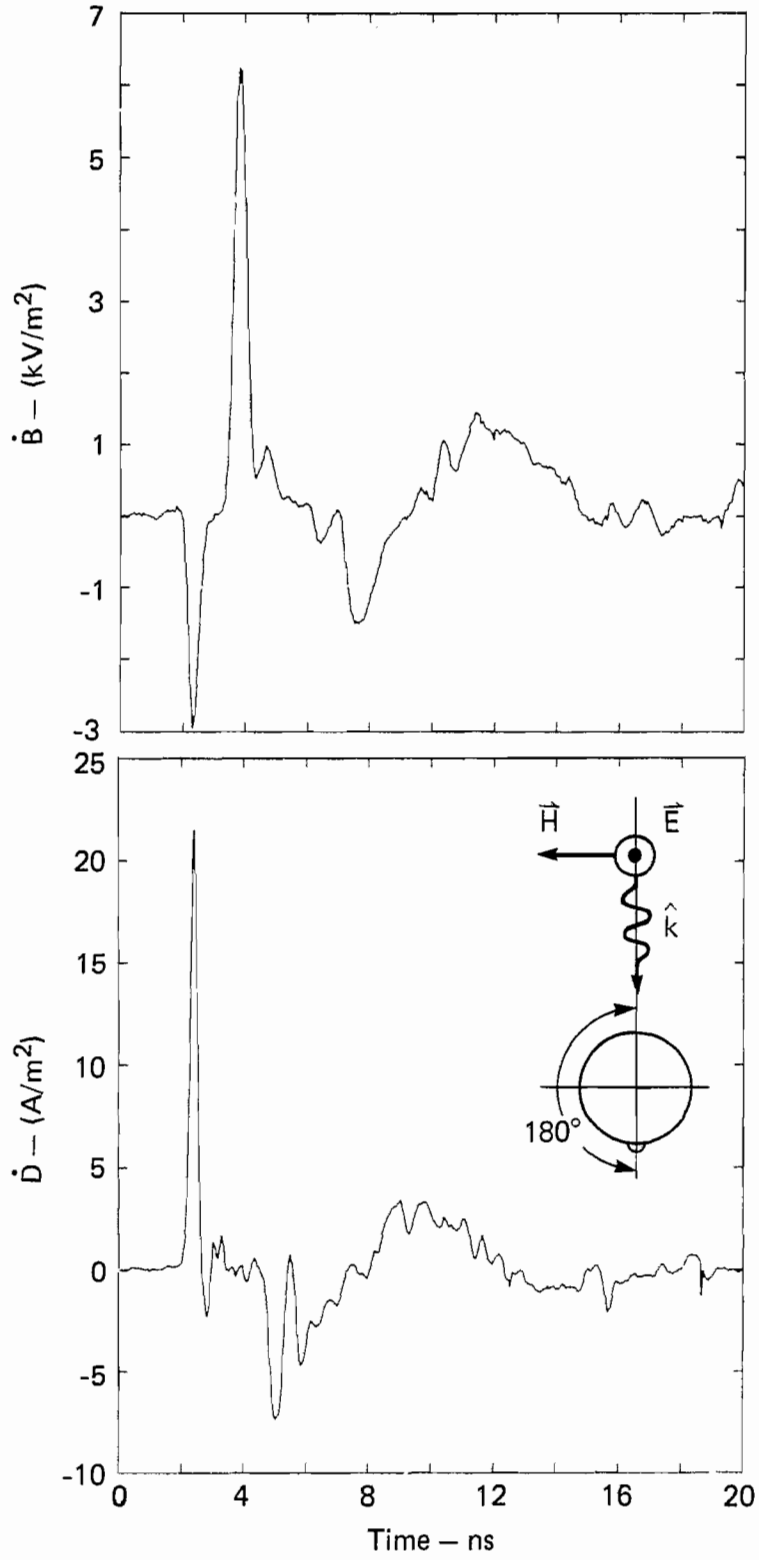

Figure D5. Time domain $\dot{B}$ and $\dot{D}$ sensor outputs for cylinder in free space ($\theta = 180^\circ$).

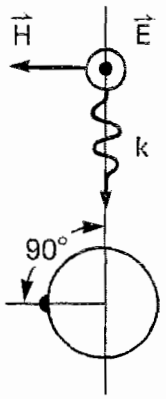

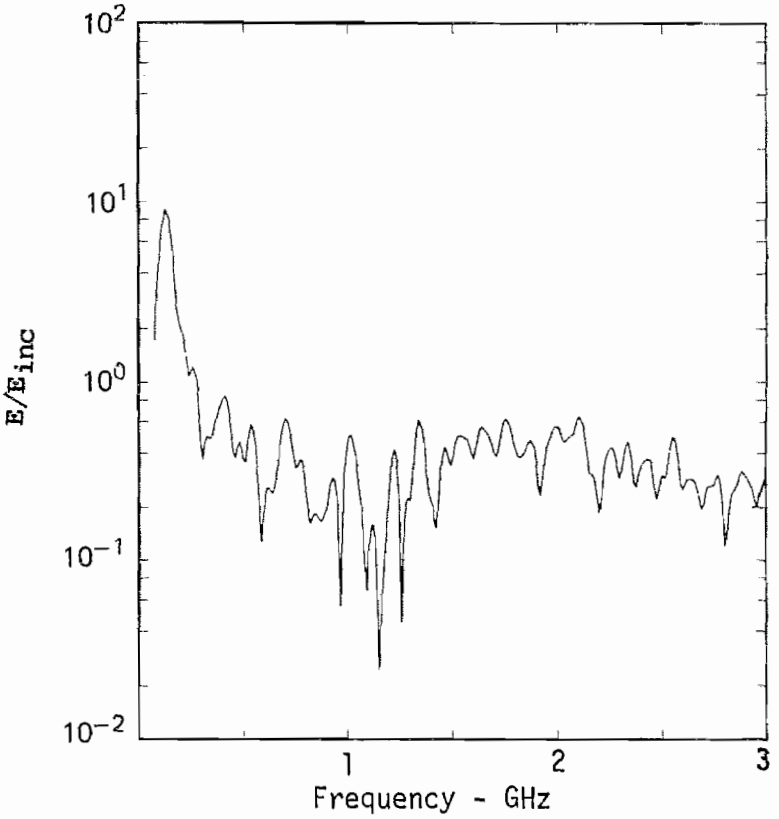

Figure D6. Magnitude of E/E_{inc} for cylinder model ($\theta = 0°$).

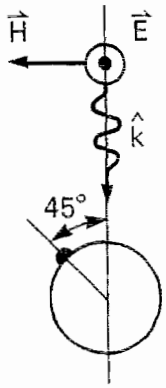

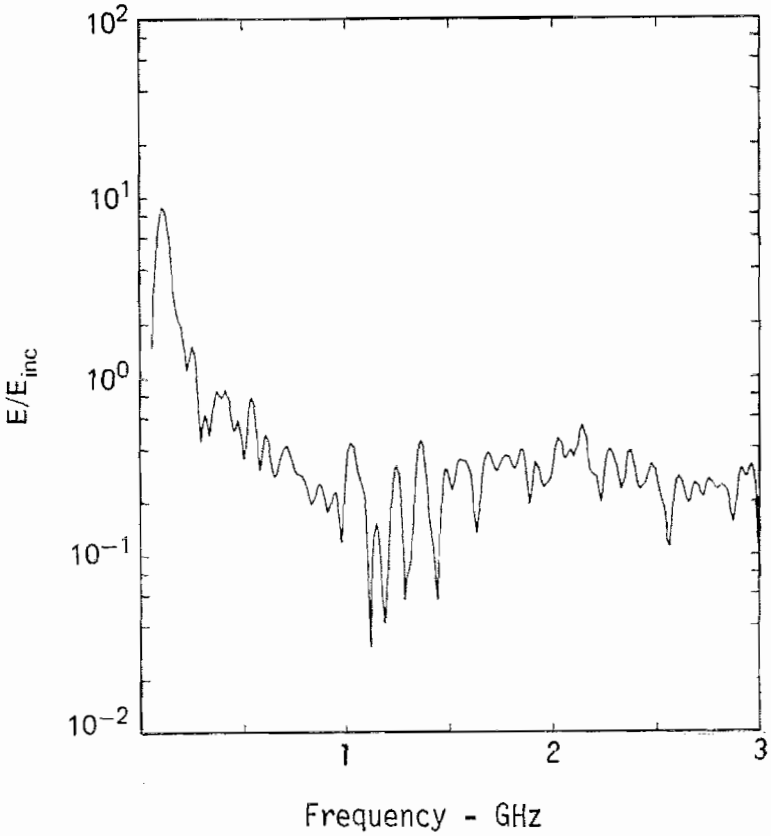

Figure D7. Magnitude of E/E_{inc} for cylinder model ($\theta = 45°$)

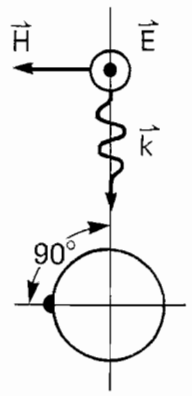

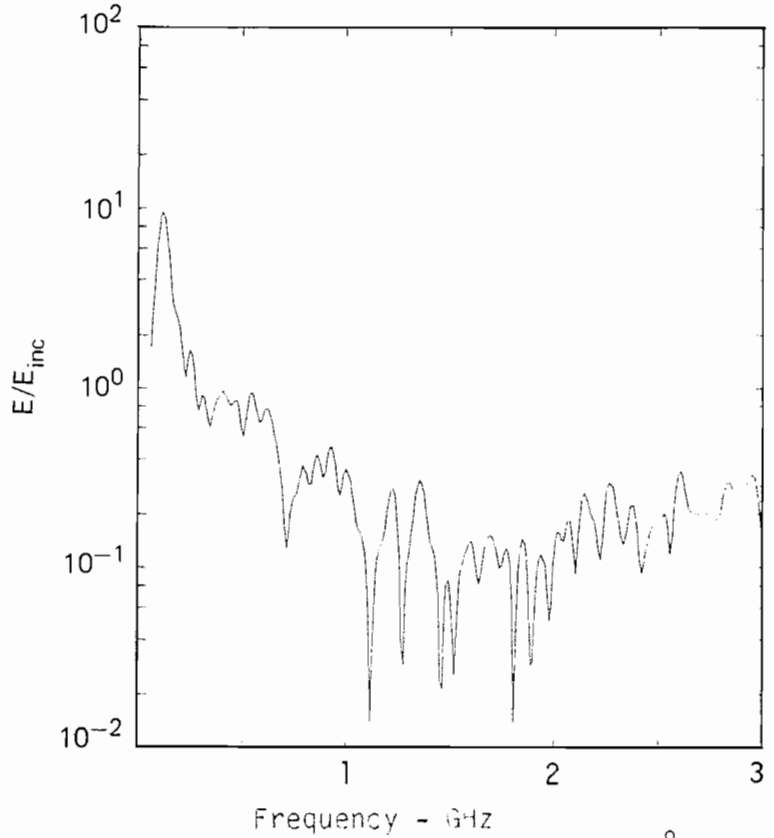

Figure D8. Magnitude of E/E_{inc} for cylinder model ($\theta = 90^\circ$).

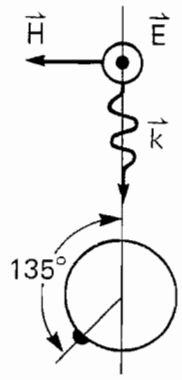

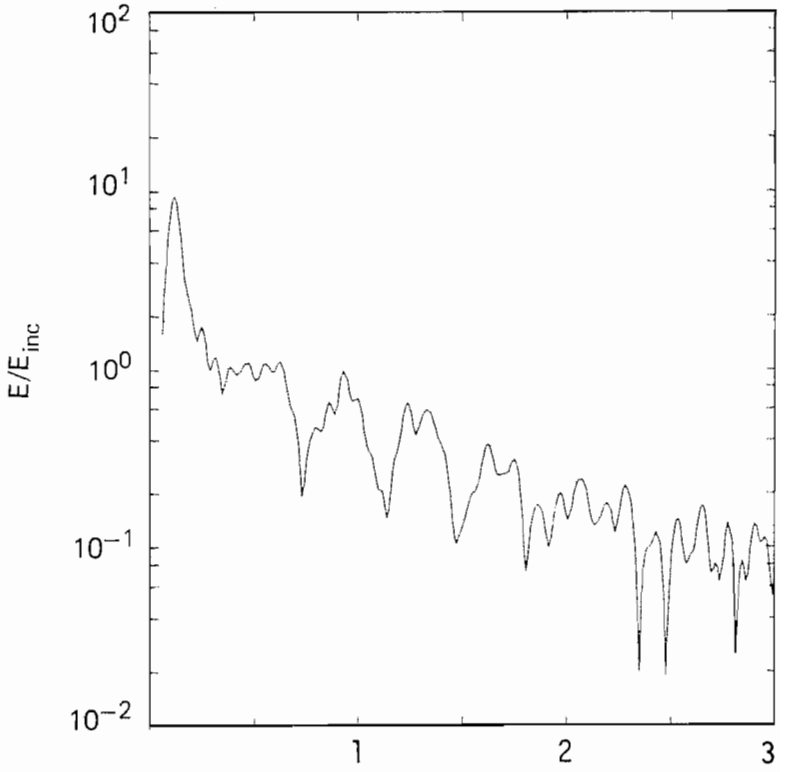

Figure D9. Magnitude of E/E_{inc} for cylinder model ($\theta = 135^\circ$).

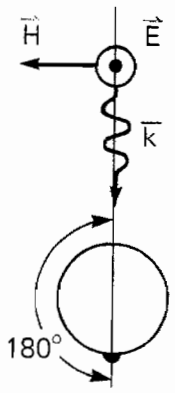

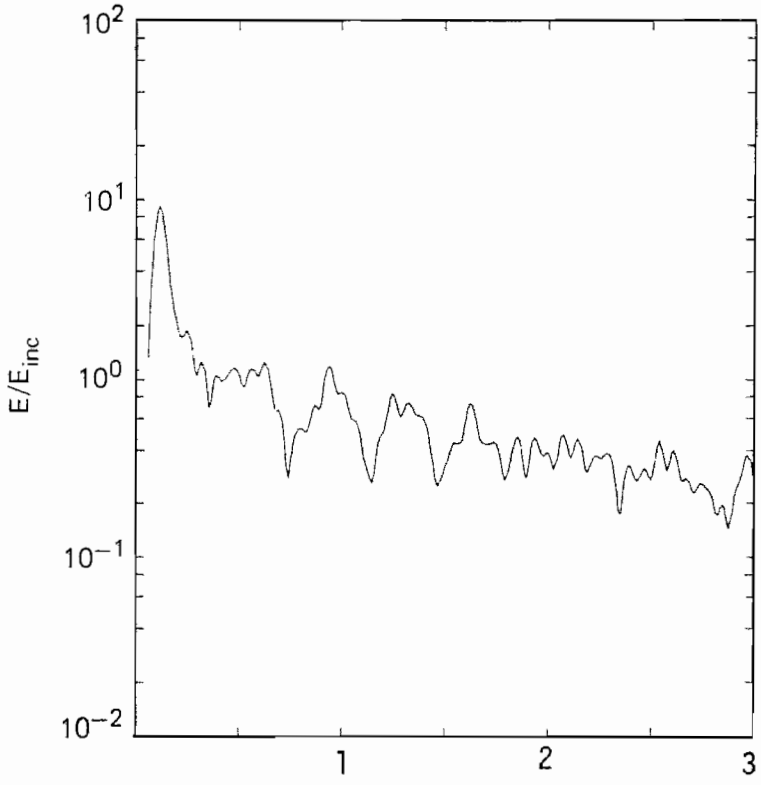

Figure D10. Magnitude of E/E_{inc} for cylinder model ($\theta = 180°$).

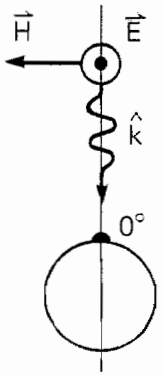

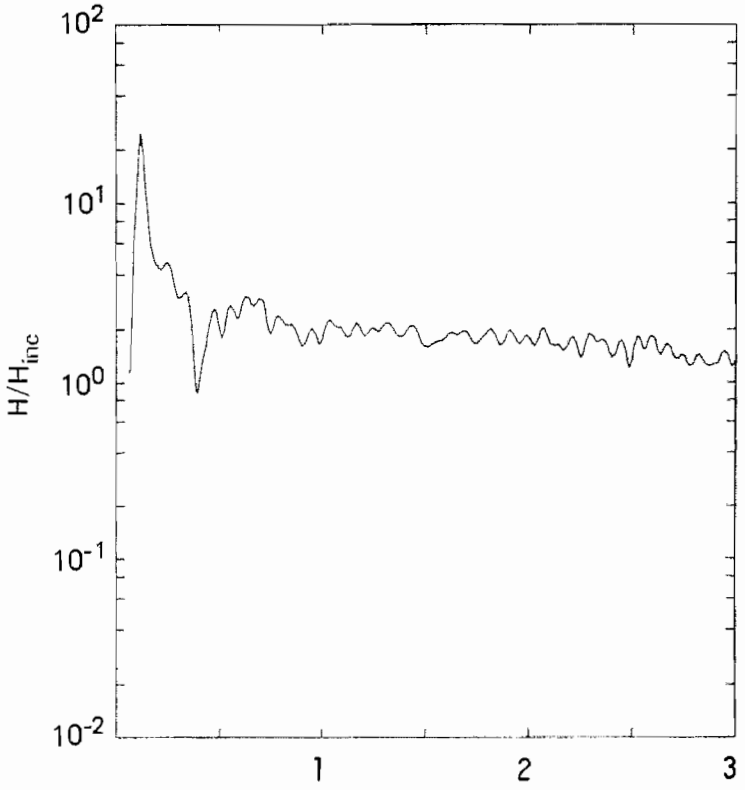

Figure D11. Magnitude of H/H_{inc} for cylinder model ($\theta = 0°$).

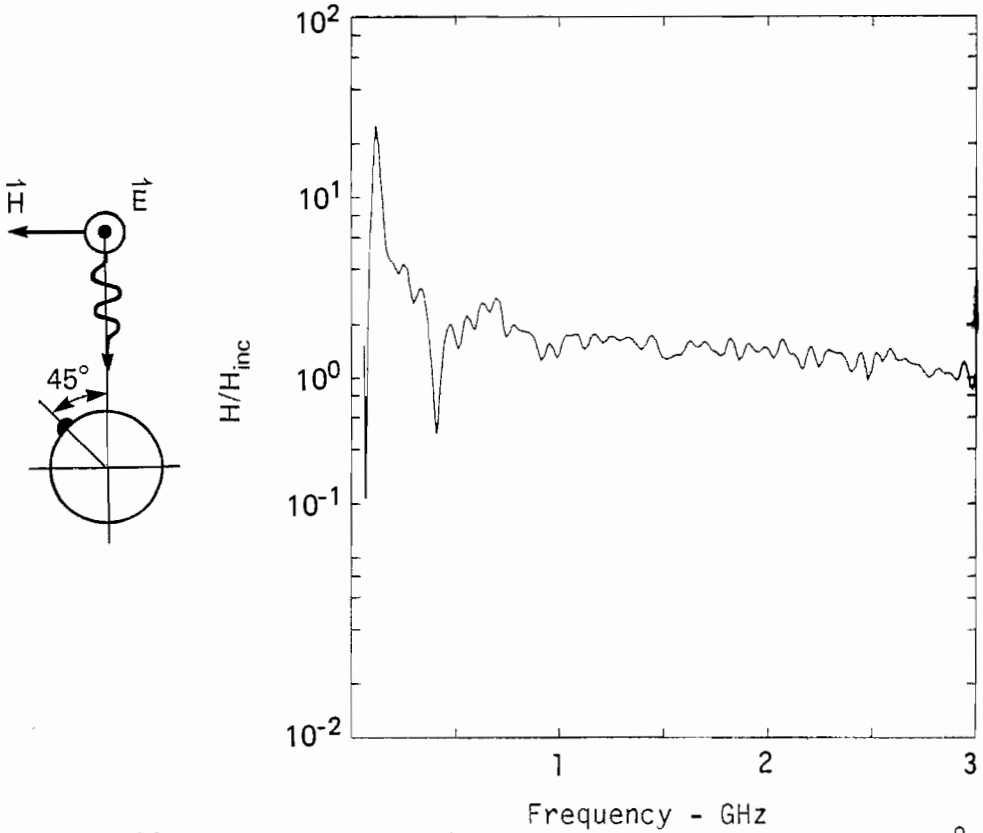

Figure D12. Magnitude of H/H_{inc} for cylinder model ($\theta = 45°$).

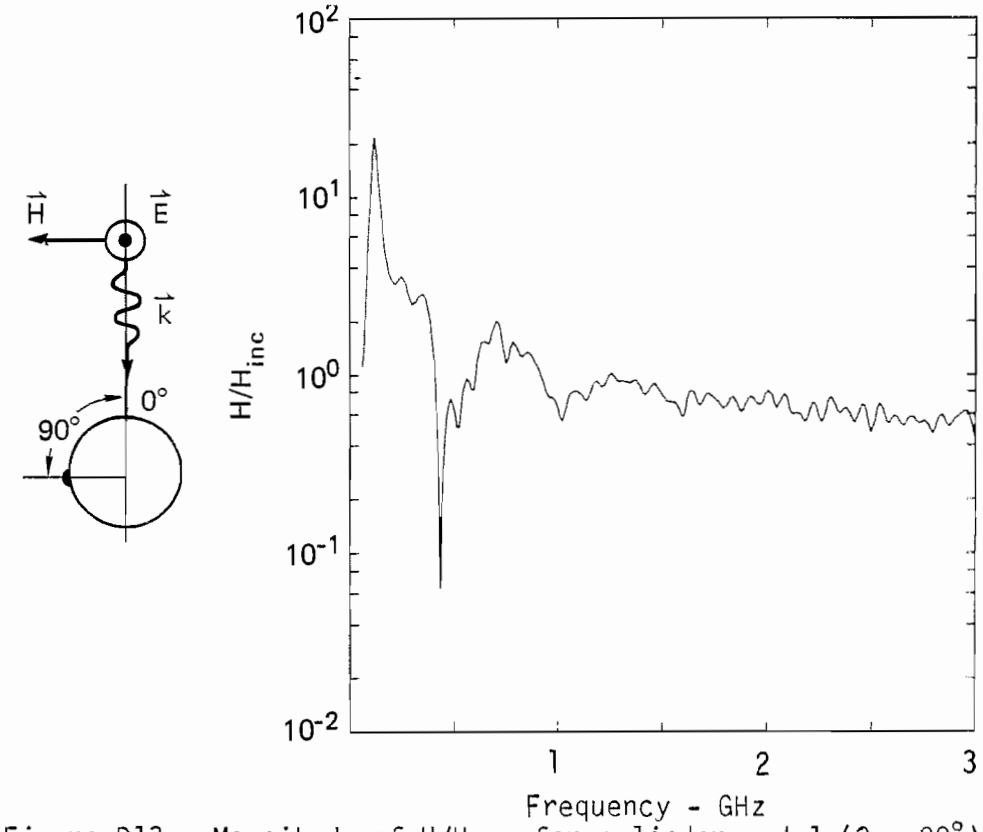

Figure D13. Magnitude of H/H_{inc} for cylinder model ($\theta = 90°$).

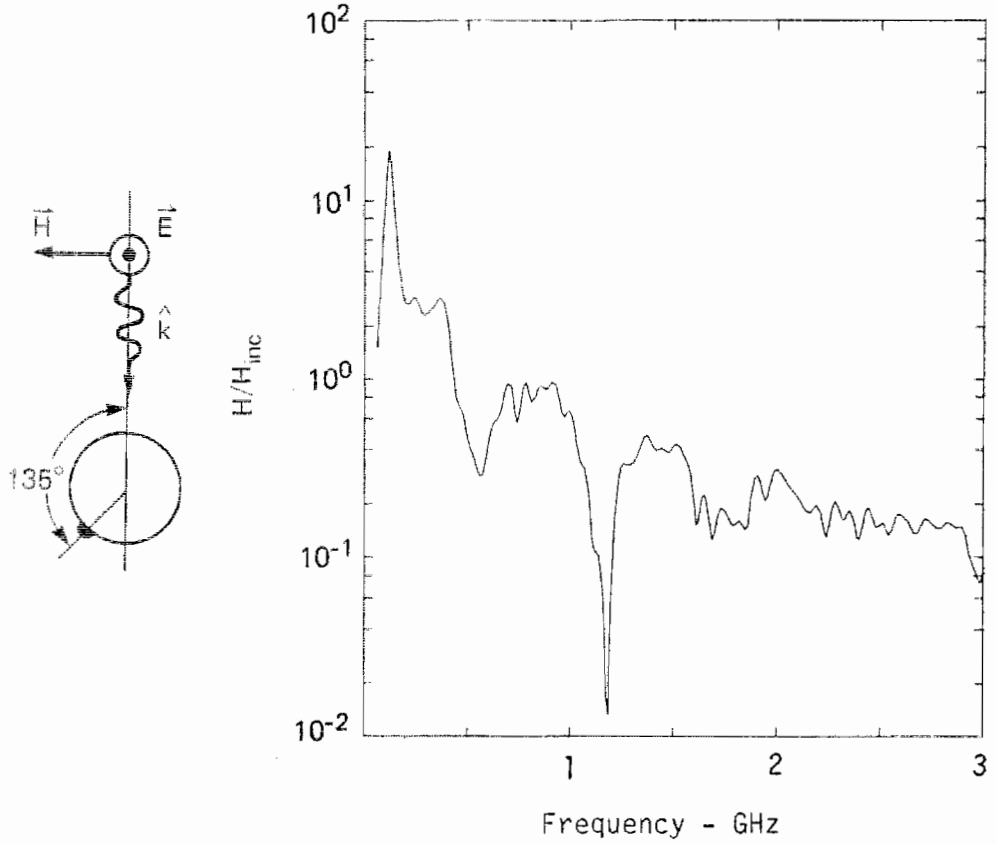

Figure D14. Magnitude of H/H_{inc} for cylinder model ($\theta = 135°$).

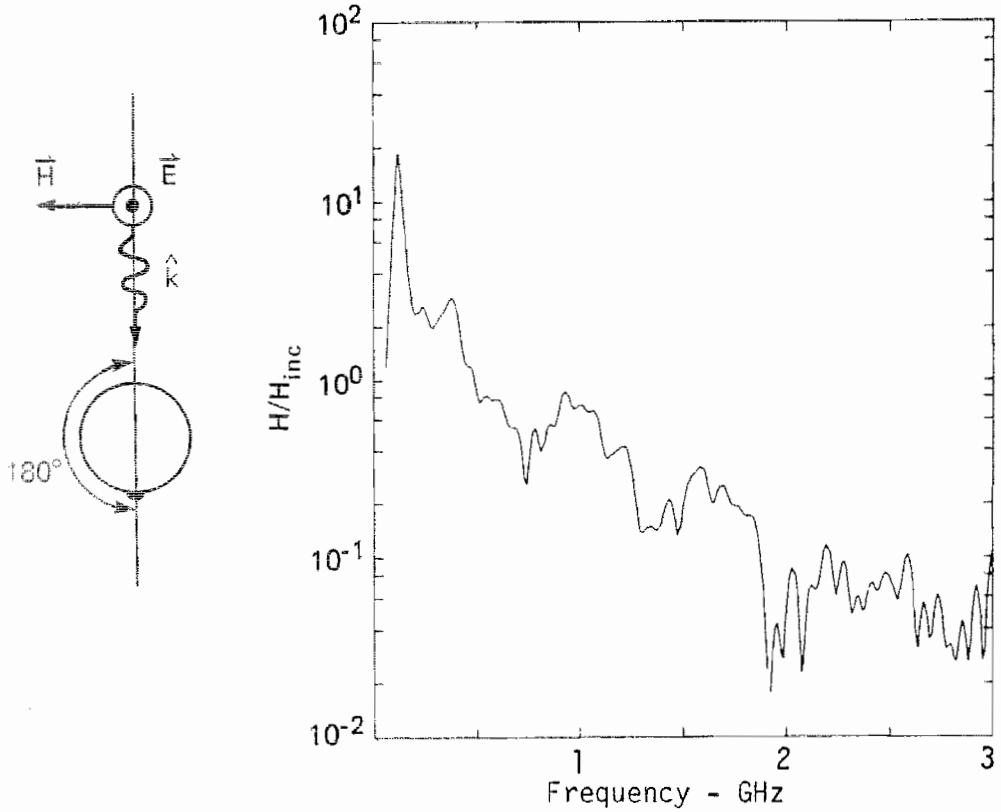

Figure D15. Magnitude of H/H_{inc} for cylinder model ($\theta = 180°$).

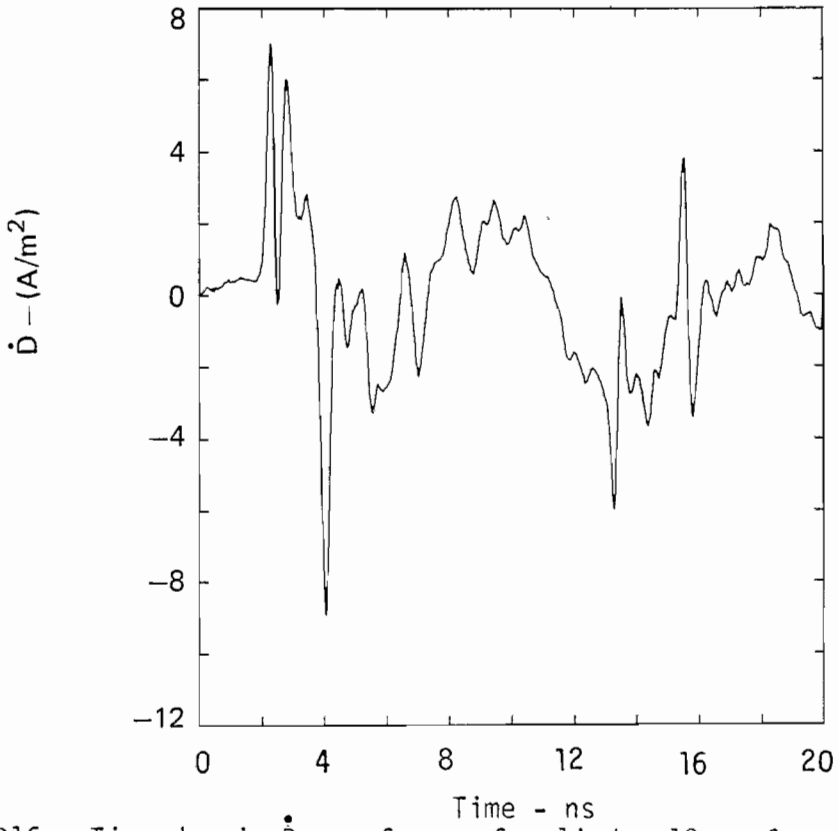

Figure D16. Time domain $\dot{D}$ waveforms of cylinder 10 cm from ground plane ($\theta = 0°$).

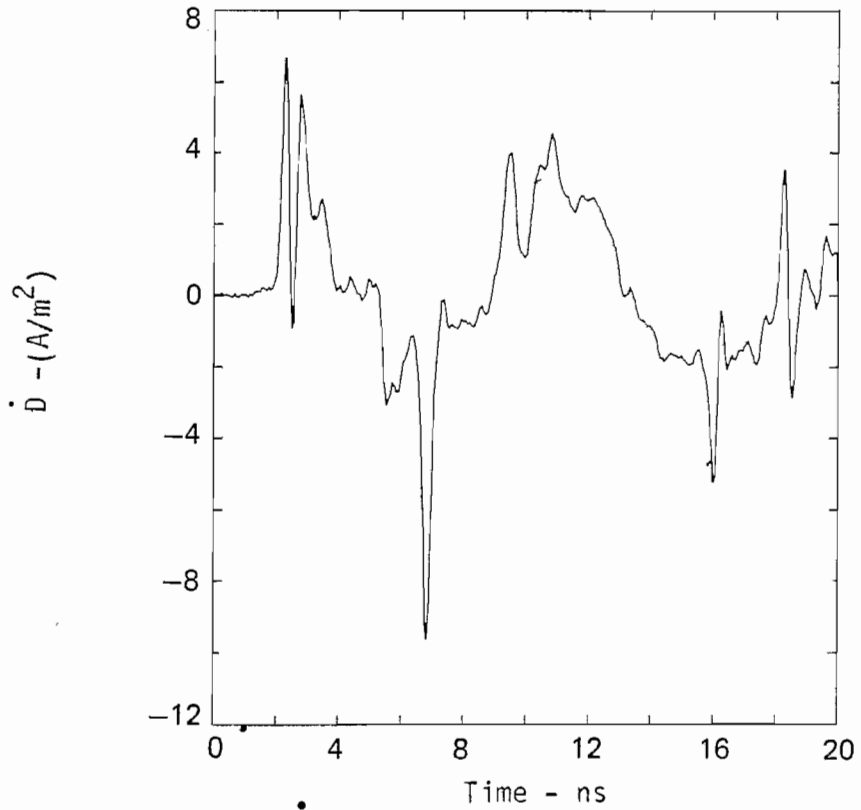

Figure D17. Time domain $\dot{D}$ waveform for cylinder 50 cm from ground plane ($\theta = 0°$).

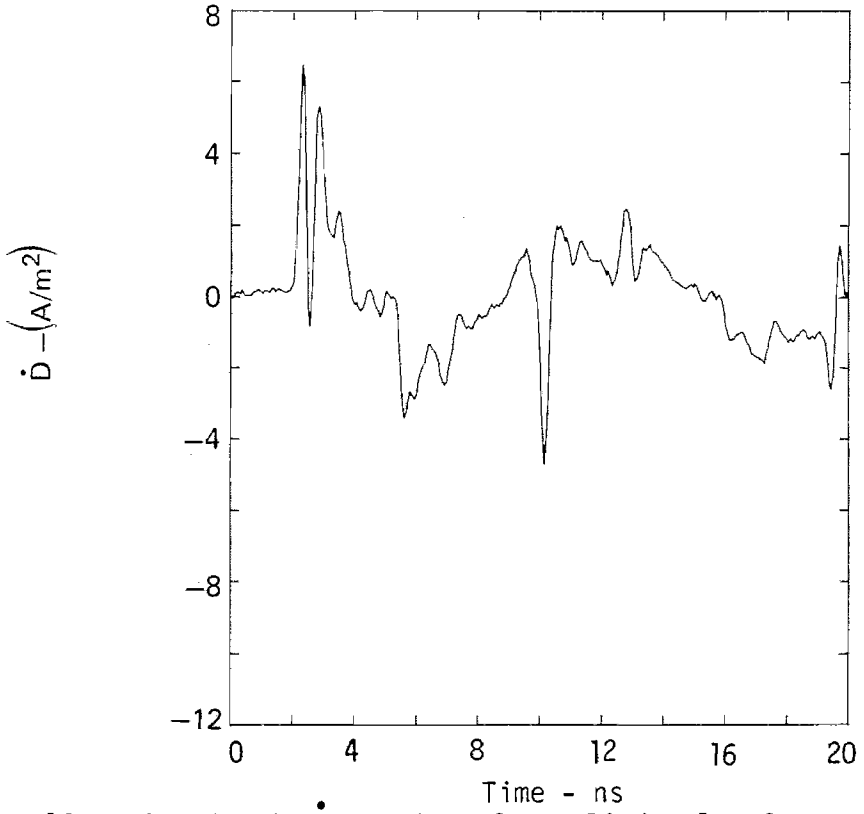

Figure D18. Time domain $\dot{D}$ waveform for cylinder 1 m from ground plane ($\theta = 0^\circ$).

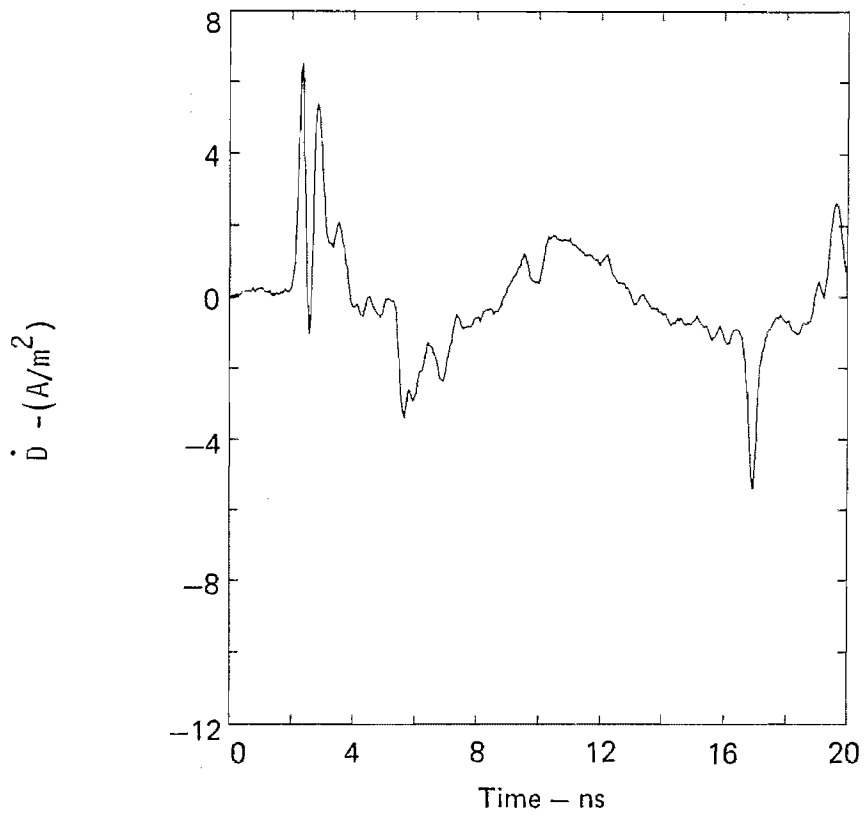

Figure D19. Time domain $\dot{D}$ waveform for cylinder 2 m from ground plane ($\theta = 0^\circ$).

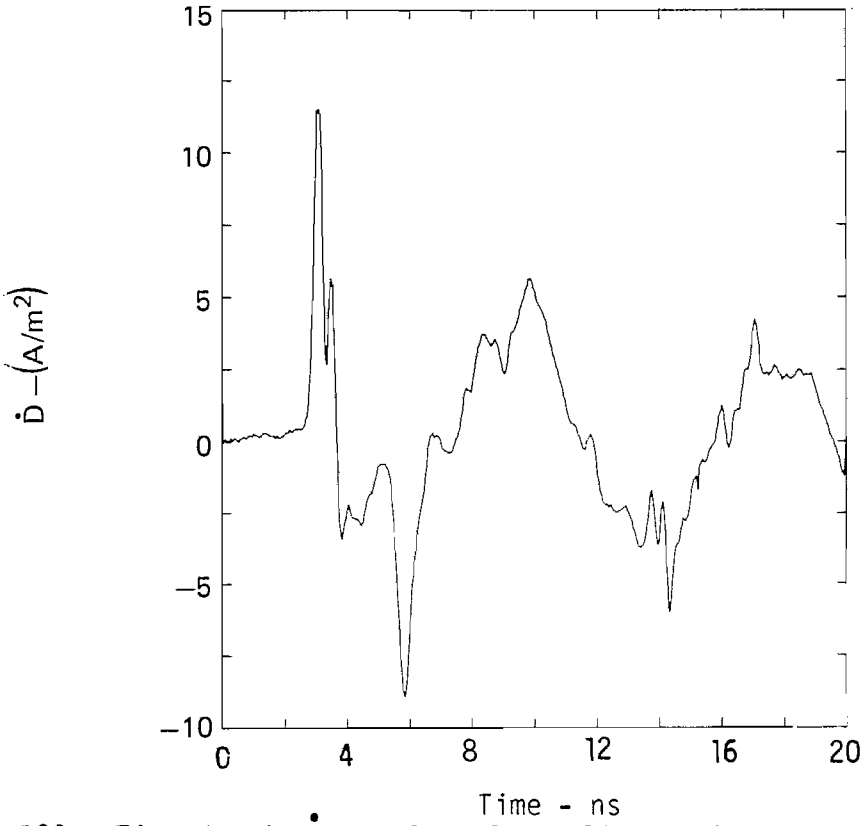

Figure D20. Time domain $\dot{D}$ waveform for cylinder 10 cm from ground plane ($\theta = 180°$)

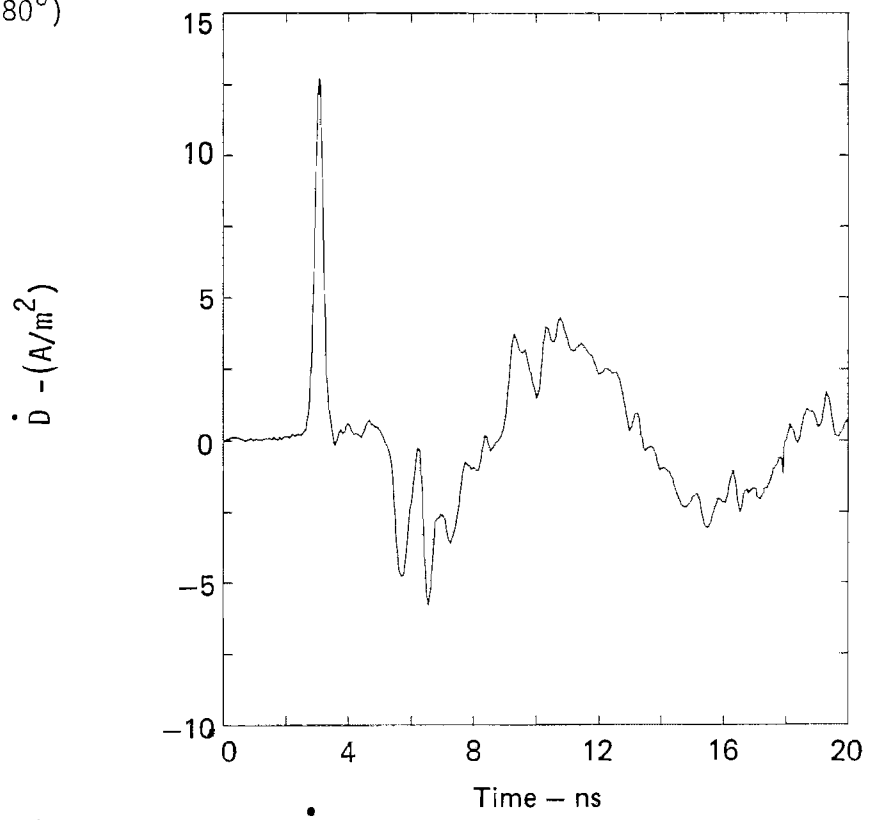

Figure D21. Time domain $\dot{D}$ waveform for cylinder 50 cm from ground plane ($\theta = 180°$).

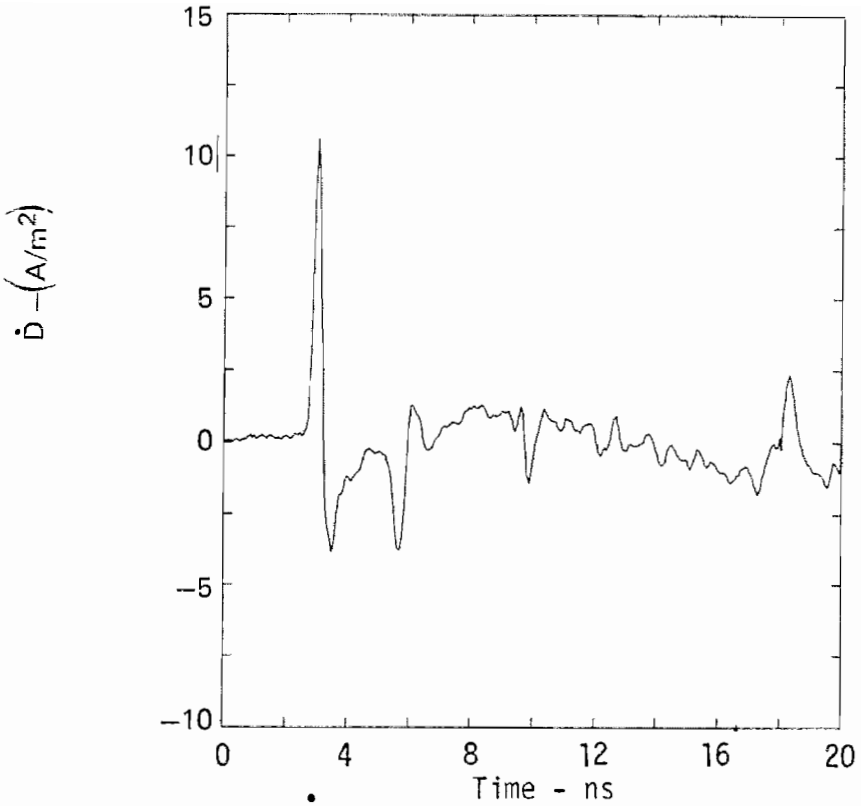

Figure D22. Time domain $\dot{D}$ waveform for cylinder 1 m from ground plane (θ = 180°).

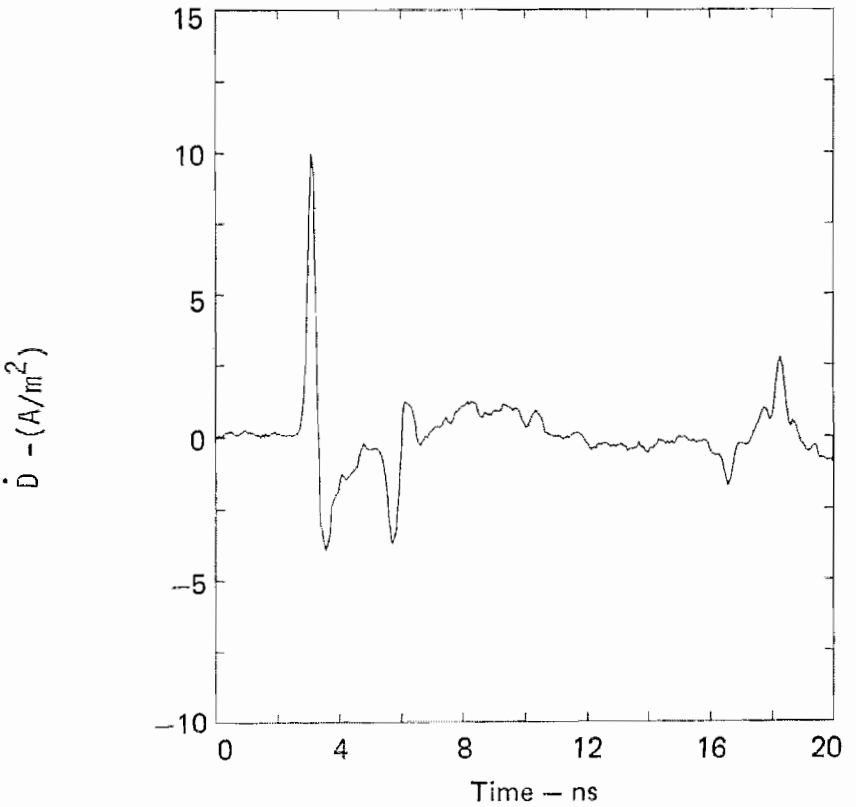

Figure D23. Time domain $\dot{D}$ waveform for cylinder 2 m from ground plane (θ = 180°).

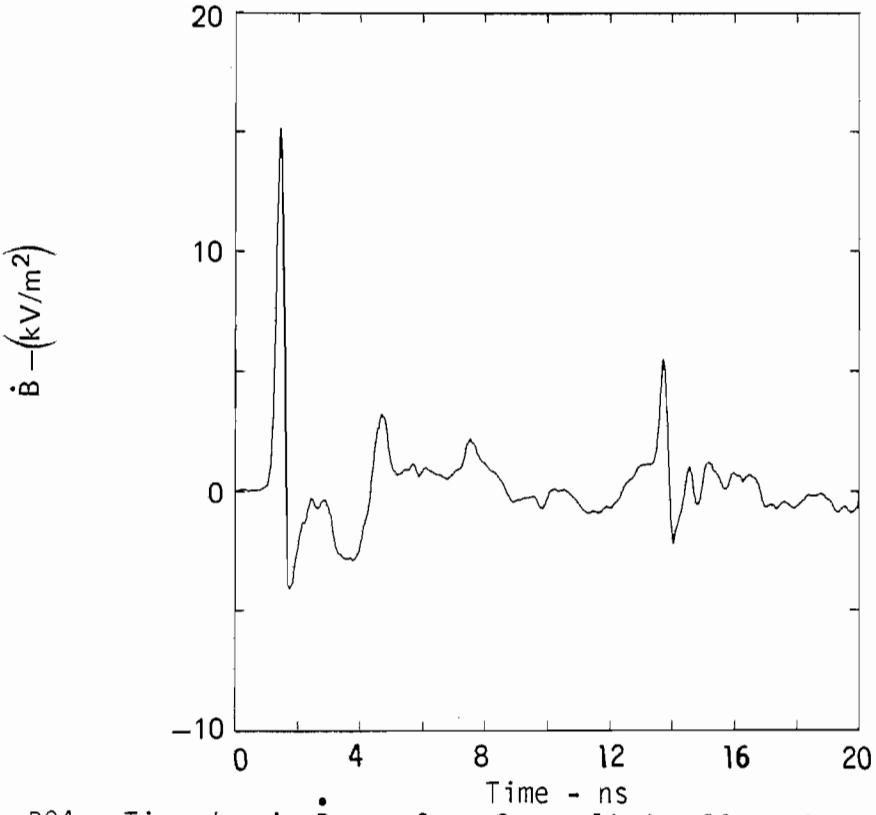

Figure D24. Time domain $\dot{B}$ waveform for cylinder 10 cm from ground plane ($\theta = 0°$).

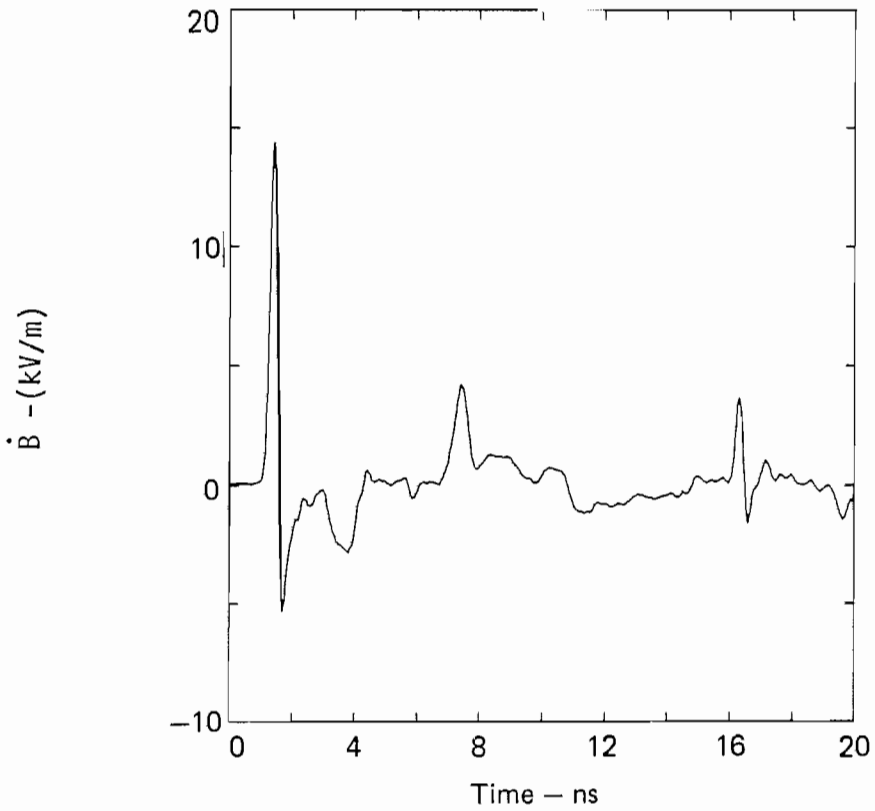

Figure D25. $\dot{B}$ 50 cm from ground plane ($\theta = 0°$).

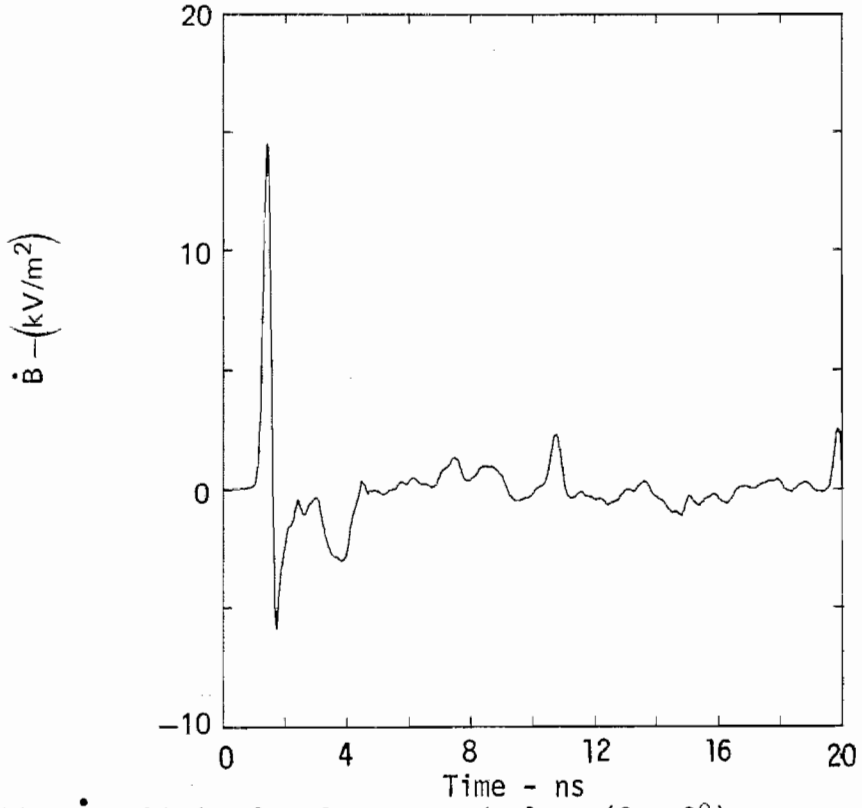

Figure D26. $\dot{B}$ cylinder 1 m from ground plane (θ = 0°).

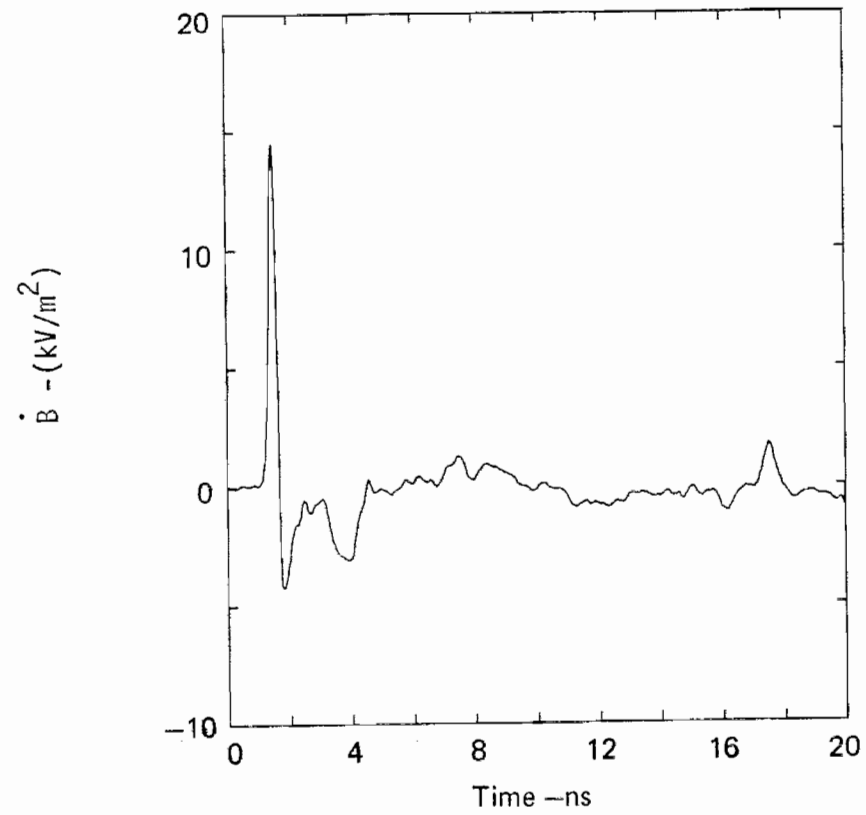

Figure D27. $\dot{B}$ cylinder 2 m from ground plane (θ = 0°).

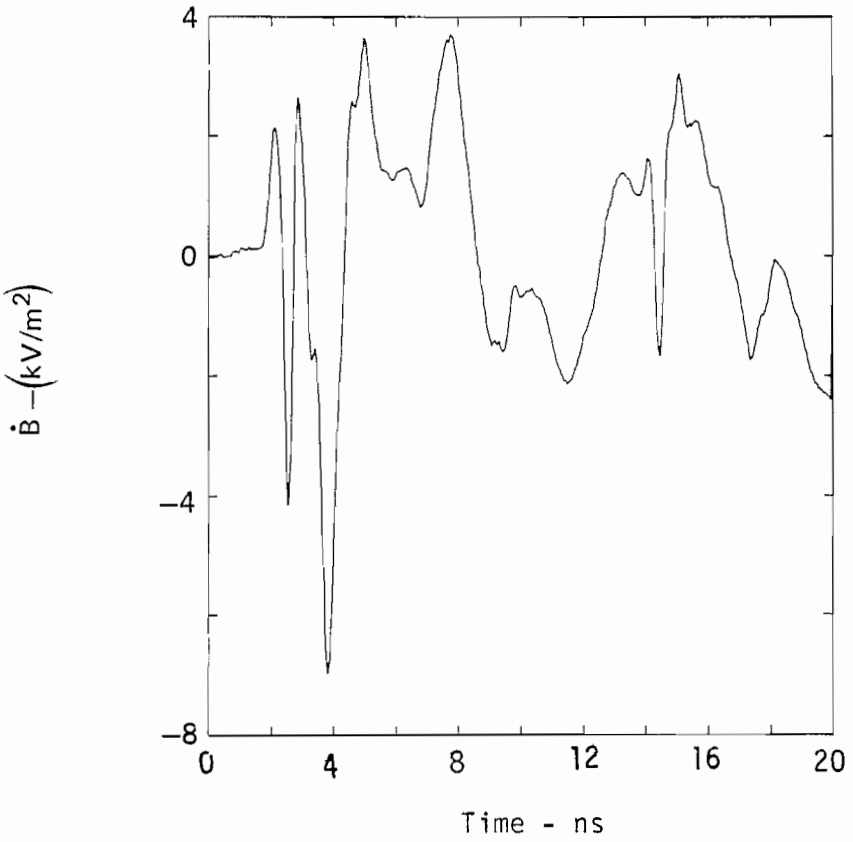

Figure D28. $\dot{B}$ 10 cm from ground plane (θ = 180°).

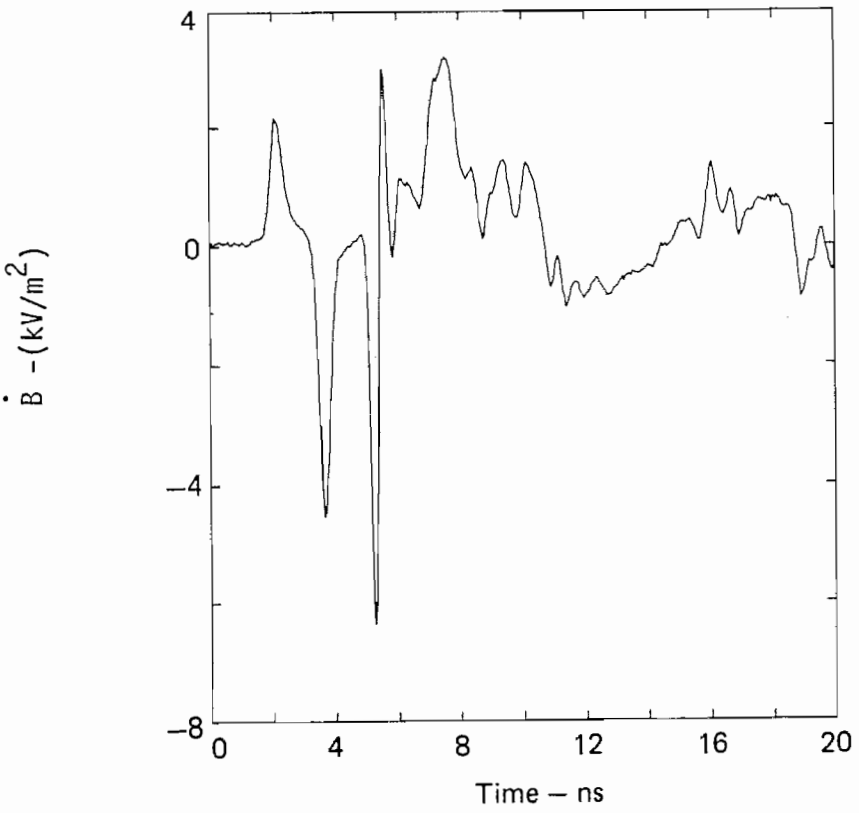

Figure D29. $\dot{B}$ waveform cylinder 50 cm from ground plane (θ = 180°).

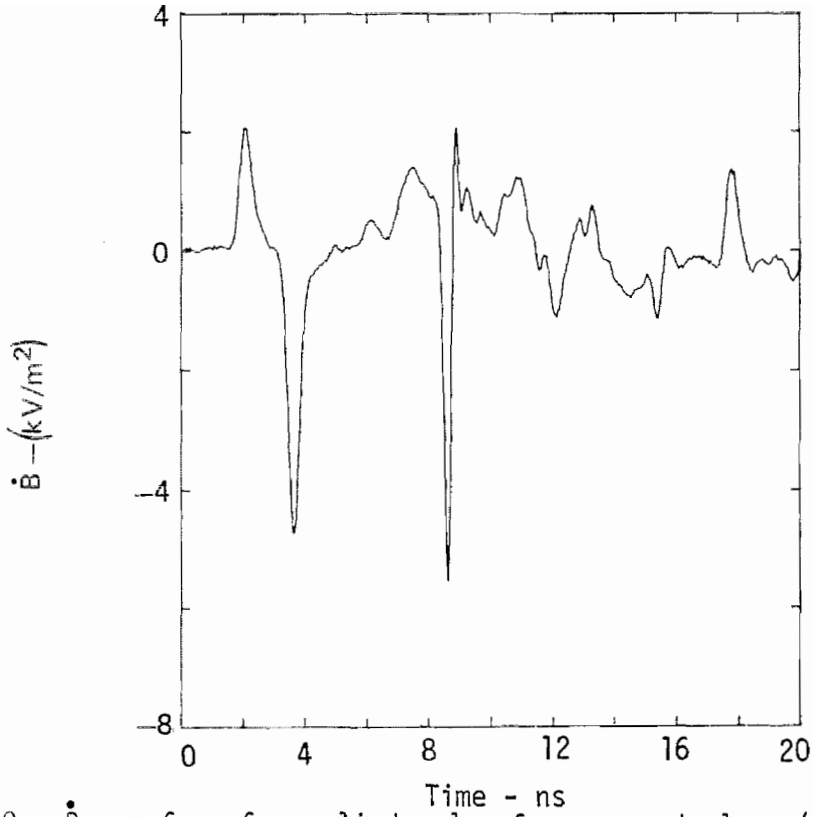

Figure D30. $\dot{B}$ waveform for cylinder 1 m from ground plane (θ = 180°).

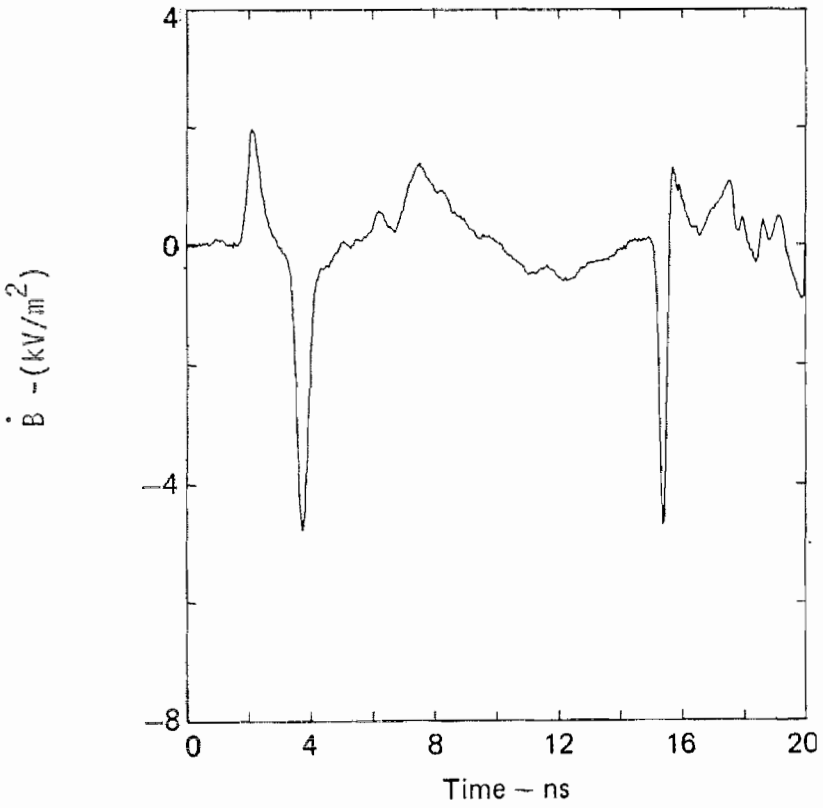

Figure D31. $\dot{B}$ waveform for cylinder 2 m from ground plane (θ = 180°).

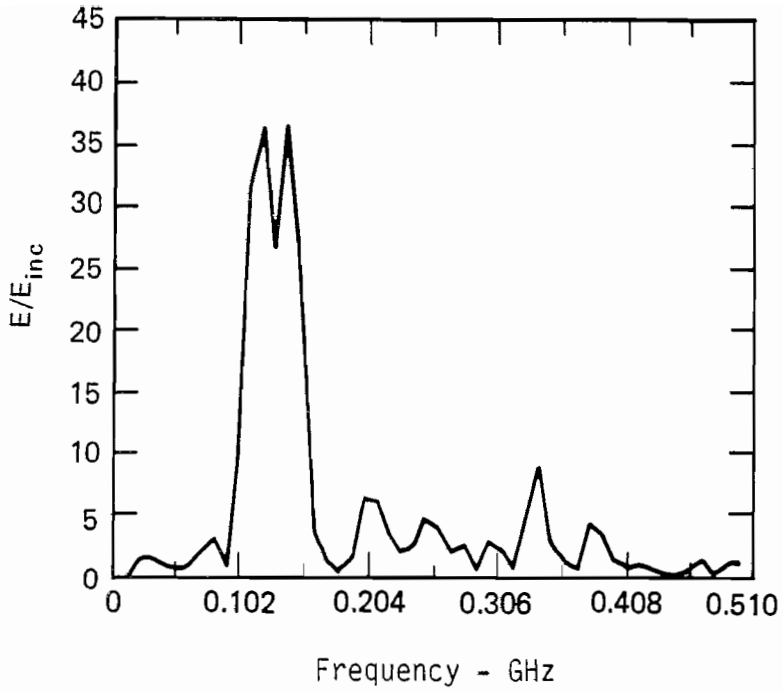

Figure D32. Magnitude of E/E_{inc} for cylinder 10 cm from ground plane ($\theta = 0°$).

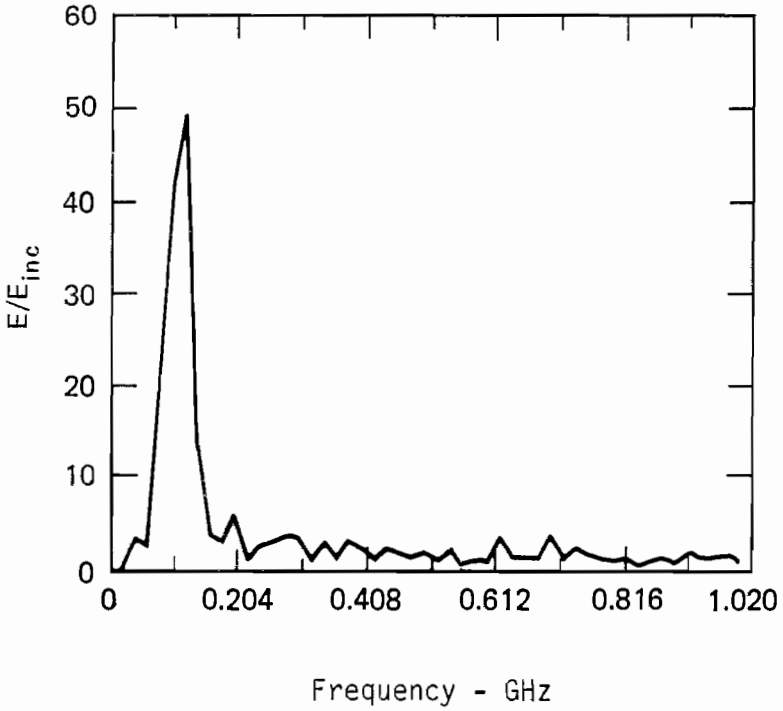

Figure D33. Magnitude of E/E_{inc} for cylinder 50 cm from ground plane ($\theta = 0°$).

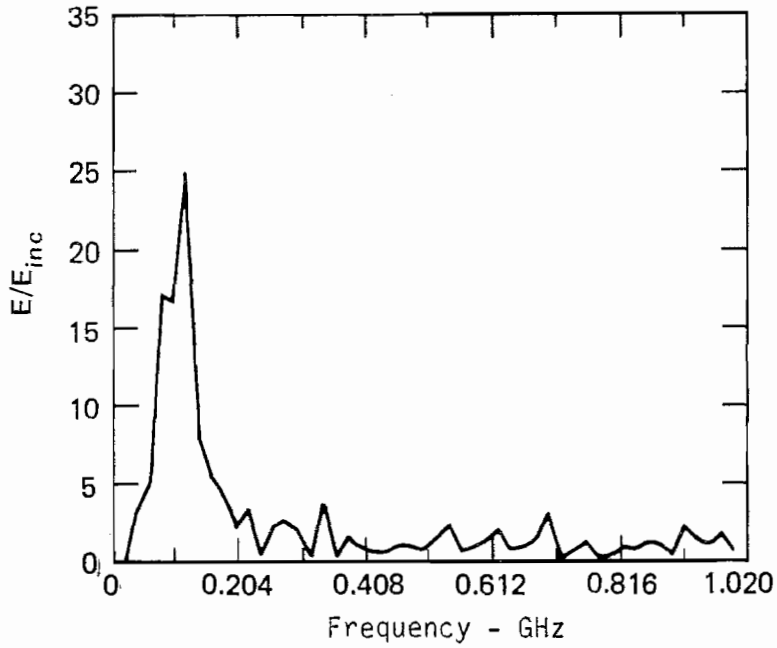

Figure D34. Magnitude of E/E_{inc} for cyinder 1 m from perfectly conducting ground plane ($\theta = 0°$).

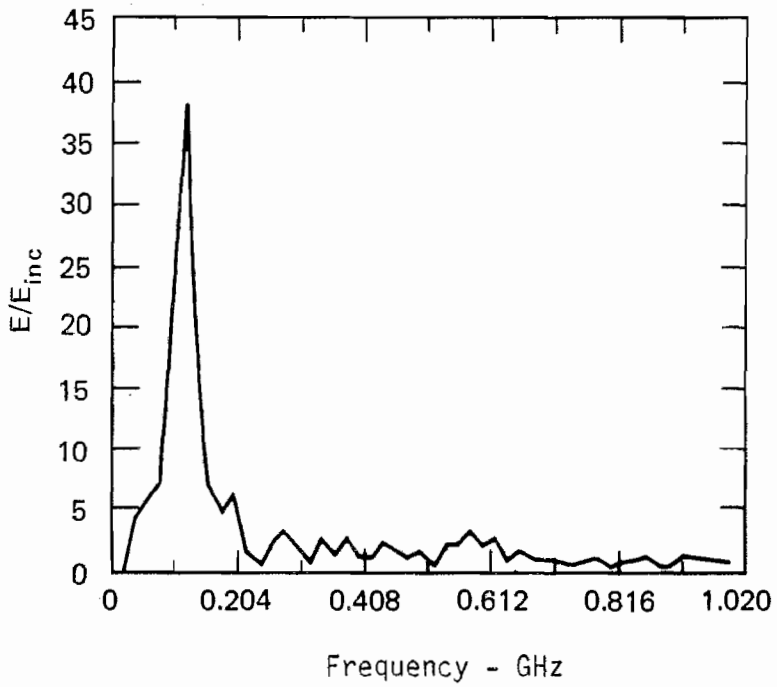

Figure D35. Magnitude of E/E_{inc} for cylinder 2 m from perfectly conducting ground plane ($\theta = 0°$).

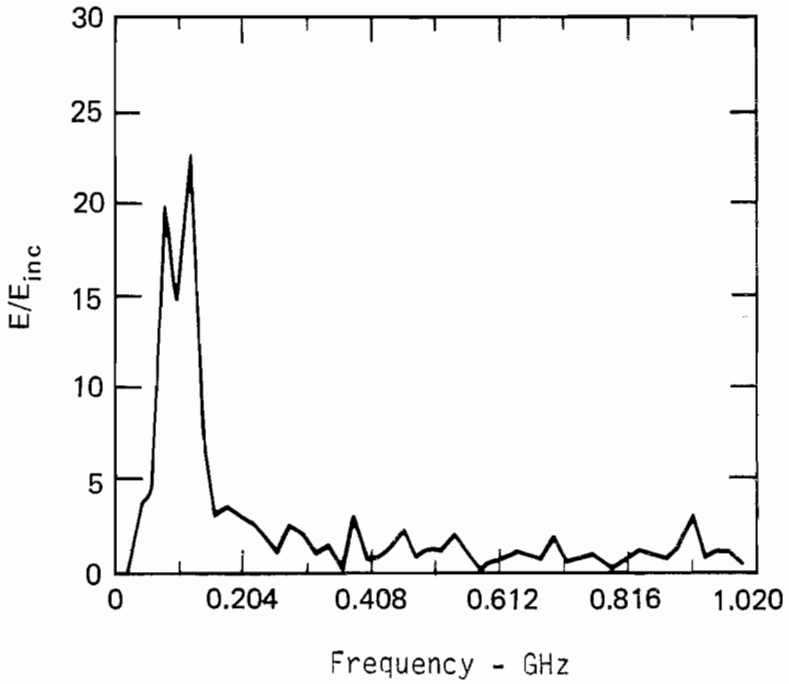

Figure D36. Magnitude of E/E_{inc} for cylinder 10 cm from ground plane (θ = 180°).

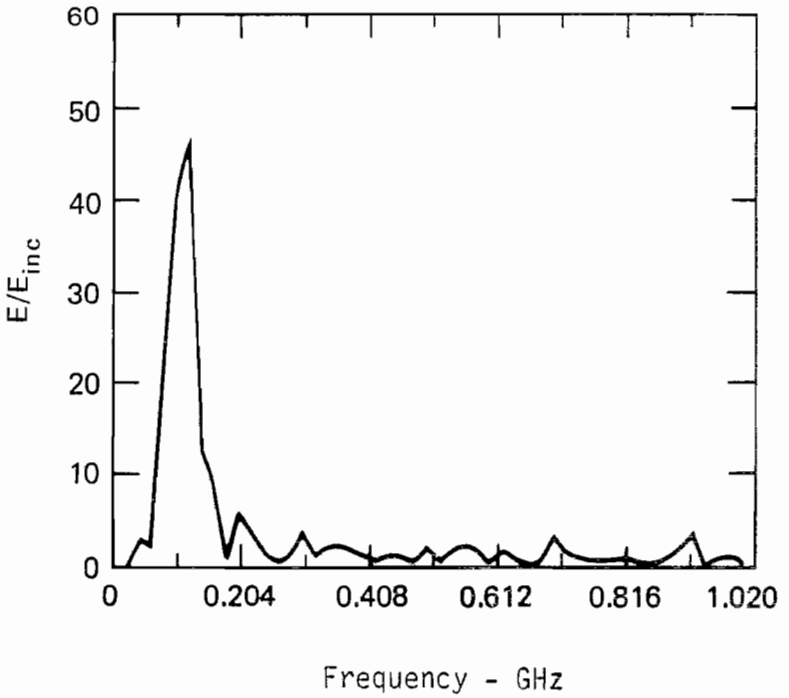

Figure D37. Magnitude of E/E_{inc} for cylinder 50 cm from ground plane (θ = 180°).

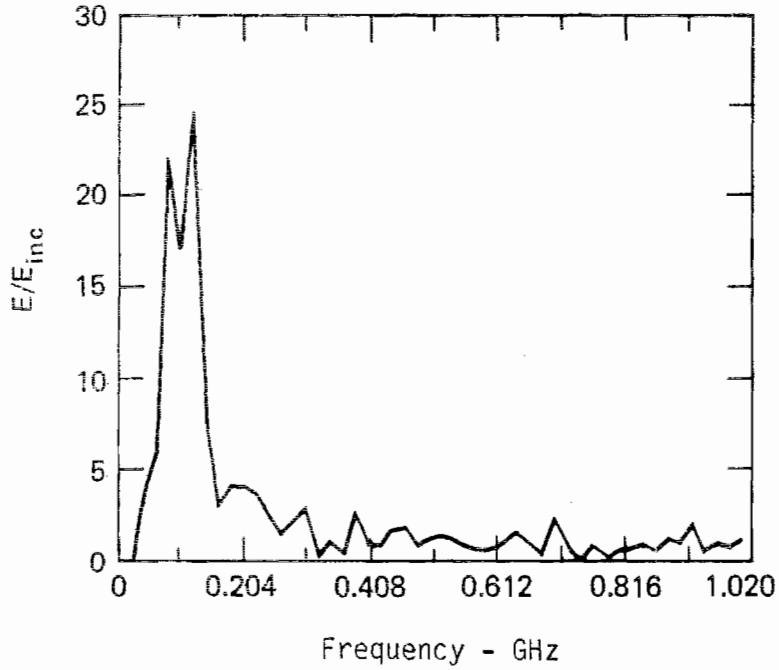

Figure D38. Magnitude of E/E_{inc} for cylinder 1 m from ground plane ($\theta = 180°$).

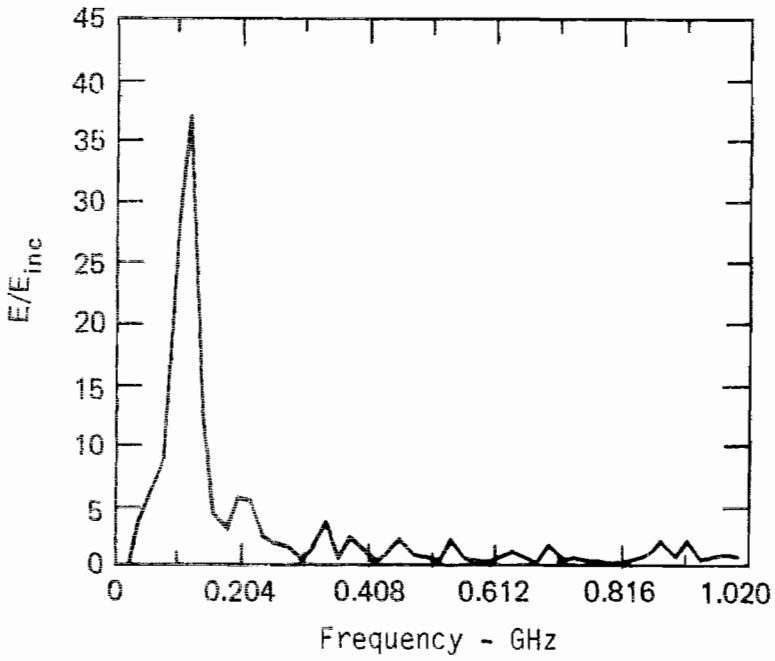

Figure D39. Magnitude of E/E_{inc} for cylinder 2 m from ground plane ($\theta = 180°$)

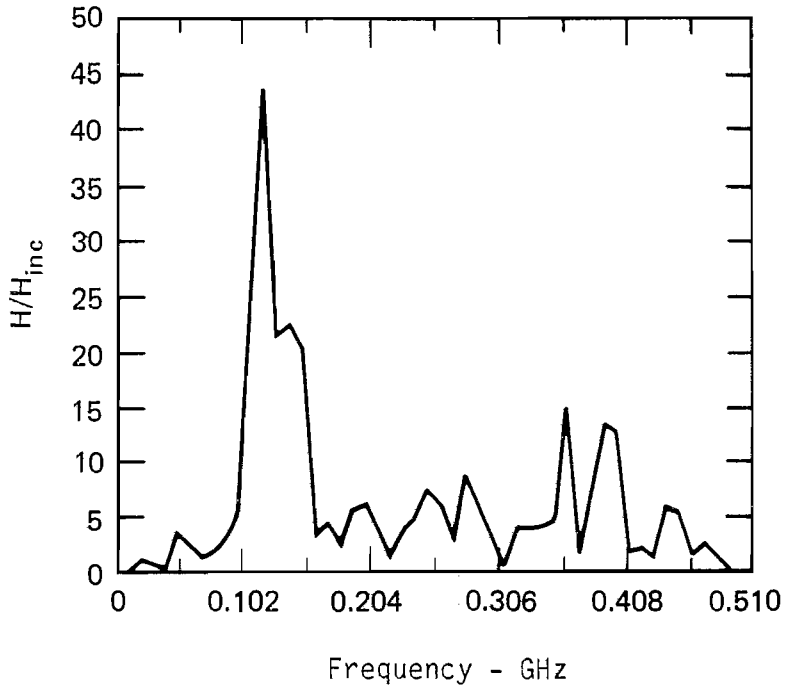

Figure D40. Magnitude of H/H_{inc} for cylinder 10 cm from ground plane ($\theta = 0°$).

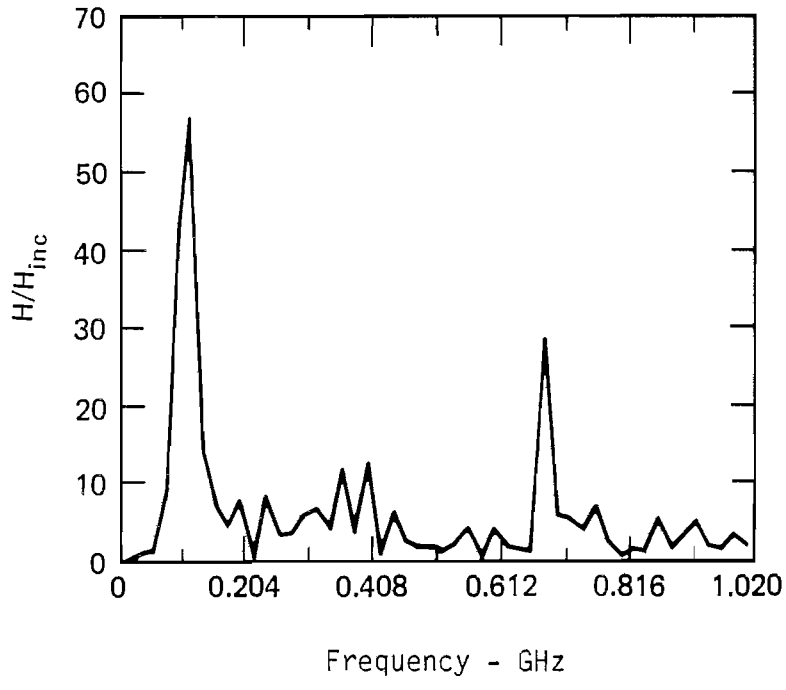

Figure D41. Magnitude of H/H_{inc} for cylinder 50 cm from ground plane ($\theta = 0°$).

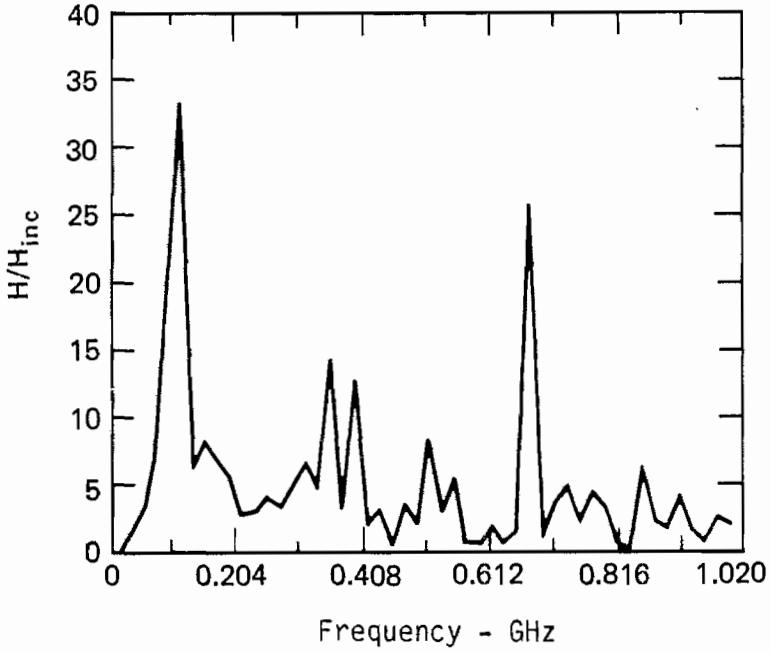

Figure D42. Magnitude of H/H_{inc} for cylinder 1 m from ground plane ($\theta = 0°$).

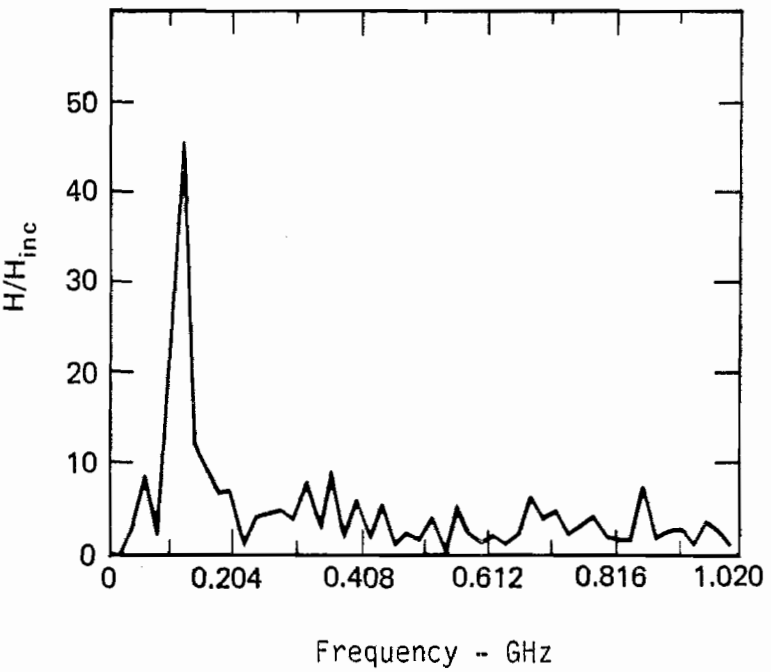

Figure D43. Magnitude of H/H_{inc} for cylinder 2 m from ground plane ($\theta = 0°$).

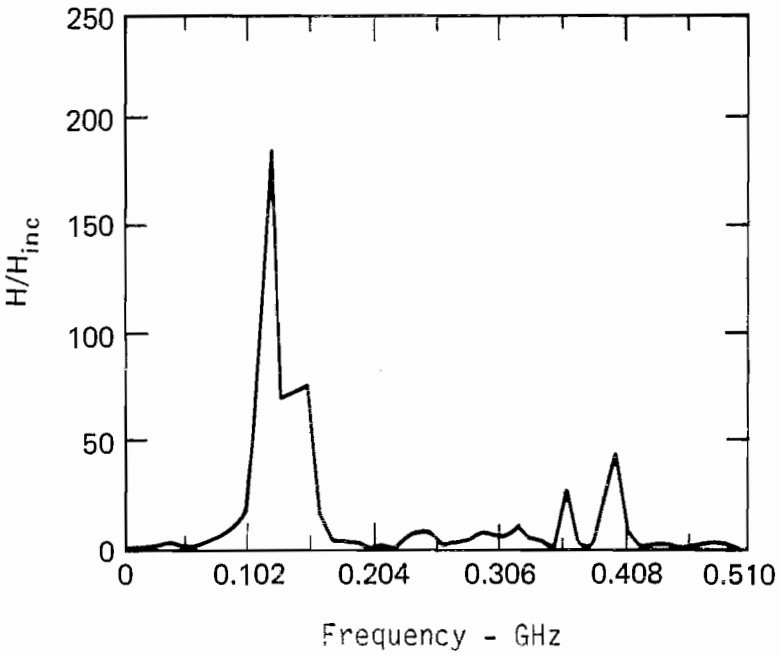

Figure D44. Magnitude of H/H_{inc} for cylinder 10 cm from ground plane ($\theta = 180°$).

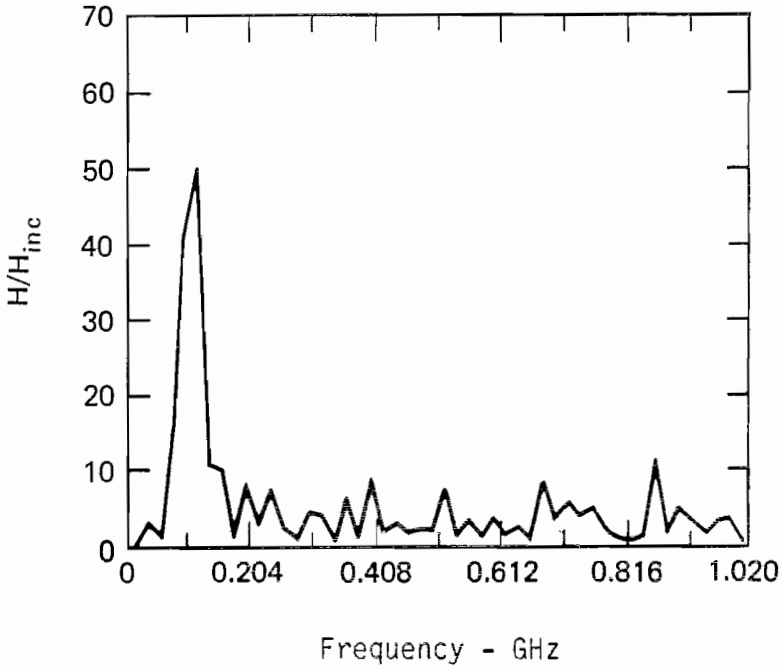

Figure D45. Magnitude of H/H_{inc} for cylinder 50 cm from ground plane ($\theta = 180°$).

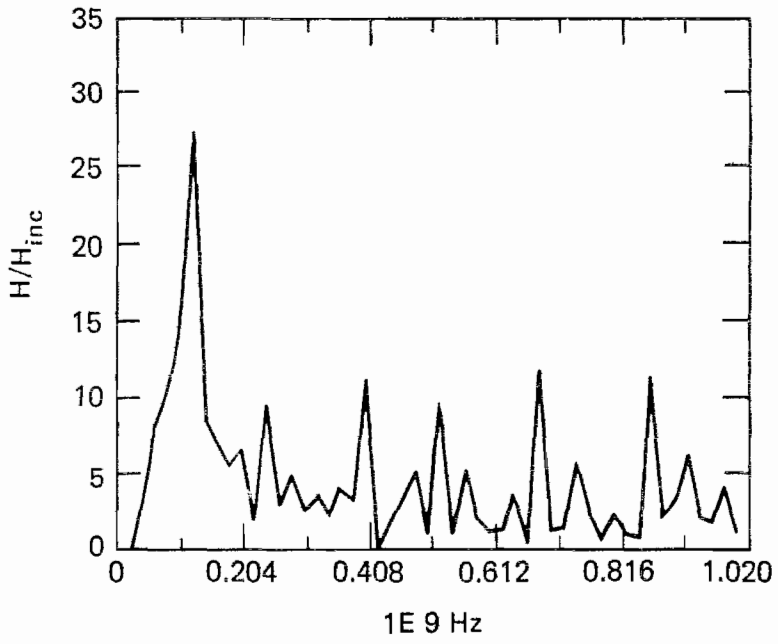

Frequency - GHz

Figure D46. Magnitude of H/H_{inc} for cylinder 1 m from ground plane ($\theta = 180°$)

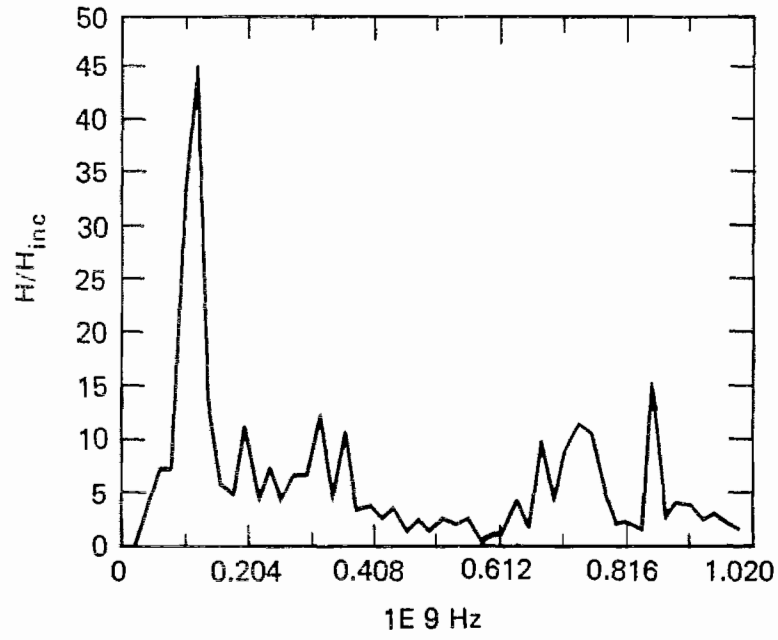

Frequency - GHz

Figure D47. Magnitude of H/H_{inc} for cylinder 2 m from ground plane ($\theta = 180°$)

Appendix E
Crossed Cylinder Data

The measurements were performed for both a free-space configuration and in the presence of a perfectly conducting ground plane. For the crossed cylinder, only a 0° and 180° incident field was used. Figures E1 through E4 show the $\dot{D}$ and $\dot{B}$ sensor outputs for the free-space measurements at 0° and 180° incidence angles, respectively.

The frequency-domain transfer functions were obtained in a manner similar to that used for the cylinder measurements; i.e., the Fourier transforms of the $\dot{D}$ and $\dot{B}$ responses were divided by the Fourier transform of the incident EM pulse measured at the base of the model, but with the model removed. These transfer functions are shown in Figures E5 through E8.

The measurements for the crossed cylinder near a perfectly conducting ground plane are shown first in the time domain in Figures E9 through E24, and then in the frequency domain in Figures E25 through E40. For the time domain waveform, only the first 20 ns of the response is shown.

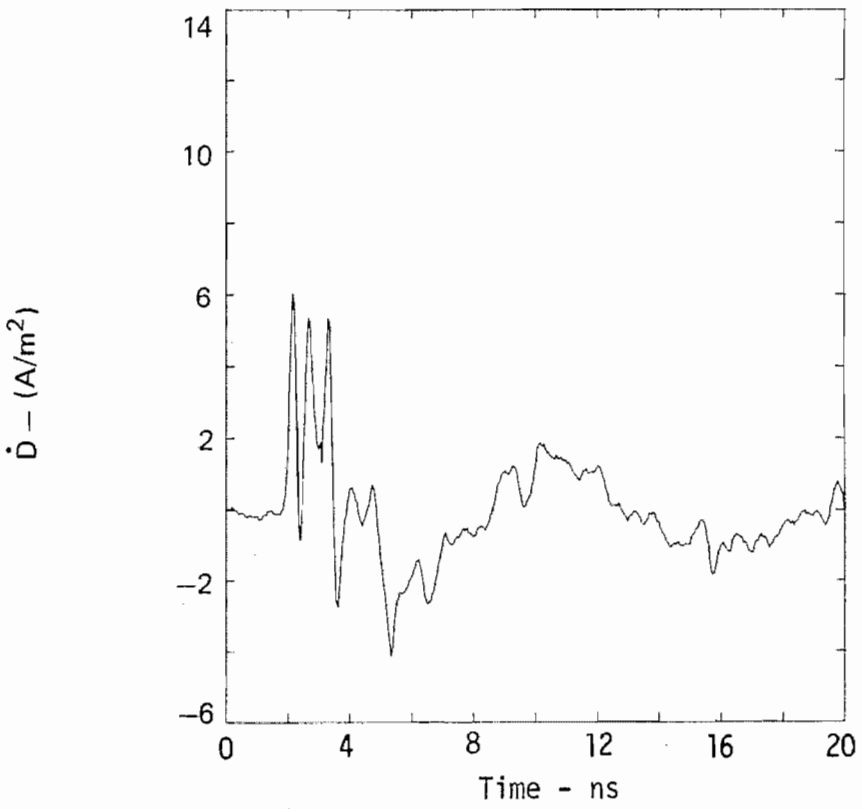

Figure E1. Time domain $\dot{D}$ waveform for crossed cylinder in free space ($\theta = 0°$).

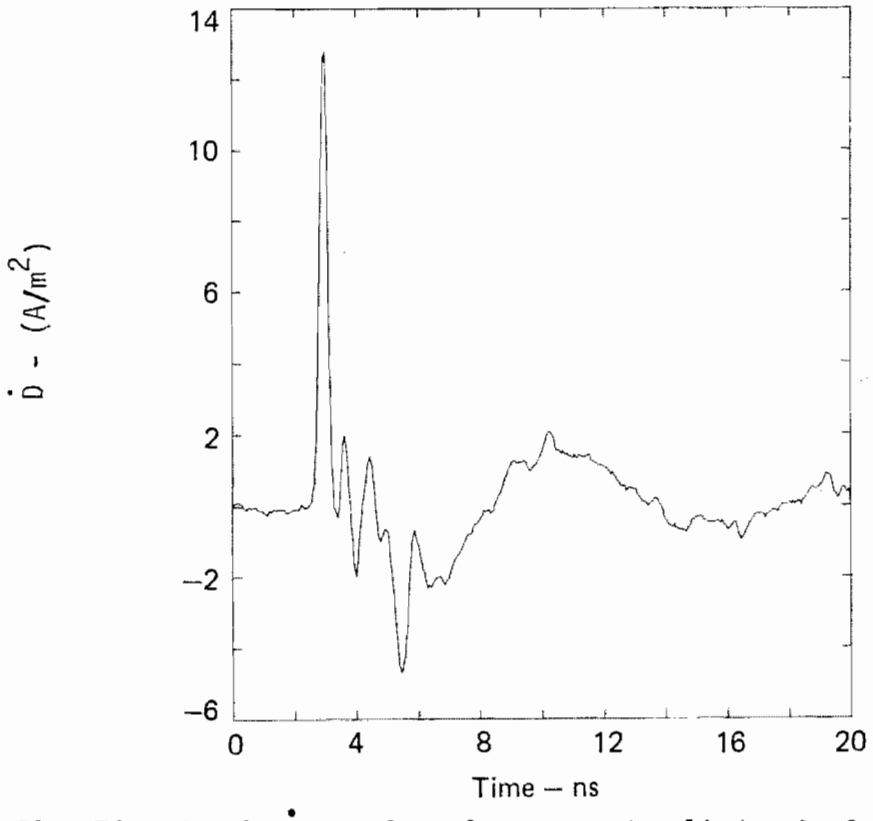

Figure E2. Time domain $\dot{D}$ waveform for crossed cylinder in free space ($\theta = 180°$).

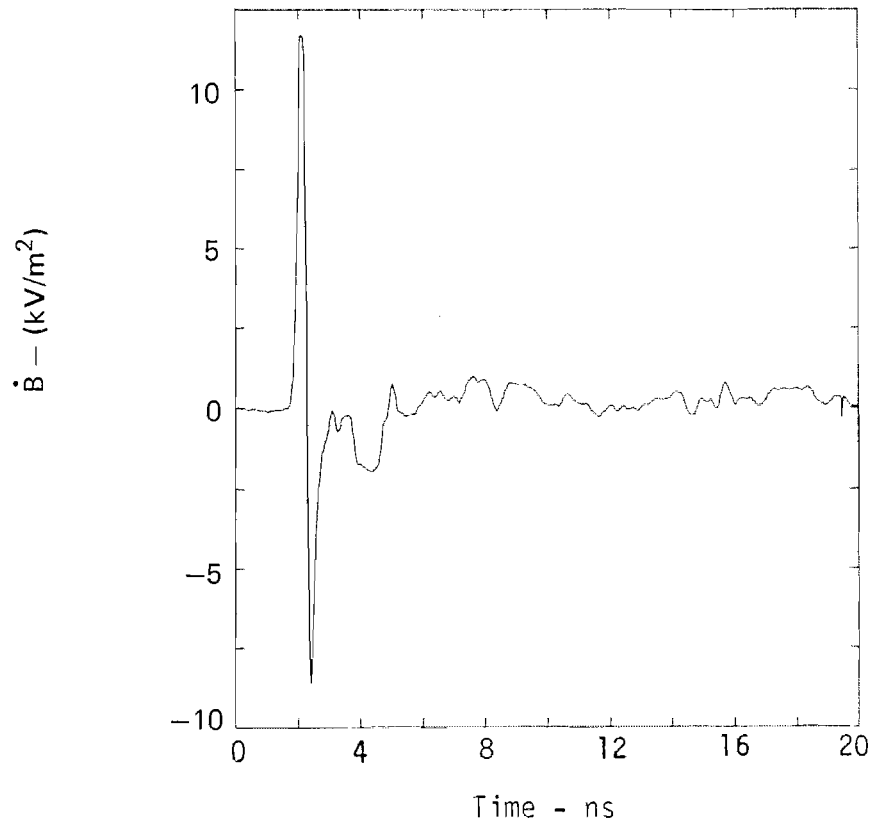

Figure E3. Time domain $\dot{B}$ waveform for crossed cylinder in free space ($\theta = 0°$).

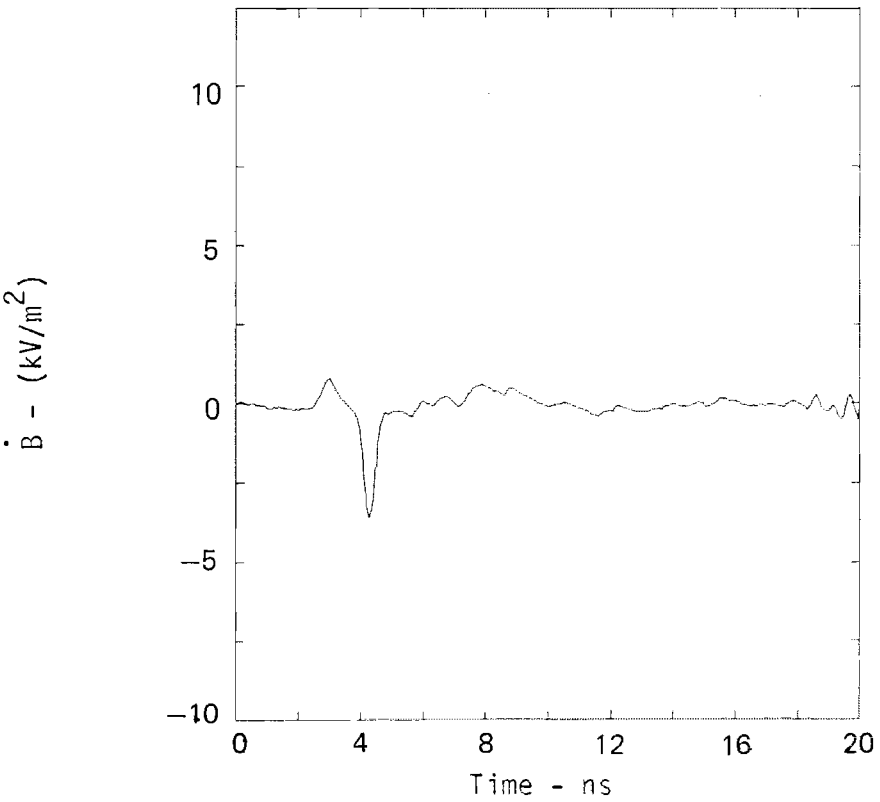

Figure E4. Time domain $\dot{B}$ waveform for crossed cylinder in free space ($\theta = 180°$).

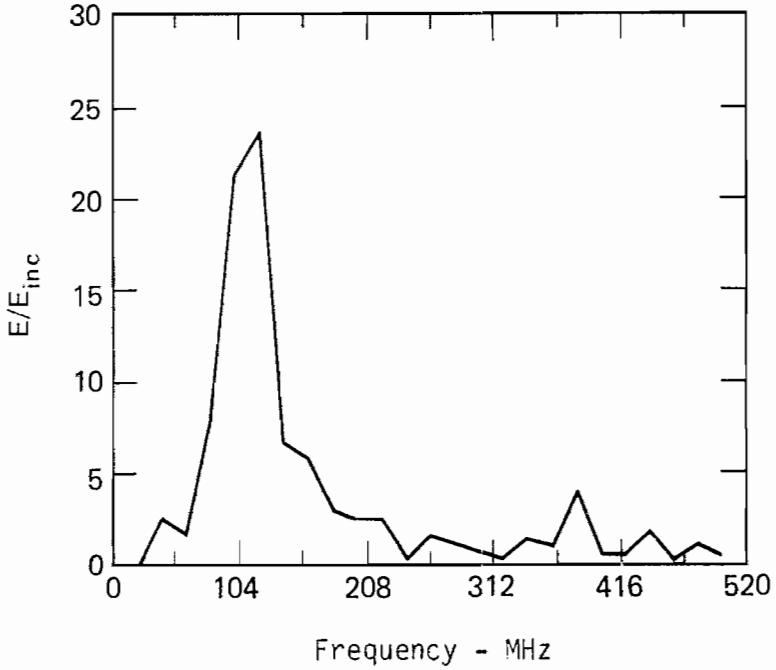

Figure E5. Magnitude of E/E_{inc} for crossed cylinder in free space ($\theta = 0^{\circ}$).

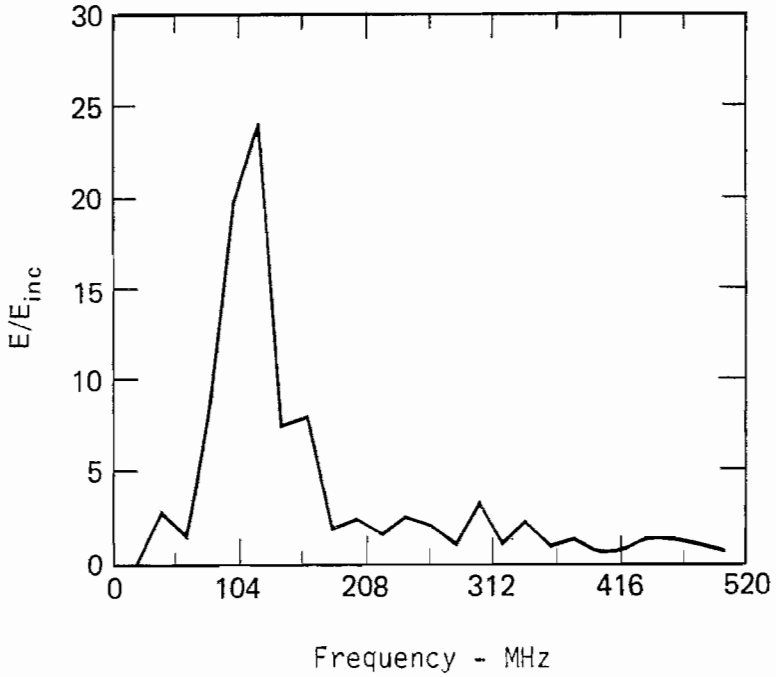

Figure E6. Magnitude of E/E_{inc} for crossed cylinder in free space for incident field ($\theta = 180^{\circ}$).

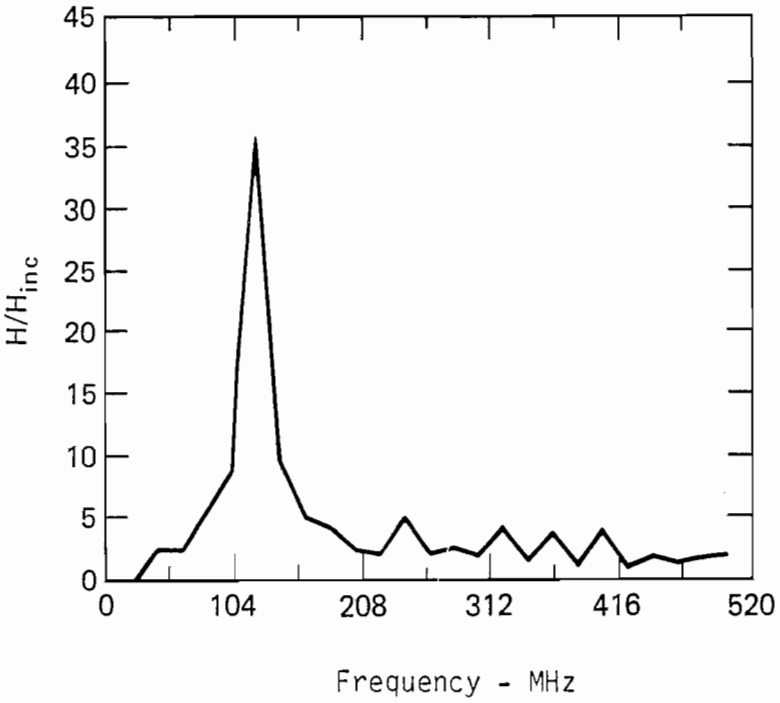

Figure E7. Magnitude of H/H_{inc} on crossed cylinder ($\theta = 0^{\circ}$).

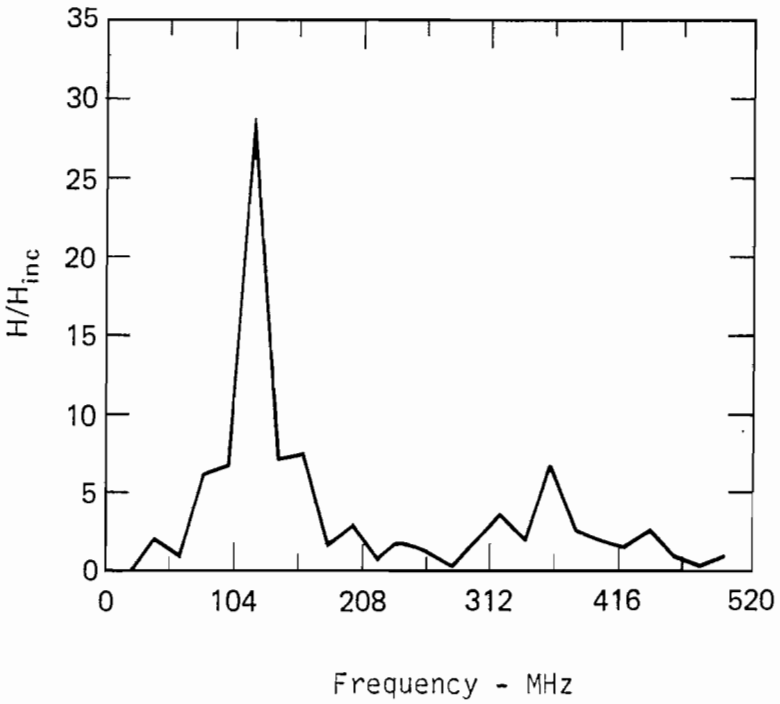

Figure E8. Magnitude of H/H_{inc} on crossed cylinder. H/H_{inc} is from ($\theta = 180^{\circ}$).

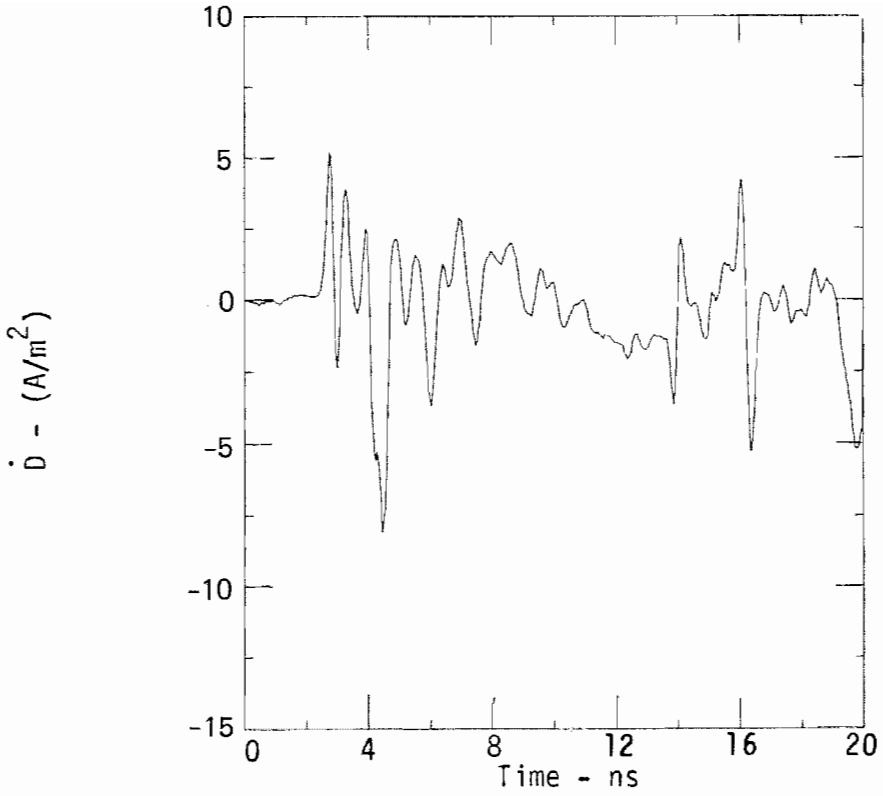

Figure E9. Time domain $\dot{D}$ waveform for crossed cylinder 10 cm from ground plane ($\theta = 0°$).

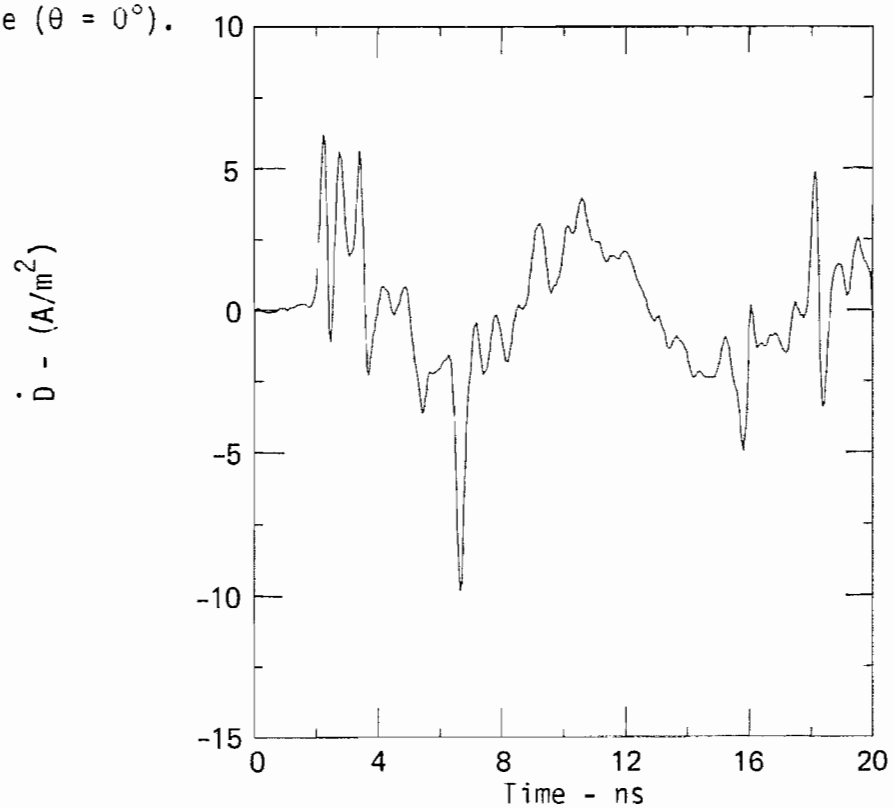

Figure E10. Time domain $\dot{D}$ waveform for crossed cylinder 50 cm from ground plane ($\theta = 0°$).

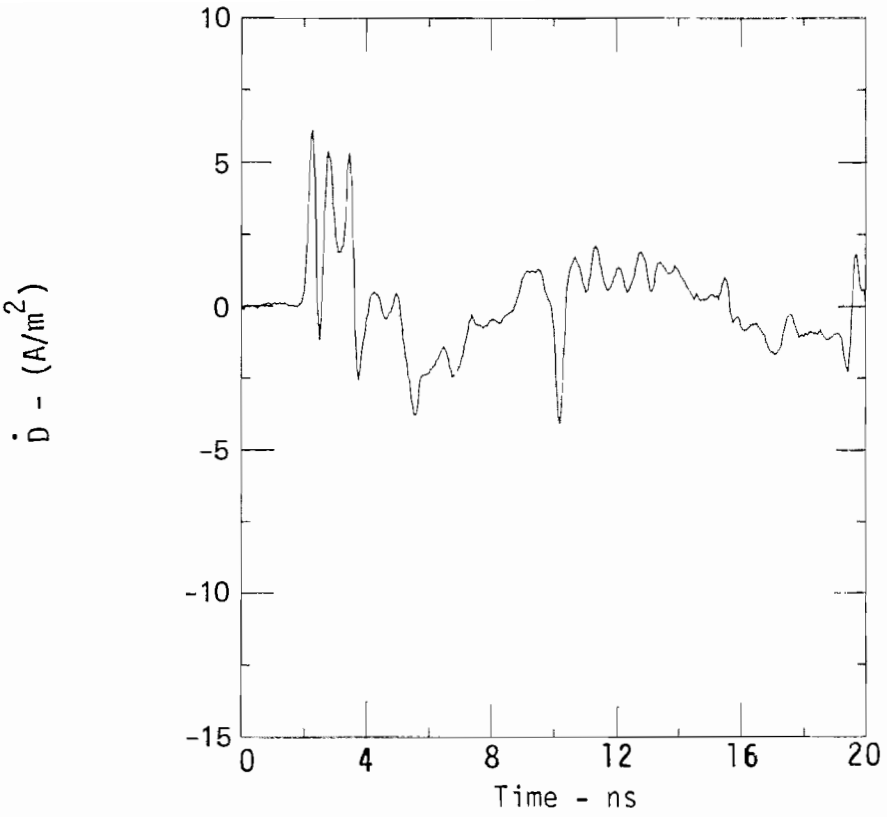

Figure E11. Time domain waveform for $\dot{D}$ sensor on crossed cylinder 1 m from ground plane ($\theta = 0°$).

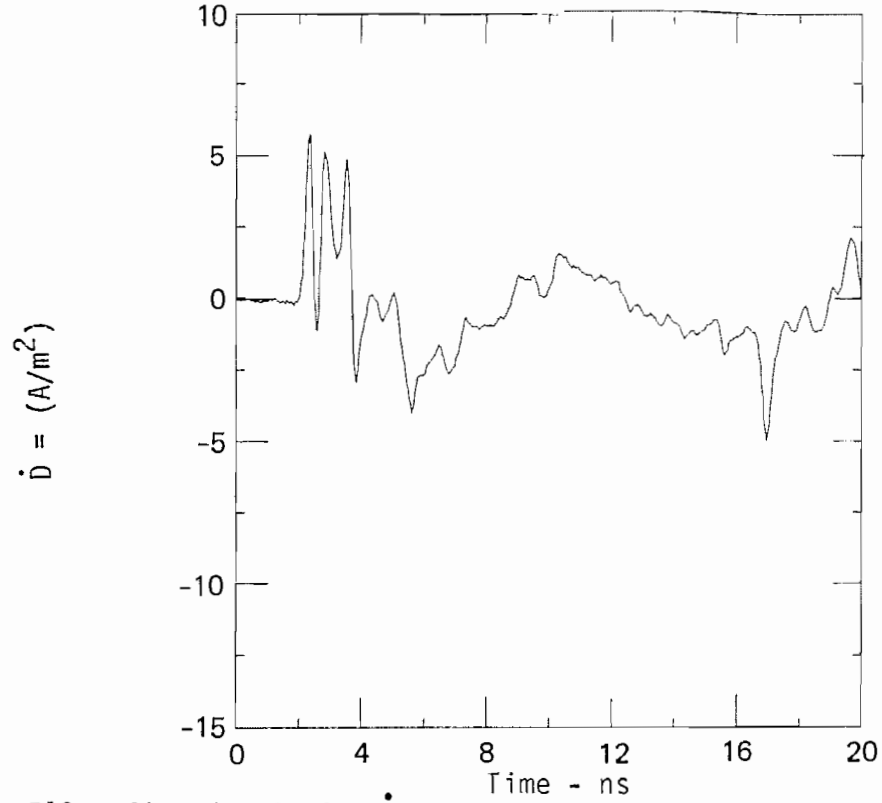

Figure E12. Time domain for $\dot{D}$ sensor on crossed cylinder 2 m from ground plane ($\theta = 0°$).

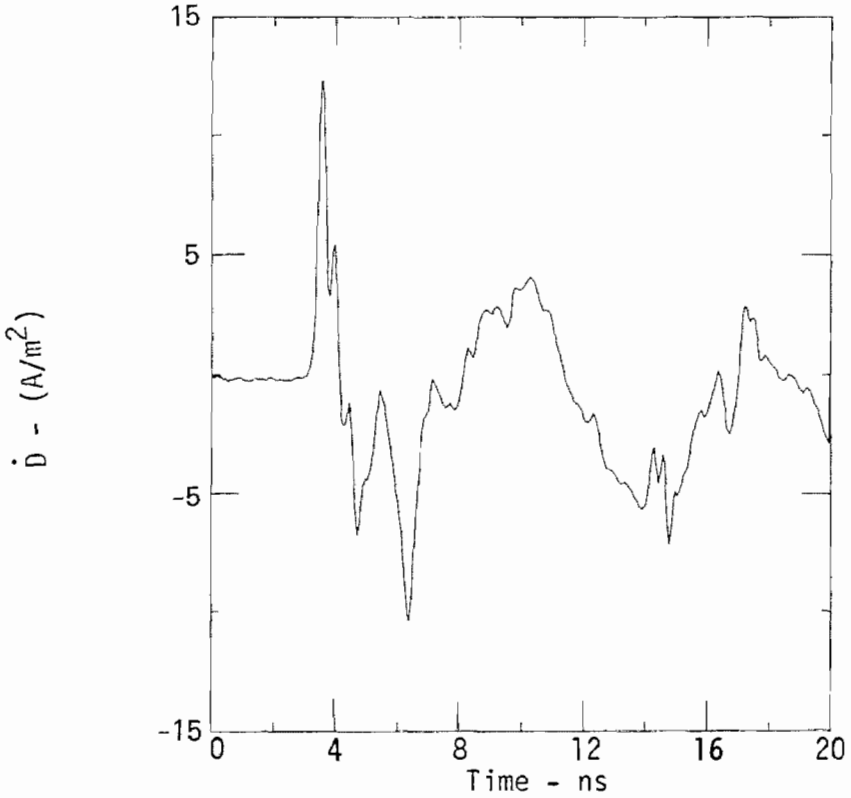

Figure E13. Time domain waveform for $\dot{D}$ sensor on crossed cylinder 10 cm from ground plane (θ = 180°).

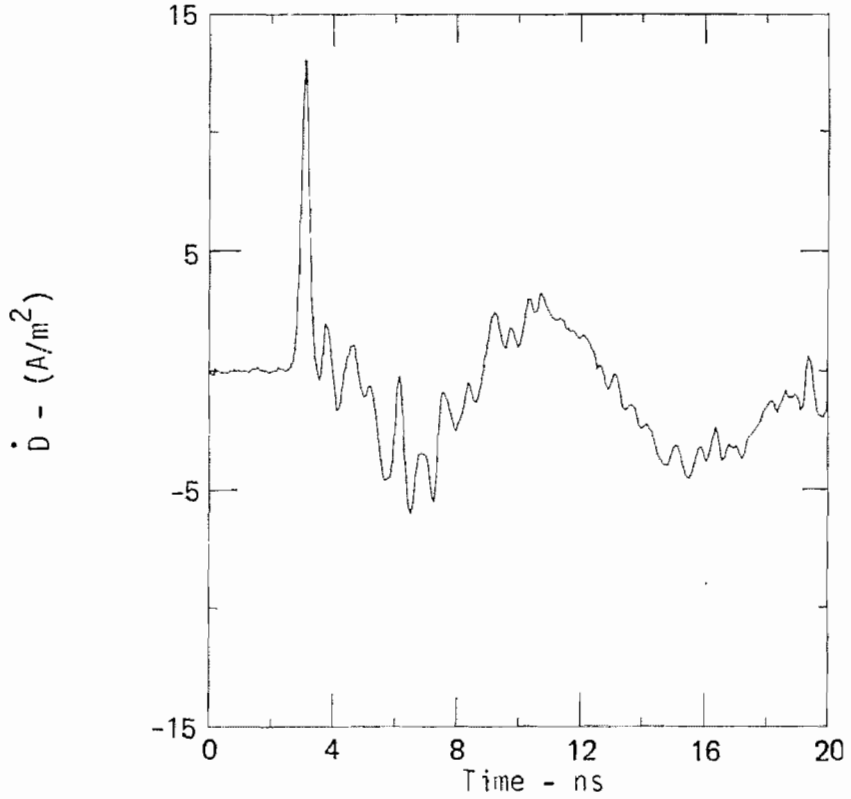

Figure E14. Time domain waveform for $\dot{D}$ sensor on crossed cylinder 50 cm from ground plane (θ = 180°).

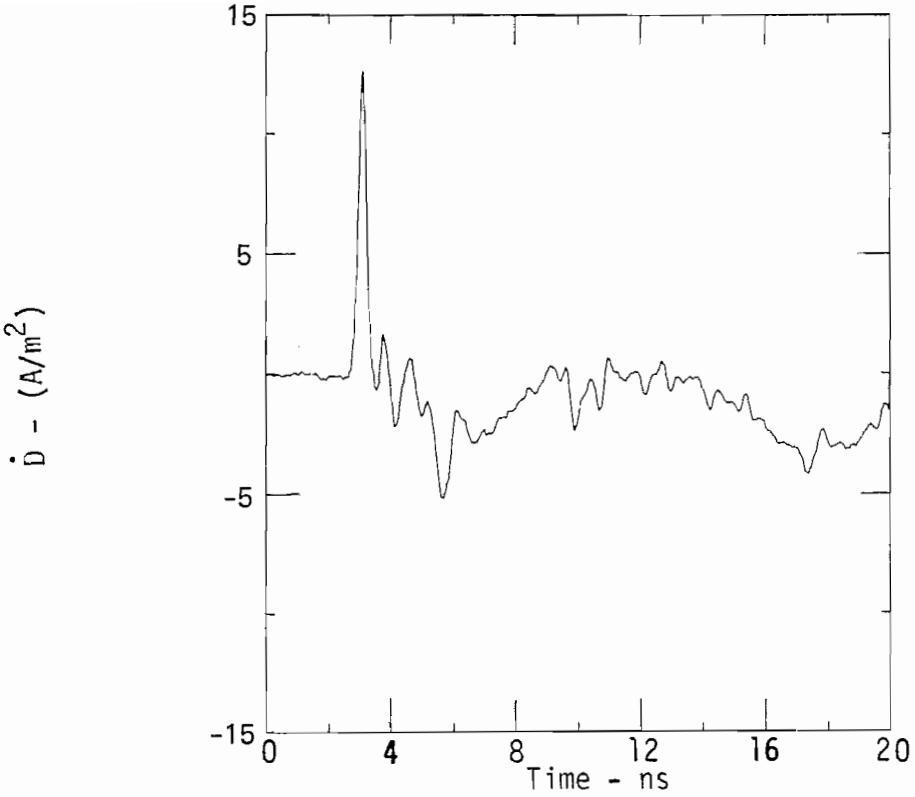

Figure E15. Time domain $\dot{D}$ sensor output for crossed cylinder 1 m from ground plane (θ = 180°).

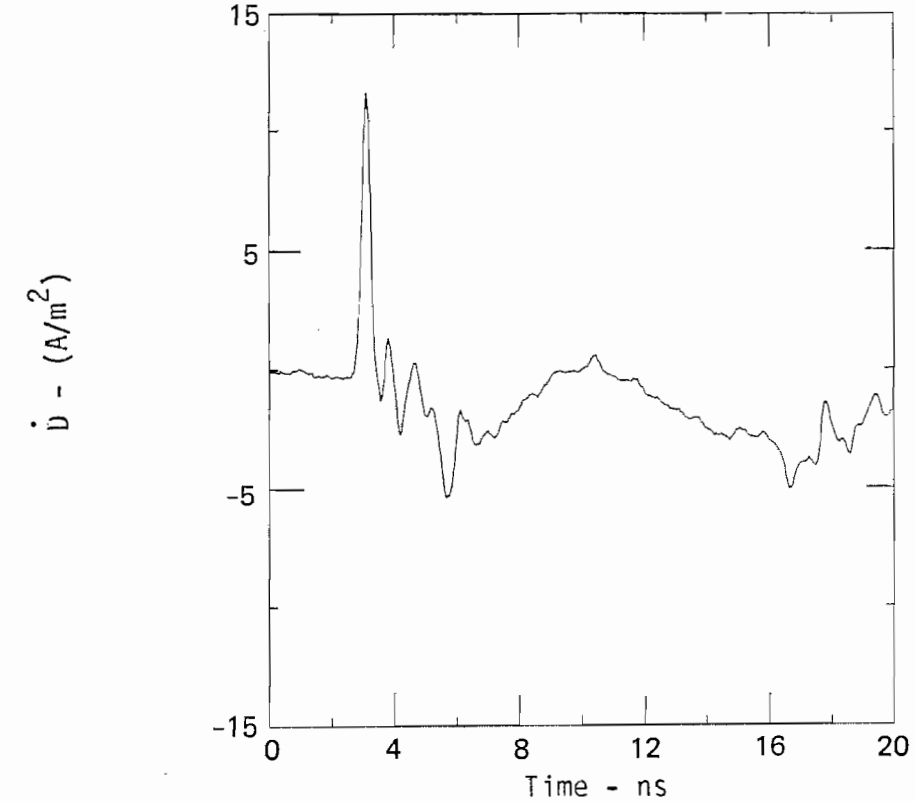

Figure E16. Time domain $\dot{D}$ sensor output for crossed cylinder 2 m from ground plane (θ = 180°).

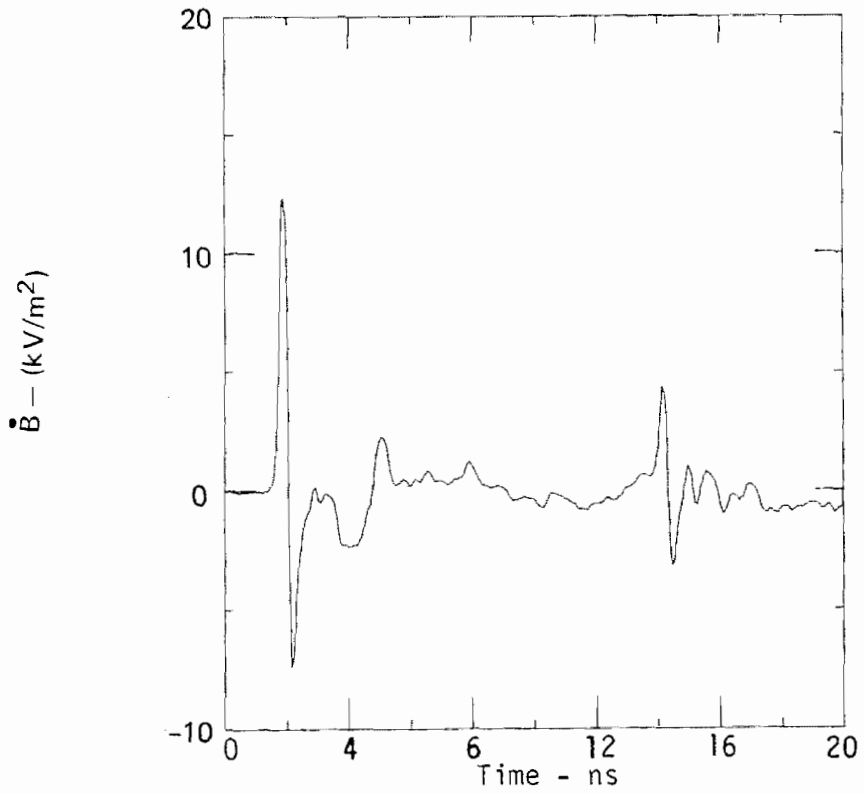

Figure E17. Time domain waveform for $\dot{B}$ sensor on crossed cylinder located 10 cm from ground plane (θ = 0°).

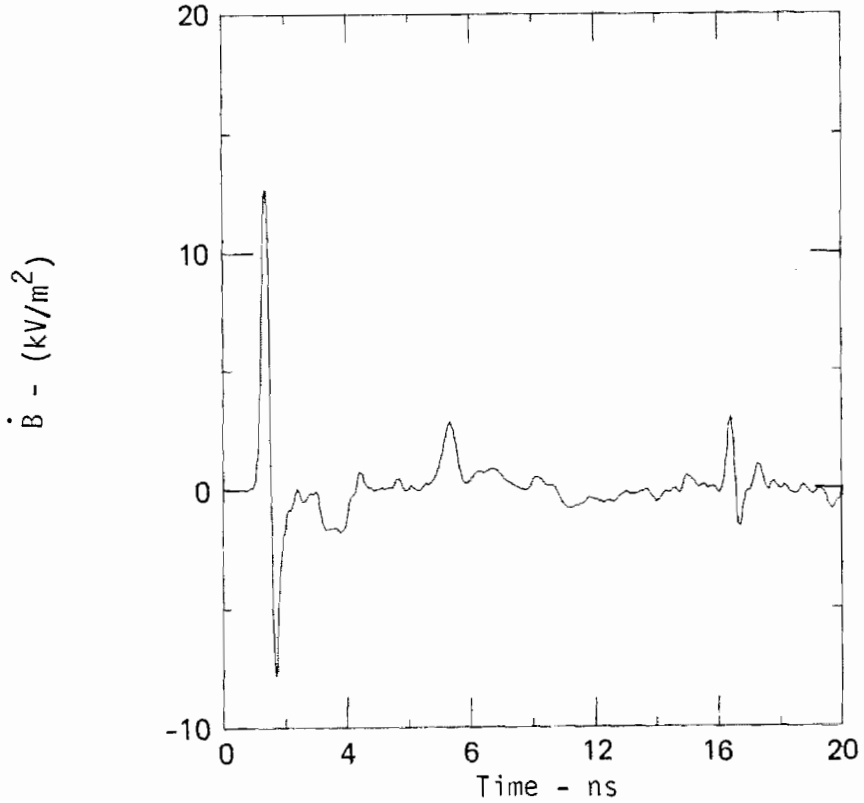

Figure E18. Time domain waveform for $\dot{B}$ sensor on crossed cylinder 50 cm from gound plane (θ = 0°).

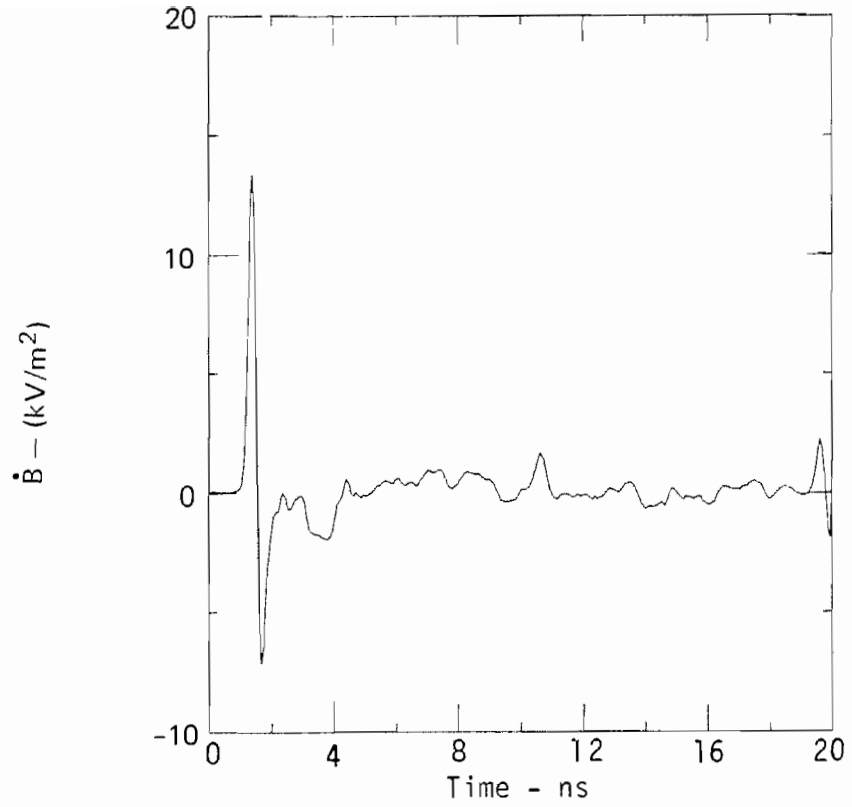

Figure E19. Time domain $\dot{B}$ sensor output for crossed cylinder 1 m from ground plane ($\theta = 0°$).

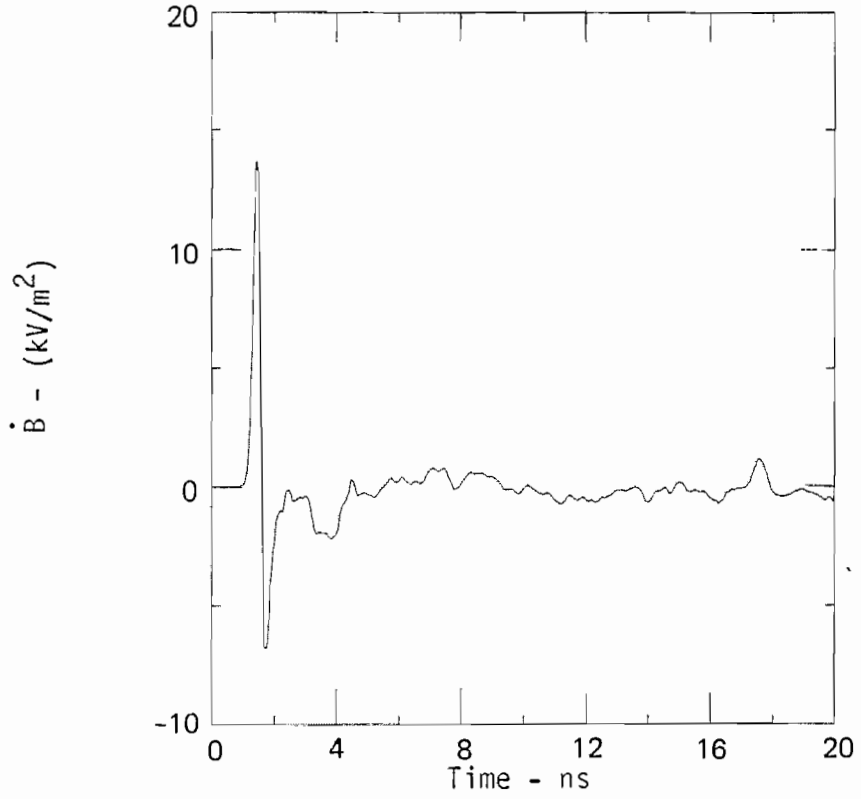

Figure E20. Time domain $\dot{B}$ sensor output for crossed cylinder 2 m from ground plane ($\theta = 0°$).

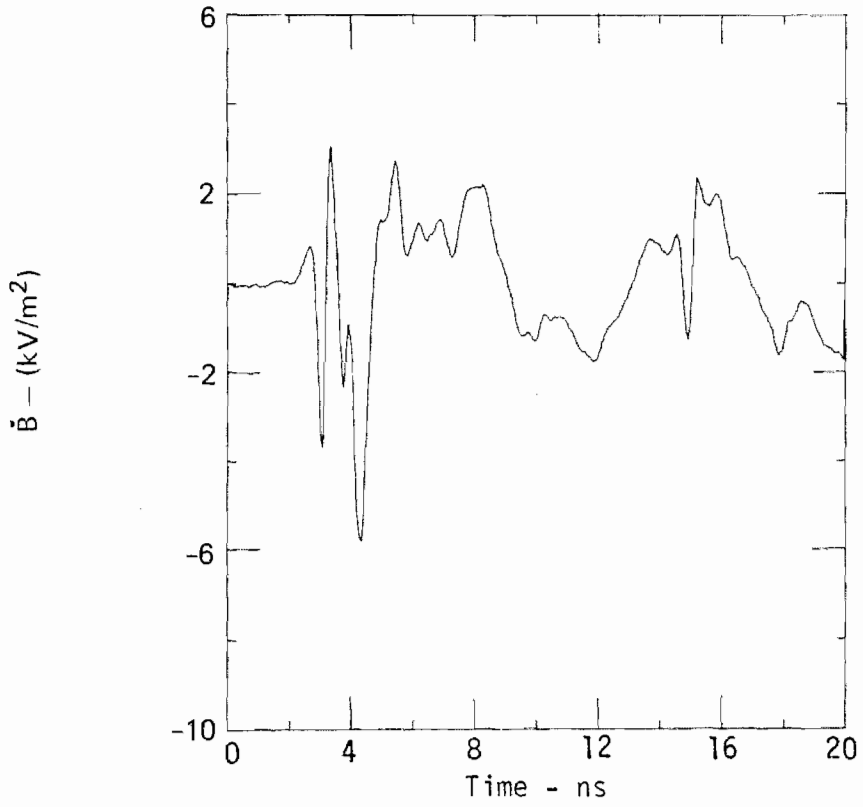

Figure E21. Time domain waveforms for $\dot{B}$ sensor on crossed cylinder located 10 cm from ground plane (θ = 180°).

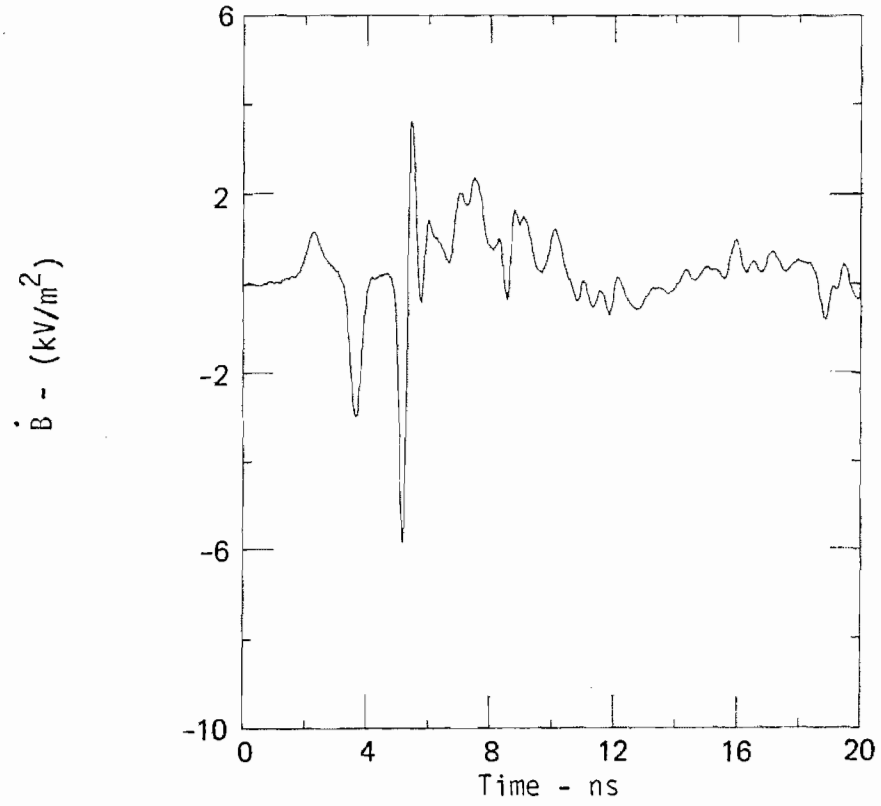

Figure E22. Time domain waveform for $\dot{B}$ sensor on crossed cylinder located 50 cm from ground plane (θ = 180°).

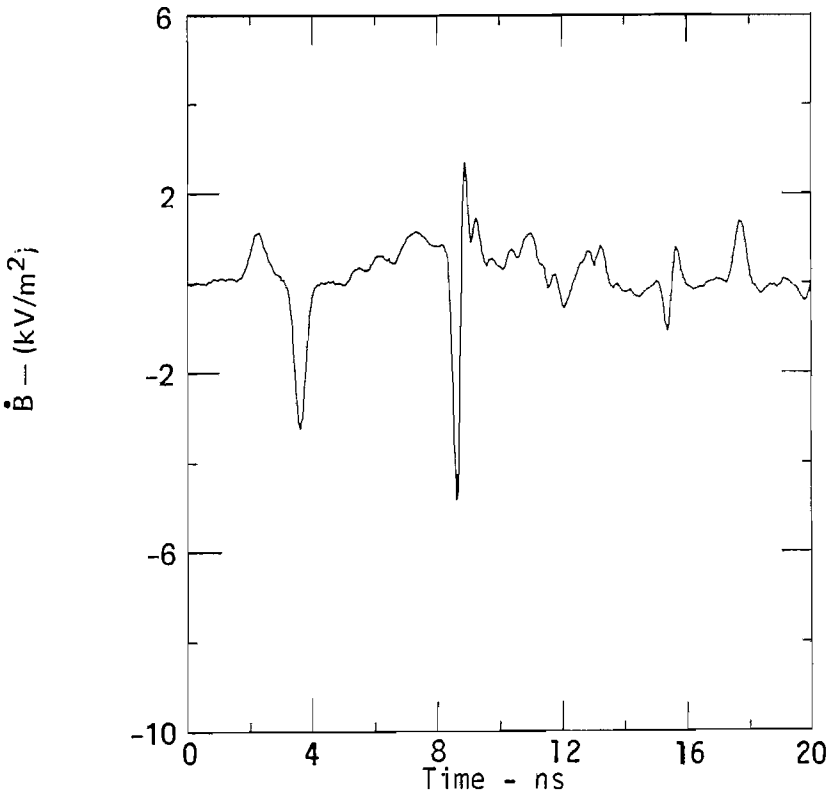

Figure E23. Time domain waveform for $\dot{B}$ sensor on crossed cylinder located 1 m from ground plane (θ = 180°).

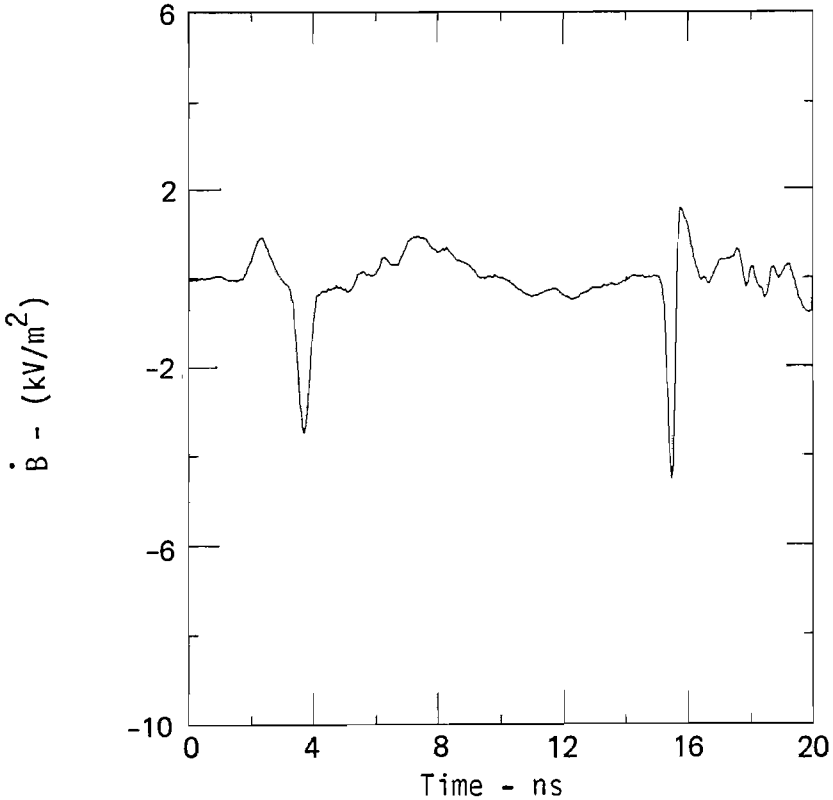

Figure E24. Time domain waveform for $\dot{B}$ sensor on crossed cylinder located 2 m from ground plane (θ = 180°).

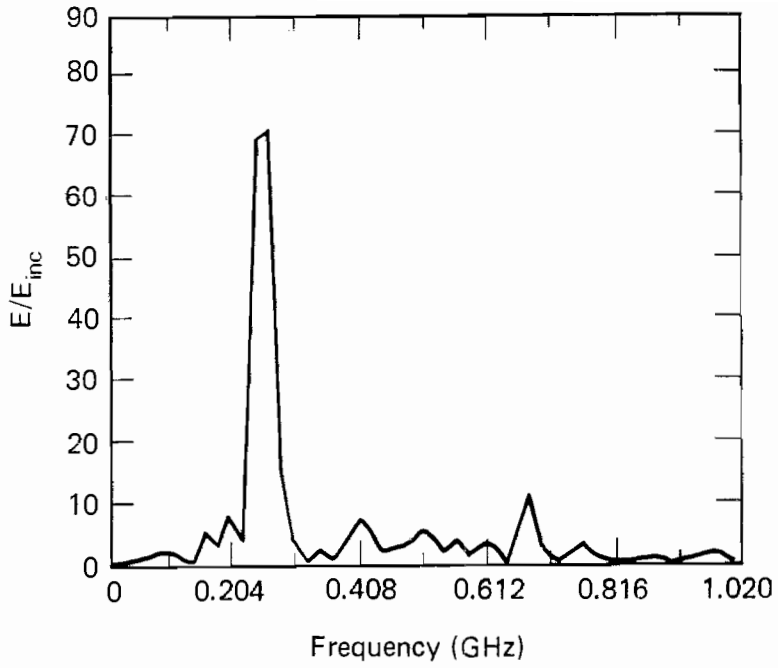

Figure E25. Magnitude of E/E_{inc} for crossed cylinder 17 cm from a perfect ground plane (θ = 0°).

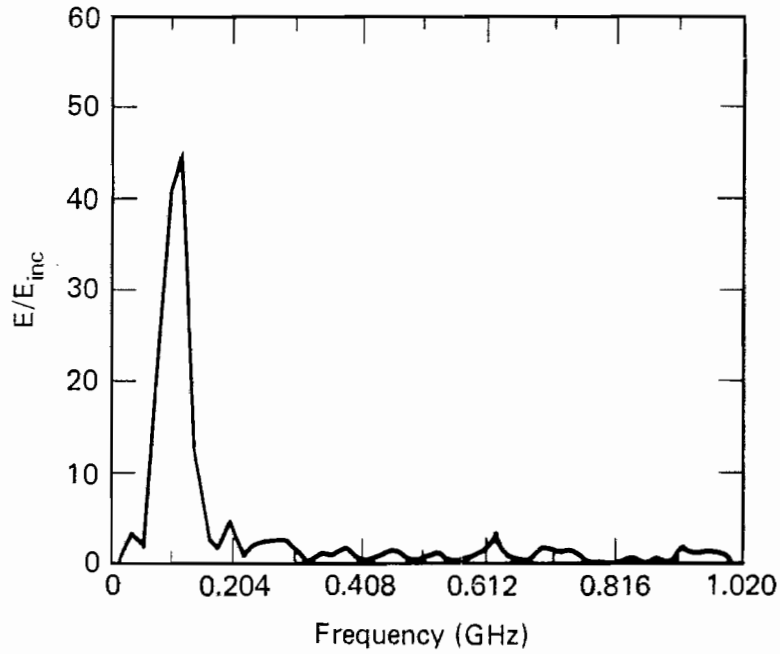

Figure E26. Magnitude of E/E_{inc} for crossed cylinder 50 cm from a perfect ground plane (θ = 0°).

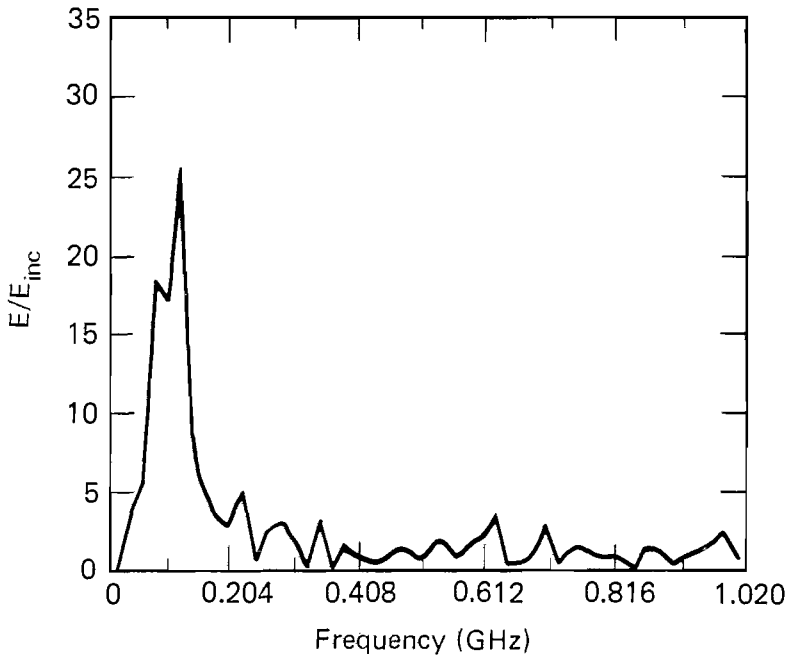

Figure E27. Magnitude of E/E_{inc} for crossed cylinder 1 m from ground plane ($\theta = 0°$).

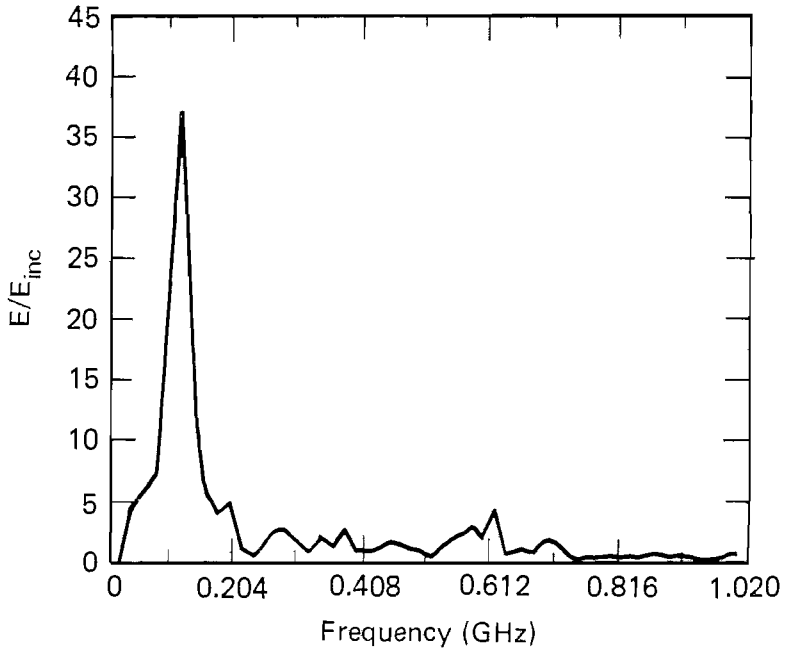

Figure E28. Magnitude of E/E_{inc} for crossed cylinder 2 m from ground plane ($\theta = 0°$).

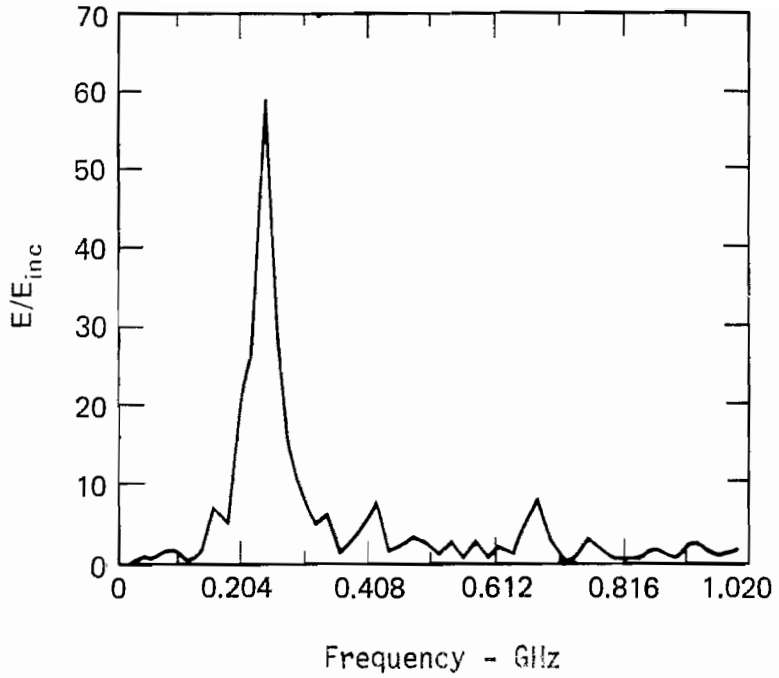

Figure E29. Magnitude of E/E_{inc} for crossed cylinder 17 cm from ground plane (θ = 180°).

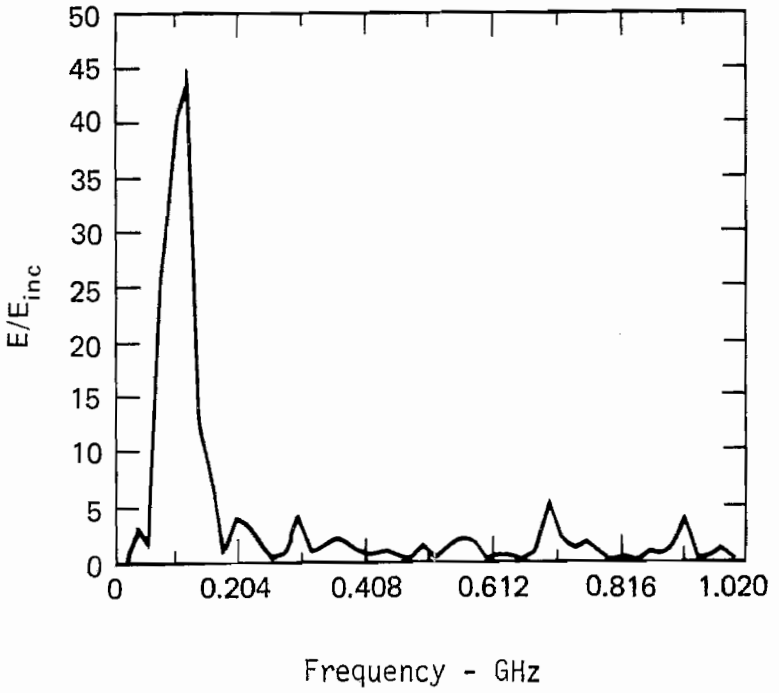

Figure E30. Magnitude of E/E_{inc} for crossed cylinder 50 cm from ground plane (θ = 180°).

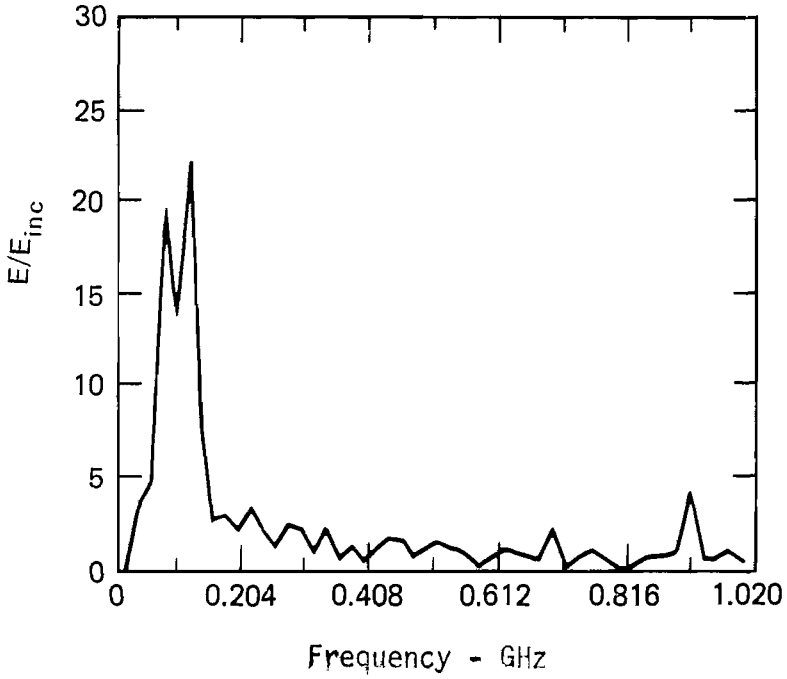

Figure E31. Magnitude of E/E_{inc} for crossed cylinder 1 m from ground plane (θ = 180°).

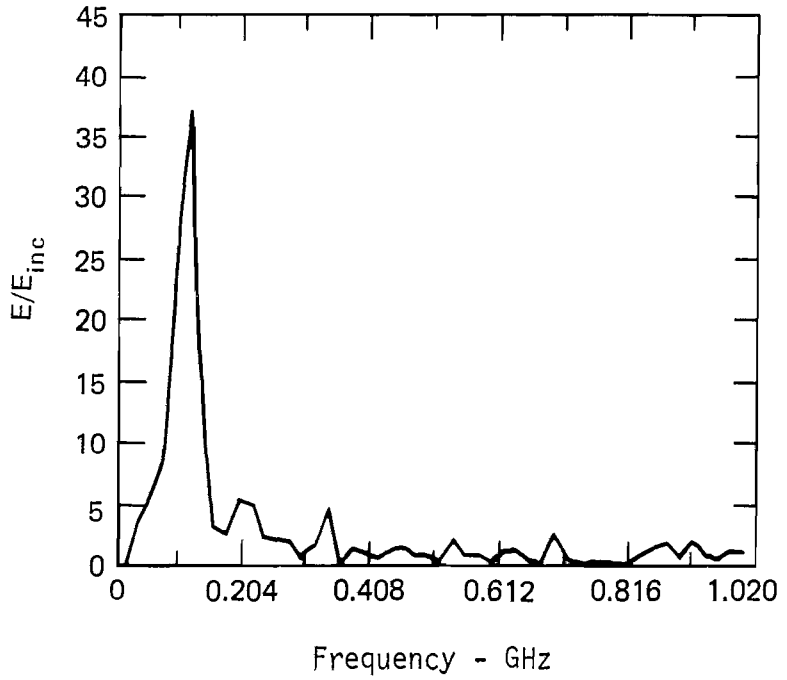

Figure E32. Magnitude of E/E_{inc} for crossed cylinder 2 m from ground plane (θ = 180°).

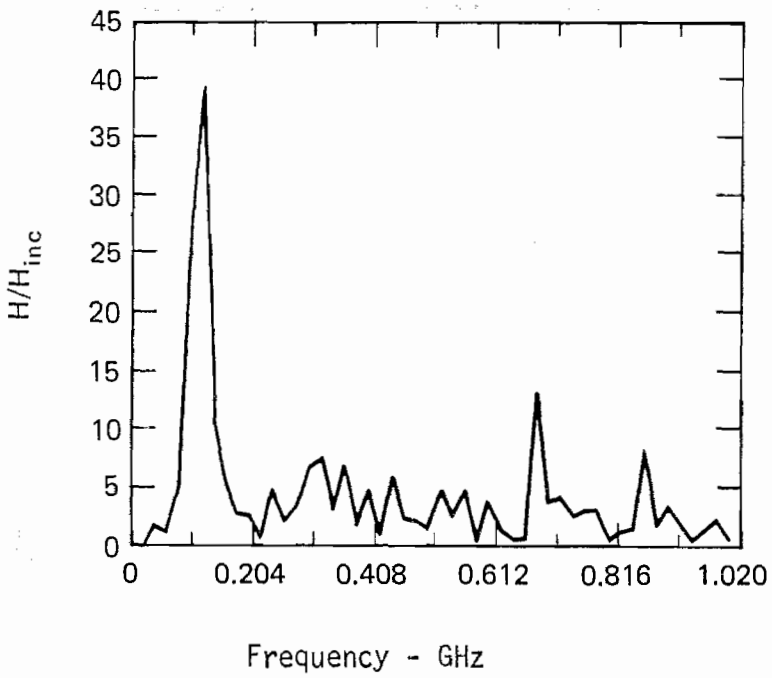

Figure E33. Magnitude of H/H_{inc} for crossed cylinder 10 cm from ground plane ($\theta = 0^{\circ}$).

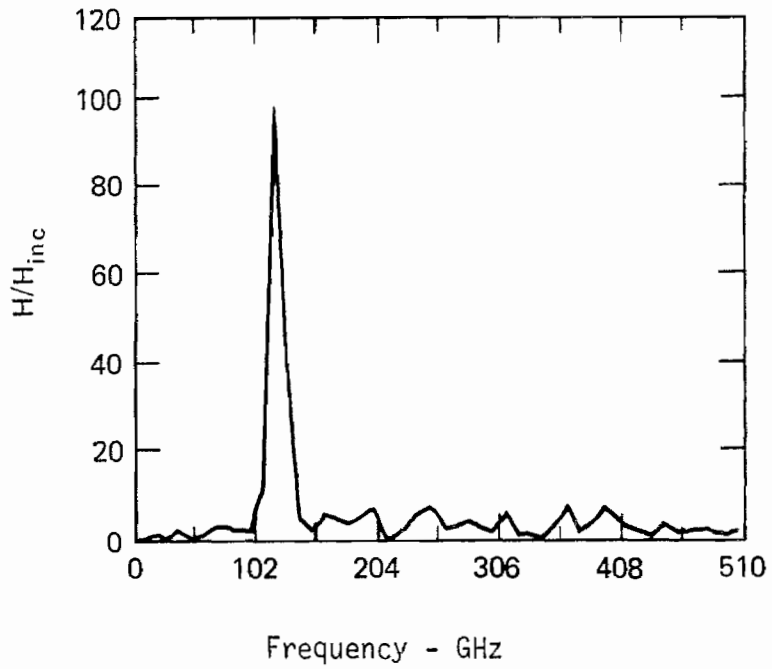

Figure E34. Magnitude of H/H_{inc} for crossed cylinder 50 cm from ground plane ($\theta = 0^{\circ}$).

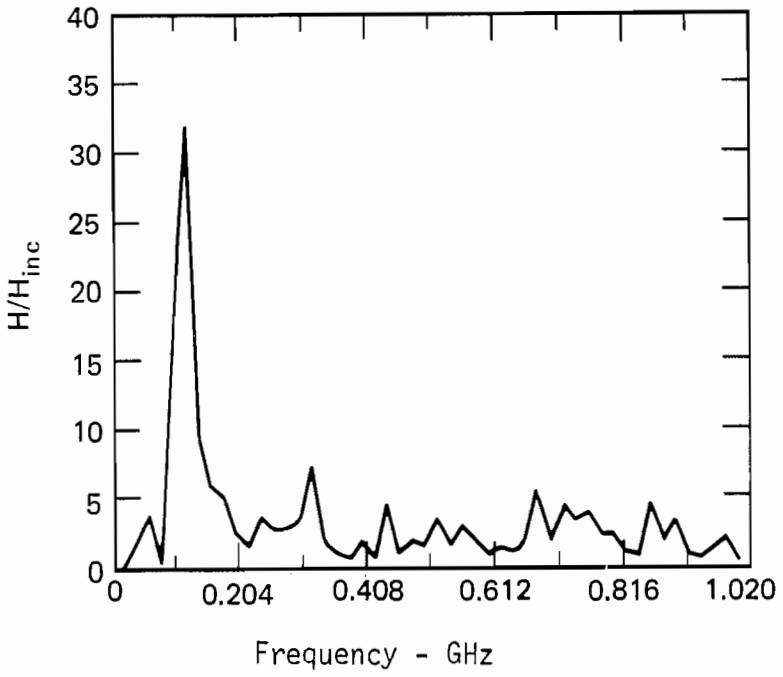

Figure E35. Magnitude of H/H_{inc} for crossed cylinder 1 m from ground plane ($\theta = 0°$).

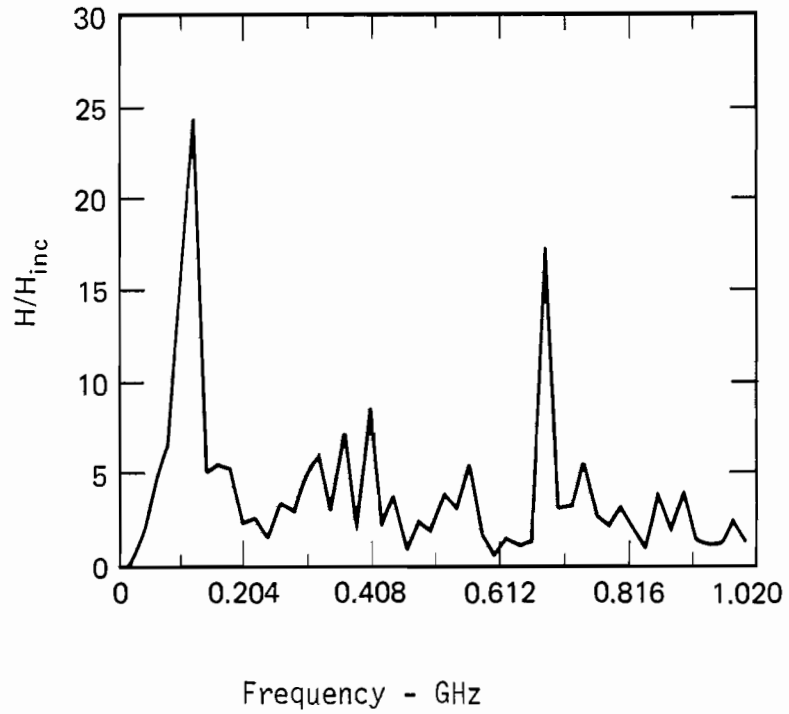

Figure E36. Magnitude of H/H_{inc} for crossed cylinder 2 m from ground plane ($\theta = 0°$).

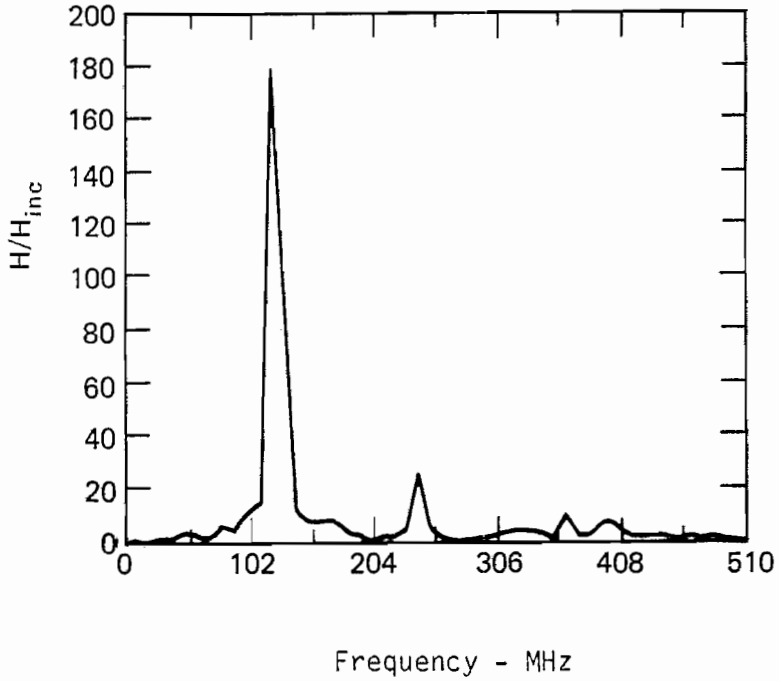

Figure E37. Magnitude of H/H_{inc} for crossed cylinder 17 cm from ground plane (θ = 180°).

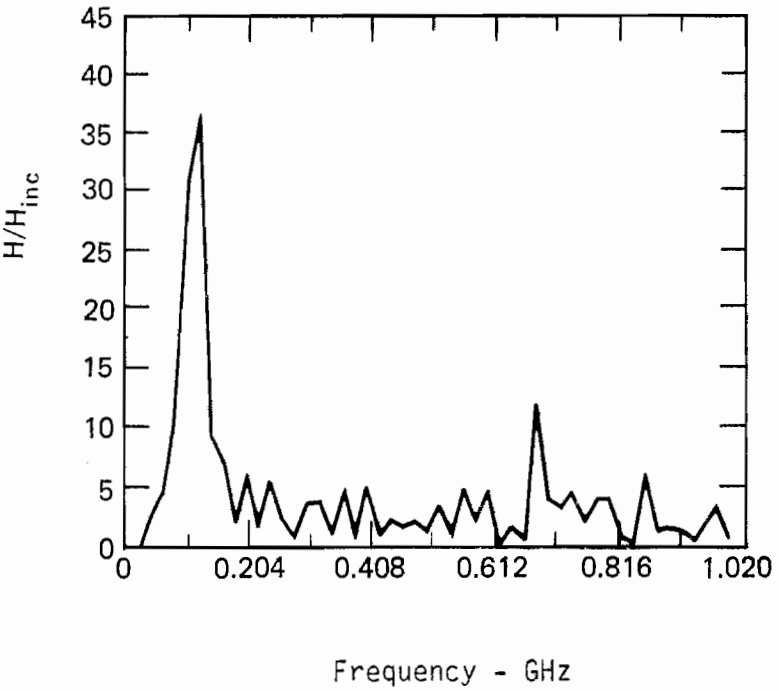

Figure E38. Magnitude of H/H_{inc} for crossed cylinder 50 cm from ground plane (θ = 180°).

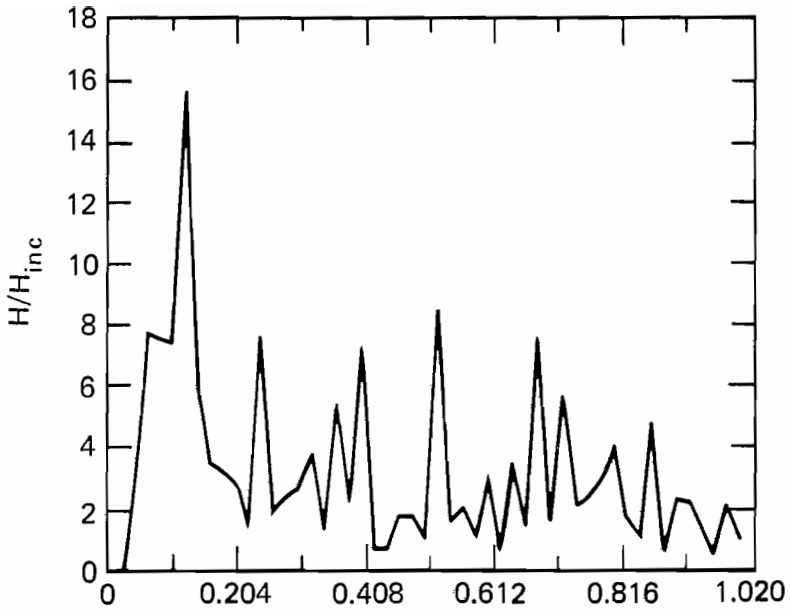

Figure E39. Magnitude of H/H_{inc} for crosed cylinder 1 m from qround plane (θ = 180°).

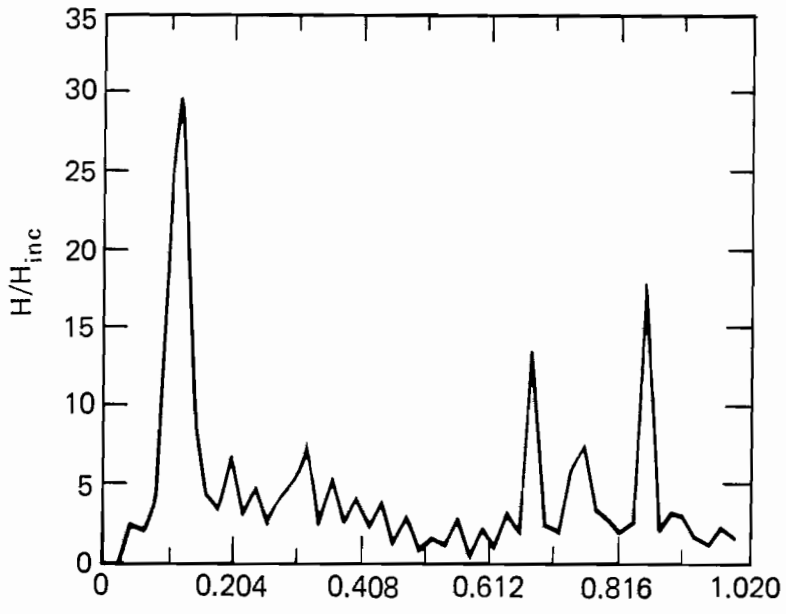

Figure E40. Magnitude of H/H_{inc} for crossed cylinder 2 m from ground plane (θ = 180°).

Appendix F
747 Scale-Model Aircraft Data

Two types of measurements were made on the aircraft model. The first was for a free-space configuration with the incident electric field parallel to the wings from the top. Charge measurements were made at the top of the wing tip and midway along the wing, while the surface current was measured at the same midwing point and at the wing root. The surface currents were also measured at the test point on the fuselage.

The other half of the 747 model was mounted as before. However, this time the sensor locations were formed on the bottom of the wing. The wheel wells were again closed and painted over, but the model was placed an equivalent distance from the ground plane as if it were sitting on its wheels. This placed the bottom of the fuselage at the wings 2 cm from the ground plane. With this configuration, it was necessary to run the coaxial cable from the $\dot{D}$ sensor at the wing tip along the top (incident field side) of the wing. We used a very thin section of the semirigid coaxial cable to connect the sensor, and covered the coaxial with the conductive copper tape. No noticeable change was observed if the coaxial section was covered or not.

The time-domain results of the free-space measurements are shown first in Figures F1 through F5 for each of the test points. As before, the temporal measurements were then transformed to the frequency domain to obtain the desired frequency-domain functions. These results are shown in Figures F6 through F10.

Figures F11 and F12 show the time-domain responses obtained for two specified test points with the model located over the perfect ground. For comparison, we also measured the model response with the ground plane removed. These waveforms are shown in Figures F13 and F14. (In all cases, only the first 20 ns of the response are shown.)

Finally, the time-domain waveforms were converted to the frequency domain and normalized to obtain the transfer functions, shown in Figures F15 through F18, which correspond to the ground plane and bottom side free-space results.

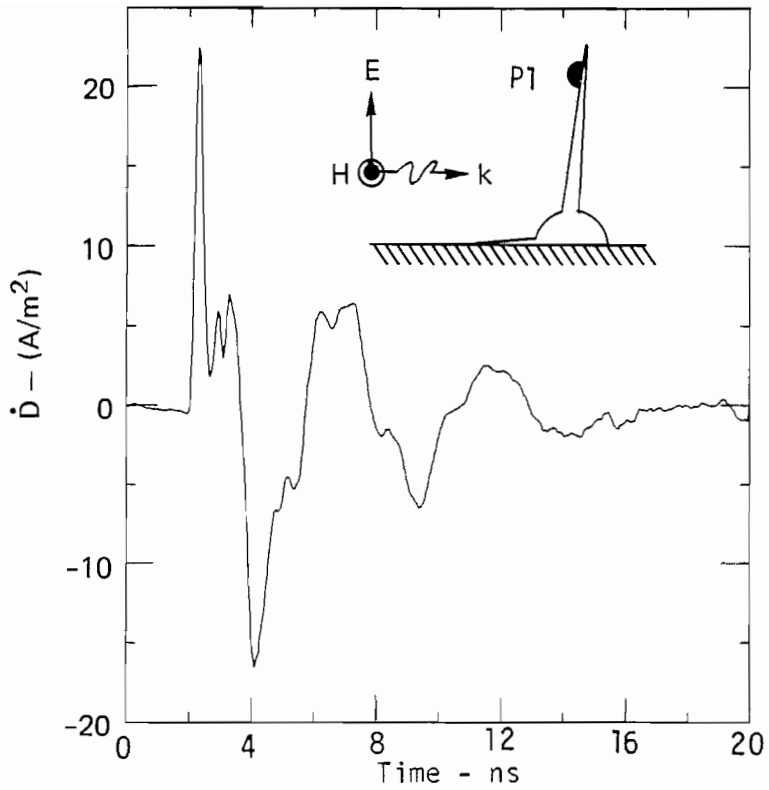

Figure F1. Transient $\dot{D}$ response for sensor located at wing tip with aircraft model in free space.

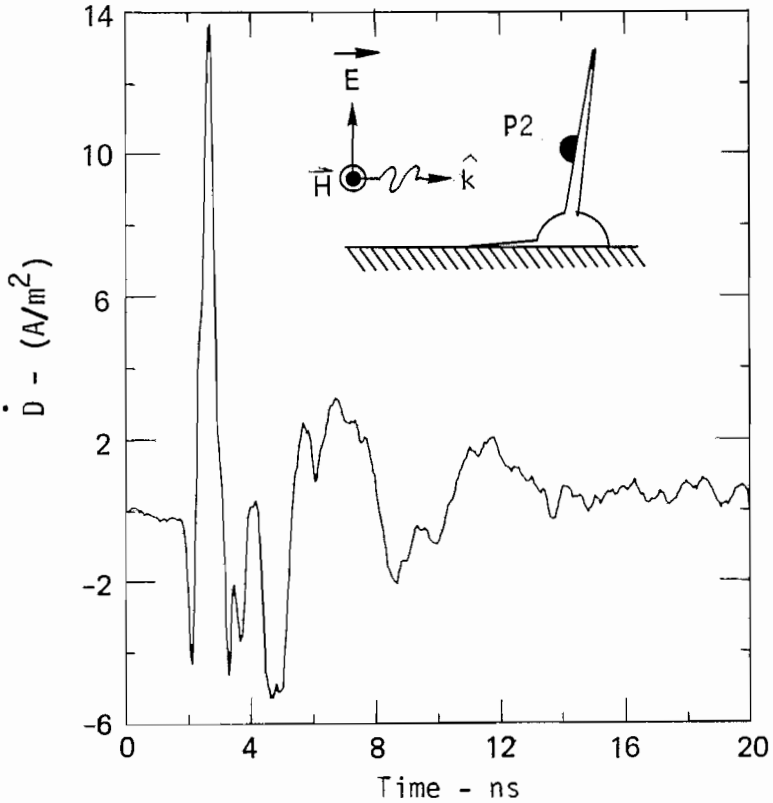

Figure F2. Transient $\dot{D}$ response for sensor located at top side, midwing with aircraft model in free space.

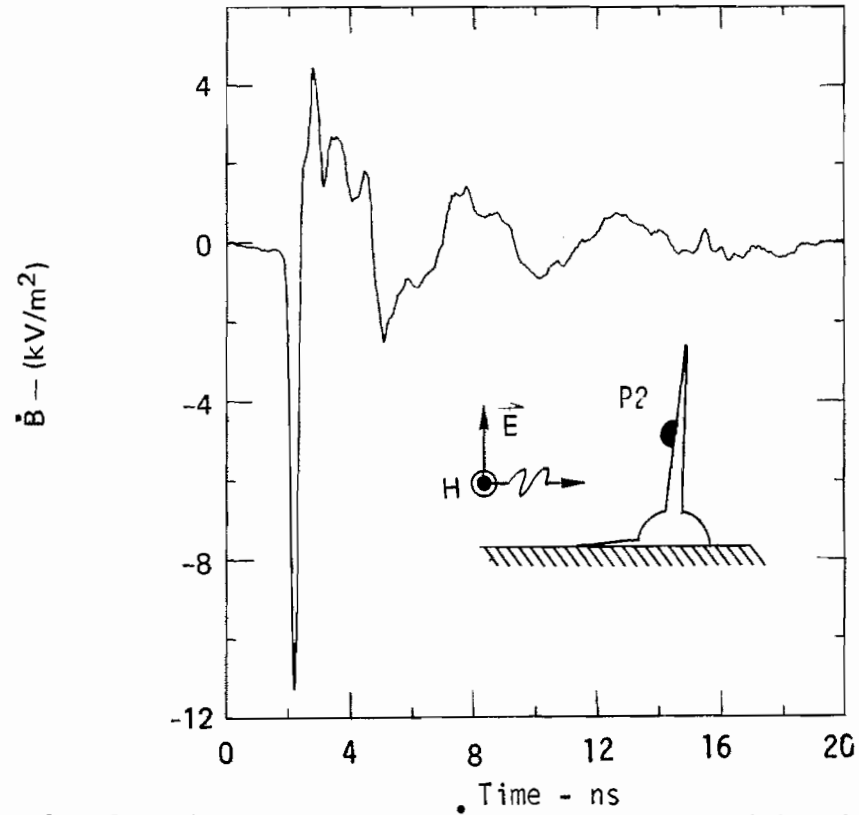

Figure F3. Transient response of $\dot{B}$ sensor at top midwing for model in free space.

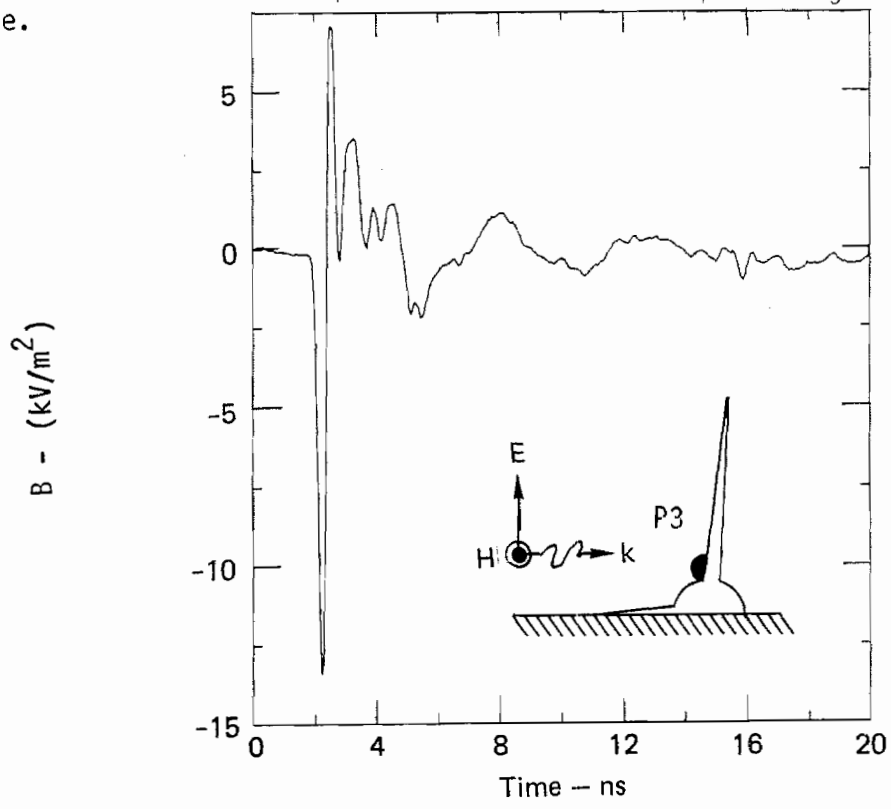

Figure F4. Transient response or $\dot{B}$ sensor at wing root for model in free space.

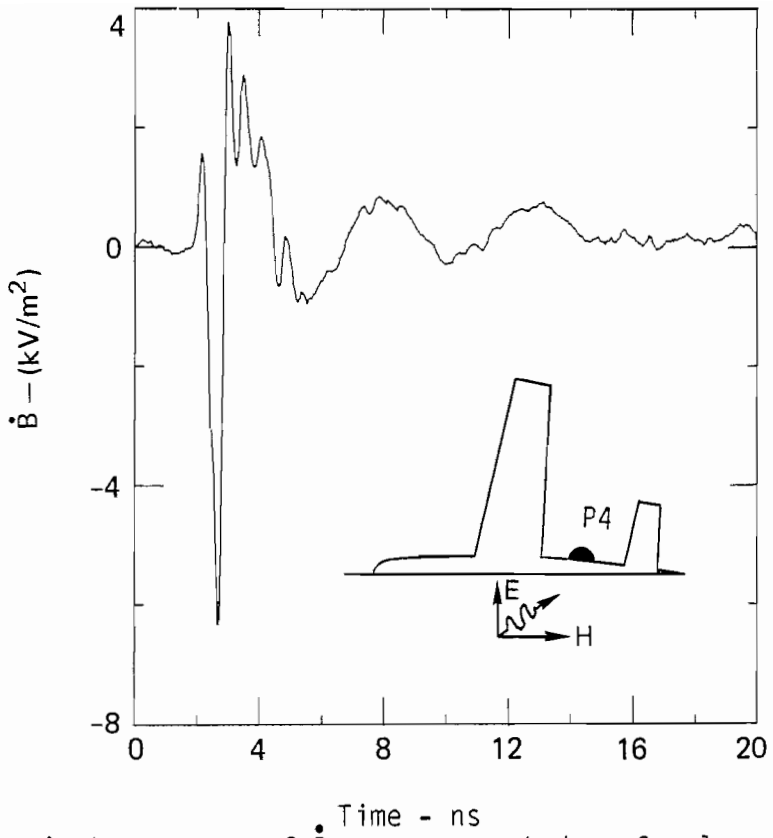

Figure F5. Transient response of $\dot{B}$ sensor mounted on fuselage for model in free-space.

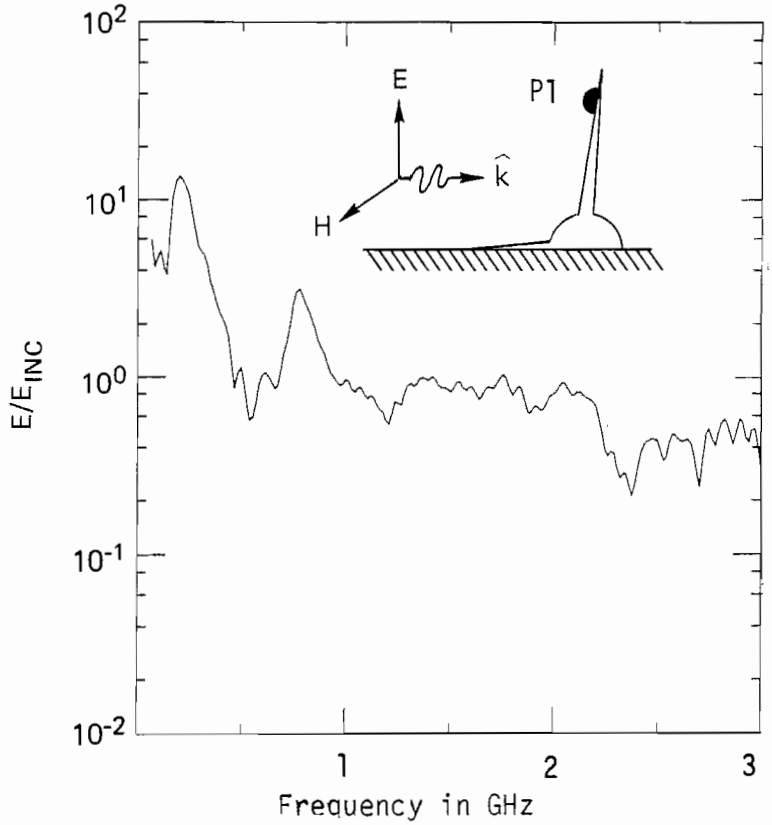

Figure F6. Magnitude of E/E_{inc} for sensor at wing tip. Aircraft in a free-space configuration.

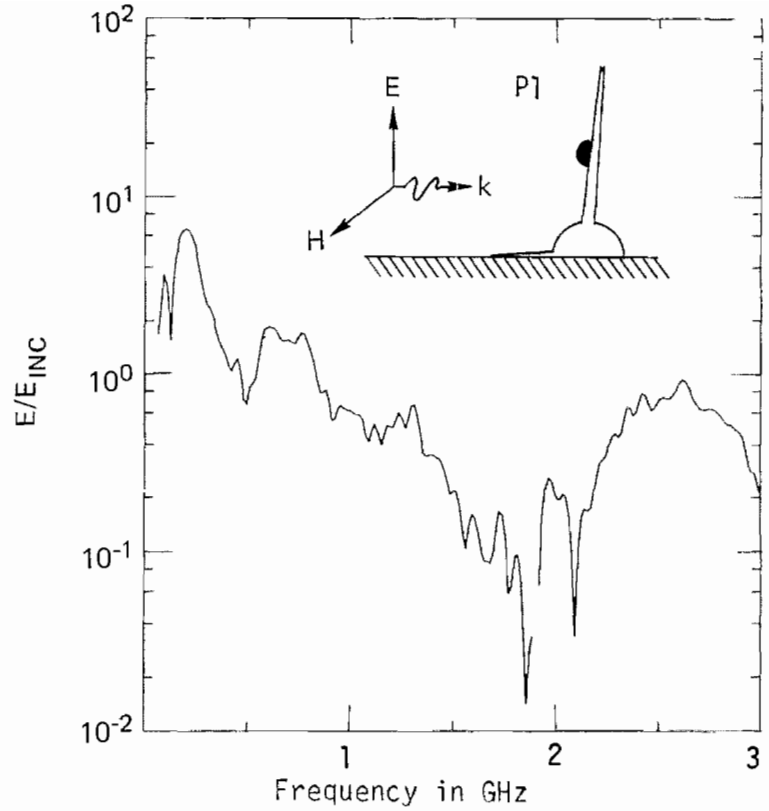

Figure F7. Magnitude of E/E_{inc} for a point midway on top of wing. Aircraft in a free-space mode.

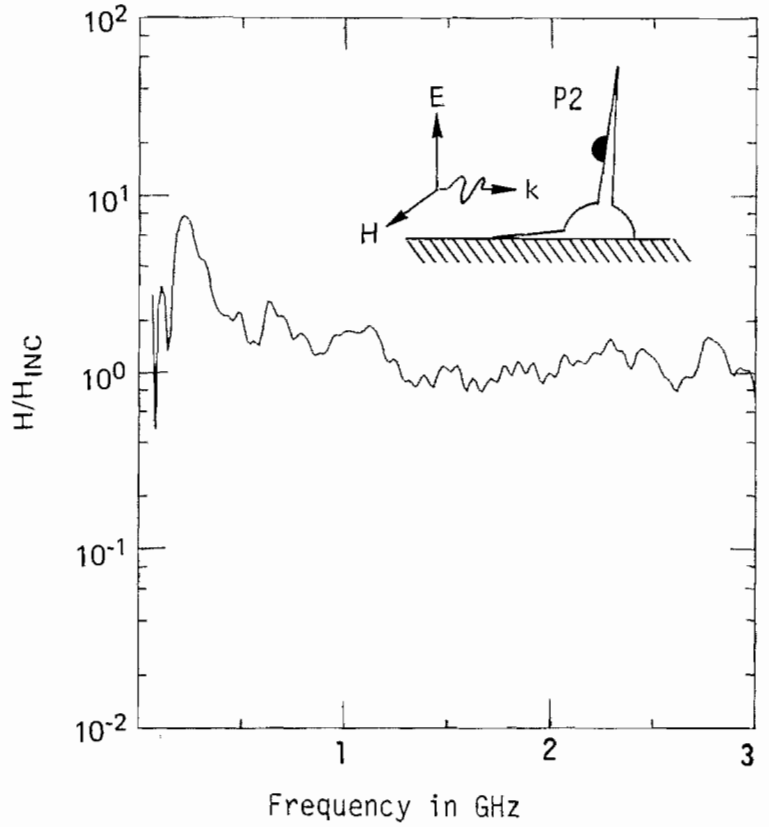

Figure F8. Magnitude of H/H_{inc} for a test point located on top of wing.

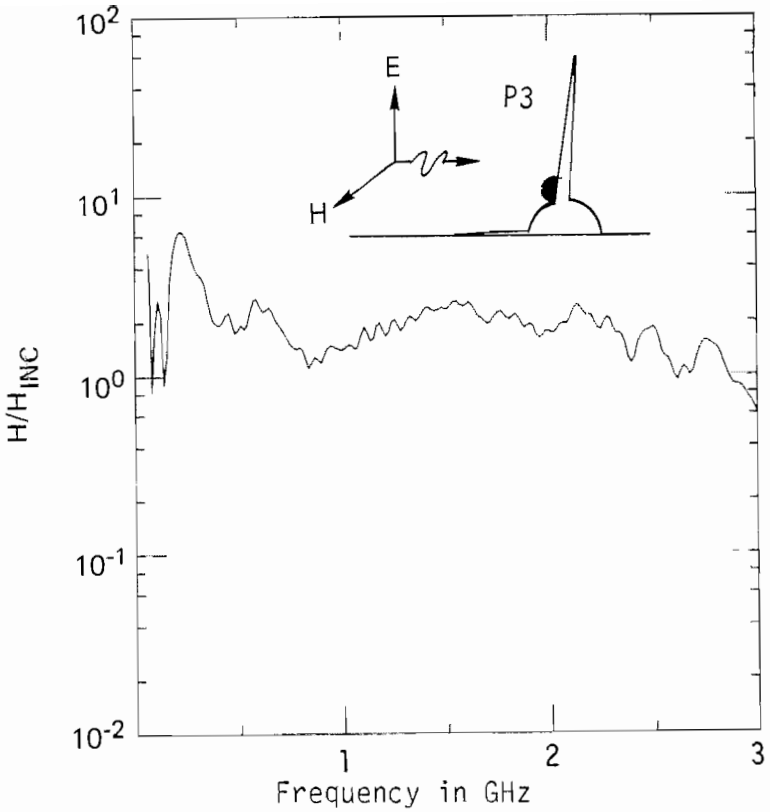

Figure F9. Magnitude of H/H_{inc} for test point located on top of wing root.

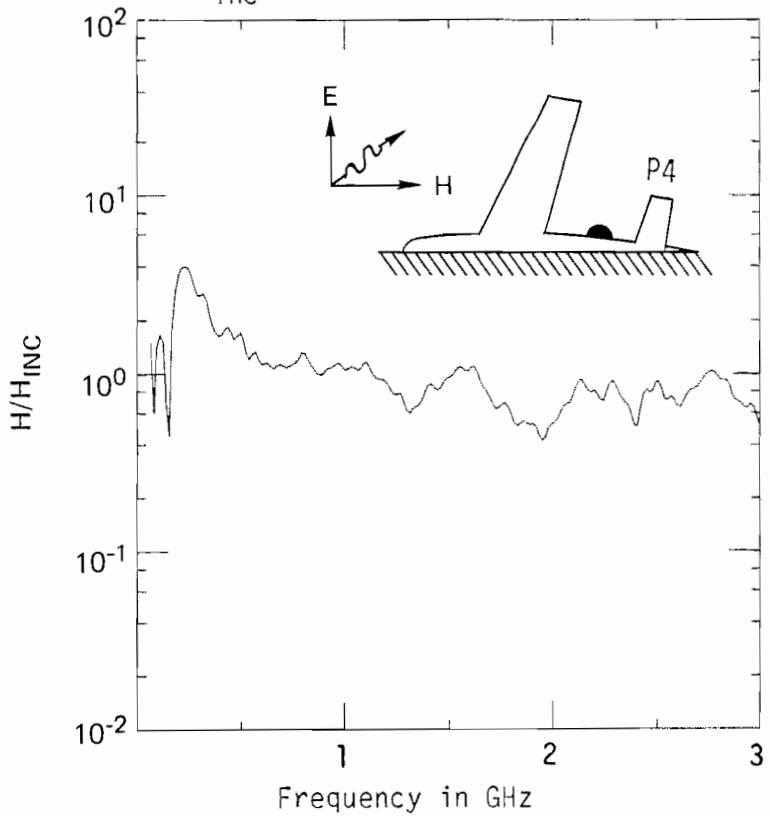

Figure F10. Magnitude of H/H_{inc} for test point on fuselage of 747 model. Aircraft in free space.

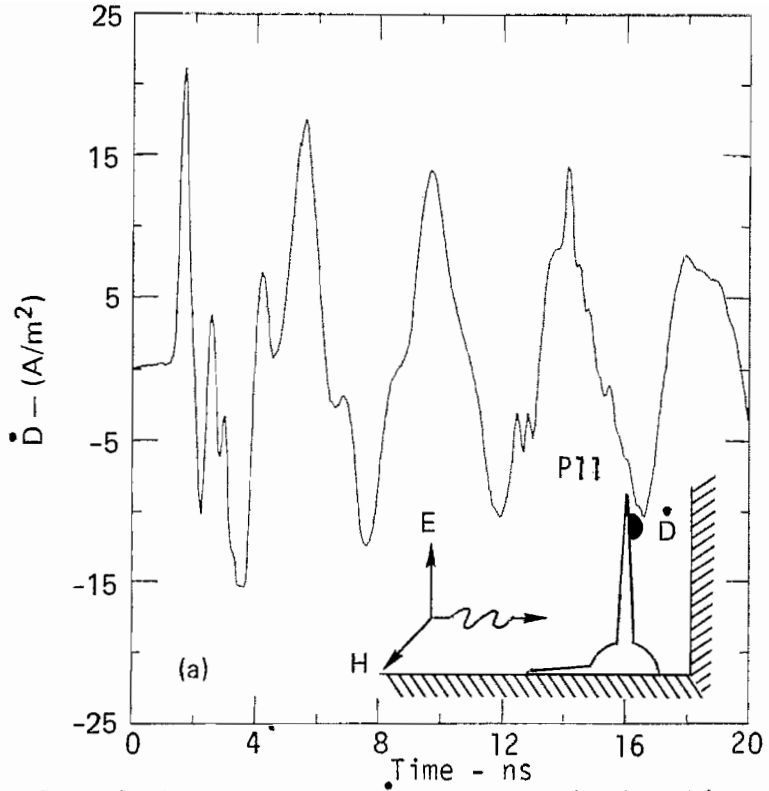

Figure F11. Transient response or $\dot{D}$ sensor on bottom tip of wing with aircraft over a perfectly conducting ground plane.

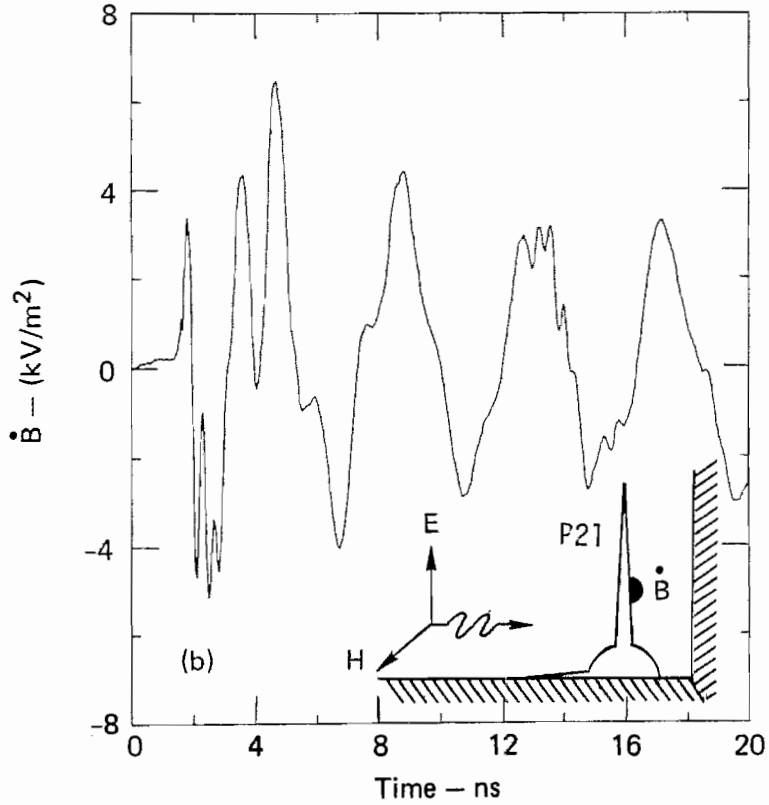

Figure F12. Transient response of $\dot{B}$ on bottom surface of wing with aircraft over a perfectly conducting ground plan.

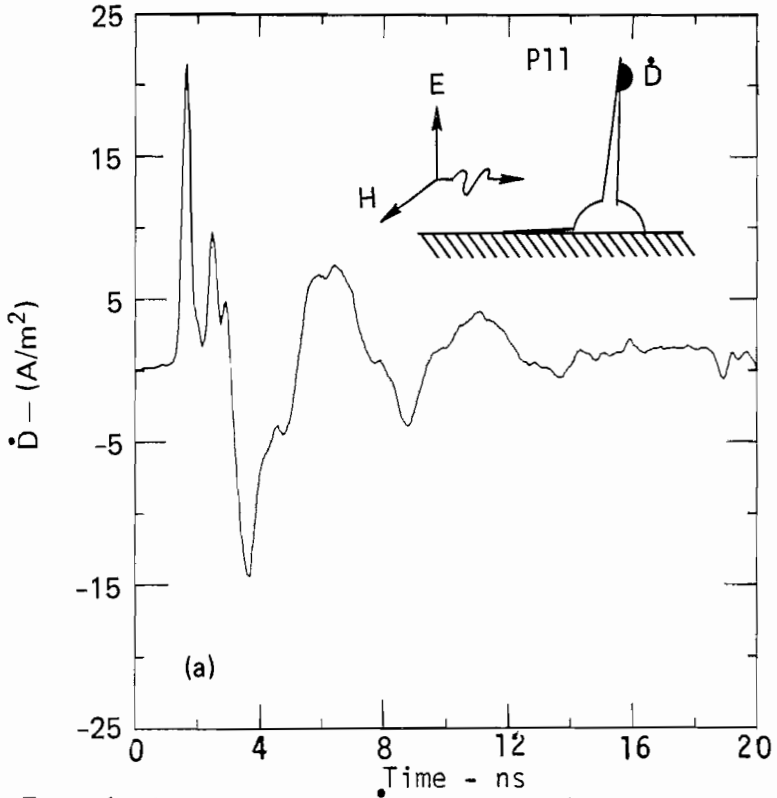

Figure F13. Transient response of $\dot{D}$ sensor on bottom tip of wing with aircraft in free-space mode.

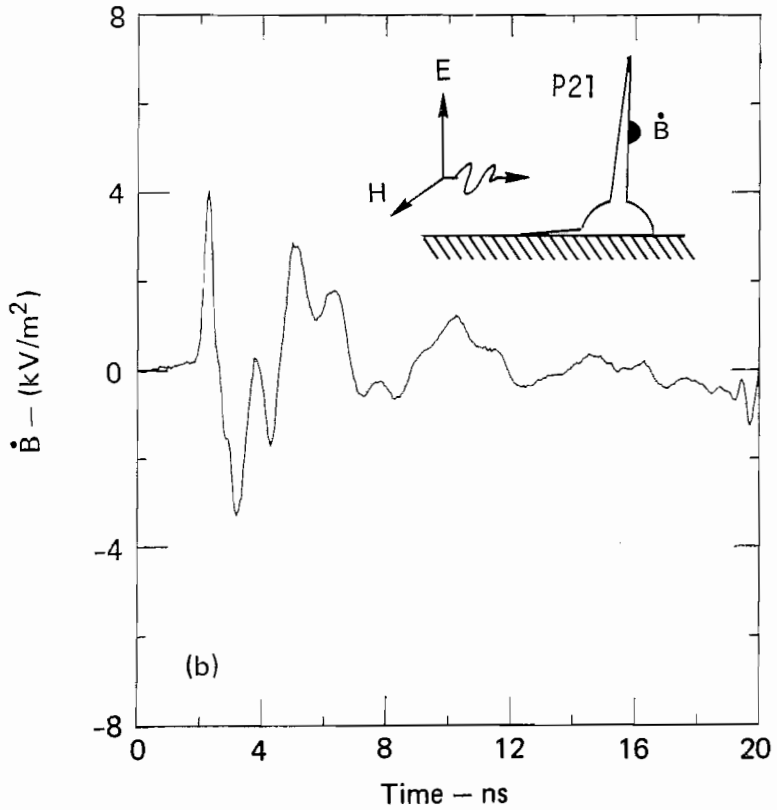

Figure F14. Transient response of $\dot{B}$ sensor on bottom surface of wing with aircraft in free-space mode.

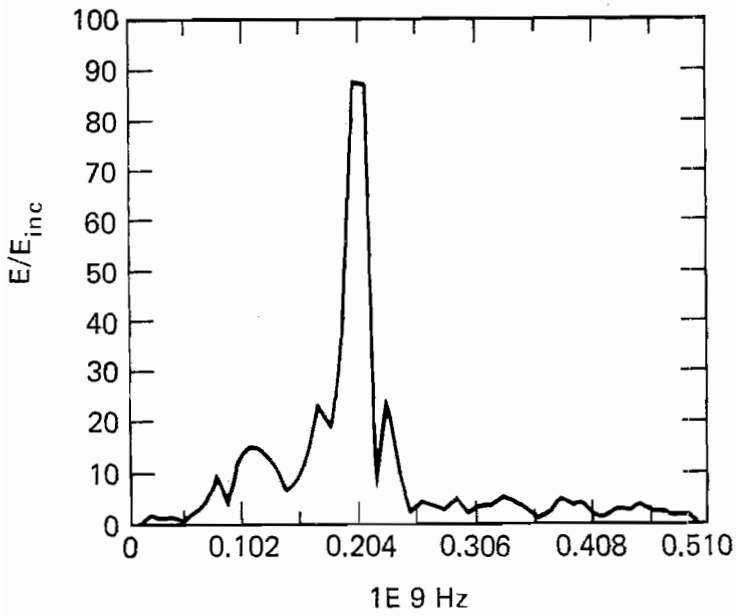

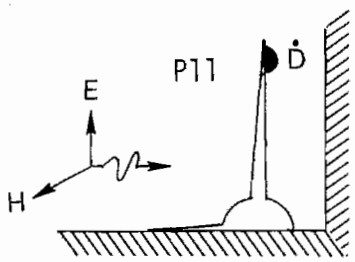

Figure F15. Magnitude of E/E_{inc} for $\dot{D}$ sensor on bottom of wing tip. Aircraft is over a perfectly conducting ground plane.

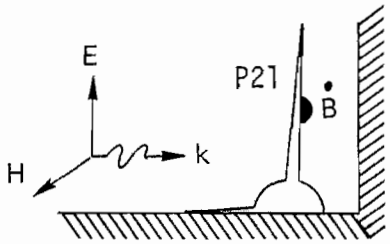

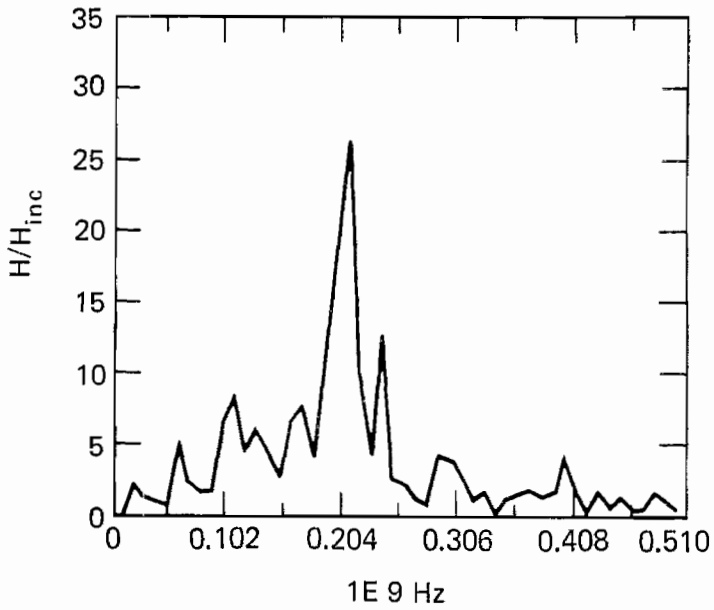

Figure F16. Magnitude of H/H_{inc} for $\dot{B}$ sensor at bottom surface midwing. Aircraft is over a perfectly conducting ground plane.

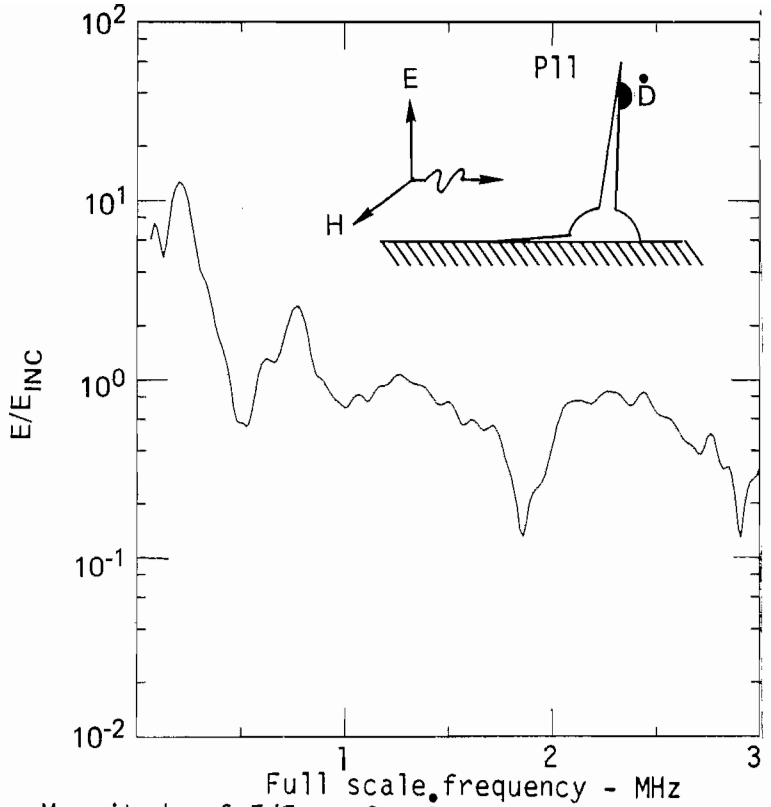

Figure F17. Magnitude of E/E_{inc} for D sensor on bottom of wing tip. Aircraft is in free space.

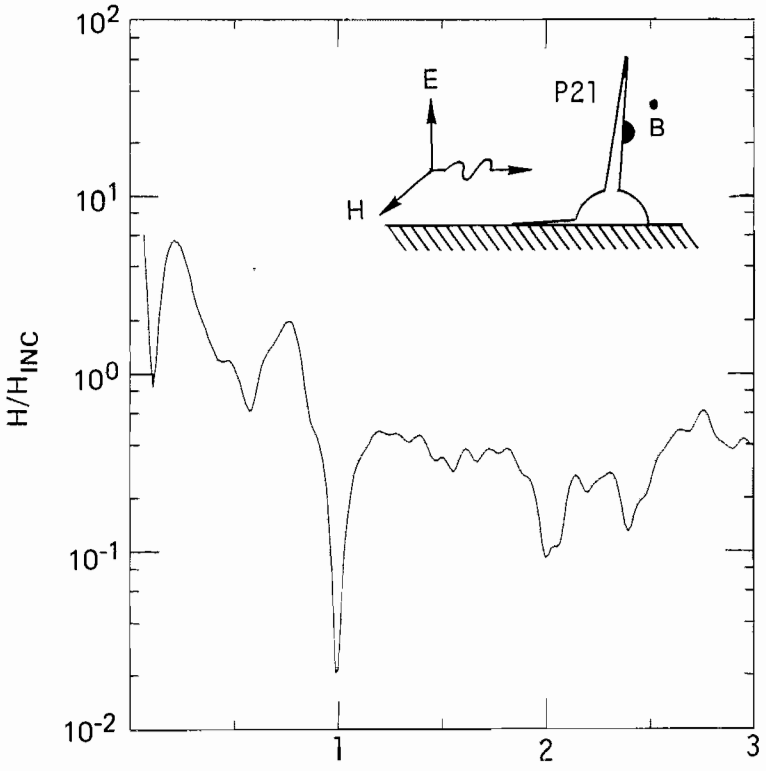

Figure F18. Magnitude of H/H_{inc} for B sensor at bottom surface midwing. Aircraft is in free space.

Appendix G

PRONY PROCESSING OF THE TRANSIENT DATA

The Singularity Expansion Method, (Ref. G1 and G2), and the use of Prony's algorithm (Ref. G3) to extract singulartities from transient time-domain data has seen considerable attention in electromagnetics during the past 3-4 years (Refs. G4 and G5). Basically, Prony's algorithm is a method of determining the coefficients α_i and S_i in the complex exponential series representation of a time series:

$$f(t_j) = \sum_{i=1}^{N} R_i e^{s_i t_j}, \qquad j = 1,\text{------}m^{th} \text{ time sample} \qquad (G1)$$

where the $s_i = \sigma + j\omega$ are the complex singularities or poles of the time function, and the R_i are the complex residues. The s_i's obtained from Prony's procedure have particular significance in electromagnetics because they are characteristic of the natural frequencies of oscillation found for bodies, such as the cylinder and the aircraft, when they are excited by an impulse of energy.

Once the complex $\left[R_i, s_i\right]$ pole-residue set is obtained, the corresponding frequency-domain response is given by the Laplace transform of the above time series representation:

$$F(S) = \sum_{i=1}^{N} R_i \Big/ (s - s_i) \qquad (G2)$$

Several computer programs have been written to do the Prony Processing of time-domain data, including the SEMPEX code used at LLNL (Ref. G6). All known Prony techniques, however, suffer from degraded performance if noise is present in the input data, particularly if the data is indiscriminately processed. At LLNL, work has been done on finding ways to minimize the detrimental effects of the noise on the Prony process. These techniques

include the use of prefilters to limit unwanted high-frequency noise content in the waveforms, and the use of multiple-run averaging to smooth out the effects of noise.

The latest program development has been incorporation of the Prony processor into a large general purpose data analysis program called GPDAP (Ref. G7). GPDAP runs on a committed mini computer system and has utilities such as fast Fourier transforms and filtering programs which allow the user to easily and quickly manipulate the process data and then plot the results on-line. The flexibility of this program, coupled with a high degree of interactivity, gives the user new insight into the application of the Prony program to process real experimental data, because the user can quickly see the outcome of his work and make any desired changes while the many paramenters are fresh in his mind. The results presented in the next subsections are those obtained with this new system.

References

G1. Baum, C. E., "On the Singularity Expansion Method for the Solution of Electromagnetic Interaction Problems," Air Force Weapons Laboratory, Kirtland AFB, NM, 1971, Interactions Note 88.

G2. Tesche, F. M., "On the Singularity Expansion Method as Applied to Electromagnetic Scattering from Thin Wires," Air Force Weapons Laboratory, Kirtland AFB, NM, 1972, EMP Interaction Note 102.

G3. Prony, R., "Essai Experimental et analytique sur les lois de la dilatabilitie des fluids elastiques et sur celles de la force expansive de la vapeur de l'eau it de l'alcool a differentes temperatures," in J. L'Ecole Polytechnique (Paris), 1, NO. 2, 24-76 (1975).

G4. Van Blaricum, M. L., and Mittra, R., "A Technique for extracting the Poles and Residues of a System Directly from Its Transient Response, "IEEE Trans, on Ant. and Prop., vol. AP-23, No. 6, November (1975), and Interaction Note 245 (1975).

G5. Miller, E., et al., Radar Target Classification Using Temporal-Mode Analysis, Lawrence Livermore National Laboratory, UCRL-51825 (1975).

G6. Lager, D. L., User's Manual for SEMPEX: A Computer Code for Extracting Complex Exponentials from a Time Waveform, Lawrence Livermore National Laboratory, for Air Force Weapons Laboratory, Kirtland AFB, NM, Mathematics Note 45.

G7. Posehn, M. R., Computer Based Transportable Data Ascquisition and Control System, Lawrence Livermore National Laboratory, UCRL-78339 (1976).

Prony Analysis for the Cylinder Model

Experimental measurements on the cylinder, crossed cylinder, and the scale-model 747 aircraft were all analyzed with Prony's method. In this subsection the results for the cylinder in free space and near a perfect ground are presented.

All of the measurements we performed were made on a plane of symmetry, which implies that only odd modes are excited by the incident field, as illustrated in Figure G1. I should be noted from this figure that some modes may not have large modal amplitudes at the point of observation used in these experiments; and, in fact, some of the modes may be unobservable or at least below the useful signal-to-noise ratio needed to obtain good results from the Prony processor. The transient response waveforms used for these Prony calculations were the direct $\dot{B}$ and $\dot{D}$ sensor outputs, and as such they were not normalized to the incident exciting field.

While all of the measurements obtained from this series of experiments could be analyzed by the Prony program, we have chosen a subset of the measurements for the response near a perfect ground plane to determine the effects of the nearby reflector. Additionally, measurements for the cases of 180° incidence were selected for the $\dot{B}$ and $\dot{D}$ sensors. Figures G2 (a), (b), and (c) illustrate the transient waveforms from the $\dot{B}$ sensor with the cylinder located 10 cm (2a), 50 cm (10a) and 2 m (40a) away from the ground plane, respectively.

The choice of the time-window to use for the Prony analysis depends upon several factors. First, because, the primary interest is finding the natural modes of the body, we select a free-response or undriven portion of the waveform after the incident pulse has passed. Second, to observe the effect of the ground plane, we must wait a time sufficient for the incident pulse to strike the body, reach the ground plane, and then reflect back to the body again. (This ground plane reflection can clearly be seen occurring at different times in Figure G2.) Finally, the duration of the measurment interval must be sufficiently long to allow a separation of closely spaced modes, the window of observation must be $\geq 1/\Delta f$.

These requirements mean that we can determine the effects of the ground plane for the cases of the object at 10 cm and 50 cm spacing of the ground plane, but are unable to analyze the cases of 1 m and 2 m because the measurement interval was insufficiently long to meet the observation period criteria. Instead, the case of the 2 m spacing is used as a free-space case for the period between the initial incident pulse and the reflected pulse from the ground plane.

To condition the time-domain waveform for Prony processing, the Fourier transform of the signal if first obtained. The spectrum is then truncated above a chosen cutoff frequency (2.08 GHz). Next, an inverse Fourier transform is made of the truncated data to get the signal back to a filtered time-domain waveform which is then used as the Prony input.

The Prony processor is then used on the filtered data to form a complex exponential curve fit to the time series data. This procedure determines first α_i's, which are the complex poles of the structure in conjugate pairs. With these poles and the original data, the complex residues, S_i, are computed to fit the time data. The primary interest here is in the location of the poles in the complex plane ($s = \sigma + j\omega$). For the cylinder, we show in Figures G3 (a) through (c) the location of the resulting poles in the upper left-half plane determined for the cases of the ground plane 10 cm, 50 cm away from the cylinder, and also the free space result. The pole locations result from a curve-fitting process where we intially asked for 30 pole terms to fit the data, and then selected closely grouped clusters of significant poles by drawing boxes around the clusters, as shown in Figure G4. Here each dot on the plot represent a pole location, and the cluster result from 10 separate curve fits to the time data using a sliding-window approach. All of the poles that fall within the boxes are averaged to give a mean pole location. These mean pole locations are indicated by the dots in Figures G3 (a) through (c), and the boxes drawn around the poles are the variances of the poles in both frequency and damping. Note that generally the variance in the value of the damping coefficient is much larger than the variance in the complex frequency of the pole.

Once the significant poles are selected, they are used in the curvefitting process to compute the residues (S_i). The values of the poles and residues for the three cases of the $\dot{B}$ sensor on the cylinder are tabulated in Table G1.

Figure G5 shows a composite plot of the poles for the three cases analyzed. The two lowest-order pole sets are well behaved, while the results for frequencies above 500 MHz are quite scattered. The trend, however, can be seen as the cylinder nears the ground plane.

Once the poles and residues are found, they may be used in the complex exponential series representation of the time waveform. We can see how well the curve fit preforms by examining the plots shown in Figures G6 (a) through (c), which show both the original data (solid curve) and the curve computed form the poles and residues (dotted curve).

In a manner very similar to that used for the $\dot{B}$ measurments, the $\dot{D}$ measurements on the cylinder were also analyzed with Prony. The same cases were run, and the reader can refer back to the measurements section on the cylinder to see the transient waveforms used here. Again, 30 poles were initially requested in the curve-fitting process, and 10 sample data were made to form pole clusters. The resulting pole plots are shown in Figures G7 (a) through (c) for the two ground-plane spacings and the free space case. The poles and residues are also tabulated in Table G2 for the $\dot{D}$ sensor on the cylinder, along with a composite pole plot for the three cases shown in Figure G8. To see how well the selected poles fit the input waveform, the reconstructed curves are shown along with the input in Figures G9 (a) through (c).

Prony Analysis for the Crossed Cylinder Model

In addition to the cylinder, Prony's method was also used on the experimental measurements obtained for the crossed cylinder. Again a selction of the runs in the presence of a perfectly conducting ground plane was made. The cases of $\theta = 180$ incidence with the $\dot{B}$ and $\dot{D}$ sensors were also selected, as with the cylinder. Figures G10 (a) through (c) show the transient $\dot{B}$ waveforms, while Figures G11 (a) through (c) show the analogous measurements for the $\dot{D}$ sensor.

TABLE G1.

POLE VALUES FOR CYLINDER $\dot{B}$ SENSOR (θ = 180°).

Pole No.	h = 10 cm ground plane			h = 50 cm ground plane			Free space, no ground plane		
	Pole			Pole			Pole		
	Nepers x 10^6	Hz x 10^6	Residue	Nepers x 10^6	Hz x 10^6	Residue	Nepers x 10^6	Hz x 10^6	Residue
1	- 22.9	±j105.2	0.015	- 74.0	± j86.1	0.014	- 99.6	± j114.7	0.10
2	- 63.7	±j367.9	0.014	-258.9	±j389.3	0.033	-297.3	± j387.3	0.013
3	-374.8	±j592.6	0.048				-943.3	± j670.1	0.42
4	-237.3	±j793.4	0.0008	-257.4	±j713.6	0.015	-660.9	± j871.4	0.10
5				-194.3	±j996.2	0.0066	- 23.1	±j1134.0	0.002
6							-257.2	±j1473.0	0.017

TABLE G2.

POLE VALUES FOR CYLINDER $\dot{D}$-SENSOR (θ = 180°).

Pole No.	h = 10 cm ground plane			h = 50 cm ground plane			Free space, no ground plane		
	Pole			Pole			Pole		
	Nepers x 10^6	Hz x 10^6	Residue	Nepers x 10^6	Hz x 10^6	Residue	Nepers x 10^6	Hz x 10^6	Residue
1	-11.9	$\pm$j115.4	0.0125	-22.9	$\pm$j94.6	0.013	-177	$\pm$j95.9	0.012
2	-108.7	$\pm$j365.5	0.0052				-1606	$\pm$j335	4.638
3	-350.6	$\pm$j594.3	0.053	-395	$\pm$j64	0.067	-655	$\pm$j642	0.110
4				-269	$\pm$j947	0.017	-579	$\pm$j982	0.062
5				+29.7	$\pm$j1310	0.00035	-568	$\pm$j1339	0.043
6				-1313	$\pm$j1570	63.95	-802	$\pm$j1655	0.066
7				-167	$\pm$j1737	0.0036			

As with the cylinder measurements, the Fourier transforms of the time data were truncated above 2 GHz and then inverse transformed to provide filtered time-domain data for the Prony program. The results of the prony analysis are presented next.

For each of the $\dot{B}$ measurements, a 30-pole curve fit was selected, and the results for a 10-run sliding window were plotted on one pole plot to indicate clustering if the pole locations. The cases where the ground plane was located 10 cm and 50 cm away from the model were used as ground-plane measurements, while the case where the ground plane was located 2 m away form the model was used as the free-space measurement because relection back from the ground plane did not occur during the data time interval used for the Prony processor. Figures G12 (a) through (c) show the pole plots along with the variance in the pole locations for the three cases. Table G3 is a tabulation of the mean pole values along with their residues. These poles are all plotted in Figure G13. The reconstructed $\dot{B}$ waveforms using the selected poles are shown in Figures G14 (a) through (c).

Analysis for the $\dot{D}$ sensor output on the crossed cylinder follow the same path as those before. Figure G15 (a) through (c) show the pole plots for the individual measurements. Table G4 summarizes the mean pole values found, while the composite plot of Figure G16 shows the poles for all three runs. The reconstructed waveforms using the poles and residues are shown in Figures G17 (a) through (c).

Prony Analysis of the 747 Aircraft Model Measurements

Included in the time-domain measurements were two experiments performed on a 1:100 scale model of a 747 aircraft. The configuration of the experiments is shown in Figure G18 where we measured the surface charge density on the bottom of the wing tip and the axial surface current density on the bottom of the wing midway between the wing tip and the fuselage. These two measurements were repeated for the case where the aircraft would be located the same distance above the ground plane as it would with the wheels down, and the case where the ground plane was removed for a free-space measurement. In both cases the wheels were up and the wheelwell doors were closed and painted over with silver conductive paint.

TABLE G3.

POLES AND RESIUDES FOR CROSSED CYLINDER $\dot{B}$ SENSOR ($\theta = 180^{\circ}$).

Pole No. No.	h = 10 cm ground plane			h = 50 cm ground plane			No ground plane-free space		
	Pole		Residue Magnitude	Pole		Residue Magnitude	Pole		Residue Magnitude
	Nepers x 10^6	MHz x 10^6		Nepers x 10^6	MHz x 10^6		Nepers x 10^6	MHz x 10^6	
1	25.6	$\pm$j123.7	0.006	-151	$\pm$j79.68	0.023	- 152	$\pm$j111.5	0.012
2	37.1	$\pm$j386	0.006	-159	$\pm$j371	0.0069	- 273	$\pm$ 341.5	0.0066
3	-973	$\pm$j642	1.25	-401	$\pm$j664	0.066	- 324	$\pm$j733	0.0064
4	-319	$\pm$j866	0.010	-230	$\pm$j886	0.013	-1273	$\pm$j980.8	0.692
5	-336	$\pm$j1275	0.005	-353	$\pm$j1060	0.024	- 412	$\pm$j1121	0.0066
6	-448	$\pm$j1390	0.029	-652	$\pm$j1453	0.245	- 514	$\pm$j1453	0.014
7				-313	$\pm$j1794	0.019	- 612	=j1617	0.016
				-274	$\pm$j1968	0.009			

TABLE G4.

CROSSED CYLINDER POLES AND RESIDUES $\dot{D}$ SENSOR ($\theta = 180^\circ$).

Pole No.	h = 10 cm ground plane		Residue	h = 50 cm ground plane		Residue	No ground plane-free space		Residue
	Poles x 10^6			Poles x 10^6			Poles x 10^6		
1	- 82	$\pm$j129.9	0.022	- 54	$\pm$j92.5	-	-40.9	$\pm$j123.1	0.0057
2	-694	$\pm$j609.3	0.636	-439	+j659	-	-1015	$\pm$j558.2	0.727
3	-174	$\pm$j995.5	0.005	-342	$\pm$j951	-	- 668	$\pm$j942	0.099
4	905.	$\pm$1378	0.213	-968	$\pm$j1260	-	64.6	$\pm$j768	0.0028
5	201	$\pm$j1887	0.005				- 884	$\pm$j1286	0.200
6							-1187	$\pm$j1810	0.046
7							-1.685	$\pm$j1369	0.0003

The Prony poles for the surface charge density on the wing tip were determined first. Forty data points between 0.35 and 12.7 μs were used as input to Prony, and the process was repeated over 10 data windows as with the cylinder and crossed cylinder. The resulting multiple-pole plots for the upper left-half plane are shown in Figures G19 (a) and (b) for the cases of the aircraft on the ground and in free space. The boxes are shown drawn around the most dominant pole clusters, and the mean values of the boxed poles are used to calculate the residues. These results are tabulated in Table G5. The resulting fit to the sampled data is shown in reconstructed curves in Figures G20 (a) and (b), where the solid line represents the original data and the dotted curve is the resulting curve fit.

Finally, the measured results for the B sensor on the mid-location of the aircraft wing were analyzed.

The Prony cluster plots are shown in Figure G21 (a) and (b) where we have selected the two low-order dominant poles. The mean values of the poles and their residues are tabulated in Table G6. To show how well these two poles the measured data, the waveform reconstructed is shown last in Figures G22 (a) and (b).

TABLE G5

PRONY POLES FOR FULL-SCALE 747 MODEL ON THE GROUND AND IN FREE SPACE
THESE POLES ARE FOR THE CHARGE DENSITY ON THE BOTTOM SURFACE WING TIP

	747 Aircraft on ground			747 Aircraft in free space		
Pole No.	Pole Real -meganepers	Pole Imag-MHz	Residue magnitude	Pole No.	Pole Real-meganepers	Pole Imag-MHz	Residue magnitude
1	-0.229	±j2.30	0.2863	1	-1.74	±j2.17	0.2704
2	-2.27	±j5.19	0.382	2	- .88	±j5.62	0.0315
3	-1.70	±j5.30	0.1744	3	-2.20	±j7.73	0.0778

TABLE G6

POLES AND RESIDUES FOR FULL-SCALE 747 AIRCRAFT ON THE GROUND AND IN FREE SPACE.
RESULTS ARE FOR CURRENT DENSITY MEASUREMENT ON BOTTOM OF AIRCRAFT WING.

	747 Aircraft on ground				747 Aircraft in free space		
Pole No.	Pole Real-Nepers X 10^6	Pole Imag-MHz	Residue magnitude	Pole No.	Pole Real-Nepers X 10	Pole Imag MHz	Residue magnitude
1	- .325	±j2.31	0.018	1	-1.47	±j2.11	0.017
2	-2.34	±j7589	0.016	2	-4.48	±j7.75	0.010

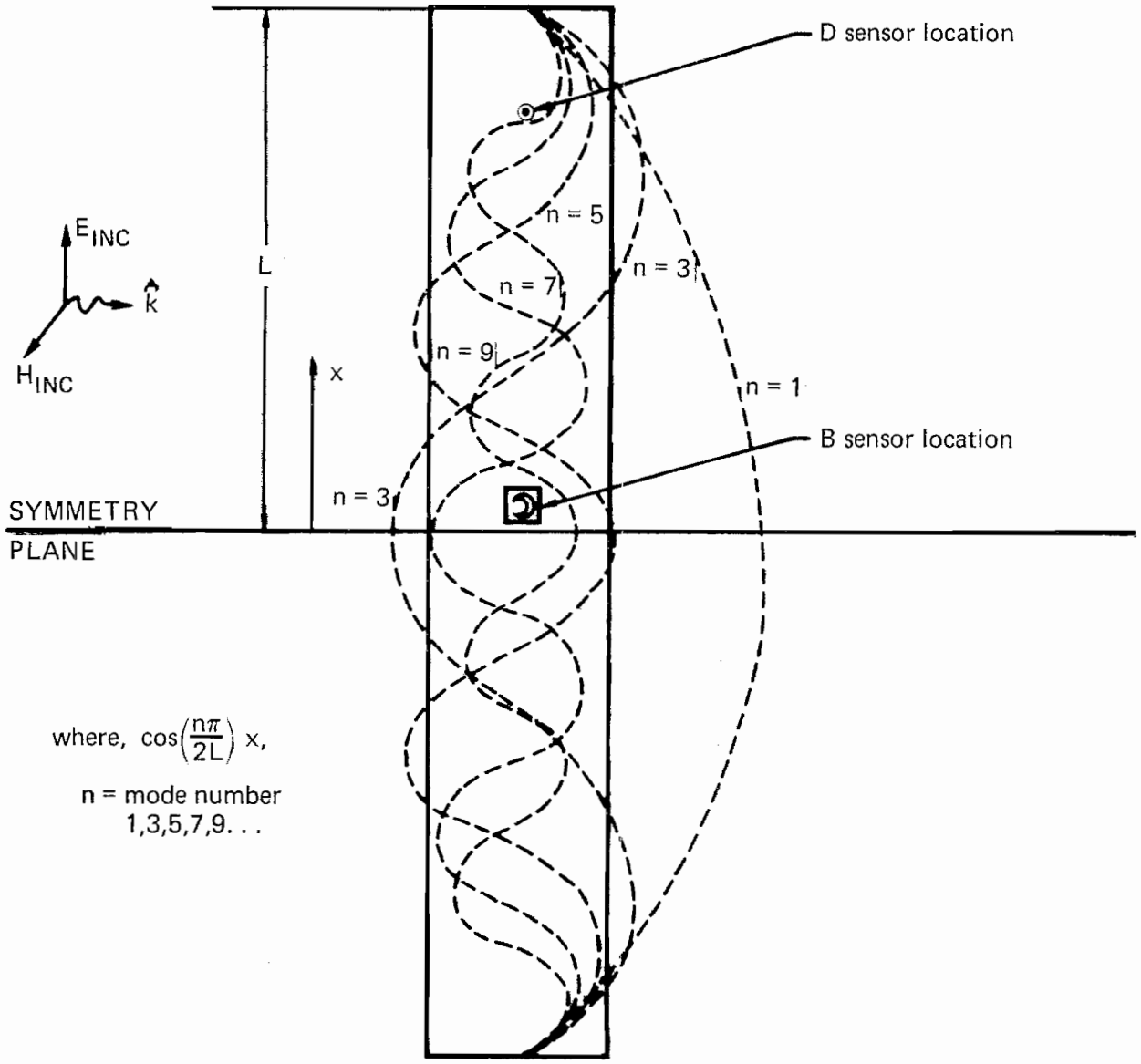

Figure G1. Current modes on cylinder over a symmetry plane.

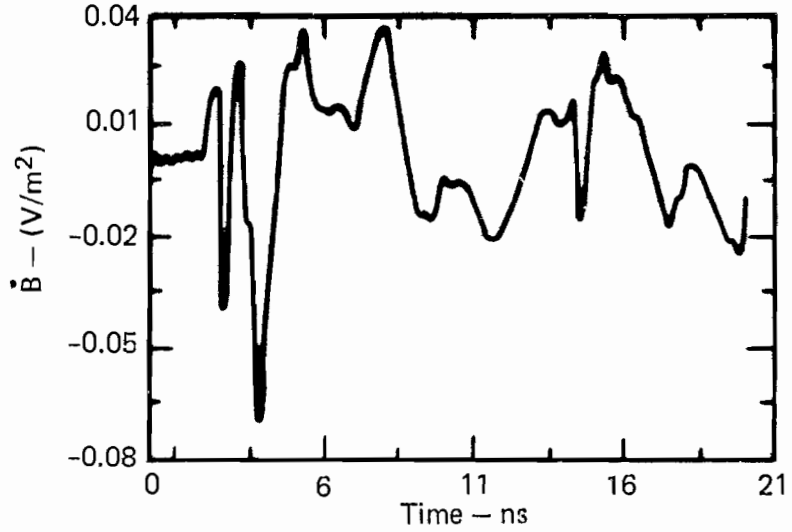

Figure G2. (a) $\dot{B}$ sensor response for cylinder 10 cm from ground plane (θ = 180°).

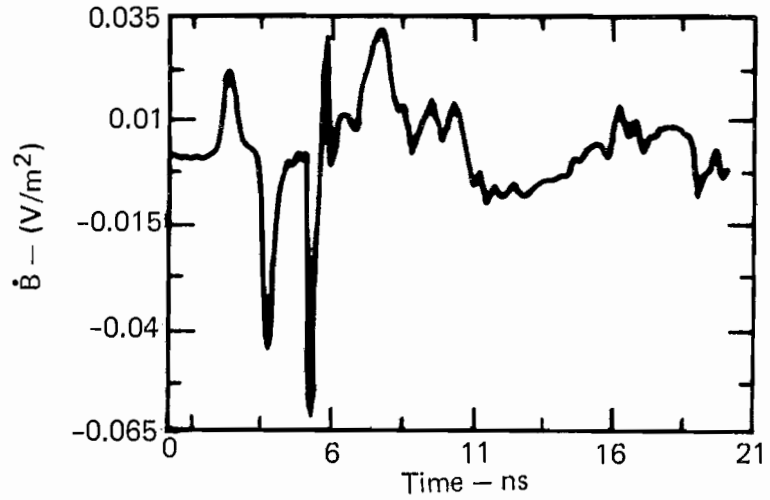

Figure G2. (b) $\dot{B}$ sensor response for cylinder 50 cm from ground plane (θ = 180°).

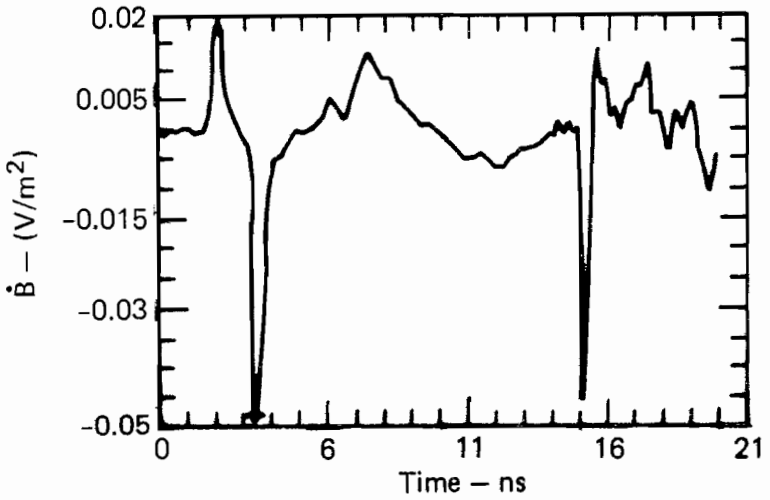

Figure G2. (c) $\dot{B}$ sensor response for cylinder 2 m from ground plane (θ = 180°).

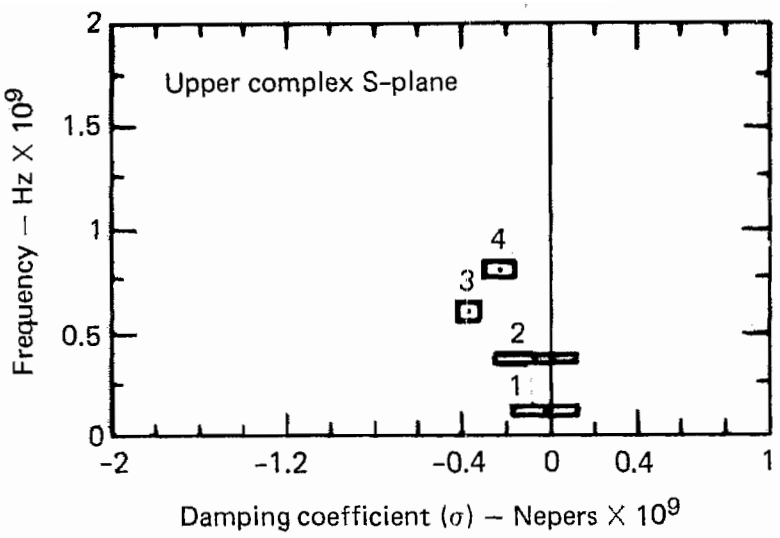

Figure G3. (a) Mean $\dot{B}$ pole locations for cylinder 10 cm from perfectly conducting ground plane ($\theta = 180^\circ$).

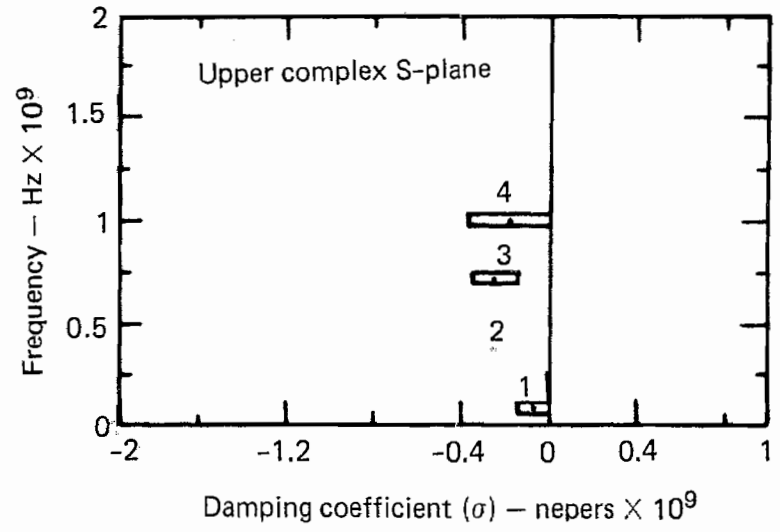

Figure G3. (b) Mean $\dot{B}$ pole locations for cylinder 50 cm from perfectly conducting ground plane ($\theta = 180^\circ$).

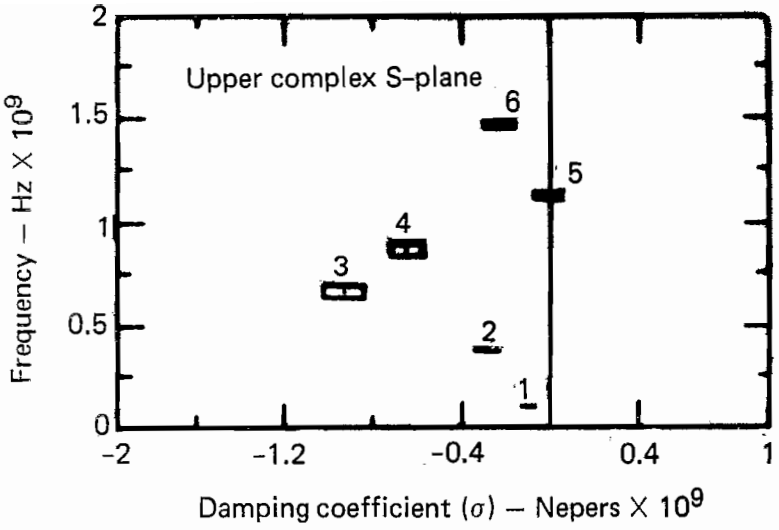

Figure G3. (c) Mean $\dot{B}$ pole locations for cylinder 2 m from perfectly conducting ground plane (θ = 180°). (Note: This case corresponds to the "free-space" $\dot{B}$ configurations.)

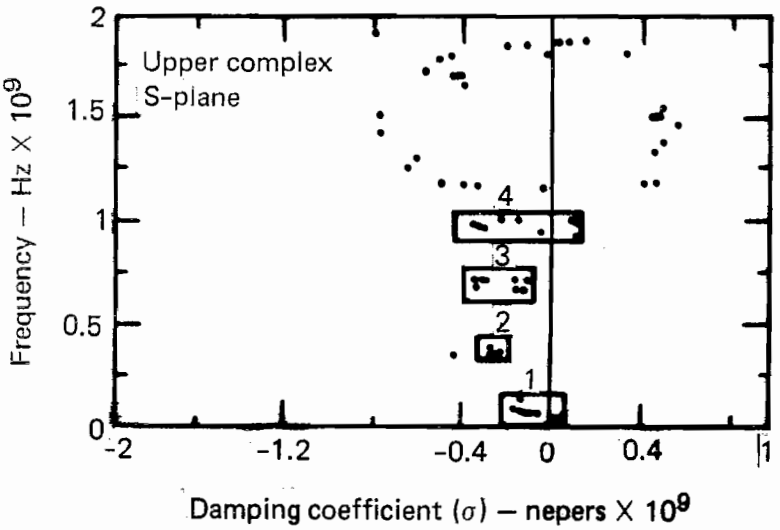

Figure G4. Plot of pole locations in complex plane. Boxes are shown drawn around pole clusters.

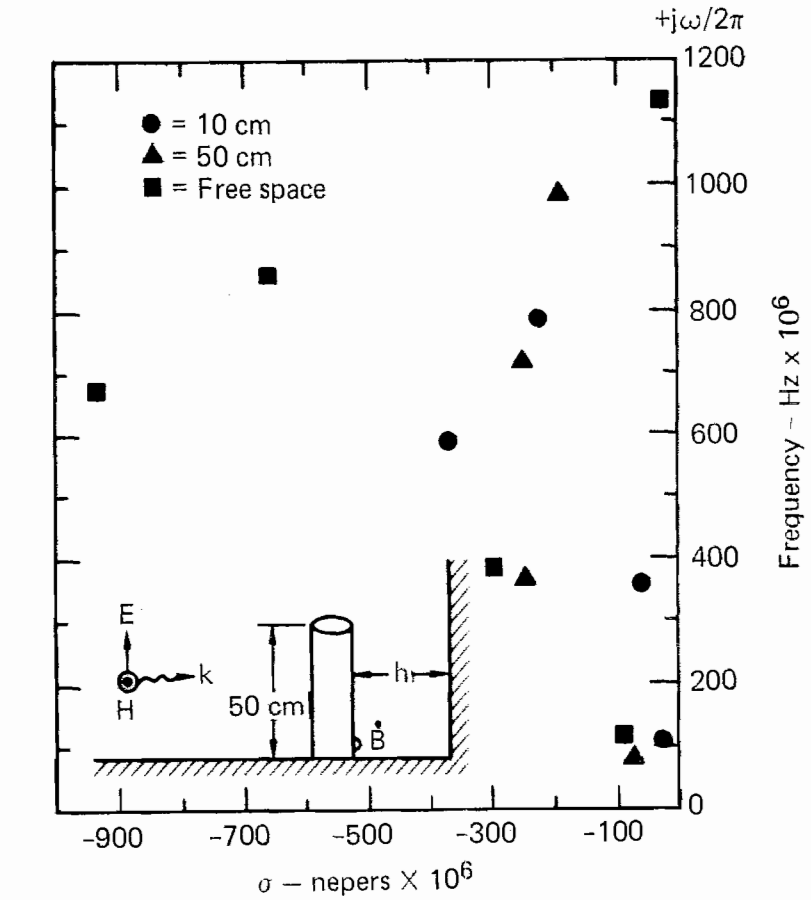

Figure G5. Composite plot of poles found for the cylinder. These results are for the $\dot{B}$ sensor.

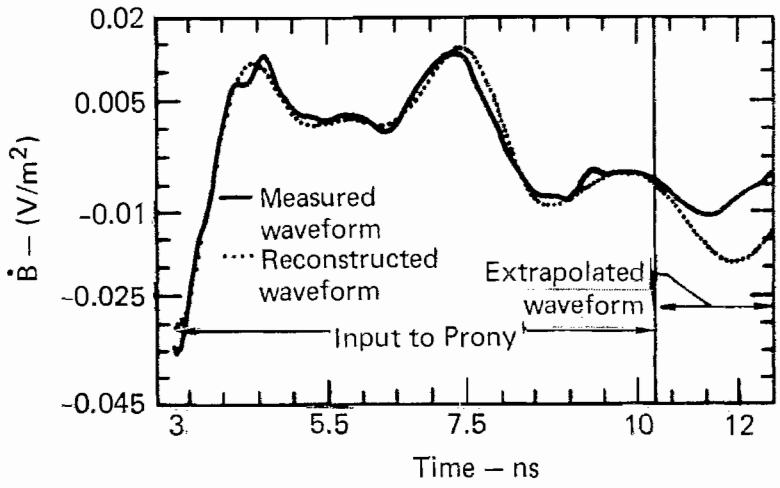

Figure G6. (a) Measured and reconstructed waveforms, showing portions of waveform used as input to Prony, and the extrapolated waveform based on the computed poles and residues.

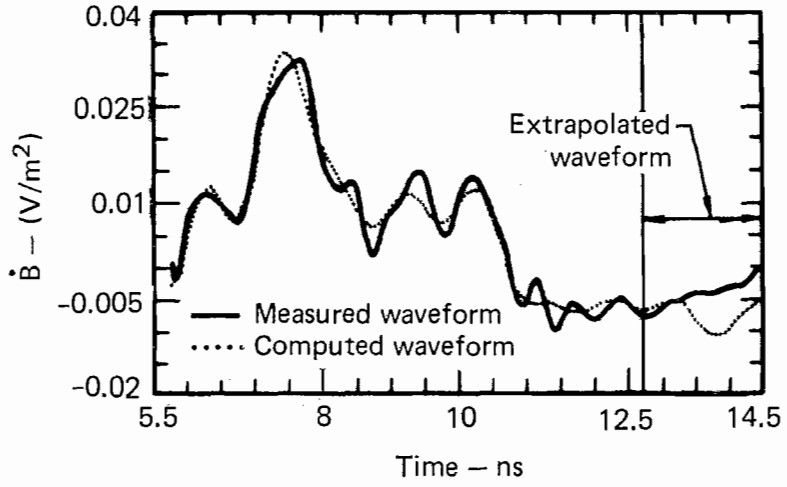

Figure G6. (b) Measured and reconstructed waveforms for cylinder 50 cm from ground plane.

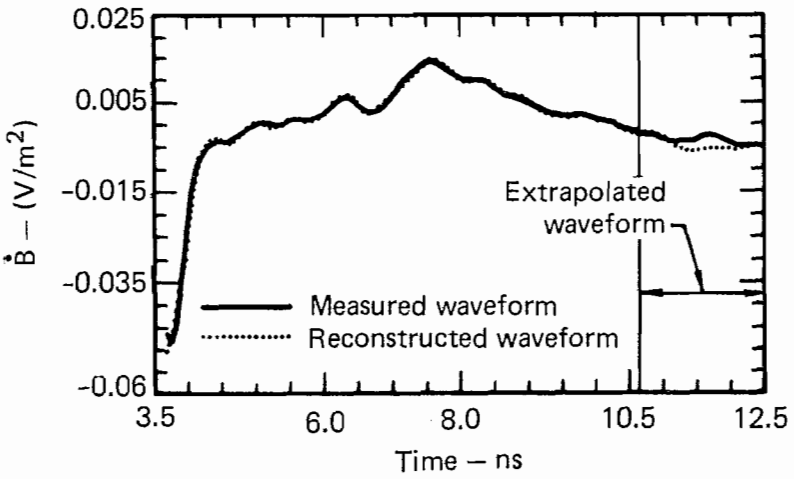

Figure G6. (c) Measured and reconstructed waveforms for cylinder 2 m from ground plane. (Note: Only free-space portion of waveform is used for the Prony analysis.)

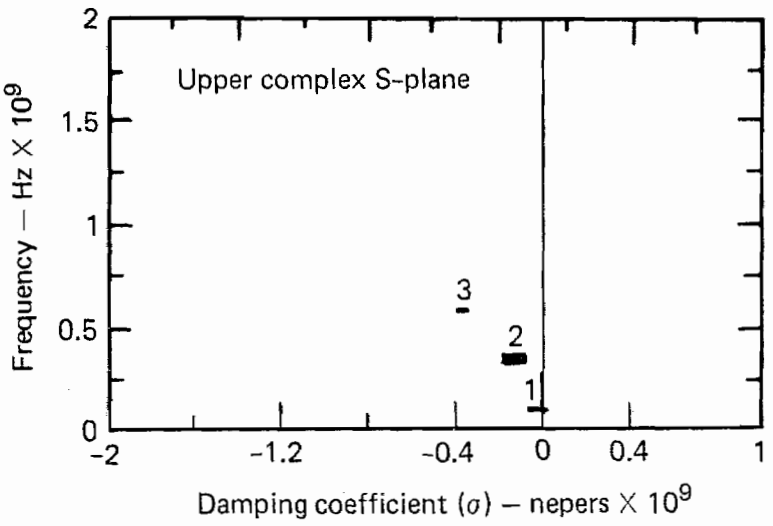

Figure G7. (a) Mean pole locations for cylinder 10 cm from perfectly conducting ground plane. Poles are obtained from $\dot{D}$ sensor output.

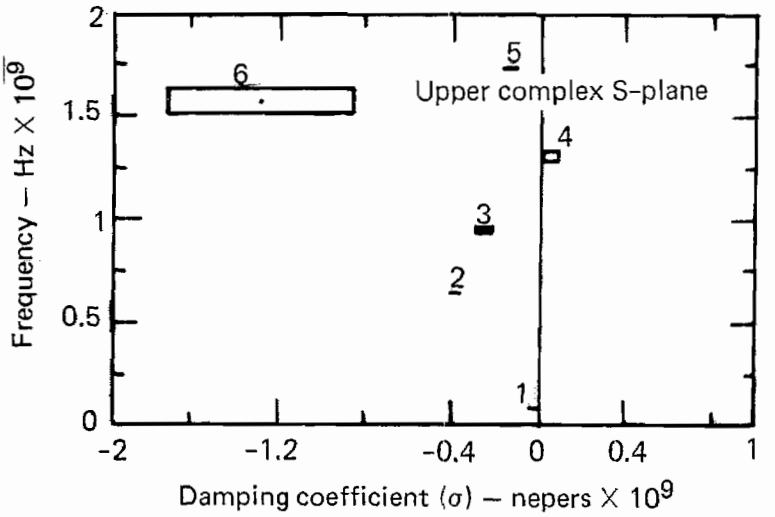

Figure G7. (b) Mean pole locations for cylinder 50 cm from perfectly conducting ground plane. Poles are obtained from $\dot{D}$ sensor output.

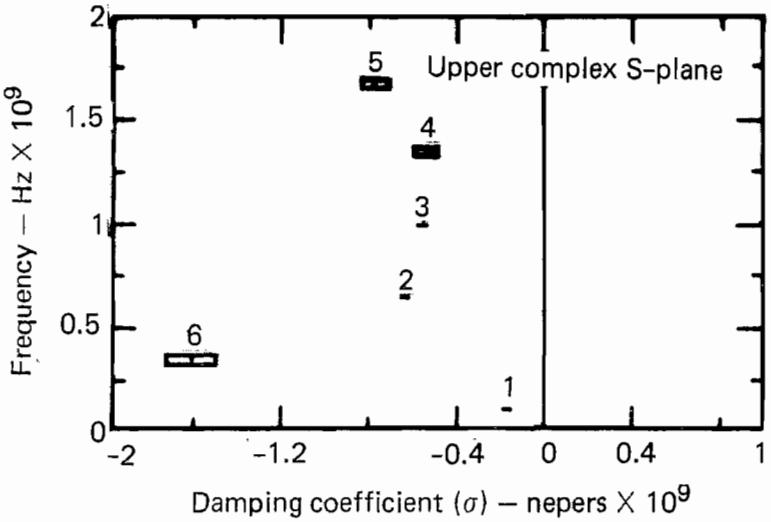

Figure G7. (c) Mean pole locations for cylinder 2 m (free-space) from perfectly conducting ground plane. Poles are obtained from $\dot{D}$ sensor output.

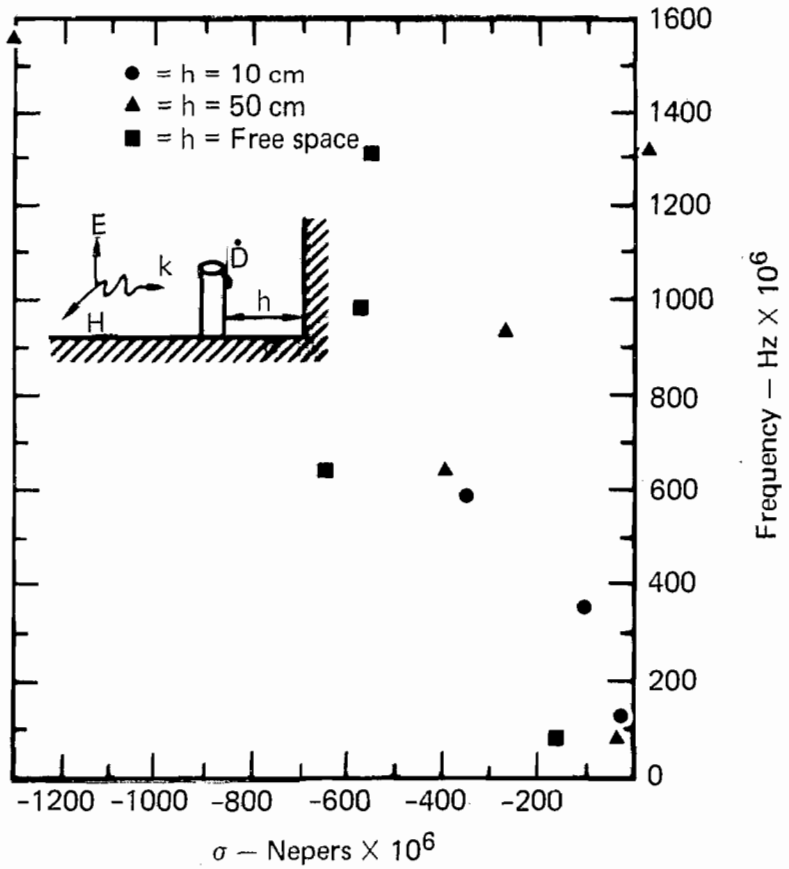

Figure G8. Composite pole plot for the $\dot{D}$ sensor on the cylinder.

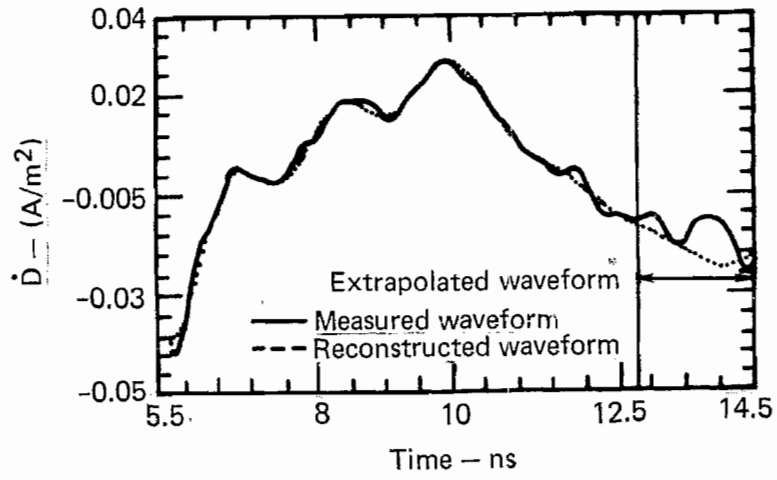

Figure G9. (a) Measured and reconstructed waveforms for $\dot{D}$ sensor output on cylinder 10 cm from ground plane.

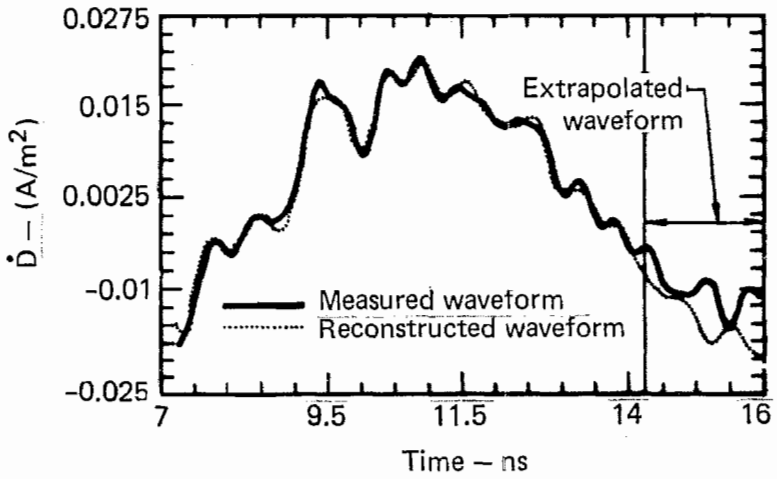

Figure G9. (b) Measured and reconstructed waveforms for $\dot{D}$ sensor output on cylinder 50 cm from ground plane.

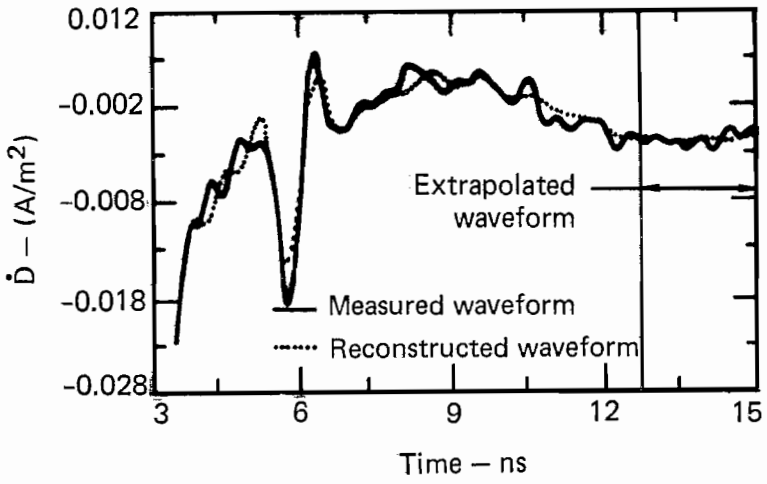

Figure G9. (c) Measured and reconstructed waveforms for $\dot{D}$ sensor output on cylinder 2 m from ground.

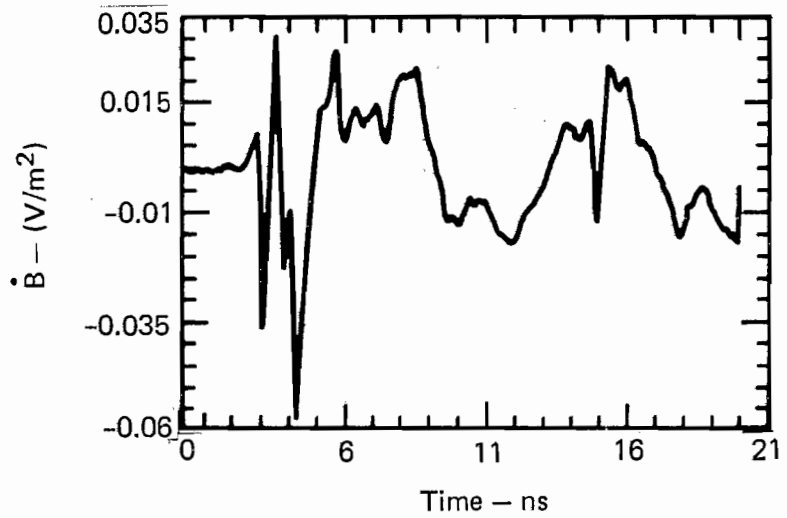

Figure G10. (a) $\dot{B}$ sensor response for crossed cylinder 10 cm (2a) from ground plane.

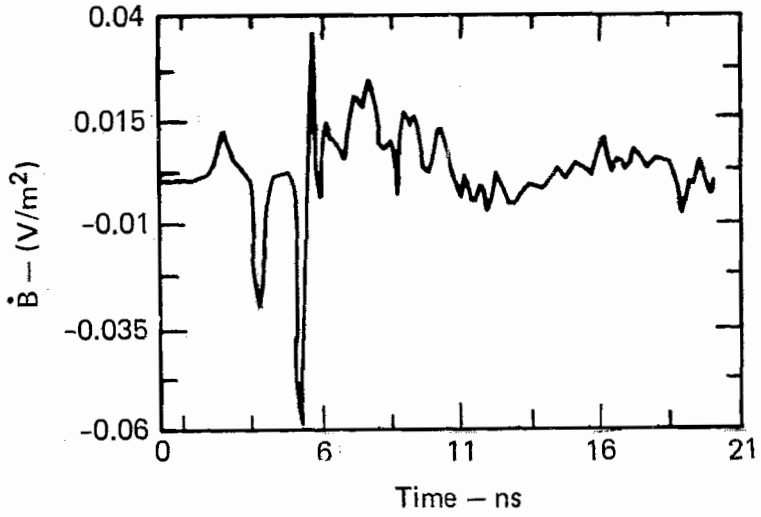

Figure G10. (b) $\dot{B}$ sensor output for crossed cylinder 50 cm (10a) from ground plane.

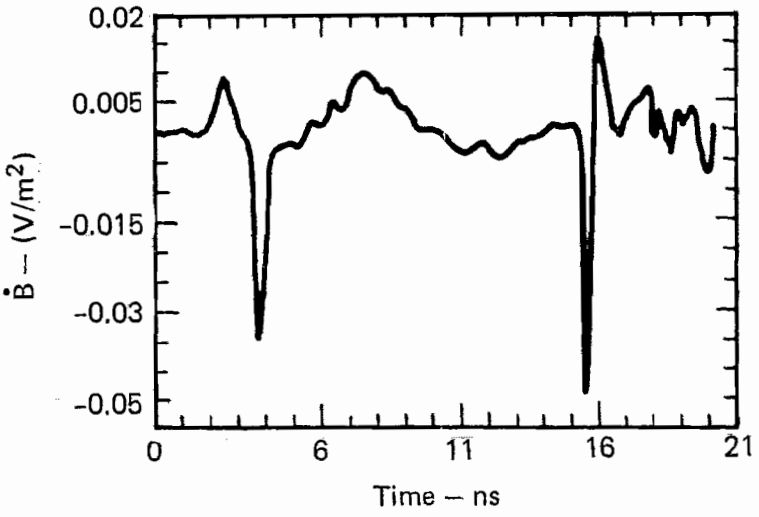

Figure G10. (c) $\dot{B}$ sensor output for crossed cylinder 2 m (40a) from ground plane.

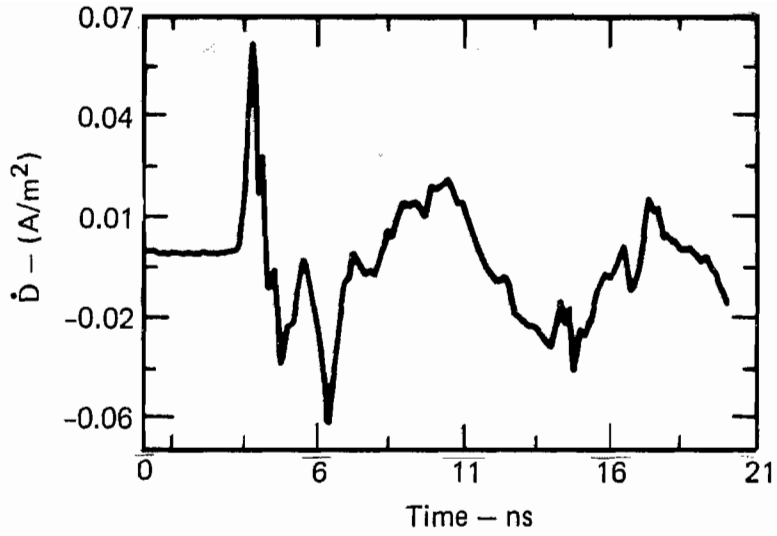

161

Figure G11. (a) $\dot{D}$ sensor output for crossed cylinder 10 cm (2a) from ground plane.

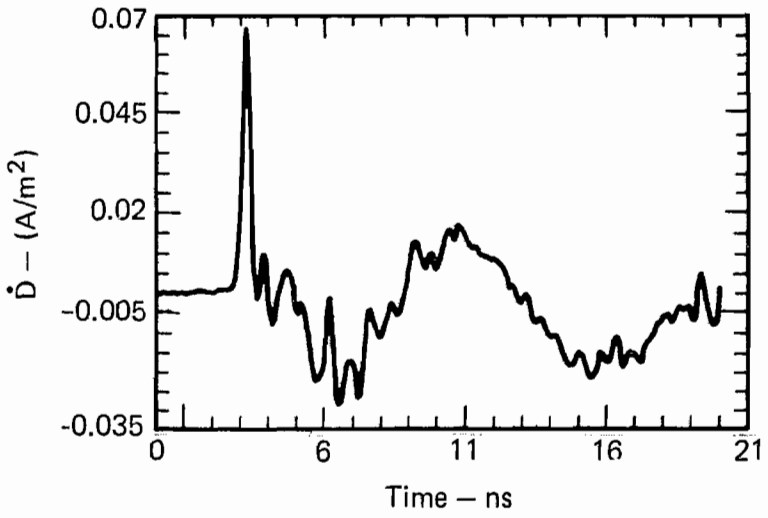

Figure G11 (b) $\dot{D}$ sensor output for crossed cylinder 50 cm from ground plane.

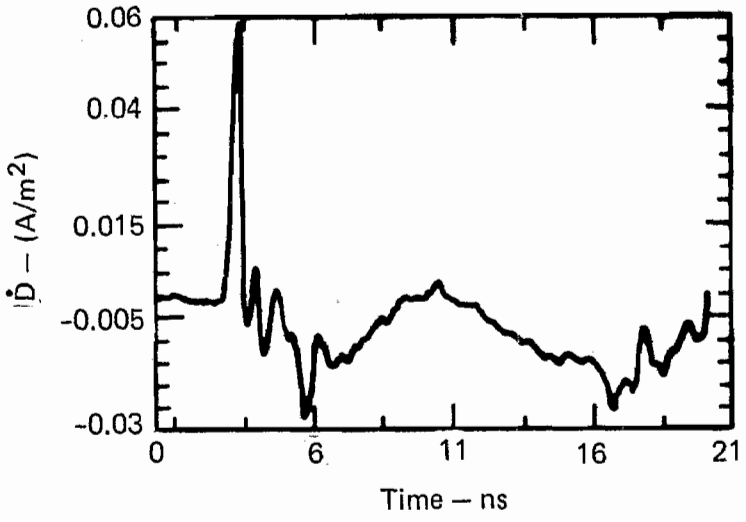

Figure G11. (c) $\dot{D}$ sensor output for crossed cylinder 2 m from ground plane.

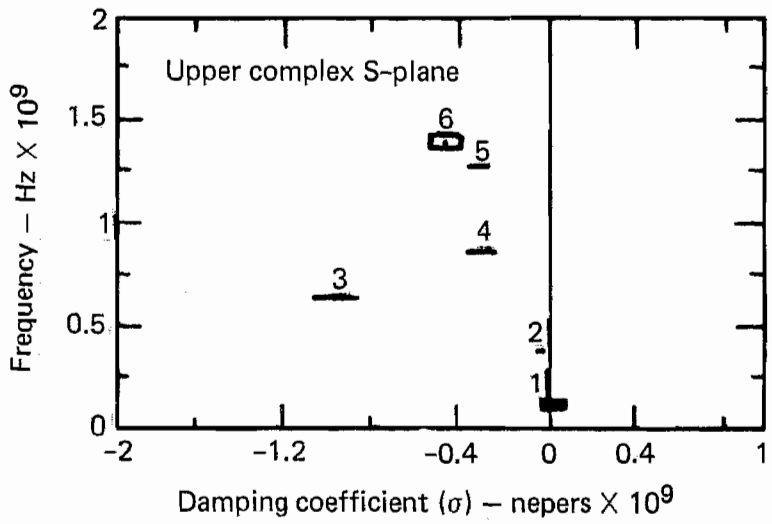

Figure G12. (a) Mean $\dot{B}$ pole location for crossed cylinder 10 cm from perfectly conducting gorund plane (θ = 180°).

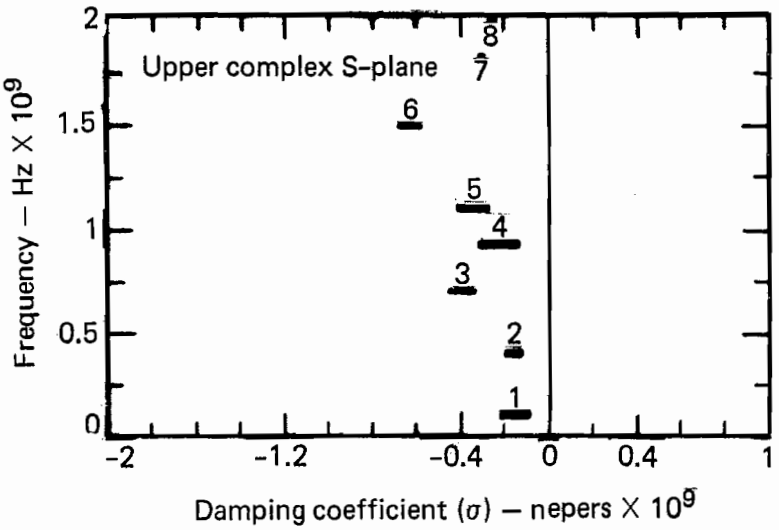

Figure G12. (b) Mean $\dot{B}$ pole locations for crossed cylinder 50 cm from perfectly conducting ground plane (θ = 180°).

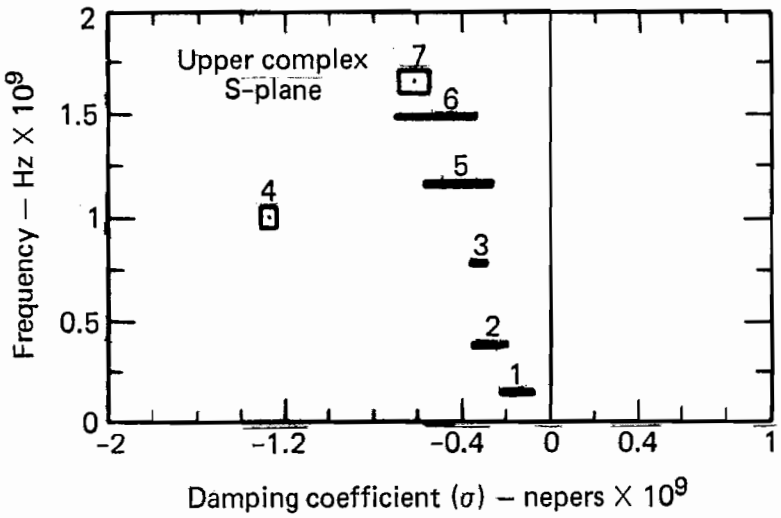

Figure G12. (c) Mean $\dot{B}$ pole locations for crossed cylinder 2 m from perfectly conducting ground plane (θ = 180°).

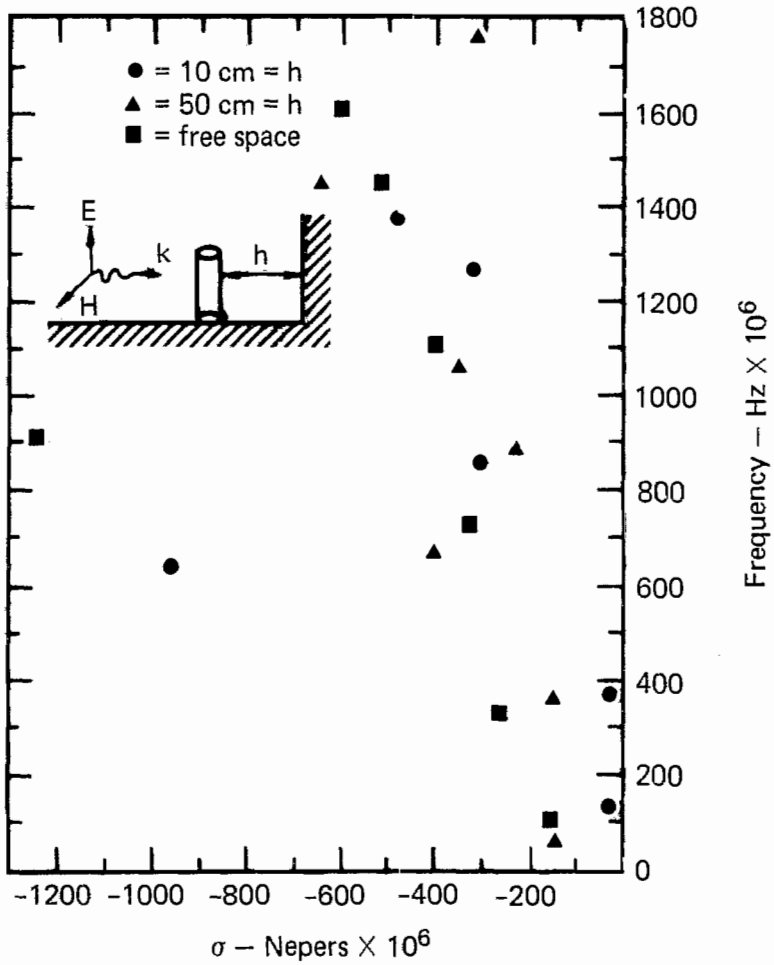

Figure G13. Pole locations for crossed cylinder $\dot{B}$ sensor (θ = 180°).

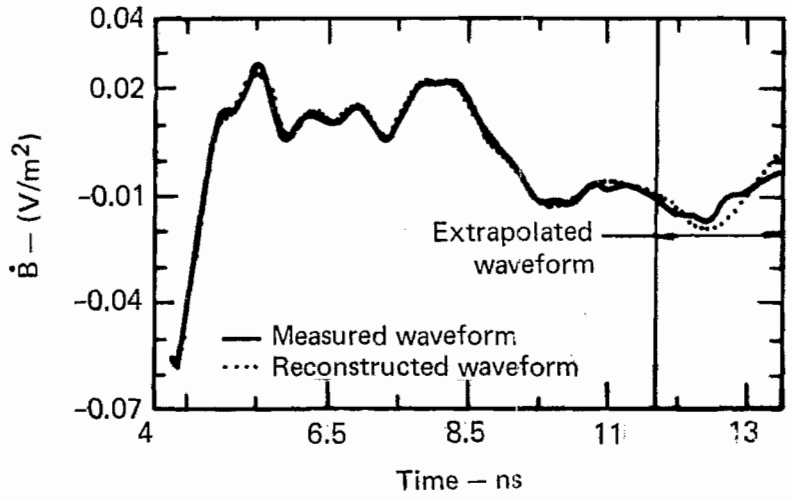

Figure G14. (a) Measured and reconstructed $\dot{B}$ waveforms for crossed cylinder 10 cm from ground plane.

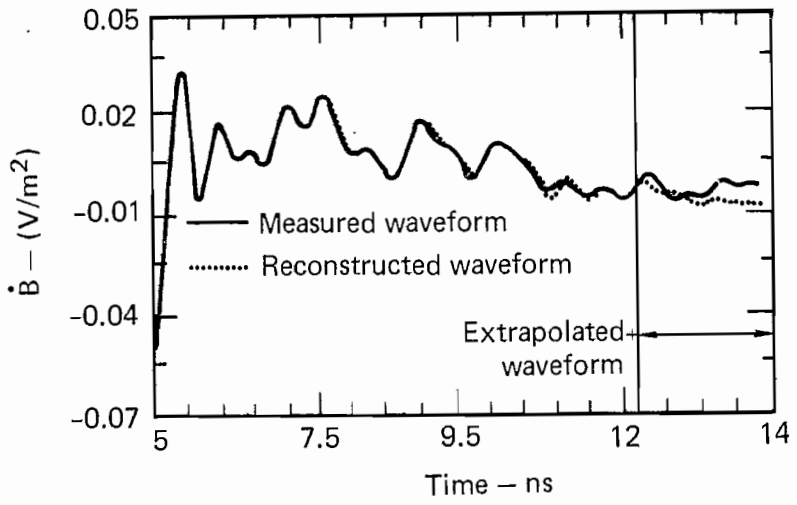

Figure G14. (b) Measured and reconstructed $\dot{B}$ waveforms for crossed cylinder 50 cm from ground plane

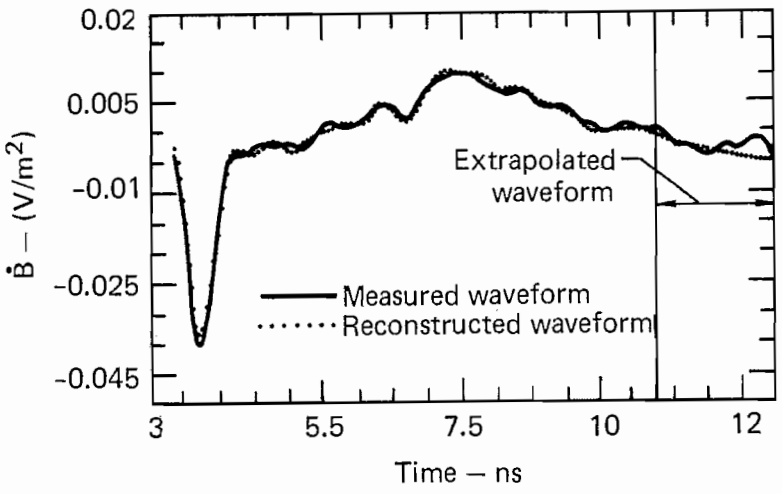

Figure G14. (c) Measured and reconstructed $\dot{B}$ waveforms for crossed cylinder 2 m from ground plane.

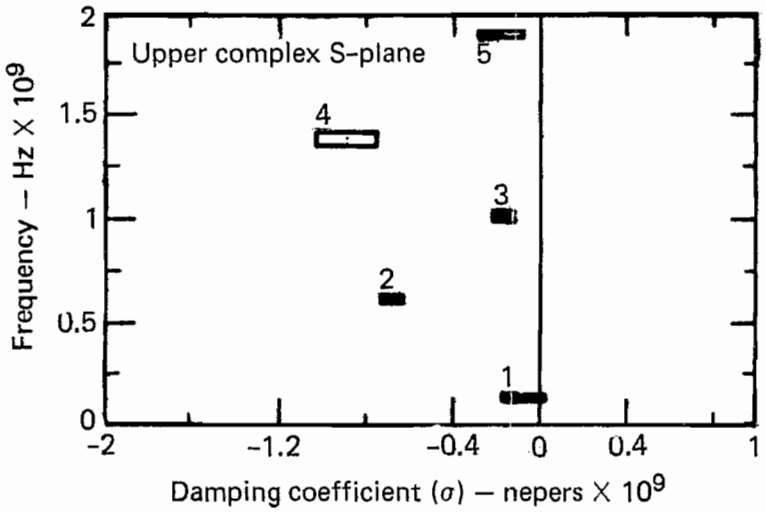

Figure G15. (a) Mean $\dot{D}$ pole locations for crossed cylinder 10 cm from ground plane (θ = 180°).

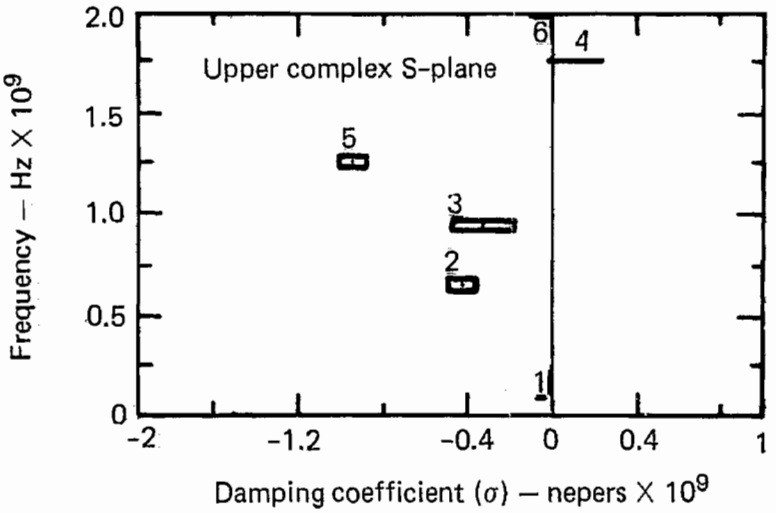

Figure G15. (b) Mean $\dot{D}$ pole locations for crossed cylinder 50 cm from ground plane (θ = 180°).

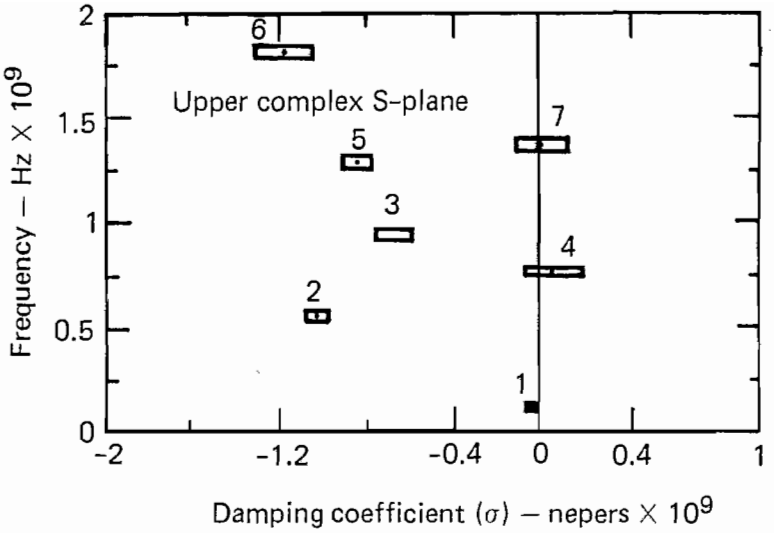

Figure G15 (c). Mean $\dot{D}$ pole locations for crossed cylinder 2 m from ground plane (θ = 180).

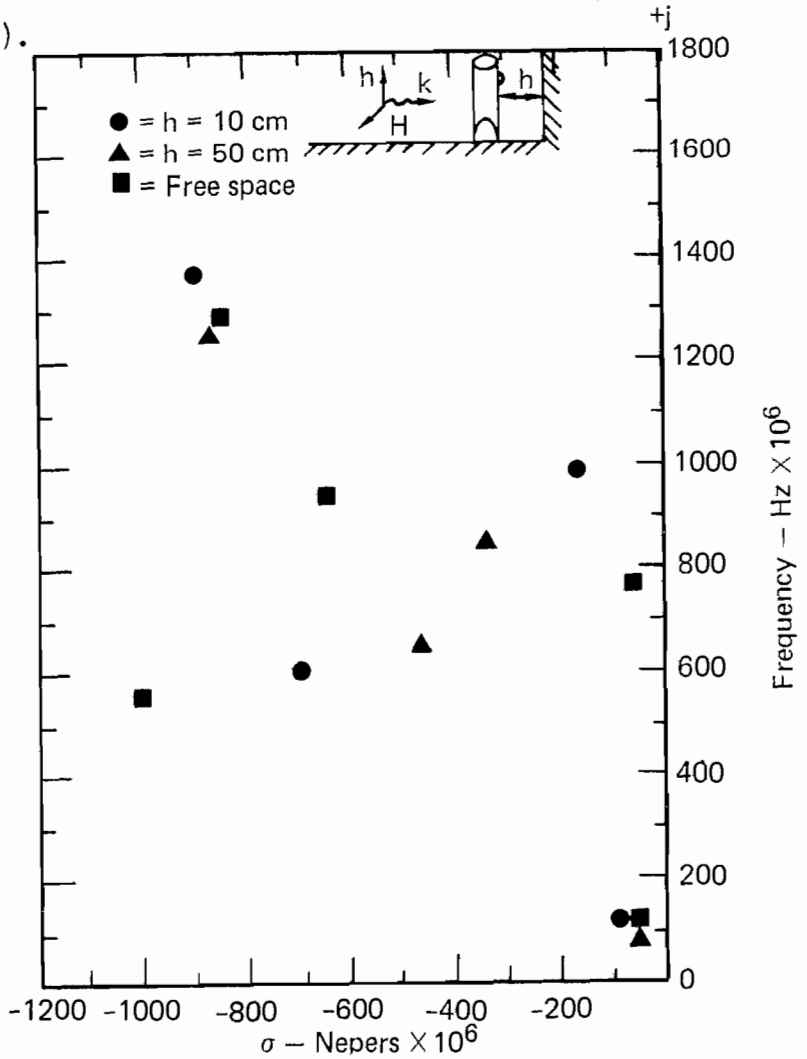

Figure G16. Pole plot for $\dot{D}$ sensor on crossed cylinder.

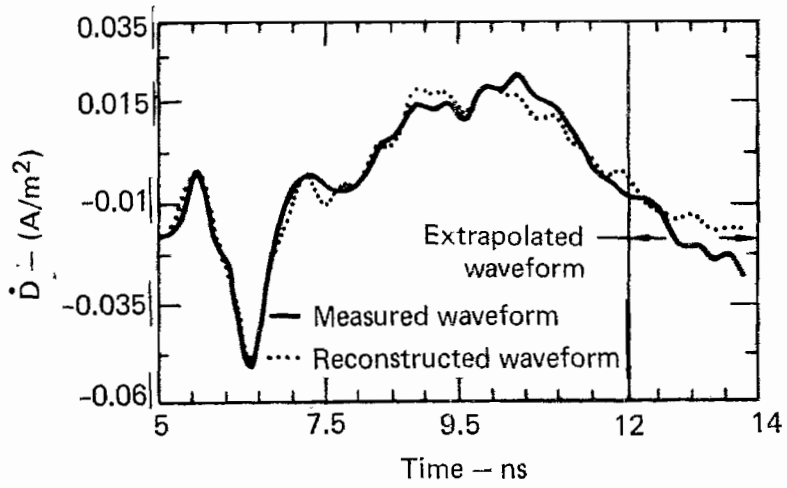

Figure G17. (a) Measured and reconstructed $\dot{D}$ waveforms for crossed cylinder 10 cm from ground plane.

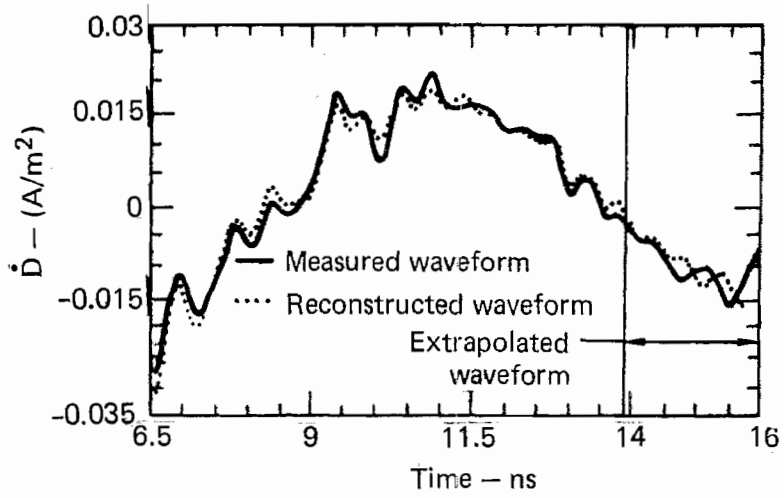

Figure G17. (b) Measured and reconstructed $\dot{D}$ waveforms for crossed cylinder 50 cm from ground plane.

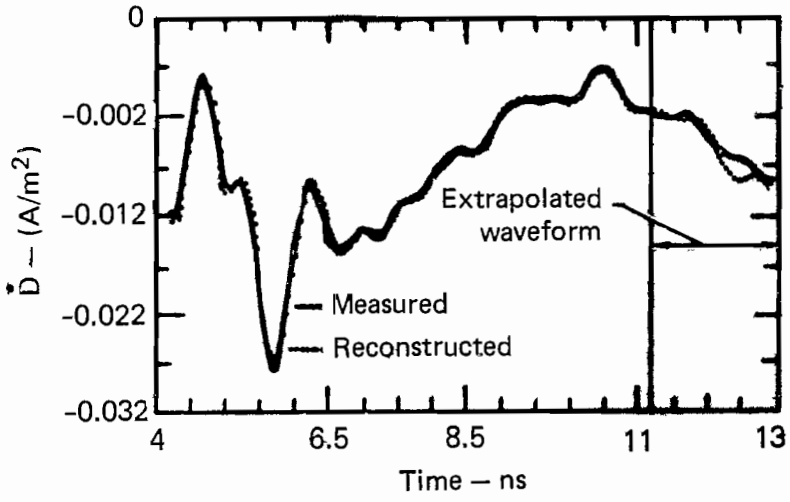

Figure G17. (c) Measured and reconstructed $\dot{D}$ waveforms for crossed cylinder 2 m from ground plane.

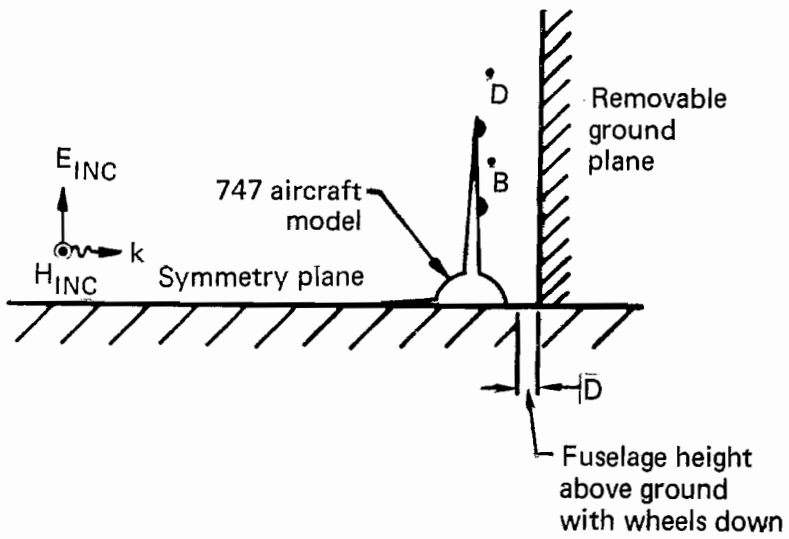

Figure G18. Experimental configuration for 747 measurements over a perfectly conducting ground plane.

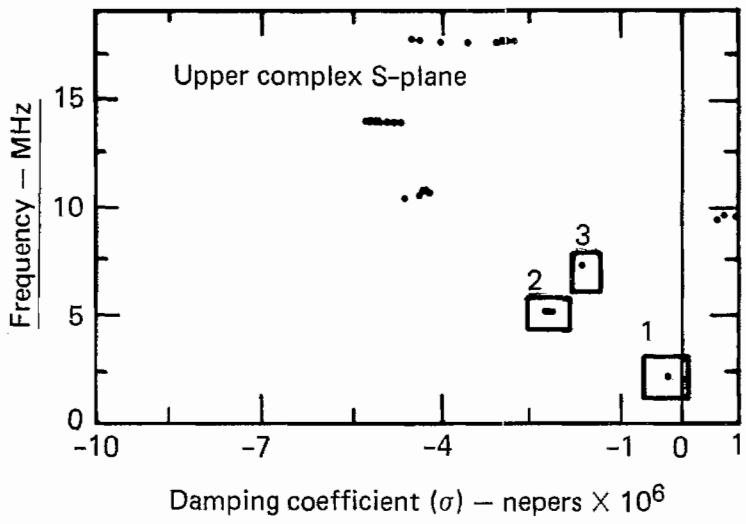

Figure G19. (a) Pole locations found for $\dot{D}$ signal on 747 wing tip with aircraft over a perfectly conducting ground plane.

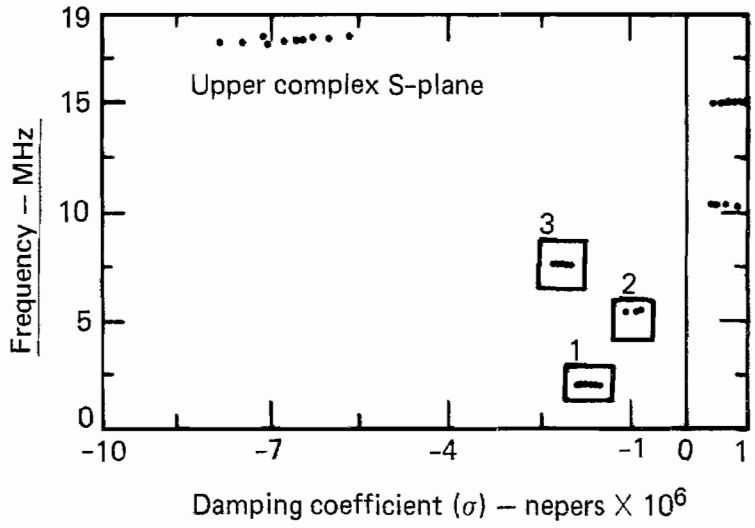

Figure G19. (b) Pole locations found for $\dot{D}$ signal on 747 wing tip with aircraft in free space.

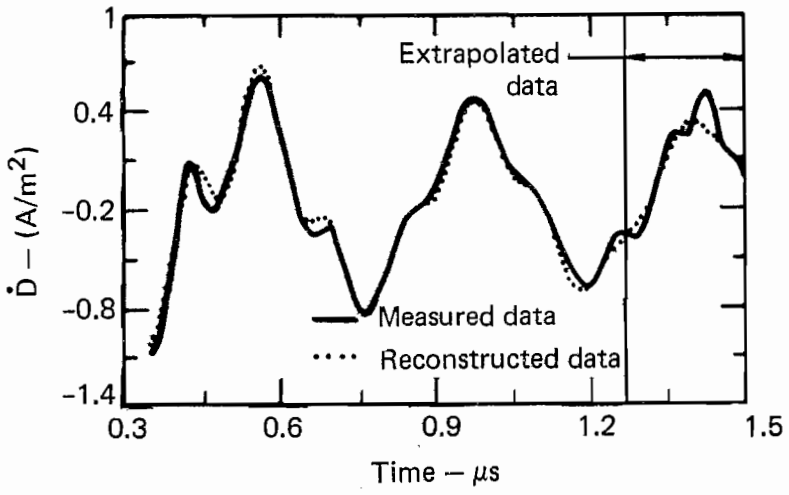

Figure G20. (a) Prony reconstruction of time-domain $\dot{D}$ signal on wing tip with ground plane in place.

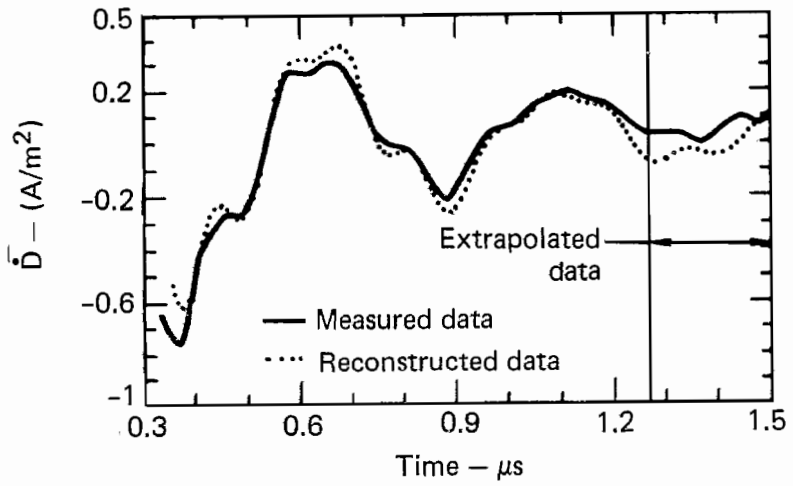

Figure G20. (b) Prony reconstruction of time-domain signal on wing tip with ground plane absent.

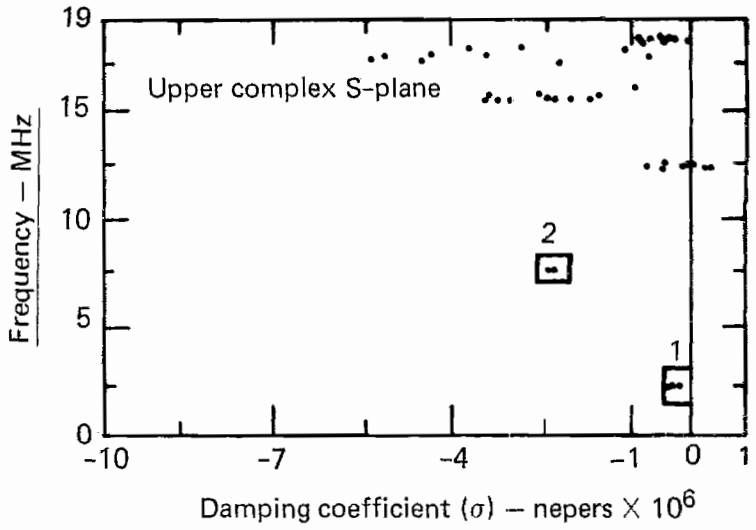

Figure G21. (a) Pole locations found for $\dot{B}$ sensor on 747 wing with aircraft over a perfectly conducting ground plane.

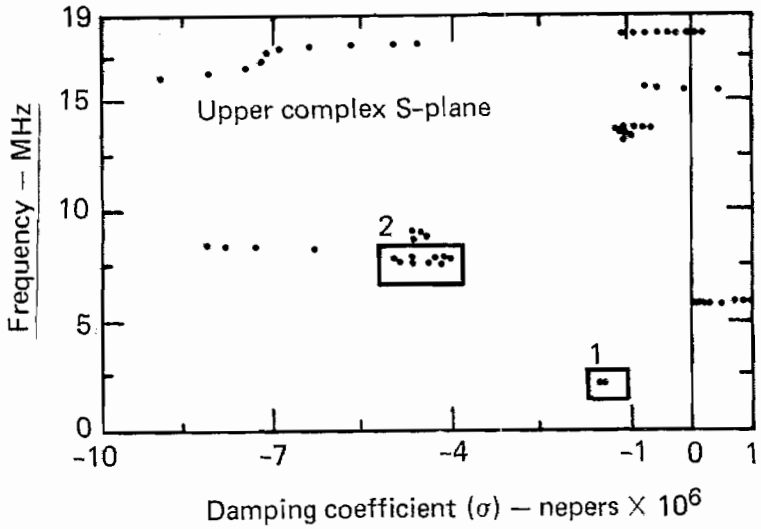

Figure G21. (b) Pole locations found for $\dot{B}$ sensor on 747 aircraft in free space.

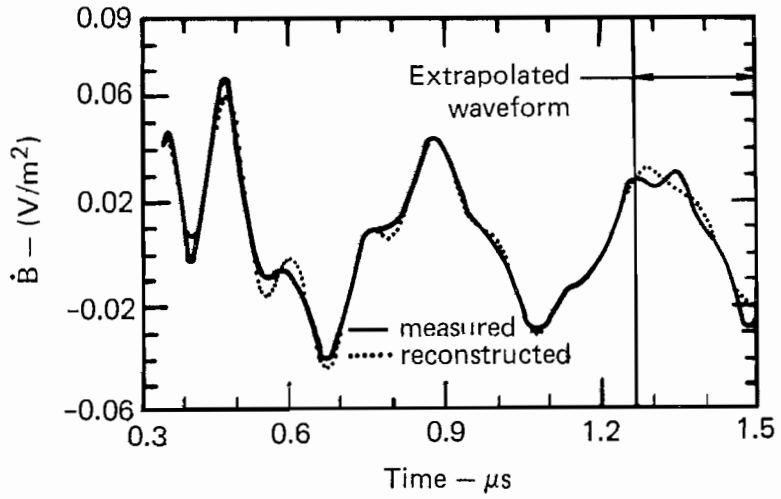

Figure G22. (a) Measured and reconstructed $\dot{B}$ waveforms for 747 over a perfectly constructed ground plane.

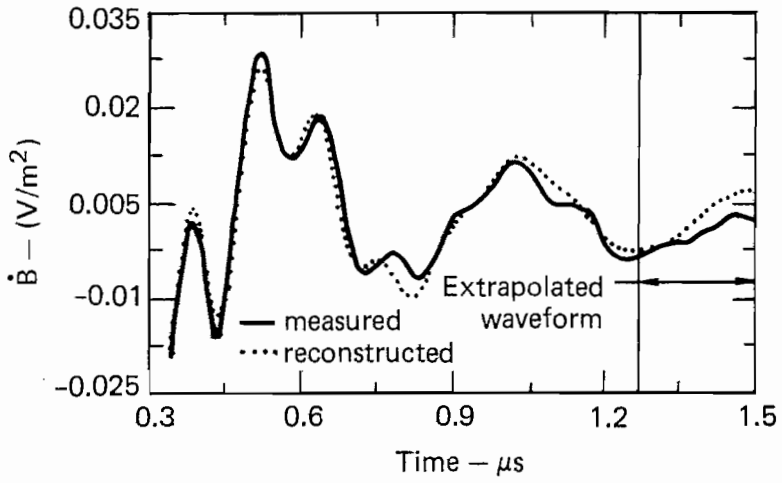

Figure G22. (b) Measured and reconstructed $\dot{B}$ waveforms for 747 in free space.

☆U.S. GOVERNMENT PRINTING OFFICE : 1981–576-115/518